Meshfree micromechanical modelling of the mechanical properties and responses of woven composites

Yanhong Chen

Department of Aeronautics

Imperial College London

London SW7 2AZ

This thesis is submitted for the degree of Doctor of Philosophy and the Diploma of Imperial College London

March 2017

DECLARATION

I hereby declare that this thesis, and the research to which it refers, are the product of my own work, and has not been submitted for any other degree or award. Ideas and results from the work of other people are fully acknowledged.

Yanhong Chen

March 2017

ACKNOWLEDGEMENTS

First and foremost, I would like to express my deepest gratitude to my supervisor Prof Ferri M. H. Aliabadi for his inspirational guidance, encouragement and endless support throughout my PhD research. Without these, it would be not possible for me to complete the work presented in this thesis.

I am really grateful to Dr Pihua Wen from School of Engineering and Materials Science, Queen Mary University of London. For his invaluable suggestions on developing unit cell models and the application of meshfree methods, I am indebted.

I would like to take this opportunity to express my sincere appreciation to Dr Zhongwei Guan at the Centre for Materials and Structures, the University of Liverpool for offering composite materials, as well as access to their Polymer Lab and Impact Lab to fabricate woven composite specimens and conduct experimental tests.

Special thanks go to my external examiner Prof Nik Petrinic and internal examiner Dr Giuliano Allegri for their helpful discussions on my work and invaluable suggestions for improving my thesis.

Finally, I wish to express my gratefulness to my family for their encouragement and my wife for her everlasting love and support. Without their encouragement and support, this work would never come to fruition.

ABSTRACT

Obtaining a clear understanding of the elastic properties and overall responses of woven composites is a significant prerequisite for cost-effective design of these materials. Such an understanding is often achieved via developing unit cell (UC) models using analytical or the FEM-based approaches, which leads to either the problem of a reduced accuracy, resulting from the analytical nature, or the concern of high complexity, associated with using elements. The aim of this work is to simultaneously address the above concerns by developing a meshfree-based UC modelling approach to predict the elastic properties and overall responses of woven composites. Specifically, high-fidelity UC models have been developed to describe the internal architecture of woven composites, which addresses the accuracy problem in analytical approaches. Also, meshfree methods have been employed to implicitly implement the UC models, eliminating the complexity problem in the FEM-based approaches. For predicting the overall responses, constitutive modelling has been performed for the constituents of woven composites, with a viscoplasticity-based model being selected to describe the nonlinear and rate-dependent behaviour of polymer matrix and Weibull function based formulations being proposed to identify the damage of yarn material. Furthermore, in-house computer programs implementing the UC models, the constitutive models and the meshfree methods have been coded, and numerical examples have been conducted for predicting the elastic properties and overall responses of woven composites. It has been demonstrated that the meshfree predictions agree well with the experimental results and the data in the literature, validating the proposed approach. The significance of this work is that it eliminates the problems in traditional approaches and meanwhile extends the capability of the UC modelling methodology from homogenising only the elastic properties in the normal directions to predicting the elastic properties and overall responses of woven composites in both the normal and off-axis directions.

CONTENTS

Contents

LIST OF FIGURES

LIST OF TABLES

NOMENCLATURE

Symbols for material models

α	Material constant of the original damage model
β	Material constant of the improved damage model
β_i	Material constant of the improved damage model ($i = 1, ... ,6$)
β_m	Damage evolution coefficient of polymer matrix
γ_{ij}	Engineering shear strain component ($ij = 12, 23, 31$)
δ_{ij}	Kronecker delta tensor or component
ε	Uniaxial strain
$\dot{\varepsilon}$	Uniaxial strain rate
$\dot{\varepsilon}_0$	Reference strain rate
ε_{ij}	Strain tensor or component ($i, j = 1,2,3$)
$\dot{\varepsilon}_{ij}$	Strain rate tensor or component ($i, j = 1,2,3$)
$\dot{\varepsilon}_{ij}^{\mathrm{E}}$	Elastic strain rate tensor or component ($i, j = 1,2,3$)
$\dot{\varepsilon}_{ij}^{\mathrm{I}}$	Inelastic strain rate tensor or component ($i, j = 1,2,3$)
$\varepsilon_s^{\mathrm{I}}$	Inelastic strain at saturation
$\varepsilon_{\mathrm{m0}}$	Failure strain of matrix material at reference strain rate
$\varepsilon_{\mathrm{mf}}$	Failure strain of matrix material
$\boldsymbol{\varepsilon}$	Strain vector or tensor
$\boldsymbol{\varepsilon}_{\mathrm{m}}$	Strain vector of matrix material
$\boldsymbol{\varepsilon}_{\mathrm{y}}$	Strain vector of yarn material
$\boldsymbol{\varepsilon}^l$	Strain vector of yarn material in the LCS
$\boldsymbol{\varepsilon}^g$	Strain vector of yarn material in the GCS
ρ_{m}	Density of matrix material
ρ_{y}	Density of yarn material
σ	Uniaxial stress

Nomenclature

σ_{ij}	Stress tensor or component ($i, j = 1, 2, 3$)
σ_s	Stress at saturation
$\boldsymbol{\sigma}$	Stress vector or tensor
$\boldsymbol{\sigma}_m$	Stress vector of matrix material
$\boldsymbol{\sigma}_y$	Stress vector of yarn material
$\boldsymbol{\sigma}^l$	Stress vector of yarn material in the LCS
$\boldsymbol{\sigma}^g$	Stress vector of yarn material in the GCS
τ_{ij}	Shear stress component ($ij = 12, 23, 31$)
ω_i	Damage variable ($i = 1, \ldots, 6$)
ω_{iaB}	Damage variable of failure mode $iaB = 1fT, 1fC \ldots$
Ω_m	Internal stress at saturation
Ω_{ij}	Internal stress tensor or component
$\dot{\Omega}_{ij}$	Internal stress rate tensor or component
c_{ijkl}	The fourth-order elasticity tensor or component
C_{EL}	Rate-dependence parameter of yarn material
$C_{m\varepsilon}$	Rate-dependence parameter of matrix material
$\mathbf{C}$	Elasticity matrix
$\mathbf{C}_m$	Elasticity matrix of matrix material
$\mathbf{C}^l$	Elasticity matrix of yarn material in the LCS
$\mathbf{C}^g$	Elasticity matrix of yarn material in the GCS
$\mathbf{C}(\omega)$	Damaged elasticity matrix of yarn material
D_0	Maximum inelastic strain rate
E_m	Young's modulus of matrix material
E_L	Longitudinal Young's modulus of yarn material
E_{L0}	Longitudinal Young's modulus of yarn material at reference strain rate
E_T	Transverse Young's modulus of yarn material
f_{iaB}	Failure function of failure mode $iaB = 1fT, 1fC, 2mC, 2mS, 3mC, 3mS$
G_m	Shear modulus of matrix material
G_{LT}	Longitudinal-transverse shear modulus of yarn material
G_{TL}	Transverse-longitudinal shear modulus of yarn material
G_{TT}	Transverse shear modulus of yarn material

J_2	The second invariant of the overstress
n_{r}	Material constant of the viscoplasticity-based model
q	Hardening rate of matrix material
$\mathbf{R}$	Rotation matrix
S_{LT}	Longitudinal-transverse shear strength of yarn material
S_{TT}	Transverse-longitudinal shear strength of yarn material
S_{TL}	Transverse shear strength of yarn material
S_{ij}	Deviatoric stress tensor or component
$\mathbf{S}$	Inverse of elasticity matrix
$\mathbf{S}_{\mathrm{m}}$	Inverse of elasticity matrix of matrix material
$\mathbf{S}^l$	Inverse of elasticity matrix of yarn material in the LCS
$\mathbf{S}^g$	Inverse of elasticity matrix of yarn material in the GCS
$\mathbf{S}(\omega)$	Inverse of damaged elasticity matrix of yarn material
$\mathbf{S}_{\mathrm{d}}(\omega)$	Direct part of $\mathbf{S}(\omega)$
$\mathbf{S}_{\mathrm{s}}(\omega)$	Shear part of $\mathbf{S}(\omega)$
$\mathbf{T}$	Transformation matrix of the equivalence approach
$\mathbf{T}_i$	Transformation matrix of the ith equivalent domain, D_i
$\mathbf{T}_\varepsilon^{g|l}$	Transformation matrix for strain from the LCS to the GCS
$\mathbf{T}_\varepsilon^{l|g}$	Transformation matrix for strain from the GCS to the LCS
$\mathbf{T}_\sigma^{g|l}$	Transformation matrix for stress from the LCS to the GCS
$\mathbf{T}_\sigma^{l|g}$	Transformation matrix for stress from the GCS to the LCS
$\mathbf{T}_c^{g|l}$	Transformation matrix for elasticity matrix from the LCS to the GCS
$\mathbf{T}_c^{l|g}$	Transformation matrix for elasticity matrix from the GCS to the LCS
v_{m}	Poisson's ratio of matrix material
v_{LT}	Longitudinal-transverse Poisson's ratio of yarn material
v_{TL}	Transverse-longitudinal Poisson's ratio of yarn material
v_{TT}	Transverse Poisson's ratio of yarn material
X_{T}	Longitudinal tensile strength of yarn material
X_{C}	Longitudinal compressive strength of yarn material
Y_{T}	In-plane transverse tensile strength of yarn material
Y_{C}	In-plane transverse compressive strength of yarn material

Z_T	Out-of-plane transverse tensile strength of yarn material
Z_C	Out-of-plane transverse compressive strength of yarn material
Z_0	Initial hardness of matrix material
$\langle \ \rangle$	Volume average operator or the Macaulay brackets

Symbols for meshfree methods

α_s	Support domain scaling coefficient
$\boldsymbol{\alpha}(\boldsymbol{x})$	Vector of unknown coefficients
Γ	Boundary
δ	Differentiation operator
$\boldsymbol{\zeta}$	Intermediate vector for shape function derivatives
η	Free parameter of the RBF method
θ	Free parameter of the RBF or MK method
$\boldsymbol{\lambda}$	Periodicity vector
$\boldsymbol{\xi}$	Difference vector of displacements
$\dot{\boldsymbol{\xi}}$	Difference vector of velocities
$\ddot{\boldsymbol{\xi}}$	Difference vector of accelerations
Π	Total potential energy
ρ	Density
$\boldsymbol{\phi}$	Shape function vector
$\boldsymbol{\phi}_{,i}$	First-order partial derivative of $\boldsymbol{\phi}$
$\boldsymbol{\phi}_{,ij}$	Second-order partial derivative of $\boldsymbol{\phi}$
$\boldsymbol{\Phi}$	Shape function matrix
$\boldsymbol{\Phi}_I$	Nodal shape function matrix
Ω	Domain
$\mathcal{L}$	Lagrangian function
a_0	Free parameter of the RBF or MK method
a_1	Free parameter of the RBF or MK method
a_2	Free parameter of the RBF or MK method
a_3	Free parameter of the RBF or MK method

A_s	Estimated support domain area
$\mathbf{A}(\boldsymbol{x})$	MLS weighted moment matrix
$\boldsymbol{b}$	Body force vector
$\boldsymbol{b}_I(\boldsymbol{x})$	I-th vector of moment matrix $\mathbf{B}$
$\mathbf{B}$	Strain matrix or moment matrix of the RBF or MK method
d_c	Average nodal spacing
$d_{\text{c}x}$	Average nodal spacing in X direction
$d_{\text{c}y}$	Average nodal spacing in Y direction
$d_{\text{c}z}$	Average nodal spacing in Z direction
d_I	Distance between node $\boldsymbol{x}_I$ and the point of interest $\boldsymbol{x}$
d_s	Size of support domain
D_s	Estimated support domain distance
$\boldsymbol{F}^\text{e}$	External force vector
$\boldsymbol{F}^\text{b}$	External body force vector
$\boldsymbol{F}^\text{i}$	Internal force vector
$\boldsymbol{F}^\text{t}$	External traction force vector
$\boldsymbol{g}$	Intermediate vector of the MK method
$\boldsymbol{G}$	Correlation matrix of the MK method
$\mathbf{I}_0$	Identity matrix
$\mathbf{K}$	Discretised stiffness matrix
$\mathbf{L}$	Differential operator
m	Number of polynomial terms
$\mathbf{M}$	Global or consistent mass matrix
$\mathbf{M}_\text{L}$	Lumped mass matrix
n	Number of support nodes
n_A	Number of field nodes within A_s
n_D	Number of field nodes within D_s
n_V	Number of field nodes within V_s
$n\text{F}x$	Number of field nodes in X direction
$n\text{F}y$	Number of field nodes in Y direction
$n\text{F}z$	Number of field nodes in Z direction
$n\text{C}x$	Number of background cells in X direction

nCy	Number of background cells in Y direction
nCz	Number of background cells in Z direction
N	Total number of field nodes
N_F	Total number of field nodes
N_C	Total number of background cells
$\boldsymbol{n}$	Unit outward normal vector
$\boldsymbol{n}^+$	Unit outward normal vector
$\boldsymbol{n}^-$	Unit inward normal vector
p	Order of polynomial basis function
$\boldsymbol{p}(\boldsymbol{x})$	Polynomial basis function
q	Free parameter of the RBF method
R_{mls}	Weighted residual of the MLS method
$\boldsymbol{r}(\boldsymbol{x})$	Vector of radial basis functions
$\mathbf{R}$	Moment matrix of the RBF method
t	time
T	Kinematic energy
$\boldsymbol{t}$	Traction force vector
u^h	Approximated field variable
U	Elastic strain energy
$\boldsymbol{u}$	Displacement vector of a field node or an integration point
$\dot{\boldsymbol{u}}$	Velocity vector of a field node or an integration point
$\ddot{\boldsymbol{u}}$	Acceleration vector of a field node or an integration point
$\boldsymbol{u}^\mathrm{s}$	Displacement vector of the field nodes in a local support domain
$\dot{\boldsymbol{u}}^\mathrm{s}$	Velocity vector of the field nodes in a local support domain
$\boldsymbol{U}$	Displacement vector of all field nodes in the whole problem domain
$\dot{\boldsymbol{U}}$	Velocity vector of all field nodes in the whole problem domain
$\ddot{\boldsymbol{U}}$	Acceleration vector of all field nodes in the whole problem domain
V_s	Estimated support domain volume
W	Work associated with external forces
$W(\boldsymbol{x})$	Weighted function
$\boldsymbol{x}$	Point of interest
$Z(\boldsymbol{x})$	Stochastic term of the MK method

Symbols for unit cells and PBCs

γ	Load reversal factor
γ_i	Load reversal factor corresponding to the ith equivalent domain, D_i
θ_0	Geometry parameter of the 3D woven normal mUC
θ_{binder}	Undulation angle of binder yarn
θ_{fill}	Undulation angle of fill yarn
θ_{warp}	Undulation angle of warp yarn
θ_{A}	Geometry parameter of the 3D woven off-axis mUC
θ_{B}	Geometry parameter of the 3D woven off-axis mUC
λ	Dimensionless parameter of mUC models
λ_{b}	Ratio parameter of the binder yarn of the 3D woven mUC
λ_{fa}	Ratio parameter of the lower or upper fill yarn of the 3D woven mUC
λ_{fb}	Ratio parameter of the middle layer of fill yarn of the 3D woven mUC
λ_{w}	Ratio parameter of the warp yarn of the 3D woven mUC
H	Height of normal or off-axis mUC models
H_{b}	Thickness of the binder yarn of the 3D woven mUC
H_{fa}	Thickness of the lower or upper fill yarn of the 3D woven mUC
H_{fb}	Thickness of the middle layer of fill yarn of the 3D woven mUC
H_{w}	Thickness of the warp yarn of the 3D woven mUC
L	Length of normal mUC models
L_{o}	Length of off-axis mUC models
m_0	Geometry parameter of the 3D woven normal mUC
p_{A}	Geometry parameter of the 3D woven off-axis mUC
p_{B}	Geometry parameter of the 3D woven off-axis mUC
s_0	Geometry parameter of the 3D woven normal mUC
$\mathbf{T}$	Transformation matrix of the equivalence approach
$\mathbf{T}_i$	Transformation matrix of the ith equivalent domain, D_i
v_{yarn}	Volume fraction of yarn material
v_{yf}	Intra-yarn fibre volume fraction
W	Width of normal mUC models
W_{o}	Width of off-axis mUC models

Abbreviations

ASTM	American Society for Testing and Materials
BEM	Boundary element method
CDM	Continuum damage mechanics
CFRP	Carbon fibre-reinforced polymer
CLT	Classical laminate theory
DBC	Derivative boundary condition
DEM	Diffuse element method
ECS	Equivalent coordinate system
EFGM	Element-free Galerkin method
FDM	Finite difference method
FEA	Finite element analysis
FEM	Finite element method
FPM	Finite point method
FRP	Fibre-reinforced polymer (or fibre-reinforced plastic)
FVF	Fibre volume fraction
GCS	Global coordinate system
GFRP	Glass fibre-reinforced polymer
GRF	Gaussian radial function
LCS	Local coordinate system
LRBF	Logarithmic radial basis function
LRPIM	Local radial point interpolation method
MK	Moving kriging
MLPGM	Meshless local Petrov-Galerkin method
MLS	Moving least squares
MQF	Multiquadric function
MSE	Mean squared error
mUC	Minimum unit cell
ODE	Ordinary differential equation
PBC	Periodic boundary condition
PDE	Partial differential equation
RBF	Radial basis function

RKPM	Reproducing kernel particle method
RPIM	Radial point interpolation method
rUC	Reduced unit cell
RVE	Representative volume element
SHPB	Split Hopkinson pressure bar
SPHM	Smooth particle hydrodynamics method
TPSF	Thin plate spline function
VBO	Viscoplasticity theory based on overstress

CHAPTER 1: INTRODUCTION

1.1 Background and literature review

1.1.1 General background

Fibre-reinforced polymers (FRPs), also referred to as fibre-reinforced plastics, are a class of composite materials made from a polymer matrix reinforced with fibres, such as carbon fibres, glass fibres and aramid fibres. The polymer matrix, which is generally low in density and strength, supports fibres and binds them together in the transverse directions, whereas the fibre reinforcement in return enhances the mechanical properties of the composites in the fibre direction. Compared to traditional materials, such as metals, the combination of the low-density polymer matrix and the high strength fibres offers FRP composites many advantages, such as a high strength-to-weight ratio, a high stiffness-to-weight ratio, the ability to be tailored to obtain enhanced properties in target directions, an improved corrosion resistance [1].

These desirable features have made the applications of FRP composites expanding from initially technology-intensive industries such as aerospace and military to today almost every field. The rapid expansion of FRP composites is accompanied by extensive research on experimentally characterising the mechanical behaviour of these materials. Therefore, many standardised experimental techniques have been developed to identify the static or quasi-static material properties of FRP composites. For example, the American Society for Testing and Materials (ASTM) has developed for polymer matrix composites a variety of standard test methods including ASTM D3039 [2] for measuring tensile properties, ASTM D3410 [3] and D6641 [4] for conducting compression tests with unsupported gauge section with shear loading and using a combined loading compression test fixture, ASTM D4255 [5] and D5379 [6] for obtaining shear properties by utilising the rail shear method and the V-notched beam method, and ASTM D7264 [7] for measuring flexural properties. Also, since FRP composites can be exposed to not only static applications but

also to dynamic loading scenarios, numerous experimental studies have been conducted and a variety of experimental techniques have been established to determine the material properties and overall responses of FRP composites subjected to various dynamic loading conditions, including 1) low velocity impact, where the strain rate is typically in between 10^{-3}/s and 10^2/s and servo-hydraulic or drop-weight test machines are often used [8-13]; 2) crash, where the strain rate can reach 10^2/s ~ 10^4/s and split Hopkinson pressure bars (SHPBs) can be utilised [14-25]; and 3) ballistic impact or explosion, where the strain rate is generally higher than 10^4/s and gas guns are often employed [26-30]. Furthermore, micromechanical test methods [31-37] such as the fibre pull-out/push-out and single fibre fragmentation techniques have been developed to characterise the fibre-matrix interface behaviour of FRP composites.

In addition to the development of experimental techniques, numerous theories, analytical methods and predictive models have been proposed to further our understanding of FRP composites from a mechanics point of view. For instance, analytical theories such as rules of mixtures and the classical laminate theory (CLT) have been established for predicting the elastic properties and analysing the stress or strain of unidirectional laminates. Also, many predictive models have been developed to identify the nonlinear, rate-dependent deformation of the polymer matrix in composites or that of the composite material as a whole [38-45]. Extensive research studies have been also conducted on characterising the complicated failure modes and mechanisms in FRP composites, such as matrix cracking [46-49], fibre kinking [50-62], delamination [63-72], matrix/fibre interface debonding [73-80] and progressive damage [81-84].

However, most of the existing experimental techniques, analytical theories and predictive models have been mainly designed for unidirectional FRP composites, and surprisingly, textile FRP composites have received much less attention even though these materials offer many advantages, such as a reduced notch sensitivity, a better impact resistance, an improved fracture toughness, a better drapability and lower fabrication costs, compared to their unidirectional counterparts. Admittedly, most of the experimental techniques that are initially designed for evaluating the overall behaviours of unidirectional composites are still applicable to textile composites. However, the analytical theories and numerical models that have been developed for unidirectional composites generally cannot be applied to textile composites owing to the significant difference in the internal geometries

of the two classes of composites. For example, it is very common to use different rules of mixtures to approximate the elastic properties of unidirectional composites based on the material properties and the volume fractions of the individual constituents; however, the exceptionally complex architecture of the fabric reinforcement in textile composites makes rules of mixtures totally collapse for evaluating the elastic properties. In sum, the understanding of textile FRP composites, from a modelling point of view, is not nearly as well-established as is the case of unidirectional FRP composites, and also the current methodologies for designing textile FRP composite structures are still largely based on time-consuming and sometimes financially prohibitive experiments or empirical trials. In the following two sections, a literature review will be conducted from the perspectives of both the elastic property prediction and the overall response prediction of textile FRP composites.

1.1.2 Elastic property prediction
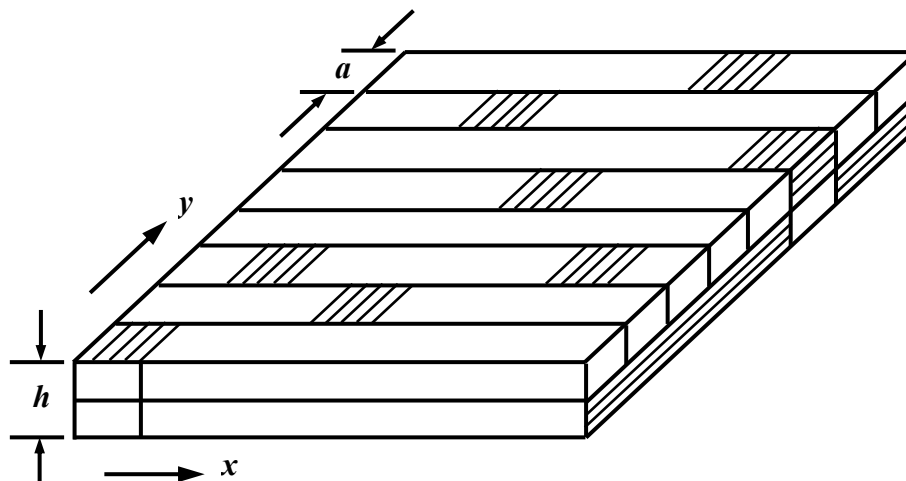
Figure 1.1: CLT-based idealisation of woven fabric composites [85]

To accurately predict the elastic properties of textile FRP composites, the main concern is how to effectively and efficiently account for the highly complex architecture of the fabric. However, the highly complex nature of textile composites makes it impractical to develop predictive models at the structure scale since modelling all the yarns within the composite structure would require unaffordable computational time and costs. To save time, the current methodology is mainly based on the concept of unit cell (UC), which is a small unit or region whose properties and response can be utilised to represent those of

the composite material. The UC modelling methodology typically involves three steps. First, a UC is identified by considering the periodicity of the composite material and the geometries of the constituents are explicitly modelled based on the UC. Then, the elastic behaviours of both the polymer matrix and the yarn material are modelled separately using material models such as the generalised Hooke's law. Lastly, based on the geometry and elasticity models of the constituents, the volume average stress and strain of the UC can be obtained for any prescribed boundary condition (typically in the form of applying displacement constraints to boundary nodes). By combining the volume average strain with the volume average stress of the UC, the effective (or homogenised) elastic constants and consequently the elastic properties of the composite material can be calculated.

The research on predicting the elastic properties of textile composites was pioneered by Ishikawa and Chou [85-88], Whitney and Chou [89], and Naik and Shembekar [90-92]. In their work, they focused on adapting the CLT to idealise textile composites as an assemblage of laminate plates arranged in parallel and/or series manners (see Fig. 1.1). Due to the use of such an idealisation, these CLT-based models allow for the development of analytical equations that are capable of efficiently calculating the elastic properties of textile composites. However, the analytical nature of the CLT-based models introduces a limitation, which is that the internal architecture of textile composites is oversimplified and thus the accuracy of the prediction may not be always guaranteed.

Because of the recent development in computer technology and computational methods such as the finite element method (FEM), several numerical models have been proposed for predicting the elastic properties of textile composites. Notable examples include those developed by Chung and Tamma [93], Wen and Aliabadi [94] and Bacarreza *et al.* [95] for plain woven composites, by Ng *et al.* [96], Whitcomb and Tang [97] and Dixit *et al.* [98] for twill woven composites, and by Tan *et al.* [99], Lee *et al.* [100] and Bogdanovich [101] for three-dimensional (3D) orthogonal woven composites. In these numerical UC models, the internal architecture of textile composites including the cross-section and waviness of yarns is considered in detail. More sophisticated models have also been developed by Lomov and co-workers [102, 103], Hallett and co-workers [104-107] and Durville [108, 109], where the effect of fabric compaction and/or layer interaction in the material properties of textile composites are taken into account, apart from considering the internal architecture.

4

As the models outlined above account for the internal architecture in detail, they can predict the elastic properties of textile FRP composites with high accuracy. However, a concern of using the existing numerical models is that most of them are designed to be implemented using the standard FEM, requiring additional efforts in explicitly building the highly complex geometries for the individual constituents and discretising them using high-quality elements and meshes, see Fig. 1.2 for example. Furthermore, the detailed modelling of the internal features of textile composites poses an increased complexity for assigning the material properties for the constituents, particularly, the ever-changing material orientations for the yarns, see Fig. 1.3 for example. Although the above problems might be addressed using pre-processing toolkits for textile composites, such as WiseTex [110, 111], which is developed by the Composites Materials Group at the University of Leuven, and TexGen [112-114], which is developed by the Composites Research Group at the University of Nottingham, it is still of both academic and practical interests to bypass these problems whenever possible.
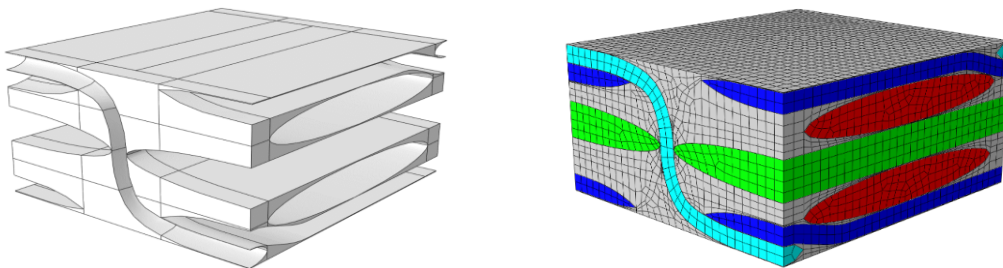
Figure 1.2: Complex constituent geometry & mesh design in 3D composites [95]
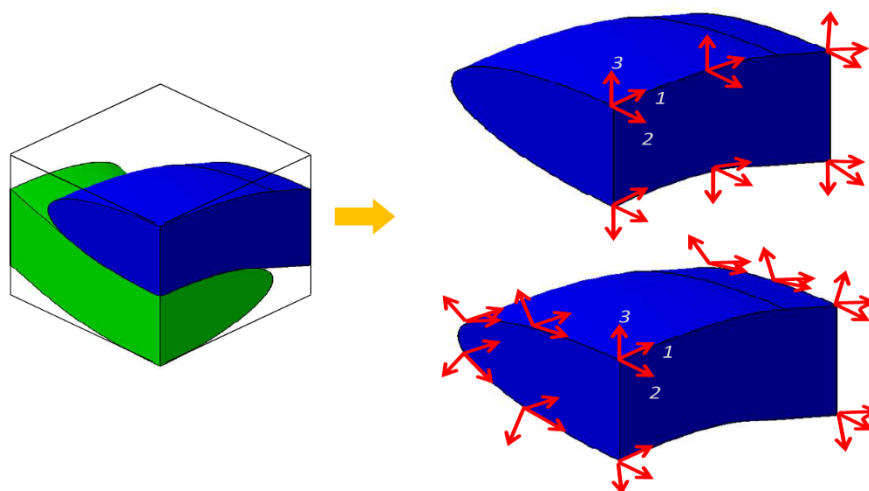
Figure 1.3: Ever-changing material orientations in the yarns [115]

1.1.3 Overall response prediction

Apparently, addressing the above concerns contributes to a better understanding of textile composites in terms of their elastic properties or behaviours. However, obtaining a clear understanding of textile composites requires predicting not only the elastic properties but also the overall response in the inelastic regime. In addition, it is sometimes desirable to obtain an understanding of how the individual behaviour (e.g. the nonlinear behaviour of the polymer matrix) of each constituent contributes to the overall response of the whole composite structure. Compared to the former, which involves only the prediction of the elastic properties, the latter remains a significant challenge.

Recently, however, several detailed studies have been performed to predict the overall response of textile FRP composites. The modelling methods utilised in these studies can be largely classified into two categories, namely, macromechanics-based approaches and micromechanics-based approaches. When utilising macromechanics-based approaches, a textile composite material is often assumed to be a smeared, homogenous and orthotropic material, and its response is characterised in an average sense without considering the behaviours or responses of the constituents separately. Also, the initiation of damage in composites is determined using failure criteria, and the damage propagation is identified phenomenologically using damage variables. In many cases, the inelastic response of the composites is assumed to be the result of damage development. Based on the technique that is used to model damage evolution, macromechanics-based approaches can be further divided into continuum damage mechanics (CDM)-based approaches and energy-based approaches. The main difference between the two types of approaches is that the former models the damage evolution in textile composites based on strain softening techniques, while the latter using energy terms.

A notable example of using CDM-based approaches is the model jointly developed by Materials Science Corporation [116] and the University of Delaware [117]. Adapting from the strain softening theory proposed by Matzenmiller *et al.* [118], this model has been incorporated into the commercially available finite element software LY-DYNA as a user material model termed as MAT162. This material model was later adopted with or without modifications by some researchers [13, 119-121] to perform impact simulations of woven composites. Typical examples of using energy-based approaches include the

models proposed by Jenq *et al.* [122], Schwer and Whirley [123], Iannucci [124], Iannucci and Willows [125, 126] and Naik *et al.* [127, 128]. As both CDM-based and energy-based approaches model composites in an average sense, they are very efficient and suitable for the prediction of the overall response of textile composites even at the structure scale. However, the main disadvantage is that the detailed responses and failure characteristics of the individual constituents cannot be effectively captured.

As opposed to macromechanics-based approaches, micromechanics-based approaches are essentially based on the UC methodology since they model textile composites at least at the constituent scale, where both the yarn phase and the polymer matrix are addressed explicitly and separately. If the overall properties or response evaluated at the constituent scale are used as inputs for coarse scales such as the macroscopic scale, they become multiscale approaches. It should be noted that the modelling of a micromechanics UC here is different from that in the case of predicting elastic properties. This is because to ensure an accurate prediction of the overall response the constitutive behaviours of the individual constituents must be modelled both in the elastic and inelastic regimes, whereas in the case of predicting the elastic properties the behaviours of the constituents need to be accounted for only in the elastic regime.

Based on the manner of modelling a UC, micromechanical-based approaches can be further classified into analytical approaches and the FEM-based approaches [129]. In analytical approaches, the geometries of the constituents in a UC are modelled with different levels of simplifications, typically using simple blocks. Based on the simplified UC and the material models for the polymer matrix and the yarns, the volume average stress of the UC can be correlated using analytical equations with the stresses and strains of the constituents and consequently with the macroscopic strain prescribed to the UC. For a prescribed history of macroscopic strains, a history of the volume average stresses of the UC can be calculated using the analytical equations, leading to the overall response of the composites of investigation. Recently, analytical approaches have been adopted by some researchers to develop multiscale models for the finite element analysis (FEA) of textile composites. A notable example can be found in Aminjikarai and Tabiei [130], where they extended a micromechanics model developed by Tanov and Tabiei [131] originally for predicting the elastic properties of plain woven composites. In the extended model, the UC was simplified as an assemblage of four subcells with each subcell

representing the warp and fill yarns, the pure matrix and the yarn-matrix mixed parts (see Fig. 1.4). Iso-strain boundary conditions were applied to the full-size UC to calculate the homogenised response, which was subsequently utilised to represent the response of the corresponding material point of the composite structure. This model was later adapted by both Bacarreza *et al.* [132] and Raimondo and Aliabadi [133] for multiscale progressive damage analysis of plain woven composites. Some other analytical models have been also developed by Tabiei and co-workers [134-136] for plain woven composites and by Sun *et al.* [137] for 3D orthogonal woven composites. Similar to the analytical methods used for predicting the elastic properties (e.g. the CLT-based approaches), as discussed in Section 1.1.2, the main advantage of the analytical approaches that have been developed for predicting the overall response of textile composites is their exceptional efficiency, whereas the main concern is a reduced accuracy originated from the simplifications that are needed to model the geometries of the constituents.

| Four-subcell model | Subcell "ff" | Subcell "mf" |
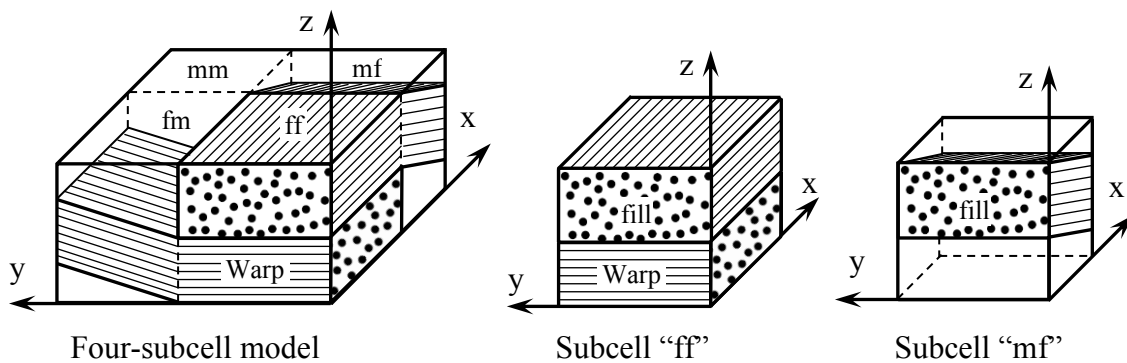
Figure 1.4: Analytical UC model developed by Tanov and Tabiei [112]

In contrast to analytical approaches, the FEM-based approaches explicitly model the geometries of the individual constituents with high fidelity. Several predictive models based on such approaches have been developed for predicting the response of textile composites under different loading conditions [138-143]. A common feature of the FEM-based approaches is that both the waviness and cross-section of the yarns are usually modelled sophisticatedly, allowing these approaches to effectively capture the detailed information of the individual constituents (e.g. stress concentration in the constituents, damage distribution in the yarns and the debonding between the polymer matrix and the yarns). Clearly, the capability of the FEM-based models in terms of capturing the detailed information is a significant advantage over the models developed based on analytical

approaches. However, the main disadvantage of such models is again the complexities associated with explicitly building the detailed geometries, discretising the constituents with high-quality elements and meshes, and assigning the ever-changing orientations for the yarns.

1.2 Research aim and methodology

1.2.1 Research questions
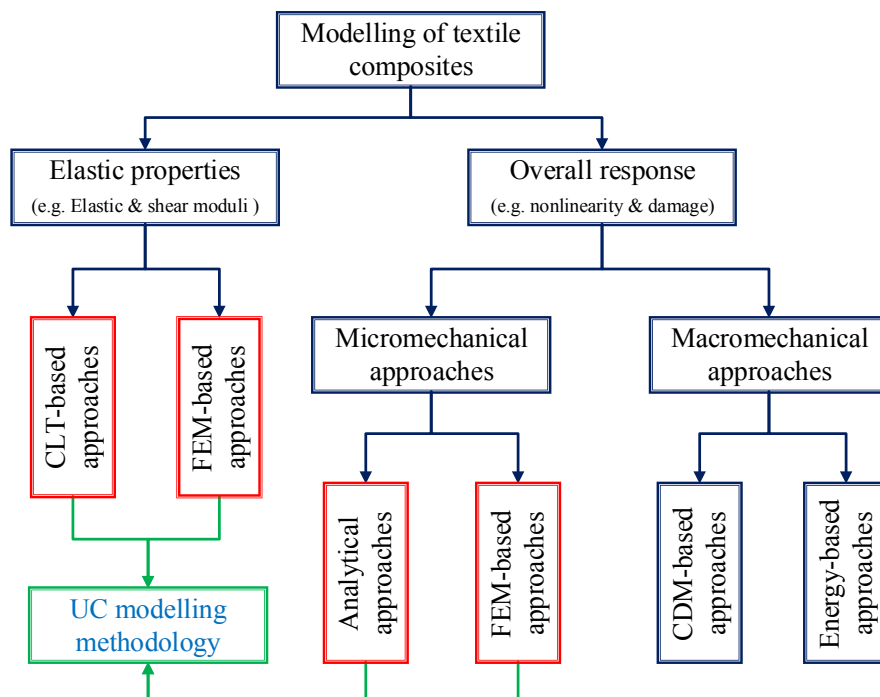
Figure 1.5: Summary of the existing approaches for modelling textile composites

The previous section briefly reviews the research studies that have been conducted on the topic of predictive modelling of the elastic properties and mechanical response of textile FRP composites. An examination of these studies suggests that the current methodologies (either for predicting the elastic properties or the overall response of textile composites) mainly takes the so-called UC modelling methodology, with a UC being modelled based on either analytical approaches or the FEM-based approaches, as summarised in Fig. 1.5. In the case of using the UC modelling methodology for predicting the elastic properties of textile composites, it typically takes three steps, which consist of 1) defining a UC and modelling the geometries of the constituents, 2) modelling the elastic behaviours of the

constituents, and 3) prescribing an appropriate boundary condition to the UC to calculate the volume average quantities (e.g. stress) of the UC. In the case of predicting the overall response based on the UC modelling methodology, it also takes three similar steps. One of the differences is in the second step, where both the elastic and inelastic behaviours of the constituents must be modelled. The other difference is in the third step, where a history of boundary conditions must be enforced to the UC to calculate the history of the volume average quantities.

In addition to the above general conclusions, it can be revealed from the literature review that the main problem of using analytical approaches (which are generally simple and thus efficient) is a reduced accuracy resulting from the geometry simplifications required to implement the analytical nature, while the concern of using the FEM-based approaches (which are generally sophisticated and therefore accurate) is the time-consuming pre-processing required to explicitly address the highly complex geometry modelling. What we can also conclude after analysing the two categories of modelling approaches is that the pursuit of simplicity in developing predictive models for textile composites seemingly has to be compromised by a reduced accuracy, while the pursuit of accuracy seemingly has to be accompanied by an increased complexity or a reduced simplicity. Thus, one of the most critical questions in modelling textile composites is:

Is it possible and how can it be possible to develop an approach which is able to combine the advantages of analytical and the FEM-based approaches (i.e. simplicity and accuracy) and address the two inherently concerns existing in the two types of approaches (i.e. reduced accuracy and high complexity) for predicting the elastic properties and overall response of textile composites – in other words, is it possible and how can it be possible to develop an accurate but simple approach for modelling textile composites?

By taking a closer examination of the published research, it can also be found that most of these studies have focused on developing models for predicting the elastic properties of textile composites in the fibre directions (e.g. the warp direction) and no much attempt has been made to predict the elastic properties in off-axis directions (e.g. 45° to the warp or weft direction). In addition, it should be noted that most of the existing studies on predicting the overall response of textile composites have been essentially based on large

composite structures, which requires expensive computational costs, rather than utilising UCs only, which is computationally efficient. Thus, another critical research question in modelling textile composites is:

Is it possible and how can it be possible to develop an approach within the framework of the UC modelling methodology to predict the elastic properties and the overall response of textile composites in not only the normal but also the off-axis directions?

1.2.2 Research aim and scope

In response to the above two research questions, the aim of this research is to develop within the framework of the UC modelling methodology a novel approach that is capable of addressing the problem of a reduced accuracy in analytical approaches and meanwhile eliminating the complex and time-consuming pre-processing required in the FEM-based approaches, and thus to accurately and simply predict the elastic properties and the overall responses of textile composites in both the normal and off-axis directions.

Plain woven

2D triaxial braid
(stitched & unstitched)

Multiaxial warp knit
(stitched & unstitched)

3D orthogonal woven

3D braid

Knitted & stitched

Woven [95]   **Braided [144]**   **Stitched [144]**
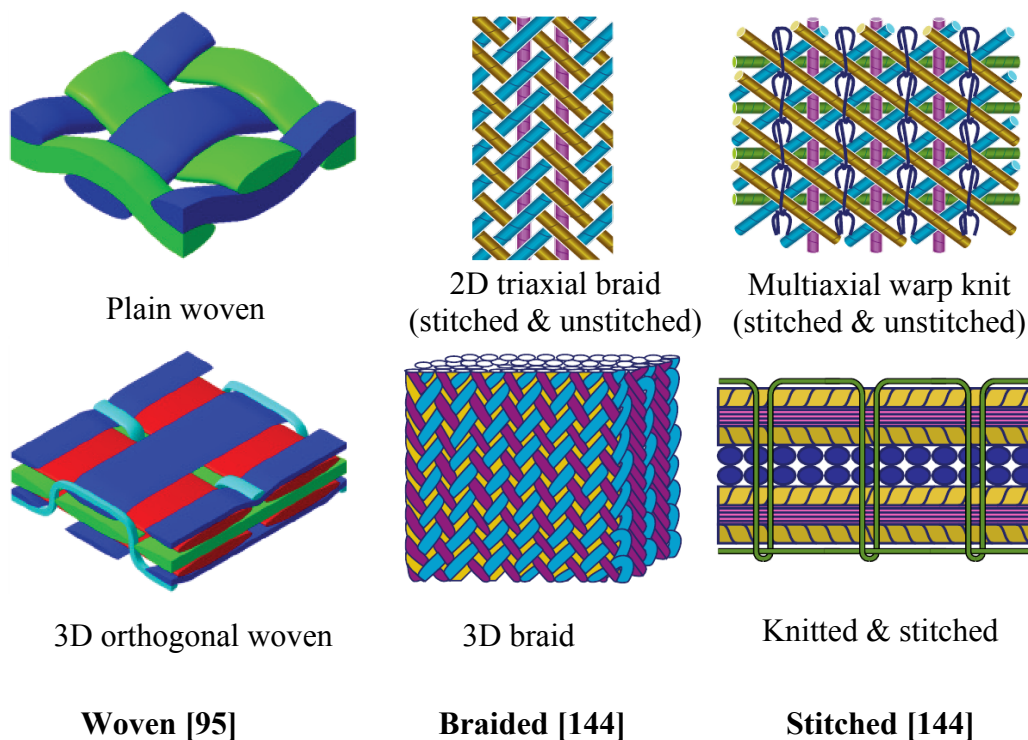
Figure 1.6: Typical textile fabric geometries (woven, braided and stitched)

The material properties and the overall response of textile composites depend on not only those of the constituent materials but also the internal weave structure of the composites. In view of the fact that there is a wide variety of weave structures in textile composites, as shown in Fig. 1.6, the present work focuses on developing predictive models for three types of woven composites (i.e. plain, twill and 3D orthogonal woven composites) since they are commonly used and less complex compared to other types of textile composites such as 3D braided or knitted composites. However, it should be noted that the approach developed in the present work can be theoretically utilised for any other types of textile composites as such an approach does not depend on the weave structure, which will be demonstrated in Chapters 4 and 5. Furthermore, since it is always impossible to develop a single predictive model capable of predicting the overall response of textile composites under all kinds of loading conditions, this research focuses on predicting the response of woven composites under in-plane tensile loading conditions.

1.2.3 Research methodology

The present work is conducted within the framework of the UC modelling methodology. To simultaneously address the two concerns discussed earlier, the specific approach of this work is based on the idea of developing high-fidelity analytical UC models for woven composites and subsequently implementing the analytical UC models using numerical methods that do not require the use of elements and/or meshes, i.e. meshfree methods, which is a relatively new class of numerical methods that discretise a problem domain simply using nodes (see Chapter 3 for detail). In this thesis, this approach is termed as the *meshfree-based UC modelling approach*.

To develop analytical UC models with high fidelity, micrographs of a typical woven composite material have been taken to observe the internal features, i.e. the cross-section and the waviness of yarns. Based on the data extracted from the micrographs, analytical functions that fit the geometrical features of yarns have been proposed, and analytical equations have been developed to describe the surfaces and waviness of yarns in plain, twill and 3D woven composites. To enable the proposed approach to accurately predict the elastic properties and the overall responses in the normal and off-axis directions, both normal and off-axis UC models have been developed. Here, the term "normal" refers to the UC model is developed based on an orthogonal coordinate system where the warp,

weft and through-the-thickness directions of the composites coincide with the X, Y and Z axes of the coordinate system, respectively. On the other hand, an off-axis UC model refers to that it is developed when the warp or weft direction of the composites has an angle (e.g. 45°) to the X or Y axis, whereas the through-the-thickness direction coincides with the Z axis of the coordinate system.

One of the theoretical implications of developing high-fidelity analytical UC models is that it retains an analytical nature, allowing the proposed approach to have the possibility of being simple. Additionally, the high-fidelity description of the constituents ensures the proposed approach to be accurate from the perspective of geometry modelling. More importantly, since analytical equations have been developed to describe both the surfaces and waviness of yarns, they can be utilised to determine the relative location of any given material point, as well as its orientation. In combination with meshfree methods, which discretise a problem domain using nodes only, the high-fidelity analytical UC models can therefore be implicitly implemented (which will be demonstrated in detail in Section 4.6, Chapter 4), avoiding the need for explicitly building the geometries of the constituents and assigning the ever-changing orientations of yarns, and thus ensuring the proposed approach to be simple but accurate.

Since the specific procedure for utilising the UC modelling methodology in the case of predicting the elastic properties is different from that in the case of predicting the overall response, as previously summarised in Section 1.2.1, two different meshfree methods have been chosen to implement the high-fidelity analytical UC models. By examining the two procedures, it is evident that the case of predicting the elastic properties is essentially a static boundary-value problem of elasticity, while that of predicting the overall response can be treated as a dynamic problem with initial conditions. In this thesis, the meshfree methods that have been adopted for solving the two types of problems are termed as the standard and explicit weak-form meshfree methods, respectively. It should be noted that periodic boundary conditions (PBCs) have been utilised in this research for predicting both the elastic properties and the overall response of woven composites, instead of using any other types of boundary conditions. Therefore, the basic equations for implementing PBCs in combination with the two meshfree methods have also been formulated, which will be detailed in Section 3.6, Chapter 3.

Apart from developing high-fidelity analytical UC models and adapting proper meshfree methods, another significant aspect of the present research is the modelling of the material behaviours of the individual constituents, particularly in the inelastic regime. To describe the inelastic behaviours, a viscoplasticity-based model has been chosen to characterise the nonlinear, rate-dependent behaviour of the polymer matrix, and an improved Weibull function based formulation has been proposed to identify the damage evolution of the yarn material in woven composites. Based on the material models of the constituents, the high-fidelity UC models and the two meshfree methods, in-house computer programs have been developed for conducting meshfree predictions of the elastic properties and the overall responses of the three types of woven composites.

1.3 Original contributions

The idea of using meshfree methods in combination with the UC modelling methodology is not completely new. It was initially proposed by Wen and Aliabadi [94] for predicting the normal elastic properties of plain woven composites and was later adopted by Li *et al.* [145] for predicting the normal elastic properties of 3D woven composites. The present research is an extension of their research, and the main original contributions of this work are the formalisation of the above idea into the meshfree-based UC modelling approach and the extension of the capability of the UC modelling methodology from traditionally the homogenisation of only the normal elastic properties to that of both the normal and off-axis elastic properties, as well as to the regime of predicting the overall responses of woven composites under both normal and off-axis loading scenarios. To be specific, the original contributions of the present work are summarised as follows:

1) The improvements to the normal UC models of plain woven composites originally developed by Wen and Aliabadi [94] and also the normal UC model of 3D woven composites developed by Li *et al.* [145], from the perspective of describing the internal architectures of the two types of woven composites.

2) The development of a high-fidelity normal UC model for twill woven composites and that of off-axis UC models for plain, twill and 3D woven composites.

3) The formulation of the basic equations for implementing PBCs in combination with the standard and explicit weak-form meshfree methods.

4) The proposal of an improved Weibull function based formulation for describing the damage evolutions associated with the predominant failure modes in the yarn material of woven composites.

5) The extension of the UC modelling methodology for predicting the off-axis elastic properties and the overall response of woven composites under normal and off-axis loading conditions.

1.4 Thesis structure

This research involves various aspects of knowledge including mechanics of composites, micromechanical homogenisation of periodic materials such as woven composites and meshfree methods. For the sake of clarity, the remainder of this thesis will be presented by firstly introducing the background knowledge and theories relating to this work. Then, it will be progressed by the description of the high-fidelity UC models and the utilisation and validation of the meshfree-based UC approach in predicting the elastic properties and the overall response of woven composites.

In Chapter 2, the mechanics knowledge involved in the elastic constitutive modelling of the polymer matrix and the yarn material in woven composites will be firstly presented. Due to the presence of waviness in the yarn material, it is always desirable to perform the constitutive modelling of the yarn material in its local coordinate system (LCS). Thus, the procedure for conducting coordinate transformations between the LCS of the yarn material and the global coordinate system (GCS) of the UC will then be detailed. Finally, the general theories and concepts associated with the micromechanical homogenisation of periodic materials, as well as the basic equations for deriving PBCs, will be briefed.

In Chapter 3, the background knowledge and concepts relating to meshfree methods will be briefly introduced in comparison with the FEM. Then, three types of shape function construction techniques in meshfree methods will be detailed, and a numerical example will be presented following the description of each technique to discuss the features that are possessed by the corresponding shape functions. Finally, the formulation procedures

for the standard and explicit weak-form meshfree methods, as well as the implementation of PBCs in combination with the two methods, will be detailed.

In Chapter 4, the high-fidelity normal UC models that have been developed or improved for describing the internal features of plain, twill and 3D orthogonal woven composites will be firstly detailed. Then, a generic approach for calculating the PBCs at the scale of reduced UC of woven composites will be described, and the PBCs for the UC models of woven composites will be summarised. After that, an in-house computer program which has been developed to implement the high-fidelity UC models using the standard weak-form meshfree method will be introduced. Finally, numerical examples conducted based on the computer program for predicting the elastic properties of the three types of woven composites will be discussed, and the predicted results will be validated by comparing with the numerical and/or experimental data found in the relevant literature.

In Chapter 5, the high-fidelity off-axis UCs of the three types of woven composites will be firstly presented. Then, a viscoplasticity-based model for describing the nonlinearity and rate-dependence of the polymer matrix and a CDM-based model for identifying the damage initiations and evolutions of the yarn material will be detailed. After that, an in-house computer program that has been developed to implement the high-fidelity UCs and the material models by using the explicit weak-form meshfree method will be introduced. Following the description of this program, a numerical example for predicting the overall responses of a plain woven carbon fibre-reinforced polymer (CFRP) composite material subjected to some in-plane loading conditions will be presented, and the predicted results will be validated by comparing against the experimental results. Finally, the application of the meshfree-based UC approach will be exemplified through qualitatively analysing the influences of fibre tow size and weave structure on the response of woven composites.

In the last chapter, the conclusions of the present research will be summarised from the perspectives of the development of high-fidelity UC models, the implementation of the weak-form meshfree methods and the material behaviour modelling for the constituents in woven composites. Recommendations for future work will also be discussed.

CHAPTER 2: MECHANICS PRELIMINARIES

2.1 Introduction

As summarised in Section 1.2.1, the utilisation of the UC modelling methodology in the case of homogenising the elastic properties or the case of predicting the overall response of textile composites involves three similar steps, as follows:

1) Identify a representative domain or unit cell (UC) for the textile composites of investigation and model the internal architecture of the UC;

2) Model the material behaviours of the constituents in the elastic regime for the former case or in both the elastic and inelastic regimes for the latter case;

3) Apply a proper boundary condition for the former case or a history of boundary conditions for the latter case so as to calculate the volume average quantities or the histories of the volume average quantities.

As is clearly seen from the above description, a fundament step in both cases is to model the behaviours of the constituents. In such a step, performing constitutive modelling in the former case is different from that in the latter case. Specifically, the constitutive modelling in the former case needs to be performed only in the elastic regime. On the contrary, the constitutive modelling in the latter case should be conducted in both the elastic regime and the inelastic regime, where the material behaviours of the constituents such as yarn damage, material nonlinearity and strain rate dependence should often be considered. To avoid repetition, the background knowledge related to the constitutive modelling of the constituents (i.e. the polymer matrix and the yarn material) in the elastic regime will be introduced in this chapter, leaving the constitutive modelling in the inelastic regime to be addressed in Chapter 5.

In addition, due to the presence of yarn waviness in woven composites, it is desirable to address the mechanics quantities (e.g. stress and strain) of wavy yarns initially in its local coordinate system (LCS), and then to transform them into the global coordinate system (GCS) of the (UC). Again, this is a shared feature between the case of the elastic property homogenisation and that of the overall response prediction. Thus, the basic equations for performing coordinate transformations between the LCS of the yarn material and the GCS of the UC will be detailed in this chapter.

Furthermore, the fundamental knowledge associated with conducting micromechanical homogenisation of periodic materials such as woven composites will be introduced at the end of this chapter. In this thesis, to distinguish the quantities associated with the polymer matrix from those associated with the yarn material, the former quantities will be denoted with a subscript "m", while no subscript will be used for the latter quantities.

2.2 Hooke's law for polymer matrix

In woven FRP composites, the polymer matrix, which is often assumed as a homogeneous isotropic material, typically exhibits linear elastic behaviour at small strains and becomes nonlinear if the strain applied exceeds the elastic threshold. As a homogeneous isotropic material, its constitutive behaviour in the elastic regime can be described using Hooke's law for isotropic materials, as follows:

$$\boldsymbol{\sigma}_m = \mathbf{C}_m \boldsymbol{\varepsilon}_m \tag{2.1}$$

or alternatively as:

$$\boldsymbol{\varepsilon}_m = \mathbf{S}_m \boldsymbol{\sigma}_m \tag{2.2}$$

where the four symbols, $\boldsymbol{\sigma}_m$, $\boldsymbol{\varepsilon}_m$, $\mathbf{C}_m$ and $\mathbf{S}_m$, are the stress vector, the engineering strain vector, the elasticity matrix and the inverse of the elasticity matrix, and they are defined using the following equations:

$$\boldsymbol{\sigma}_m = \{\sigma_{11} \quad \sigma_{22} \quad \sigma_{33} \quad \tau_{12} \quad \tau_{23} \quad \tau_{31}\}^T \tag{2.3}$$

$$\boldsymbol{\varepsilon}_m = \{\varepsilon_{11} \quad \varepsilon_{22} \quad \varepsilon_{33} \quad \gamma_{12} \quad \gamma_{23} \quad \gamma_{31}\}^T \tag{2.4}$$

$$\mathbf{C_m} = \begin{bmatrix} \dfrac{E_m(1-v_m)}{\Delta_m} & \dfrac{E_m v_m}{\Delta_m} & \dfrac{E_m v_m}{\Delta_m} & 0 & 0 & 0 \\[2mm] \dfrac{E_m v_m}{\Delta_m} & \dfrac{E_m(1-v_m)}{\Delta_m} & \dfrac{E_m v_m}{\Delta_m} & 0 & 0 & 0 \\[2mm] \dfrac{E_m v_m}{\Delta_m} & \dfrac{E_m v_m}{\Delta_m} & \dfrac{E_m(1-v_m)}{\Delta_m} & 0 & 0 & 0 \\[2mm] 0 & 0 & 0 & G_m & 0 & 0 \\[2mm] 0 & 0 & 0 & 0 & G_m & 0 \\[2mm] 0 & 0 & 0 & 0 & 0 & G_m \end{bmatrix} \tag{2.5}$$

$$\mathbf{S_m} = \begin{bmatrix} \dfrac{1}{E_m} & -\dfrac{v_m}{E_m} & -\dfrac{v_m}{E_m} & 0 & 0 & 0 \\[2mm] -\dfrac{v_m}{E_m} & \dfrac{1}{E_m} & -\dfrac{v_m}{E_m} & 0 & 0 & 0 \\[2mm] -\dfrac{v_m}{E_m} & -\dfrac{v_m}{E_m} & \dfrac{1}{E_m} & 0 & 0 & 0 \\[2mm] 0 & 0 & 0 & \dfrac{1}{G_m} & 0 & 0 \\[2mm] 0 & 0 & 0 & 0 & \dfrac{1}{G_m} & 0 \\[2mm] 0 & 0 & 0 & 0 & 0 & \dfrac{1}{G_m} \end{bmatrix} \tag{2.6}$$

where E_m, v_m, G_m are Young's modulus, Poisson's ratio and the shear modulus, and G_m and Δ_m are given by:

$$G_m = \frac{E_m}{2(1+v_m)} \tag{2.7}$$

$$\Delta_m = (1 + v_m)(1 - 2v_m) \tag{2.8}$$

2.3 Hooke's law for yarn material

In woven FRP composites, the internal fabric is woven from yarns and each yarn is further made of many fibre filaments. In its final production form, the fibre filaments in each yarn are surrounded by the polymer matrix. This indicates that the yarn material in its LCS is essentially a unidirectional composite. Therefore, the yarn material in woven composites can be largely assumed as a homogeneous transversely isotropic material in its LCS. Here, it should be noted that yarns based on glass fibres are isotropic, but they can still be assumed to be transversely isotropic as isotropy is a special case of transverse

isotropy. Based on this assumption, the stress-strain relation of the yarn material in the elastic regime can be described using the generalised Hooke's law, as follows:

$$\boldsymbol{\sigma}^l = \mathbf{C}^l \boldsymbol{\varepsilon}^l \tag{2.9}$$

$$\boldsymbol{\varepsilon}^l = \mathbf{S}^l \boldsymbol{\sigma}^l \tag{2.10}$$

where

$$\boldsymbol{\sigma}^l = \{\sigma_{11}^l \quad \sigma_{22}^l \quad \sigma_{33}^l \quad \tau_{12}^l \quad \tau_{23}^l \quad \tau_{31}^l\}^{\mathrm{T}} \tag{2.11}$$

$$\boldsymbol{\varepsilon}^l = \{\varepsilon_{11}^l \quad \varepsilon_{22}^l \quad \varepsilon_{33}^l \quad \gamma_{12}^l \quad \gamma_{23}^l \quad \gamma_{31}^l\}^{\mathrm{T}} \tag{2.12}$$

$$\mathbf{C}^l = \begin{bmatrix} \dfrac{E_{\mathrm{L}}(1-v_{\mathrm{TT}})}{\Delta} & \dfrac{E_{\mathrm{T}}v_{\mathrm{LT}}}{\Delta} & \dfrac{E_{\mathrm{T}}v_{\mathrm{LT}}}{\Delta} & 0 & 0 & 0 \\[2.5ex] \dfrac{E_{\mathrm{L}}v_{\mathrm{TL}}}{\Delta} & \dfrac{E_{\mathrm{T}}(1-v_{\mathrm{LT}}v_{\mathrm{TL}})}{\Delta(1+v_{\mathrm{TT}})} & \dfrac{E_{\mathrm{T}}(v_{\mathrm{TT}}+v_{\mathrm{LT}}v_{\mathrm{TL}})}{\Delta(1+v_{\mathrm{TT}})} & 0 & 0 & 0 \\[2.5ex] \dfrac{E_{\mathrm{L}}v_{\mathrm{TL}}}{\Delta} & \dfrac{E_{\mathrm{T}}(v_{\mathrm{TT}}+v_{\mathrm{LT}}v_{\mathrm{TL}})}{\Delta(1+v_{\mathrm{TT}})} & \dfrac{E_{\mathrm{T}}(1-v_{\mathrm{LT}}v_{\mathrm{TL}})}{\Delta(1+v_{\mathrm{TT}})} & 0 & 0 & 0 \\[2.5ex] 0 & 0 & 0 & G_{\mathrm{LT}} & 0 & 0 \\[2ex] 0 & 0 & 0 & 0 & G_{\mathrm{TT}} & 0 \\[2ex] 0 & 0 & 0 & 0 & 0 & G_{\mathrm{TL}} \end{bmatrix} \tag{2.13}$$

$$\mathbf{S}^l = \begin{bmatrix} \dfrac{1}{E_{\mathrm{L}}} & -\dfrac{v_{\mathrm{TL}}}{E_{\mathrm{T}}} & -\dfrac{v_{\mathrm{TL}}}{E_{\mathrm{T}}} & 0 & 0 & 0 \\[2.5ex] -\dfrac{v_{\mathrm{LT}}}{E_{\mathrm{L}}} & \dfrac{1}{E_{\mathrm{T}}} & -\dfrac{v_{\mathrm{TT}}}{E_{\mathrm{T}}} & 0 & 0 & 0 \\[2.5ex] -\dfrac{v_{\mathrm{LT}}}{E_{\mathrm{L}}} & -\dfrac{v_{\mathrm{TT}}}{E_{\mathrm{T}}} & \dfrac{1}{E_{\mathrm{T}}} & 0 & 0 & 0 \\[2.5ex] 0 & 0 & 0 & \dfrac{1}{G_{\mathrm{LT}}} & 0 & 0 \\[2.5ex] 0 & 0 & 0 & 0 & \dfrac{1}{G_{\mathrm{TT}}} & 0 \\[2.5ex] 0 & 0 & 0 & 0 & 0 & \dfrac{1}{G_{\mathrm{TL}}} \end{bmatrix} \tag{2.14}$$

where the superscript, l, denotes that the corresponding quantities are evaluated in the LCS; the subscripts, 1, 2 and 3, refer to the longitudinal, in-plane transverse and out-of-plan transverse directions; E_{L} is Young's modulus in the longitudinal direction; E_{T} is Young's modulus in the transverse directions; v_{ij} $(i, j = \mathrm{L}, \mathrm{T})$ is Poisson's ratio relating

to a contraction in direction j caused by a tension in direction i; G_{LT}, G_{TT} and G_{TL} are the shear moduli corresponding to the shear strains, γ_{12}, γ_{23} and γ_{31}; and

$$\Delta = 1 - v_{TT} - 2v_{LT}v_{TL} \tag{2.15}$$

It should be noted that the above equations are subjected to the following constraints:

$$E_L = E_1 \tag{2.16}$$

$$E_T = E_2 = E_3 \tag{2.17}$$

$$G_{LT} = G_{TL} \tag{2.18}$$

$$G_{TT} = \frac{E_T}{2(1+v_{TT})} \tag{2.19}$$

$$\frac{E_L}{v_{LT}} = \frac{E_T}{v_{TL}} \tag{2.20}$$

2.4 Coordinate transformation for yarn material

In the previous section, the constitutive equations and quantities (e.g. stress) for the yarn material are addressed in its LCS. This necessitates defining coordinate transformations for these quantities. In this section, the general concepts and equations for performing coordinate transformations between the LCS and the GCS will be introduced, and an example of conducting coordinate transformations for the warp and weft yarns in plain woven composites will be presented.

2.4.1 Basic equations for rotational transformation

The transformations between two coordinate systems can be rotations, translations, or a combination of them. However, in the context of constitutive modelling, the quantities involved (i.e. stress, strain and elasticity matrix) are independent of any translation. Thus, only rotations need to be considered when conducting coordinate transformations for the yarn material in woven composites. Assume that the LCS of the yarn material is denoted using $X^l Y^l Z^l$, and the GCS of the UC using $X^g Y^g Z^g$. Any form of rotation between the two coordinate systems can be mathematically described using:

$$x^g = \mathbf{R}^{g|l} x^l \tag{2.21}$$

where the superscripts, l and g, denote the LCS and the GCS; the superscript, $g|l$, refers to that the associated rotation is from the LCS to the GCS; x^l represents the coordinate vector of a point, x, in the LCS; x^g stands for the coordinate vector of this point in the GCS; and $\mathbf{R}^{g|l}$ is the matrix associated with a rotation from the LCS to the GCS and is defined by:

$$\mathbf{R}^{g|l} = \begin{bmatrix} \cos\theta_{11} & \cos\theta_{12} & \cos\theta_{13} \\ \cos\theta_{21} & \cos\theta_{22} & \cos\theta_{23} \\ \cos\theta_{31} & \cos\theta_{32} & \cos\theta_{33} \end{bmatrix} \tag{2.22}$$

where θ_{ij} $(i,j = 1,2,3)$ is the angle between the jth axis of the LCS and the ith axis of the GCS.

By rewriting Eq. (2.21) into Eq. (2.23), it can be found that the matrix for a rotation from the GCS to the LCS, $\mathbf{R}^{l|g}$, is equal to the inverse of $\mathbf{R}^{g|l}$:

$$x^l = \left(\mathbf{R}^{g|l}\right)^{-1} x^g = \mathbf{R}^{l|g} x^g \tag{2.23}$$

Also, the inverse matrix of $\mathbf{R}^{g|l}$, i.e. $\mathbf{R}^{l|g}$, is equal to the transpose of $\mathbf{R}^{l|g}$ because we have the following equation according to the definition of a rotation matrix:

$$x^l = \begin{bmatrix} \cos\theta_{11} & \cos\theta_{21} & \cos\theta_{31} \\ \cos\theta_{12} & \cos\theta_{22} & \cos\theta_{32} \\ \cos\theta_{13} & \cos\theta_{23} & \cos\theta_{33} \end{bmatrix} x^g = \left(\mathbf{R}^{l|g}\right)^{\mathrm{T}} x^g \tag{2.24}$$

Furthermore, if a coordinate transformation is comprised of more than one rotation (e.g. n rotations), the relation between the coordinate vectors before and after these rotations can be obtained by repetitively utilising Eq. (2.21), as follows:

$$x^{l1} = \mathbf{R}^{l1|l0} x^{l0} \tag{2.25}$$

$$x^{l2} = \mathbf{R}^{l2|l1} x^{l1} = \mathbf{R}^{l2|l1} \mathbf{R}^{l1|l0} x^{l0} \tag{2.26}$$

$$\boldsymbol{x}^g = \boldsymbol{x}^{ln} = \mathbf{R}^{ln|l(n-1)} \dots \mathbf{R}^{l2|l1}\mathbf{R}^{l1|l0}\boldsymbol{x}^{l0} \tag{2.27}$$

where $\mathbf{R}^{li|l(i-1)}$ $(i = 1,2,\dots,n)$ denotes the matrix corresponding to the ith rotation, and $\boldsymbol{x}^{li}$ $(i = 1,2,\dots,n)$ is the coordinate vector after the ith rotation.

2.4.2 Transformation for constitutive quantities

If the rotation matrix, $\mathbf{R}^{g|l}$, as defined in Eq. (2.21), is denoted in the tensor form as r_{ij}, the relation between the stress tensors of a material point before and after such a rotation, which is from the LCS to the GCS, can be expressed using the following tensor form:

$$\sigma_{ij}^g = r_{im}r_{jn}\sigma_{mn}^l \tag{2.28}$$

where σ_{ij}^g is the stress tensor after rotation (i.e. the stress tensor in the GCS), and σ_{mn}^l is the stress tensor before rotation (i.e. the stress tensor in the LCS). Expanding the above expression yields the following equations:

$$\sigma_{11}^g = r_{1m}r_{1n}\sigma_{mn}^l = r_{11}r_{11}\sigma_{11}^l + r_{11}r_{12}\sigma_{12}^l + r_{11}r_{13}\sigma_{13}^l$$

$$+ r_{12}r_{11}\sigma_{21}^l + r_{12}r_{12}\sigma_{22}^l + r_{12}r_{13}\sigma_{23}^l$$

$$+ r_{13}r_{11}\sigma_{31}^l + r_{13}r_{12}\sigma_{32}^l + r_{13}r_{13}\sigma_{33}^l \tag{2.29}$$

$$\sigma_{22}^g = r_{2m}r_{2n}\sigma_{mn}^l = r_{21}r_{21}\sigma_{11}^l + r_{21}r_{22}\sigma_{12}^l + r_{21}r_{23}\sigma_{13}^l$$

$$+ r_{22}r_{21}\sigma_{21}^l + r_{22}r_{22}\sigma_{22}^l + r_{22}r_{23}\sigma_{23}^l$$

$$+ r_{23}r_{21}\sigma_{31}^l + r_{23}r_{22}\sigma_{32}^l + r_{23}r_{23}\sigma_{33}^l \tag{2.30}$$

$$\sigma_{33}^g = r_{3m}r_{3n}\sigma_{mn}^l = r_{31}r_{31}\sigma_{11}^l + r_{31}r_{32}\sigma_{12}^l + r_{31}r_{33}\sigma_{13}^l$$

$$+ r_{32}r_{31}\sigma_{21}^l + r_{32}r_{32}\sigma_{22}^l + r_{32}r_{33}\sigma_{23}^l$$

$$+ r_{33}r_{31}\sigma_{31}^l + r_{33}r_{32}\sigma_{32}^l + r_{33}r_{33}\sigma_{33}^l \tag{2.31}$$

$$\sigma_{12}^g = r_{1m}r_{2n}\sigma_{mn}^l = r_{11}r_{21}\sigma_{11}^l + r_{11}r_{22}\sigma_{12}^l + r_{11}r_{23}\sigma_{13}^l$$

$$+ r_{12}r_{21}\sigma_{21}^l + r_{12}r_{22}\sigma_{22}^l + r_{12}r_{23}\sigma_{23}^l$$

$$+ r_{13}r_{21}\sigma_{31}^l + r_{13}r_{22}\sigma_{32}^l + r_{13}r_{23}\sigma_{33}^l \tag{2.32}$$

$$\sigma_{23}^g = r_{2m}r_{3n}\sigma_{mn}^l = r_{21}r_{31}\sigma_{11}^l + r_{21}r_{32}\sigma_{12}^l + r_{21}r_{33}\sigma_{13}^l$$

$$+ r_{22}r_{31}\sigma_{21}^l + r_{22}r_{32}\sigma_{22}^l + r_{22}r_{33}\sigma_{23}^l$$

$$+ r_{23}r_{31}\sigma_{31}^l + r_{23}r_{32}\sigma_{32}^l + r_{23}r_{33}\sigma_{33}^l \tag{2.33}$$

$$\sigma_{31}^g = r_{3m}r_{1n}\sigma_{mn}^l = r_{31}r_{11}\sigma_{11}^l + r_{31}r_{12}\sigma_{12}^l + r_{31}r_{13}\sigma_{13}^l$$

$$+ r_{32}r_{11}\sigma_{21}^l + r_{32}r_{12}\sigma_{22}^l + r_{32}r_{13}\sigma_{23}^l$$

$$+ r_{33}r_{11}\sigma_{31}^l + r_{33}r_{12}\sigma_{32}^l + r_{33}r_{13}\sigma_{33}^l \tag{2.34}$$

The above equations can be assembled into the following matrix form by utilising the relation of $\sigma_{mn}^l = \sigma_{nm}^l$ ($m \neq n$):

$$\boldsymbol{\sigma}^g = \mathbf{T}_\sigma^{g|l} \boldsymbol{\sigma}^l \tag{2.35}$$

$$\boldsymbol{\sigma}^g = \left\{ \sigma_{11}^g \quad \sigma_{22}^g \quad \sigma_{33}^g \quad \tau_{12}^g \quad \tau_{23}^g \quad \tau_{31}^g \right\}^\mathrm{T} \tag{2.36}$$

where $\boldsymbol{\sigma}^g$ is the stress vector in the GCS, $\boldsymbol{\sigma}^l$ is the stress vector in the LCS, and $\mathbf{T}_\sigma^{g|l}$ is the stress transformation matrix from the LCS to the GCS:

$$\mathbf{T}_\sigma^{g|l} = \begin{bmatrix} r_{11}^2 & r_{12}^2 & r_{13}^2 & 2r_{11}r_{12} & 2r_{12}r_{13} & 2r_{13}r_{11} \\ r_{21}^2 & r_{22}^2 & r_{23}^2 & 2r_{21}r_{22} & 2r_{22}r_{23} & 2r_{23}r_{21} \\ r_{31}^2 & r_{32}^2 & r_{33}^2 & 2r_{31}r_{32} & 2r_{32}r_{33} & 2r_{33}r_{31} \\ r_{11}r_{21} & r_{12}r_{22} & r_{13}r_{23} & r_{11}r_{22}+r_{12}r_{21} & r_{12}r_{23}+r_{13}r_{22} & r_{13}r_{21}+r_{11}r_{23} \\ r_{21}r_{31} & r_{22}r_{32} & r_{23}r_{33} & r_{21}r_{32}+r_{22}r_{31} & r_{22}r_{33}+r_{23}r_{32} & r_{23}r_{31}+r_{21}r_{33} \\ r_{31}r_{11} & r_{32}r_{12} & r_{33}r_{13} & r_{31}r_{12}+r_{32}r_{11} & r_{32}r_{13}+r_{33}r_{12} & r_{33}r_{11}+r_{31}r_{13} \end{bmatrix} \tag{2.37}$$

Based on Eq. (2.23) or (2.24), the relation between the stress vectors before and after the inverse rotation of $\mathbf{R}^{g|l}$, i.e. $\mathbf{R}^{l|g}$, which is from the GCS to the LCS, can be expressed using the following equation:

$$\sigma_{mn}^l = r_{mi}r_{nj}\sigma_{ij}^g \tag{2.38}$$

Following a similar procedure for obtaining $\mathbf{T}_\sigma^{g|l}$, the stress transformation matrix from the GCS to the LCS can be obtained, as follows:

$$\boldsymbol{\sigma}^l = \mathbf{T}_\sigma^{l|g}\boldsymbol{\sigma}^g \tag{2.39}$$

$$\mathbf{T}_\sigma^{l|g} = \begin{bmatrix} r_{11}^2 & r_{21}^2 & r_{31}^2 & 2r_{11}r_{21} & 2r_{21}r_{31} & 2r_{31}r_{11} \\ r_{12}^2 & r_{22}^2 & r_{32}^2 & 2r_{12}r_{22} & 2r_{22}r_{32} & 2r_{32}r_{12} \\ r_{13}^2 & r_{23}^2 & r_{33}^2 & 2r_{13}r_{23} & 2r_{23}r_{33} & 2r_{33}r_{13} \\ r_{11}r_{12} & r_{21}r_{22} & r_{31}r_{32} & r_{11}r_{22}+r_{21}r_{12} & r_{31}r_{32}+r_{31}r_{22} & r_{31}r_{12}+r_{11}r_{32} \\ r_{12}r_{13} & r_{22}r_{23} & r_{32}r_{33} & r_{12}r_{23}+r_{22}r_{13} & r_{22}r_{33}+r_{32}r_{23} & r_{32}r_{13}+r_{12}r_{33} \\ r_{13}r_{11} & r_{23}r_{21} & r_{33}r_{31} & r_{13}r_{31}+r_{23}r_{11} & r_{23}r_{31}+r_{33}r_{31} & r_{33}r_{11}+r_{13}r_{31} \end{bmatrix} \tag{2.40}$$

Combining Eqs. (2.35) and (2.39), the following relation can be obtained:

$$\mathbf{T}_\sigma^{l|g} = \left(\mathbf{T}_\sigma^{g|l}\right)^{-1} \tag{2.41}$$

Similarly, the relations between the strain vector in the LCS, $\tilde{\boldsymbol{\varepsilon}}^l$, and the strain vector in the GCS, $\tilde{\boldsymbol{\varepsilon}}^g$, can be determined by replacing $\boldsymbol{\sigma}^l$ with $\tilde{\boldsymbol{\varepsilon}}^l$ and $\boldsymbol{\sigma}^g$ with $\tilde{\boldsymbol{\varepsilon}}^g$:

$$\tilde{\boldsymbol{\varepsilon}}^g = \mathbf{T}_\sigma^{g|l}\tilde{\boldsymbol{\varepsilon}}^l \tag{2.42}$$

$$\tilde{\boldsymbol{\varepsilon}}^l = \mathbf{T}_\sigma^{l|g}\tilde{\boldsymbol{\varepsilon}}^g \tag{2.43}$$

Here, it is should be noted that the symbol of $\sim$ is used to highlight that the strains in the above two equations are tensorial strains, rather than engineering strains, i.e. $\boldsymbol{\varepsilon}^g$ and $\boldsymbol{\varepsilon}^l$. Thus, it should be kept in mind that the shear components in tensorial strains are halves of those in engineering strains, as illustrated in Eqs. (2.44) ~ (2.47):

$$\tilde{\boldsymbol{\varepsilon}}^g = \left\{\varepsilon_{11}^g \quad \varepsilon_{22}^g \quad \varepsilon_{33}^g \quad \varepsilon_{12}^g \quad \varepsilon_{23}^g \quad \varepsilon_{31}^g\right\}^{\mathrm{T}} \tag{2.44}$$

$$\tilde{\boldsymbol{\varepsilon}}^l = \left\{\varepsilon_{11}^l \quad \varepsilon_{22}^l \quad \varepsilon_{33}^l \quad \varepsilon_{12}^l \quad \varepsilon_{23}^l \quad \varepsilon_{31}^l\right\}^{\mathrm{T}} \tag{2.45}$$

$$\boldsymbol{\varepsilon}^g = \left\{\varepsilon_{11}^g \quad \varepsilon_{22}^g \quad \varepsilon_{33}^g \quad \gamma_{12}^g \quad \gamma_{23}^g \quad \gamma_{31}^g\right\}^{\mathrm{T}}$$

$$= \left\{\varepsilon_{11}^g \quad \varepsilon_{22}^g \quad \varepsilon_{33}^g \quad 2\varepsilon_{12}^g \quad 2\varepsilon_{23}^g \quad 2\varepsilon_{31}^g\right\}^{\mathrm{T}} \tag{2.46}$$

$$\boldsymbol{\varepsilon}^l = \{\varepsilon_{11}^l \quad \varepsilon_{22}^l \quad \varepsilon_{33}^l \quad \gamma_{12}^l \quad \gamma_{23}^l \quad \gamma_{31}^l\}^{\mathrm{T}}$$

$$= \{\varepsilon_{11}^l \quad \varepsilon_{22}^l \quad \varepsilon_{33}^l \quad 2\varepsilon_{12}^l \quad 2\varepsilon_{23}^l \quad 2\varepsilon_{31}^l\}^{\mathrm{T}} \tag{2.47}$$

Considering the relations between tensorial strains and engineering strains, Eqs. (2.42) and (2.43) can be rewritten as follows:

$$\boldsymbol{\varepsilon}^g = \mathbf{T}_\varepsilon^{g|l} \boldsymbol{\varepsilon}^l \tag{2.48}$$

$$\boldsymbol{\varepsilon}^l = \mathbf{T}_\varepsilon^{l|g} \boldsymbol{\varepsilon}^g \tag{2.49}$$

where the transformation matrices, $\mathbf{T}_\varepsilon^{g|l}$ and $\mathbf{T}_\varepsilon^{l|g}$, are given by:

$$\mathbf{T}_\varepsilon^{g|l} = \begin{bmatrix}
r_{11}^2 & r_{12}^2 & r_{13}^2 & r_{11}r_{12} & r_{12}r_{13} & r_{13}r_{11} \\
r_{21}^2 & r_{22}^2 & r_{23}^2 & r_{21}r_{22} & r_{22}r_{23} & r_{23}r_{21} \\
r_{31}^2 & r_{32}^2 & r_{33}^2 & r_{31}r_{32} & r_{32}r_{33} & r_{33}r_{31} \\
2r_{11}r_{21} & 2r_{12}r_{22} & 2r_{13}r_{23} & r_{11}r_{22}+r_{12}r_{21} & r_{12}r_{23}+r_{13}r_{22} & r_{13}r_{21}+r_{11}r_{23} \\
2r_{21}r_{31} & 2r_{22}r_{32} & 2r_{23}r_{33} & r_{21}r_{32}+r_{22}r_{31} & r_{22}r_{33}+r_{23}r_{32} & r_{23}r_{31}+r_{21}r_{33} \\
2r_{31}r_{11} & 2r_{32}r_{12} & 2r_{33}r_{13} & r_{31}r_{12}+r_{32}r_{11} & r_{32}r_{13}+r_{33}r_{12} & r_{33}r_{11}+r_{31}r_{13}
\end{bmatrix} \tag{2.50}$$

$$\mathbf{T}_\varepsilon^{l|g} = \begin{bmatrix}
r_{11}^2 & r_{21}^2 & r_{31}^2 & r_{11}r_{21} & r_{21}r_{31} & r_{31}r_{11} \\
r_{12}^2 & r_{22}^2 & r_{32}^2 & r_{12}r_{22} & r_{22}r_{32} & r_{32}r_{12} \\
r_{13}^2 & r_{23}^2 & r_{33}^2 & r_{13}r_{23} & r_{23}r_{33} & r_{33}r_{13} \\
2r_{11}r_{12} & 2r_{21}r_{22} & 2r_{31}r_{32} & r_{11}r_{22}+r_{21}r_{12} & r_{21}r_{32}+r_{31}r_{22} & r_{31}r_{12}+r_{11}r_{32} \\
2r_{12}r_{13} & 2r_{22}r_{23} & 2r_{32}r_{33} & r_{12}r_{23}+r_{22}r_{13} & r_{22}r_{33}+r_{32}r_{23} & r_{32}r_{13}+r_{12}r_{33} \\
2r_{13}r_{11} & 2r_{23}r_{21} & 2r_{33}r_{31} & r_{13}r_{21}+r_{23}r_{11} & r_{23}r_{31}+r_{33}r_{21} & r_{33}r_{11}+r_{13}r_{31}
\end{bmatrix} \tag{2.51}$$

Comparing Eqs. (2.50) and (2.51) with Eqs. (2.40) and (2.37), the following relations can be obtained:

$$\mathbf{T}_\varepsilon^{g|l} = \left(\mathbf{T}_\sigma^{l|g}\right)^{\mathrm{T}} \tag{2.52}$$

$$\mathbf{T}_\sigma^{l|g} = \left(\mathbf{T}_\varepsilon^{g|l}\right)^{\mathrm{T}} \tag{2.53}$$

Based on the coordinate transformations defined for stress and engineering strain and the constitutive relation given in Eq. (2.9), the transformation matrices between the elasticity matrix in the LCS, $\mathbf{C}^l$, and that in the GCS, $\mathbf{C}^g$, can be deduced, as follows:

$$\because \boldsymbol{\sigma}^g = \mathbf{T}_\sigma^{g|l}\boldsymbol{\sigma}^l \quad - \quad \text{see Eq. (2.35)}$$

$$\boldsymbol{\sigma}^l = \mathbf{C}^l\boldsymbol{\varepsilon}^l \quad - \quad \text{see Eq. (2.9)}$$

$$\boldsymbol{\varepsilon}^l = \mathbf{T}_\varepsilon^{l|g}\boldsymbol{\varepsilon}^g \quad - \quad \text{see Eq. (2.49)}$$

$$\therefore \boldsymbol{\sigma}^g = \mathbf{T}_\sigma^{g|l}\boldsymbol{\sigma}^l = \mathbf{T}_\sigma^{g|l}\mathbf{C}^l\boldsymbol{\varepsilon}^l$$

$$= \mathbf{T}_\sigma^{g|l}\mathbf{C}^l\mathbf{T}_\varepsilon^{l|g}\boldsymbol{\varepsilon}^g$$

$$\because \boldsymbol{\sigma}^g = \mathbf{C}^g\boldsymbol{\varepsilon}^g$$

$$\therefore \mathbf{C}^g = \mathbf{T}_\sigma^{g|l}\mathbf{C}^l\mathbf{T}_\varepsilon^{l|g}$$

$$\because \mathbf{T}_\varepsilon^{l|g} = \left(\mathbf{T}_\sigma^{g|l}\right)^{\mathrm{T}} \quad - \quad \text{see Eq. (2.53)}$$

$$\therefore \mathbf{C}^g = \left(\mathbf{T}_\varepsilon^{l|g}\right)^{\mathrm{T}}\mathbf{C}^l\mathbf{T}_\varepsilon^{l|g}$$

$$\therefore \mathbf{C}^l = \left(\left(\mathbf{T}_\varepsilon^{l|g}\right)^{\mathrm{T}}\right)^{-1}\mathbf{C}^g\left(\mathbf{T}_\varepsilon^{l|g}\right)^{-1}$$

$$= \left(\mathbf{T}_\sigma^{g|l}\right)^{-1}\mathbf{C}^g\left(\left(\mathbf{T}_\sigma^{g|l}\right)^{-1}\right)^{\mathrm{T}}$$

$$\because \mathbf{T}_\sigma^{l|g} = \left(\mathbf{T}_\sigma^{g|l}\right)^{-1} \quad - \quad \text{see Eq. (2.41)}$$

$$\left(\mathbf{T}_\sigma^{l|g}\right)^{\mathrm{T}} = \mathbf{T}_\varepsilon^{g|l} \quad - \quad \text{see Eq. (2.52)}$$

$$\therefore \mathbf{C}^l = \left(\mathbf{T}_\varepsilon^{g|l}\right)^{\mathrm{T}}\mathbf{C}^g\mathbf{T}_\varepsilon^{g|l}$$

If $\mathbf{T}_\varepsilon^{l|g}$ is denoted using $\mathbf{T}_c^{g|l}$ and $\mathbf{T}_\varepsilon^{g|l}$ using $\mathbf{T}_c^{l|g}$, the coordinate transformations between the elastic matrix in the LCS and that in the GCS can be expressed as follows:

$$\mathbf{C}^g = \left(\mathbf{T}_c^{g|l}\right)^{\mathrm{T}} \mathbf{C}^l \mathbf{T}_c^{g|l} \tag{2.54}$$

$$\mathbf{C}^l = \left(\mathbf{T}_c^{l|g}\right)^{\mathrm{T}} \mathbf{C}^g \mathbf{T}_c^{l|g} \tag{2.55}$$

$$\mathbf{T}_c^{g|l} = \begin{bmatrix} r_{11}^2 & r_{21}^2 & r_{31}^2 & r_{11}r_{21} & r_{21}r_{31} & r_{31}r_{11} \\ r_{12}^2 & r_{22}^2 & r_{32}^2 & r_{12}r_{22} & r_{22}r_{32} & r_{32}r_{12} \\ r_{13}^2 & r_{23}^2 & r_{33}^2 & r_{13}r_{23} & r_{23}r_{33} & r_{33}r_{13} \\ 2r_{11}r_{12} & 2r_{21}r_{22} & 2r_{31}r_{32} & r_{11}r_{22}+r_{21}r_{12} & r_{21}r_{32}+r_{31}r_{22} & r_{31}r_{12}+r_{11}r_{32} \\ 2r_{12}r_{13} & 2r_{22}r_{23} & 2r_{32}r_{33} & r_{12}r_{23}+r_{22}r_{13} & r_{22}r_{33}+r_{32}r_{23} & r_{32}r_{13}+r_{12}r_{33} \\ 2r_{13}r_{11} & 2r_{23}r_{21} & 2r_{33}r_{31} & r_{13}r_{21}+r_{23}r_{11} & r_{23}r_{31}+r_{33}r_{21} & r_{33}r_{11}+r_{13}r_{31} \end{bmatrix} \tag{2.56}$$

$$\mathbf{T}_c^{l|g} = \begin{bmatrix} r_{11}^2 & r_{12}^2 & r_{13}^2 & r_{11}r_{12} & r_{12}r_{13} & r_{13}r_{11} \\ r_{21}^2 & r_{22}^2 & r_{23}^2 & r_{21}r_{22} & r_{22}r_{23} & r_{23}r_{21} \\ r_{31}^2 & r_{32}^2 & r_{33}^2 & r_{31}r_{32} & r_{32}r_{33} & r_{33}r_{31} \\ 2r_{11}r_{21} & 2r_{12}r_{22} & 2r_{13}r_{23} & r_{11}r_{22}+r_{12}r_{21} & r_{12}r_{23}+r_{13}r_{22} & r_{13}r_{21}+r_{11}r_{23} \\ 2r_{21}r_{31} & 2r_{22}r_{32} & 2r_{23}r_{33} & r_{21}r_{32}+r_{22}r_{31} & r_{22}r_{33}+r_{23}r_{32} & r_{23}r_{31}+r_{21}r_{33} \\ 2r_{31}r_{11} & 2r_{32}r_{12} & 2r_{33}r_{13} & r_{31}r_{12}+r_{32}r_{11} & r_{32}r_{13}+r_{33}r_{12} & r_{33}r_{11}+r_{31}r_{13} \end{bmatrix} \tag{2.57}$$

In terms of the coordinate transformations between the verse matrix of $\mathbf{C}^g$ and that of $\mathbf{C}^l$, i.e. the transformations between $\mathbf{S}^g$ and $\mathbf{S}^l$, their equations can be directly obtained from Eqs. (2.54) and (2.55) by substituting $\mathbf{C}^g$ with $(\mathbf{S}^g)^{-1}$ and $\mathbf{C}^l$ with $(\mathbf{S}^l)^{-1}$.

2.4.3 Application of coordinate transformation

To successfully perform a micromechanical homogenisation for woven composites, the elasticity matrices of the individual constituents in the GCS need to be calculated. For the polymer matrix, its elasticity matrix in the GCS is essentially the one defined in Eq. (2.5), due to its isotropic nature. However, since the elasticity matrix of the yarn material is explicitly defined only in the LCS, as shown in Eq. (2.13), its elasticity matrix in the GCS should be calculated by applying the coordinate transformations introduced in Section 2.4.4. In this section, the procedure for applying coordinate transformations for the yarns in woven composites is exemplified using the plain woven composite UC model shown in Fig. 2.1.
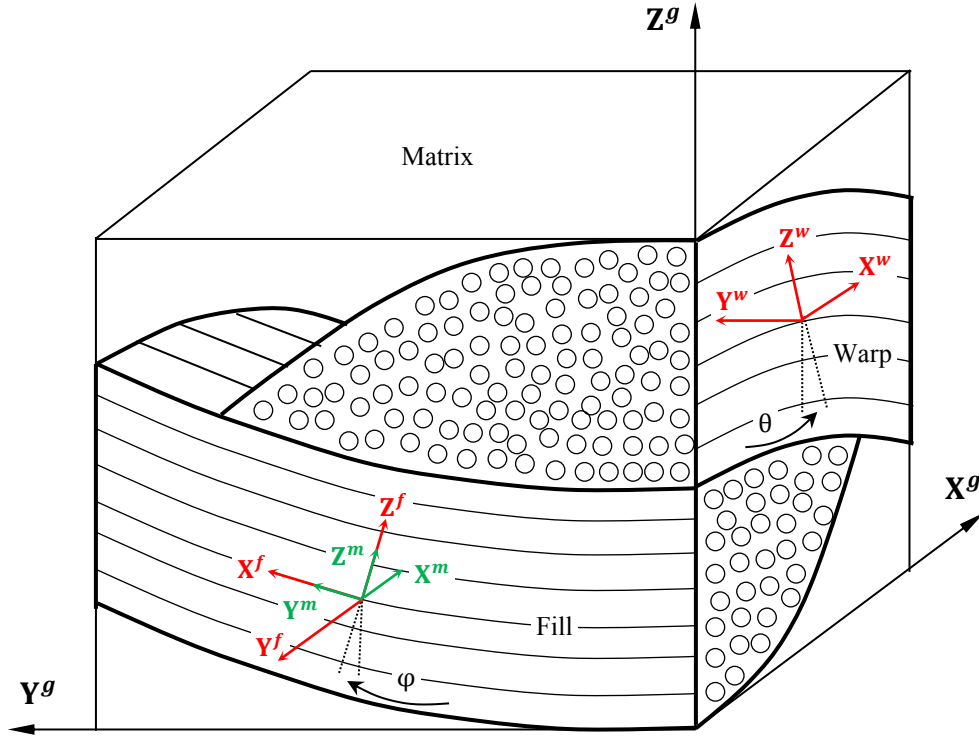
Figure 2.1: Coordinate transformations in plain woven composites

As shown in the figure, the LCS of the warp yarn, $X^w Y^w Z^w$, can be brought to be parallel to the GCS, $X^g Y^g Z^g$, by rotating it for an angle of θ with respect to the Y^w axis. Thus, the rotation matrix from $X^w Y^w Z^w$ to $X^g Y^g Z^g$ can be calculated directly using Eq. (2.22), as follows:

$$\mathbf{R}^{g|w} = \begin{bmatrix} \cos\theta & 0 & -\sin\theta \\ 0 & 1 & 0 \\ \sin\theta & 0 & \cos\theta \end{bmatrix} \tag{2.58}$$

Substituting Eq. (2.58) into Eq. (2.56), the matrix for transforming the elasticity matrix of the warp yarn from the LCS to the GCS can be obtained, as follows:

$$\mathbf{T}_c^{g|w} = \begin{bmatrix} \cos^2\theta & 0 & \sin^2\theta & 0 & 0 & \cos\theta\sin\theta \\ 0 & 1 & 0 & 0 & 0 & 0 \\ \sin^2\theta & 0 & \cos^2\theta & 0 & 0 & -\cos\theta\sin\theta \\ 0 & 0 & 0 & \cos\theta & \sin\theta & 0 \\ 0 & 0 & 0 & -\sin\theta & \cos\theta & 0 \\ -2\sin\theta\cos\theta & 0 & 2\cos\theta\sin\theta & 0 & 0 & \cos(2\theta) \end{bmatrix} \tag{2.59}$$

Assume that the elasticity matrix of the warp yarn in the LCS is $\mathbf{C}^w_{warp}$. Substituting Eq. (2.59) into Eq. (2.54) yields the elasticity matrix of the warp yarn in the GCS:

$$\mathbf{C}^g_{warp} = \left(\mathbf{T}^{g|w}_c\right)^T \mathbf{C}^w_{warp} \mathbf{T}^{g|w}_c \tag{2.60}$$

For the fill yarn, the rotation matrix from the LCS, $X^f Y^f Z^f$, to the GCS, $X^g Y^g Z^g$, cannot be written out directly as it involves two rotations. Specifically, the LCS of the fill yarn, $X^f Y^f Z^f$, should be firstly rotated with respect to the Z^f axis for an angle of 90°, which yields an intermediate coordinate system, denoted as $X^m Y^m Z^m$. This coordinate system can then be rotated with respect to the X^m axis for an angle of φ, leading to a coordinate system parallel to the GCS, $X^g Y^g Z^g$. Thus, the rotation matrix from $X^f Y^f Z^f$ to $X^g Y^g Z^g$ can be calculated using the chain rule defined in Eq. (2.27), as follows:

$$\mathbf{R}^{g|f} = \mathbf{R}^{g|m}\mathbf{R}^{m|f} = \begin{bmatrix} 1 & 0 & 0 \\ 0 & \cos\varphi & -\sin\varphi \\ 0 & \sin\varphi & \cos\varphi \end{bmatrix}\begin{bmatrix} 0 & -1 & 0 \\ 1 & 0 & 0 \\ 0 & 0 & 1 \end{bmatrix}$$

$$= \begin{bmatrix} 0 & -1 & 0 \\ \cos\varphi & 0 & -\sin\varphi \\ \sin\varphi & 0 & \cos\varphi \end{bmatrix} \tag{2.61}$$

Here, it should be kept in mind that the two-step operation is not commutative and the order of the rotations must be preserved. Therefore, the matrix associated with the latter rotation, $\mathbf{R}^{g|m}$, must present before that associated with the former rotation, $\mathbf{R}^{m|f}$, when calculating the final matrix, $\mathbf{R}^{g|f}$. Substituting Eq. (2.61) into Eq. (2.56), the matrix for transforming the elasticity matrix of the fill yarn from its LCS to the GCS can be obtained, as follows:

$$\mathbf{T}^{g|f}_c = \begin{bmatrix} 0 & \cos^2\varphi & \sin^2\varphi & 0 & \cos\varphi\sin\varphi & 0 \\ 1 & 0 & 0 & 0 & 0 & 0 \\ 0 & \sin^2\varphi & \cos^2\varphi & 0 & -\cos\varphi\sin\varphi & 0 \\ 0 & 0 & 0 & -\cos\varphi & 0 & -\sin\varphi \\ 0 & 0 & 0 & \sin\varphi & 0 & -\cos\varphi \\ 0 & -2\cos\varphi\sin\varphi & 2\cos\varphi\sin\varphi & 0 & \cos(2\varphi) & 0 \end{bmatrix} \tag{2.62}$$

Based on this equation and assuming that the elasticity matrix of the fill yarn in the LCS is $\mathbf{C}_{\text{fill}}^f$, the elasticity matrix of the fill yarn in the GCS can be calculated, as follows:

$$\mathbf{C}_{\text{fill}}^g = \left(\mathbf{T}_c^{g|f}\right)^{\text{T}} \mathbf{C}_{\text{fill}}^f \mathbf{T}_c^{g|f} \qquad (2.63)$$

Eqs. (2.5), (2.60) and (2.63) form the basis for calculating the elasticity matrices of the constituents in woven composites in the GCS. Using these equations, micromechanical analysis can be conducted to calculate the stresses and strains of the internal points of the UC, which can be subsequently used to calculate the volume average stress and strain of the UC. However, it should be noted that at this point the stresses and strains derived for the internal points of the UC are based on the GCS. Thus, in the case of homogenising the overall response, where the damage of the yarn material needs to be considered, the stresses and strains of the material points in the yarns should be transformed back to their LCSs such that the damage of the yarn material in woven composites can be evaluated locally. Fig. 2.2 is a flow chart highlighting the coordinate transformations that are often required when homogenising the overall response of woven composites, as well as the equations that can be used to perform these transformations.
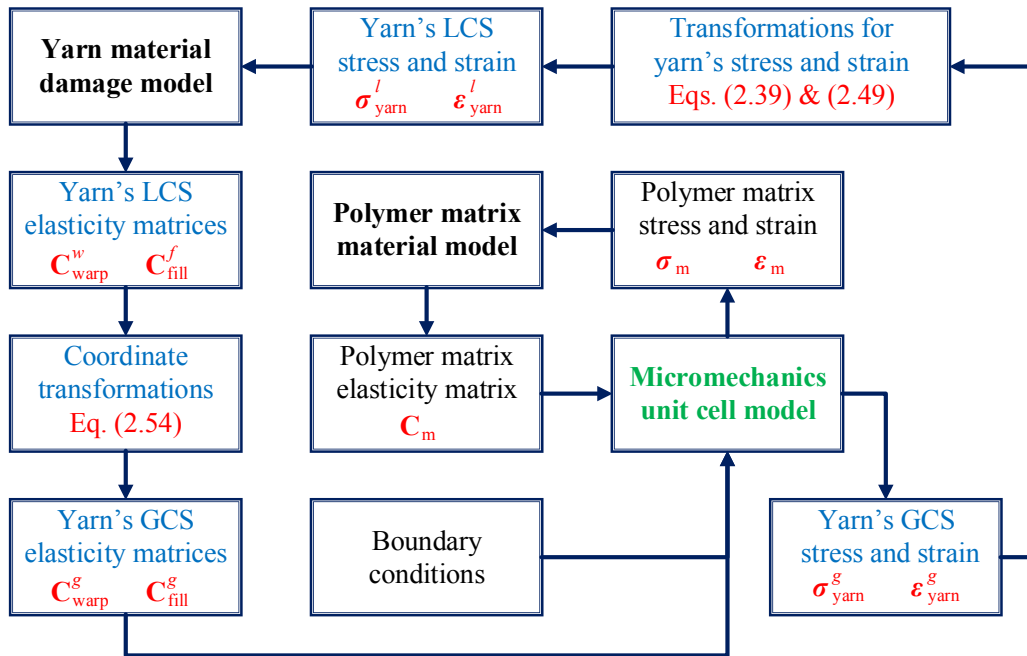
Figure 2.2: Coordinate transformations in homogenising woven composites

2.5 Micromechanical homogenisation methods

2.5.1 Averaging theory

In micromechanical homogenisation of periodic materials such as woven composites, the macroscopic (also known as effective, homogenised, or overall) quantities are evaluated often as the volume averages of the microscopic quantities. Such an averaging theory can be utilised to calculate the volume average stress and strain, as follows:

$$\langle \boldsymbol{\sigma} \rangle = \frac{1}{V} \int_{\Omega} \boldsymbol{\sigma} \, dV \tag{2.64}$$

$$\langle \boldsymbol{\varepsilon} \rangle = \frac{1}{V} \int_{\Omega} \boldsymbol{\varepsilon} \, dV \tag{2.65}$$

where V stands for the volume of the domain of homogenisation, Ω; $\boldsymbol{\sigma}$ and $\boldsymbol{\varepsilon}$ represent the microscopic stress and strain tensors; and $\langle \boldsymbol{\sigma} \rangle$ and $\langle \boldsymbol{\varepsilon} \rangle$ denote the macroscopic or volume average stress and strain tensors.

2.5.2 Uniform boundary conditions

According to the Hill-Mandel principle [146], a prior condition for the volume average properties or responses of a representative region (e.g. UC) being capable of effectively representing those of the macroscopic structure is that the macroscopic strain energy is equal to the volume average work done by the microscopic stress, as follows:

$$\langle \boldsymbol{\sigma} \rangle : \langle \boldsymbol{\varepsilon} \rangle = \langle \boldsymbol{\sigma} : \boldsymbol{\varepsilon} \rangle \tag{2.66}$$

This equation can be rewritten by performing the mathematical manipulations described in [147], as follows:

$$\oiint_{\Gamma} \left(t_i - \langle \sigma_{ij} \rangle n_j \right) \left(u_i - \langle \varepsilon_{ik} \rangle x_k \right) dS = 0 \tag{2.67}$$

where Γ is the boundary of the domain of homogenisation; t_i denotes the component of the traction vector, $\boldsymbol{t}$; u_i represents the component of the displacement vector, $\boldsymbol{u}$; n_j refers to the component of the outward normal, $\boldsymbol{n}$; x_k stands for the component of the coordinate vector, $\boldsymbol{x}$; $\langle \sigma_{ij} \rangle$ is the component of the macroscopic stress; and $\langle \varepsilon_{ik} \rangle$ is the component of the macroscopic strain.

As can be seen from Eq. (2.67), a straightforward boundary condition that satisfies the consistency condition of energy is:

$$t_i = \langle \sigma_{ij} \rangle n_j \qquad \forall \boldsymbol{x} \in \Gamma \tag{2.68}$$

This type of boundary condition is termed as the static uniform boundary condition (also known as the Neumann boundary condition), and it can be enforced by prescribing to the boundary of the problem domain with a uniform traction whose value can be calculated based on the macroscopic stress. Similarly, it can be seen that another type of boundary condition satisfying Eq. (2.67) is:

$$u_i = \langle \varepsilon_{ik} \rangle x_k \qquad \forall \boldsymbol{x} \in \Gamma \tag{2.69}$$

This type of boundary condition is termed as the kinematic uniform boundary condition (also known as the Dirichlet boundary condition), and it can be enforced by prescribing to the boundary of the problem domain with a uniform displacement whose value should be calculated based on the macroscopic strain.

In addition to the above two types of boundary conditions, another possible one is the mixed boundary condition, in which a uniform displacement is applied to one part of the whole boundary, and a uniform traction is enforced to the remaining area. This type of boundary condition was firstly proposed by Hazanov and co-workers [148-150] and was inspired by uniaxial tension tests, where one part of a specimen is often applied with a displacement constraint and the remaining part is prescribed with a force. Based on the results obtained, they argued that the mixed boundary condition can provide better predictions than the kinematic and static uniform boundary conditions. However, this type of boundary condition is found to be less commonly used in the micromechanical homogenisation of woven composites.

Furthermore, the so-called *iso-stress* or *iso-strain* boundary condition can be utilised to perform the micromechanical homogenisation of woven composites. Examples of using iso-stress and iso-strain boundary conditions can be found in Ishikawa and Chou [85-88], Naik and Shembekar [90-92], and Tabiei and his co-workers [134-136]. In these studies, the homogenisation of woven composites is conducted often by prescribing either the same stress (i.e. the iso-stress boundary condition) or the same strain (i.e. the iso-strain

boundary condition) to not only the boundary but also the UC domain itself. Thus, the iso-stress and iso-strain boundary conditions can be largely treated as special cases of the static and kinematic uniform boundary conditions, respectively. The main advantage of the two types of boundary conditions is their exceptionally low computational costs, due to the fact that the stress or strain of any material point in the domain can be calculated directly using the constitutive equation of the material point as long as an iso-strain or iso-stress is prescribed. However, they may suffer from the problem of a reduced accuracy owing to the fact that the energy consistency condition, as defined in Eq. (2.66) or (2.67), does not necessarily hold.

2.5.3 Periodic boundary condition

Compared to the boundary conditions discussed above, the periodic boundary condition (PBC) is the most commonly used in homogenising the elastic properties or the overall response of periodic materials such as woven composites. It has been found in numerous studies [147, 151-153] that the PBC provides better predictions than any other boundary conditions. In this section, the formulation of the PBC will be detailed since it has been adopted in the present research to conduct the micromechanical homogenisation of all three types of woven composites.

Consider a general periodic structure to which a macroscopic loading is applied. Then, the response (e.g. deformation) of an arbitrary point of this structure can be assumed as the sum of a constant part denoting the contribution of macroscopic uniformity and an oscillatory part representing that of microscopic inhomogeneity. If the length scale of the fluctuation in the applied load is significantly larger than the characteristic dimension of the structure (i.e. the length of periodicity), then the oscillatory part will be periodic. The above description suggests that:

$$\boldsymbol{u}(\boldsymbol{x}) = \langle \partial \boldsymbol{u}/\partial \boldsymbol{x} \rangle \boldsymbol{x} + \boldsymbol{u}^*(\boldsymbol{x}) \tag{2.70a}$$

$$\boldsymbol{u}^*(\boldsymbol{x}) = \boldsymbol{u}^*(\boldsymbol{x} + \boldsymbol{\lambda}), \tag{2.70b}$$

$$\boldsymbol{\sigma}(\boldsymbol{x}) = \langle \boldsymbol{\sigma} \rangle + \boldsymbol{\sigma}^*(\boldsymbol{x}) \tag{2.71a}$$

$$\boldsymbol{\sigma}^*(\boldsymbol{x}) = \boldsymbol{\sigma}^*(\boldsymbol{x} + \boldsymbol{\lambda}) \tag{2.71b}$$

$$\boldsymbol{\varepsilon}(\boldsymbol{x}) = \langle \boldsymbol{\varepsilon} \rangle + \boldsymbol{\varepsilon}^*(\boldsymbol{x}) \tag{2.72a}$$

$$\boldsymbol{\varepsilon}^*(\boldsymbol{x}) = \boldsymbol{\varepsilon}^*(\boldsymbol{x} + \boldsymbol{\lambda}) \tag{2.72b}$$

where $\boldsymbol{x}$ is the coordinate vector; $\boldsymbol{u}(\boldsymbol{x})$ is the displacement vector; $\boldsymbol{\sigma}(\boldsymbol{x})$ and $\boldsymbol{\varepsilon}(\boldsymbol{x})$ stand for the stress and strain tensors; $\langle \boldsymbol{\sigma} \rangle$ and $\langle \boldsymbol{\varepsilon} \rangle$ represent the macroscopic stress and strain contributions; $\langle \partial \boldsymbol{u} / \partial \boldsymbol{x} \rangle$ denotes the displacement gradient; $\boldsymbol{\lambda}$ is the periodicity vector; and $\boldsymbol{u}^*(\boldsymbol{x})$, $\boldsymbol{\sigma}^*(\boldsymbol{x})$ and $\boldsymbol{\varepsilon}^*(\boldsymbol{x})$ are the oscillatory parts.

Replacing $\boldsymbol{x}$ with $\boldsymbol{x} + \boldsymbol{\lambda}$ in Eqs. (2.70a), (2.71a) and (2.72a) and considering the relations in Eqs. (2.70b), (2.71b) and (2.72b), we can get the following equations:

$$\boldsymbol{u}(\boldsymbol{x}) = \langle \partial \boldsymbol{u} / \partial \boldsymbol{x} \rangle \boldsymbol{\lambda} + \boldsymbol{u}(\boldsymbol{x} + \boldsymbol{\lambda}) \tag{2.73}$$

$$\boldsymbol{\sigma}(\boldsymbol{x}) = \boldsymbol{\sigma}(\boldsymbol{x} + \boldsymbol{\lambda}) \tag{2.74}$$

$$\boldsymbol{\varepsilon}(\boldsymbol{x}) = \boldsymbol{\varepsilon}(\boldsymbol{x} + \boldsymbol{\lambda}) \tag{2.75}$$
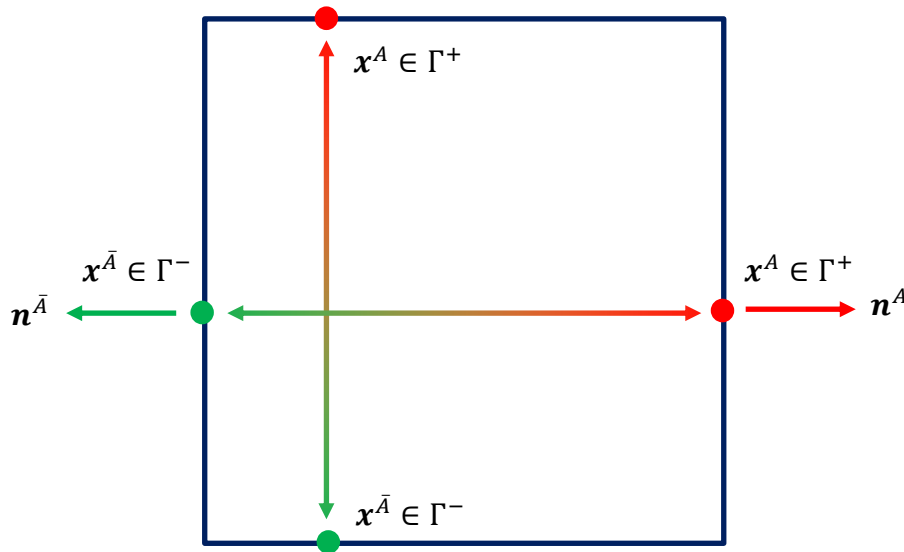
Figure 2.3: Schematic of a 2D UC for applying the PBC

By applying Eq. (2.73) to the boundary of a representative region of the structure, the standard form of PBC can be explicitly formulated, which can be illustrated using the two-dimensional (2D) UC shown in Fig. 2.3. Assume that the UC is bounded by Γ, which can be subdivided into a negative part, Γ^-, and a positive part, Γ^+. Then, for an arbitrary node on the negative boundary, $\forall \boldsymbol{x}^{\bar{A}} \in \Gamma^-$, there is an equivalent node on the positive

boundary, $\forall x^A \in \Gamma^+$, such that the two equivalent nodes, $x^{\bar{A}}$ and x^A, satisfy the relation of $x^A = x^{\bar{A}} + \lambda$. Substituting this relation into Eqs. (2.73) yields:

$$u(x^A) - u(x^{\bar{A}}) = -\langle \partial u / \partial x \rangle \lambda \tag{2.76}$$

To prevent any rigid rotation in the homogenisation, the following restriction should be imposed:

$$\langle \partial u / \partial x \rangle = \langle \partial u / \partial x \rangle^{\mathrm{T}} \tag{2.77}$$

The above equation means that the displacement gradient can be replaced by the volume average strain, $\langle \varepsilon \rangle$, since we have:

$$\langle \varepsilon \rangle = \frac{1}{2} (\langle \partial u / \partial x \rangle + \langle \partial u / \partial x \rangle^{\mathrm{T}}) = \langle \partial u / \partial x \rangle \tag{2.78}$$

Combining Eqs. (2.76) and (2.78), the standard form of PBC can be expressed, as follows:

$$u(x^A) - u(x^{\bar{A}}) = -\langle \varepsilon \rangle \lambda \quad \forall x^{\bar{A}} \in \Gamma^- \,\&\, \forall x^A \in \Gamma^+ \tag{2.79}$$

Here, it should be noted that the above equation can be used to derive PBCs only for full-size UCs, not reduced UCs (the concepts of full-size and reduced UCs will be addressed in Chapter 4). If a homogenisation is performed based on a reduced UC, then the generic form of PBC equation (which can be derived using the equivalence approach and will be detailed in Section 4.5.2, Chapter 4) should be used, as follows:

$$u(x^A) - \gamma \mathbf{T} u(x^{\bar{A}}) = -\langle \varepsilon \rangle \mathbf{T} \lambda \quad \forall x^{\bar{A}} \in \Gamma^- \,\&\, \forall x^A \in \Gamma^+ \tag{2.80}$$

In this equation, $\mathbf{T}$ is the transformation matrix representing the geometrical equivalence between the two equivalent points, $x^{\bar{A}}$ and x^A. The symbol, γ, stands for the load reversal factor, which reflects the loading admissibility between the two equivalent points. The specific meanings of $\mathbf{T}$ and γ will be addressed also in Section 4.5.2, Chapter 4.

2.6 Summary

In this chapter, the elastic constitutive behaviours of the polymer matrix and yarn material of woven composites were firstly described using the generalised Hooke's law. Then, the

basic equations for performing coordinate transformations between the LCS of the yarn material and the GCS of the UC were detailed, followed by an example showing how to use these equations to calculate the elasticity matrices in the GCS from those in the LCS for the warp and weft yarns of plain woven composites. Finally, the theories and concepts involved in the micromechanical homogenisation of periodic materials were presented, with an emphasis on deriving the basic equations of the standard form of PBC.

CHAPTER 3: MESHFREE METHODS

3.1 Introduction

Many engineering problems or phenomena can often be described using mathematical equations such as algebraic equations, ordinary differential equations (ODEs) and partial differential equations (PDEs), which are often referred to as governing equations. In many cases, obtaining the exact or analytical solution for the governing equation is impossible, particularly for the problems involving nonlinearity. The only practical way is to obtain an approximate solution, which can be generally achieved by using a suitable numerical method, such as the finite difference method (FDM), the finite element method (FEM), the boundary element method (BEM) and the meshfree (or meshless) methods.

Among different types of numerical methods, the FEM is the most widely used as it is well-suited for many engineering problems. In the FEM, the continuum of investigation is discretised with non-overlapping but seamlessly connected elements, which forms the mesh. The mesh and element based nature provides the FEM with exceptional robustness and versatility, allowing many types of engineering problems to be efficiently solved. However, the mesh and element based nature also brings about the limitations inherently associated with the utilisation of elements and meshes [154]. Such limitations become increasingly evident when the FEM is utilised for addressing the problems with high geometrical complexity and varying material orientations, e.g. the problem of performing micromechanical homogenisation of woven composites.

One of the limitations of the FEM is that creating a reasonably high-quality mesh is always a prerequisite for conducting the finite element analysis (FEA). For geometrically complex structures, the automatic generation of the mesh using pre-processing tools is difficult to achieve without compromising the quality of the mesh. Thus, heavy manual operations and human interventions are required to create a high-quality mesh, which, however, can be the main component of the time cost in the FEM analysis. This limitation

is even more evident if the FEM is used to perform micromechanical homogenisation of woven composites, where not only the modelling and discretisation of the highly complex geometries of the constituents should be addressed with manual operations, but also the ever-changing material orientations of the yarns need to be assigned manually, see Figs. 1.2 and 1.3 in Chapter 1 for examples.

Another limitation of the FEM arises from it being used to solve the problems involving large deformation, which is that the accuracy of the FEM solution might be significantly reduced as a result of the presence of element distortion. To prevent such a problem, one might take the so-called adaptive analysis to re-mesh the regions with large deformation or distortion. However, the current available re-meshing processors have been mainly designed for the adaptive analysis of two-dimensional (2D) problems due to the technical difficulty in the automatic and efficient regeneration of hexahedron elements for three-dimensional (3D) problems. Even if an adaptive scheme were available for 3D problems, the computational cost that is required to regenerate arbitrary 3D elements may still be unacceptable, particularly for the problems involving nonlinearity and dynamic loading conditions.

The FEM may suffer from the difficulty in predicting the crack propagation in solids. This is because the actual path of a crack in solids is often arbitrary and thus does not necessarily coincides with the interfaces between elements. In addition, the use of the FEM to simulate material breakage is not ideal because of that the elements in the FEM are assumed to be unbreakable, and thus the only possible way is to delete the elements that have been considered as damaged completely. Such a treatment, however, can result in a mesh-dependent prediction of the path of material breakage.

The above examinations reveal that the limitations of the FEM inherently arise from the utilisation of elements and meshes. Therefore, the idea of avoiding the use of elements has been logically formed, and the concept of meshfree (as known as element-free or meshless) has been proposed in the research community, contributing to the development of a wide variety of meshfree methods. In this chapter, an overview of meshfree methods will be firstly presented by comparing against the FEM. Since a key issue to be addressed in developing a meshfree method is how to construct shape functions for approximating field variables. Thus, following the introduction of meshfree methods, three commonly

used shape function construction techniques in meshfree methods, i.e. the moving least squares (MLS) interpolation, the radial basis function (RBF) interpolation and the moving kriging (MK) interpolation, will be detailed in combination with presenting a numerical example for each of these techniques. Another important issue in meshfree methods is how to transform the governing equation of the problem of investigation into a discretised system of equations so as to numerically obtain an approximate solution. Thus, at the end of this chapter, the specific procedures for formulating the standard and explicit weak-form meshfree methods, which have been selected in this work to address the prediction of the elastic properties and that of the overall response of woven composites, will be described, and the implementation of the generic form of PBC within the two types of meshfree methods will be presented.

3.2 Overview of meshfree methods

The key idea of meshfree methods is to discretise the problem domain of investigation with a set of arbitrarily distributed nodes (which are known as field nodes) without using any predefined elements and meshes, and meanwhile to provide an accurate and stable solution based on such a discretisation. Clearly, the use of nodes for domain discretisation is one of the differences between the FEM and meshfree methods, see the flow chart in Fig 3.1 [154]. The node-based nature also produces another significant difference, which is that shape functions in meshfree methods are constructed based on the nodes in a local domain, whereas those in the FEM are constructed based on predefined elements. In the following two sections, the theories and concepts associated with meshfree methods will be introduced by comparing against the FEM from the above two aspects.

Here, it should be noted that all discussions on domain discretisation and shape function construction in this chapter are assumed to be based on a 3D space. However, for the sake of convenience, all illustrations associated with domain discretisation in this chapter will be presented in a 2D manner, see Fig. 3.2 for example. In addition, the basic equations for shape function construction techniques will be presented only in a one-dimensional (1D) manner for simplicity, see Eq. (3.1) for example, where it will be shown that the approximation of the displacement, i.e. $\boldsymbol{u} = (u, v, w)$, of a 3D spatial point, $\boldsymbol{x} = (x, y, z)$, is described based on the first component, i.e. u, of the displacement vector.
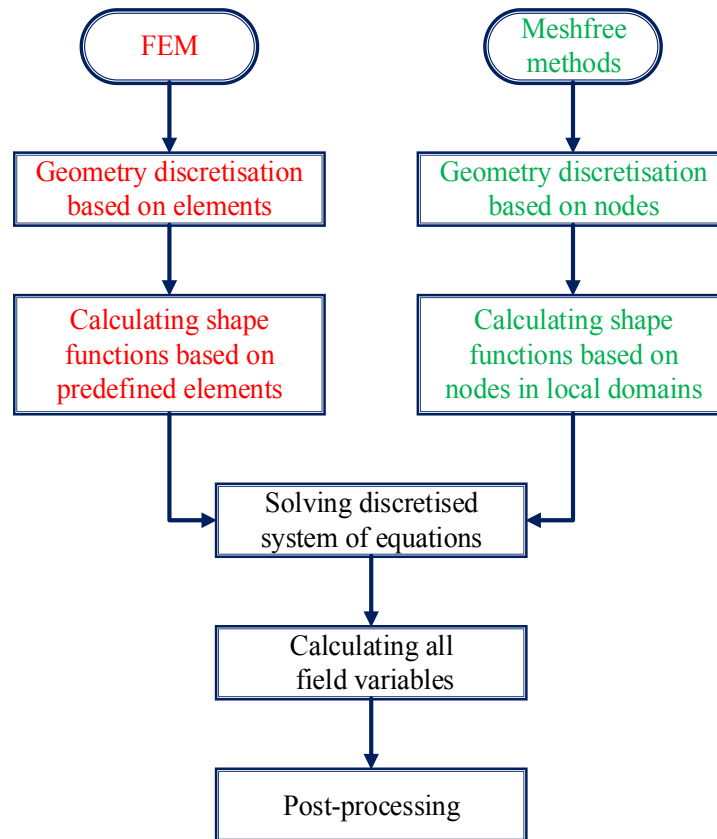
Figure 3.1: Typical procedures in the FEM and meshfree methods

3.2.1 Domain discretisation

As discussed earlier, the fundamental difference between the FEM and meshfree methods is the way of discretising the problem domain of investigation. In the FEM, the problem domain must be discretised using non-overlapping but seamlessly connected elements, see Fig. 3.2a. During the discretisation, the information such as element connectivity must be created. In general, the accuracy of the FEM solution is controlled by the number of elements and the smoothness of the element type, and a finer mesh design often produces a better approximation but requires a higher computational cost.

In meshfree methods, the problem domain is discretised simply using a set of scattered nodes (which can be arbitrarily or regularly distributed) both within the problem domain and on the boundary, see Fig. 3.2b. These nodes are often termed as field nodes as they carry information for field variables. Similar to the FEM, the accuracy of the meshfree solution is controlled by the number of field nodes used. However, compared to the FEM, meshfree methods are much simpler since there is no need to create elements and define

the connectivity between the nodes shared by adjacent elements. In addition, the adaptive analysis based on meshfree methods can be easily performed even for 3D problems since only the regeneration of nodes is needed and therefore the associated computational cost is less expensive.
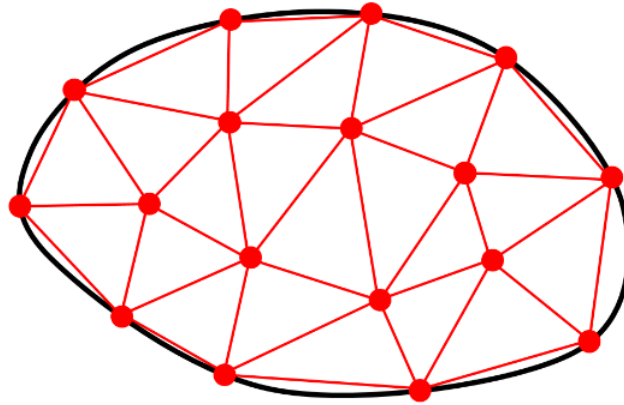
(a) Domain discretisation using the FEM
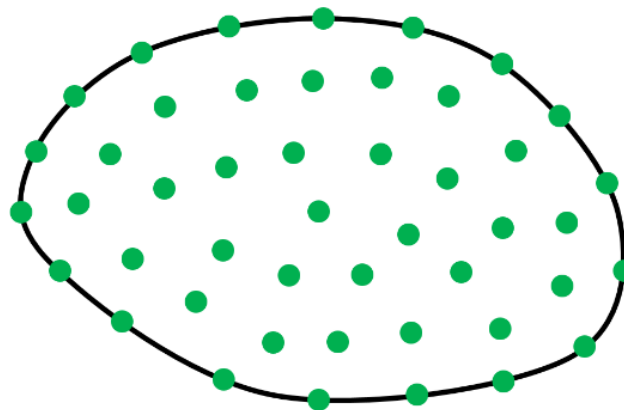
(b) Domain discretisation using meshfree methods

Figure 3.2: Domain representation in the FEM and meshfree methods

3.2.2 Shape function construction

In the FEM, a field variable (e.g. the displacement) of a point of interest, $x = (x, y, z)$ is approximated based on the nodal information of the element where the point is located. For instance, the displacement of x can be approximated as a polynomial interpolation of the nodal displacements of the element in which it is located:

$$u^h(x) = \sum_{I=1}^{n_d} \phi_I(x)u_I = \boldsymbol{\phi}^{\mathrm{T}}(x)\boldsymbol{u} \tag{3.1}$$

where $u^h(x)$ is the approximate displacement of x; the superscript, n_d, denotes the total number of the nodes that form the element; and u_I and $\phi_I(x)$ are the displacement and shape function of the Ith node.
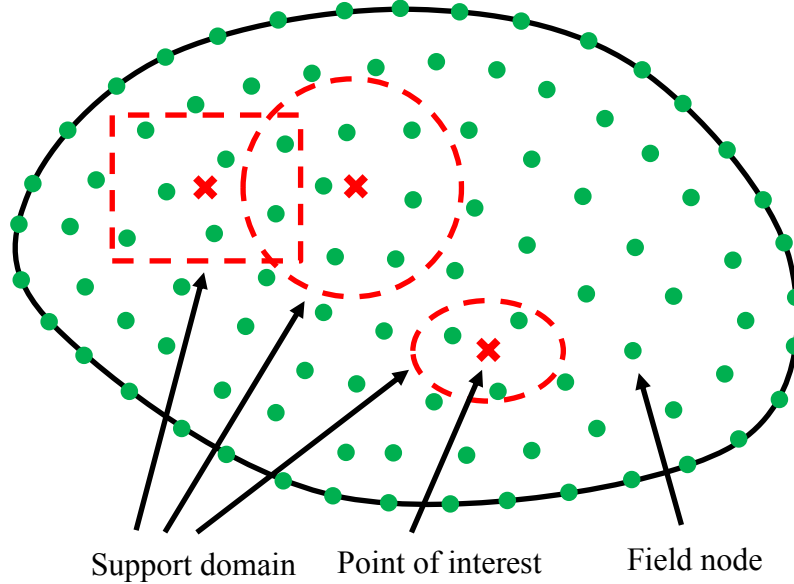
Figure 3.3: Local domain based approximation in meshfree methods

On the other hand, as there is no element used in meshfree methods, the field variable of a point of interest is approximated based on the information of the field nodes within a small local domain of it, see Fig. 3.3. This small local domain is referred to as the support domain of this point, and the field nodes within the support domain are termed as the support nodes. The shape of a support domain can be circular, elliptical or rectangular. In the same problem, the support domains can have different sizes and shapes, and they can overlap with each other. Similar to the definition of the size of an element in the FEM, the choice of the size of a support domain in meshfree methods is very flexible. In general, it can be reasonably determined using the following equation [154]:

$$d_s = \alpha_s d_c \tag{3.2}$$

where d_s is the size of the support domain, α_s is a dimensionless factor used to scale the size of the support domain, and d_c is the average spacing among the field nodes in the support domain and can be approximated using the following equation:

$$d_{\text{c}} = \begin{cases} \dfrac{D_{\text{s}}}{(1-n_{\text{D}})} & \text{1D} \\[2ex] \dfrac{\sqrt{A_{\text{s}}}}{(\sqrt{n_{\text{A}}}-1)} & \text{2D} \\[2ex] \dfrac{\sqrt{V_{\text{s}}}}{(\sqrt{n_{\text{V}}}-1)} & \text{3D} \end{cases} \qquad (3.3)$$

where D_{s}, A_{s} and V_{s} are the estimated sizes of the support domain in 1D, 2D and 3D cases, respectively; and n_{D}, n_{A} and n_{V} are the numbers of the field nodes within the estimated support domain in 1D, 2D and 3D cases.

It should be noted that the basic equations for approximating field variables in meshfree methods, which will be shown later when introducing the MLS, RBF and MK techniques, are essentially the same as that in the FEM, see Eq. 3.1. However, the way of constructing shape functions in meshfree methods is different since it is based on the use of a support domain rather an element. In addition, when approximating the field variables of the same problem, the number of nodes should be included in a support domain is generally larger than the number of nodes in a typical element in the FEM. This suggests that in general meshfree methods have lower computational efficiency but higher accuracy compared to the FEM.

3.3 MLS interpolation

The moving least squares technique was originally developed by mathematicians for data fitting and surface construction. A detailed description of such a technique can be found in Lancaster and Salkauskas [155]. Nayroles *et al.* [156] are the first researchers who adapted the MLS technique to develop the diffuse element method (DEM). The DEM was modified by Belytschko *et al.* [157], leading to the element-free Galerkin method (EFGM), which is a well-established meshfree method that is based on the utilisation of the MLS technique.

The popularity of utilising the MLS technique in meshfree methods lies in two aspects. The first one is that the field function approximated will be continuous and smooth in the entire problem domain if an enough number of interpolation points is used. This feature makes the MLS technique well-suited for formulating the constrained Galerkin weak-

form method. The seconded aspect is that it can be designed to obtain approximations at a designated order of consistency. In the following section, the procedure for applying the MLS technique for constructing the MLS-based meshfree shape functions will be detailed and discussed.

3.3.1 MLS procedure
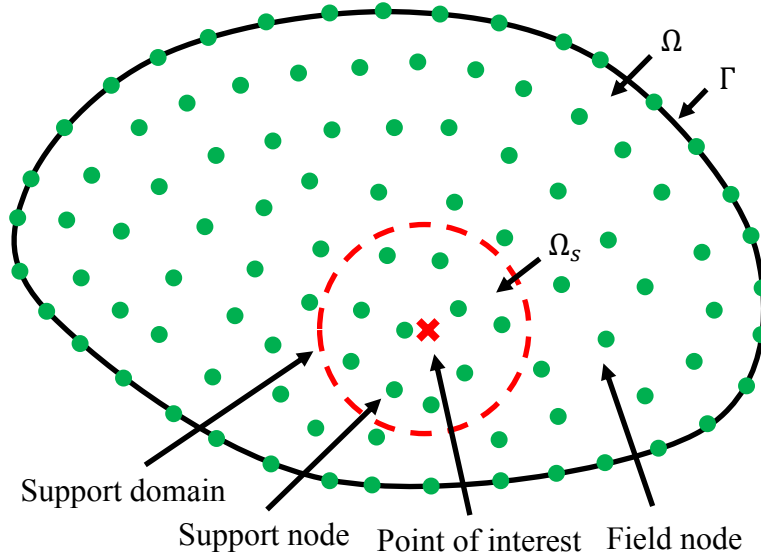
Figure 3.4: Field variable approximation in meshfree methods

To illustrate the MLS procedure, consider a general problem domain, Ω, bounded by Γ, as shown in Fig. 3.4. Assume that this domain is discretised with a number of arbitrarily distributed field nodes. For a continuous field function, $u(\boldsymbol{x})$, defined in the domain for an arbitrary point, $\boldsymbol{x} = (x, y, z)$, the MLS technique assumes that the field function can be approximated in the following form:

$$u^h(\boldsymbol{x}) = \sum_{J=1}^{m} p_J(\boldsymbol{x})\alpha_J(\boldsymbol{x}) = \boldsymbol{p}^{\mathrm{T}}(\boldsymbol{x})\boldsymbol{\alpha}(\boldsymbol{x}) \tag{3.4}$$

where $\boldsymbol{p}^{\mathrm{T}}(\boldsymbol{x})$ represents a polynomial basis with m monomial terms, and $\boldsymbol{\alpha}(\boldsymbol{x})$ is a vector of m unknown coefficients:

$$\boldsymbol{p}^{\mathrm{T}}(\boldsymbol{x}) = \{p_1(\boldsymbol{x}) \quad p_2(\boldsymbol{x}) \quad \cdots \quad p_m(\boldsymbol{x})\} \tag{3.5}$$

$$\boldsymbol{\alpha}(\boldsymbol{x}) = \{\alpha_1(\boldsymbol{x}) \quad \alpha_2(\boldsymbol{x}) \quad \cdots \quad \alpha_m(\boldsymbol{x})\}^{\mathrm{T}} \tag{3.6}$$

Theoretically, the components in $\boldsymbol{p}^{\mathrm{T}}(\boldsymbol{x})$ can be any arbitrary functions of $\boldsymbol{x}$. However, the most common choice is to utilised a complete basis, and a complete p-order polynomial can be defined by:

$$\boldsymbol{p}^{\mathrm{T}}(\boldsymbol{x}) = \begin{cases} \{1 \quad x \quad x^2 \quad \cdots \quad x^{p-1} \quad x^p\} & \text{1D} \\ \{1 \quad x \quad y \quad xy \quad x^2 \quad y^2 \quad \cdots \quad x^p \quad y^p\} & \text{2D} \\ \{1 \quad x \quad y \quad z \quad xy \quad yz \quad zx \quad x^2 \quad y^2 \quad z^2 \quad \cdots \quad x^p \quad y^p \quad z^p\} & \text{3D} \end{cases} \quad (3.7)$$

To determine the coefficients in $\boldsymbol{\alpha}(\boldsymbol{x})$, a support domain, Ω_s, is defined for the point of interest, $\boldsymbol{x}$. Assume that the number of the field nodes in the support domain is n, which should be larger than m. Applying Eq. (3.4) to all the support nodes produces:

$$u^h(\boldsymbol{x}_I) = u^h(\boldsymbol{x}, \boldsymbol{x}_I) = \sum_{J=1}^m p_J(\boldsymbol{x}_I)\alpha_J(\boldsymbol{x}) \quad (I = 1, 2, \dots, n) \quad (3.8)$$

Here, it should be noted that the value approximated for a support node using this equation is not necessarily equal to its nodal value, i.e. $u^h(\boldsymbol{x}_I) \neq u_I$. Thus, a function of weighted residual is constructed to minimise the error in the approximations, as follows:

$$R_{mls} = \sum_I^n W_I(\boldsymbol{x})\left(u^h(\boldsymbol{x}, \boldsymbol{x}_I) - u(\boldsymbol{x}_I)\right)^2 = \sum_I^n W_I(\boldsymbol{x})(\boldsymbol{p}^{\mathrm{T}}(\boldsymbol{x}_I)\boldsymbol{\alpha}(\boldsymbol{x}) - u_I)^2 \quad (3.9)$$

In this equation, $W_I(\boldsymbol{x})$ is a weight function chosen to play two roles. The first role is to control the weights of support nodes, giving bigger (or smaller) weights for the support nodes close to (or far from) $\boldsymbol{x}$. The second role is to ensure a smooth transition of the field nodes leaving or entering the support domain when the point of interest moves in the problem domain. Technically, the weight function can be any type of function as long as it satisfies the positivity, compact and decay conditions, as described in [158]. However, a weight function can effectively play the above two roles only when an enough number of support nodes is used (i.e. $n \gg m$). The commonly used weight functions include the cubic spline, the quadratic spline and the exponential weight functions. In this work, the quadratic spline weight function is utilised, as follows:

$$W_I(\boldsymbol{x}) = \begin{cases} 1 - 6\left(\frac{d_I}{d_s}\right)^2 + 8\left(\frac{d_I}{d_s}\right)^3 - 3\left(\frac{d_I}{d_s}\right)^4 & 0 \leq d_I \leq d_s \\ 0 & d_s \leq d_I \end{cases} \quad (3.10)$$

where d_I stands for the distance between the point of interest and the Ith support node, i.e. the distance between x and x_I; and d_s is the size of the support domain.

In the MLS technique, the unknown coefficients in $\alpha(x)$ are determined by minimising the weighted residual defined in Eq. (3.9). Since the condition of the residual reaching a minimum is $\partial R_{mls}/\partial \alpha = 0$, we can obtain the following linear system of equations:

$$\mathbf{A}(x)\alpha(x) = \mathbf{B}(x)u \tag{3.11}$$

where $\mathbf{A}(x)$ refers to as the MLS weighted moment matrix, $\mathbf{B}(x)$ is a matrix based on weight functions and polynomials, and u is a vector collecting the nodal values of the n support nodes:

$$\mathbf{A}(x) = \sum_I^n W_I(x)p(x_I)\,p^{\mathrm{T}}(x_I) \tag{3.12}$$

$$\mathbf{B}(x) = \{b_1(x) \quad b_2(x) \quad ... \quad b_n(x)\} \tag{3.13}$$

$$b_I(x) = W_I(x)p(x_I) \tag{3.14}$$

$$u = \{u_1 \quad u_2 \quad ... \quad u_n\}^{\mathrm{T}} \tag{3.15}$$

Assuming that the MLS moment matrix is invertible, Eq. (3.11) can be rewritten into the following form:

$$\alpha(x) = \mathbf{A}^{-1}(x)\mathbf{B}(x)u \tag{3.16}$$

Substituting this equation back into Eq. (3.4) yields the MLS approximation of the field variable, $u^h(x)$, as follows:

$$u^h(x) = \sum_{I=1}^n \left(\sum_{J=1}^m p_J(x)\big(\mathbf{A}^{-1}(x)\mathbf{B}(x)\big)_{JI}\right)u_I = \sum_{I=1}^n \phi_I(x)u_I \tag{3.17}$$

or in the matrix form:

$$u^h(x) = p^{\mathrm{T}}(x)\mathbf{A}^{-1}(x)\mathbf{B}(x)u = \phi^{\mathrm{T}}(x)u \tag{3.18}$$

where $\big(\mathbf{A}^{-1}(x)\mathbf{B}(x)\big)_{JI}$ is the JIth component of the resulting matrix of $\mathbf{A}^{-1}(x)\mathbf{B}(x)$, and ϕ is a vector consisting of the MLS shape functions, as follows:

$$\boldsymbol{\phi}^{\mathrm{T}}(\boldsymbol{x}) = \{\phi_1 \quad \phi_2 \quad \ldots \quad \phi_n\} = \boldsymbol{p}^{\mathrm{T}}(\boldsymbol{x})\mathbf{A}^{-1}(\boldsymbol{x})\mathbf{B}(\boldsymbol{x}) \tag{3.19}$$

where $\phi_I(\boldsymbol{x})$ is the MLS-based meshfree shape function of the Ith support node, and it can be expanded as follows:

$$\phi_I(\boldsymbol{x}) = \sum_{j=1}^{m} p_j(\boldsymbol{x})\big(\mathbf{A}^{-1}(\boldsymbol{x})\mathbf{B}(\boldsymbol{x})\big)_{JI} = \boldsymbol{p}^{\mathrm{T}}(\boldsymbol{x})\mathbf{A}^{-1}(\boldsymbol{x})\mathbf{B}(\boldsymbol{x}) \tag{3.20}$$

3.3.2 MLS shape function derivatives

The MLS formulation given in Eq. (3.17) or (3.18) can be utilised directly to evaluate the displacement field. However, in order to calculate field variables such as strain, the first-order and second-order partial derivatives of the MLS-based shape functions need to be derived. The procedure for calculating these derivatives is briefed as follows. By denoting $\boldsymbol{p}^{\mathrm{T}}(\boldsymbol{x})\mathbf{A}^{-1}(\boldsymbol{x})$ as $\boldsymbol{\zeta}^{\mathrm{T}}(\boldsymbol{x})$, Eq. (3.19) can be rewritten as:

$$\boldsymbol{\phi}^{\mathrm{T}}(\boldsymbol{x}) = \boldsymbol{\zeta}^{\mathrm{T}}(\boldsymbol{x})\mathbf{B}(\boldsymbol{x}) \tag{3.21}$$

where $\boldsymbol{\zeta}(\boldsymbol{x})$ can be solved using the following equation, which is obtained by considering the symmetry of $\mathbf{A}(\boldsymbol{x})$:

$$\mathbf{A}(\boldsymbol{x})\boldsymbol{\zeta}(\boldsymbol{x}) = \boldsymbol{p}(\boldsymbol{x}) \tag{3.22}$$

Then, the first-order partial derivative of $\boldsymbol{\zeta}(\boldsymbol{x})$ can be calculated by taking the derivative of the above equation with respect to $i = (x, y, z)$, as follows:

$$\boldsymbol{\zeta}_{,i} = \mathbf{A}^{-1}\big(\boldsymbol{p}_{,i} - \mathbf{A}_{,i}\boldsymbol{\zeta}\big) \tag{3.23}$$

where $(\quad)_{,i}$ stands for $\partial(\quad)/\partial x_i$. Similarly, the second-order partial derivative of $\boldsymbol{\zeta}(\boldsymbol{x})$ can be obtained by taking the derivative of Eq. (3.23) with respect to $j = (x, y, z)$, as follows:

$$\boldsymbol{\zeta}_{,ij} = \mathbf{A}^{-1}\Big(\boldsymbol{p}_{,ij} - \big(\mathbf{A}_{,i}\boldsymbol{\zeta}_{,j} + \mathbf{A}_{,j}\boldsymbol{\zeta}_{,i} + \mathbf{A}_{,ij}\boldsymbol{\zeta}\big)\Big) \tag{3.24}$$

Considering the above two equations and taking the derivatives of Eq. (3.21) and the resulting equation with respect to i and j, respectively, the first-order and second-order partial derivatives of the MLS-based shape functions can be derived, as follows:

$$\boldsymbol{\phi}_{,i}^{\mathrm{T}} = \boldsymbol{\zeta}_{,i}^{\mathrm{T}}\mathbf{B} + \boldsymbol{\zeta}^{\mathrm{T}}\mathbf{B}_{,i} \qquad (3.25)$$

$$\boldsymbol{\phi}_{,ij}^{\mathrm{T}} = \boldsymbol{\zeta}_{,ij}^{\mathrm{T}}\mathbf{B} + \boldsymbol{\zeta}_{,i}^{\mathrm{T}}\mathbf{B}_{,j} + \boldsymbol{\zeta}_{,j}^{\mathrm{T}}\mathbf{B}_{,i} + \boldsymbol{\zeta}^{\mathrm{T}}\mathbf{B}_{,ij} \qquad (3.26)$$

3.3.3 An MLS example

To investigate the features possessed by the MLS-based shape functions, an example has been conducted on a 2D square domain with dimensions of $[-0.5, 0.5] \times [-0.5, 0.5]$, and this domain is discretised with a total number of 5×5 uniformly distributed field nodes. The quadratic spline function, as defined in Eq. (3.10), is used as the weight function, and both the MLS-based shape functions and the first-order partial derivatives are calculated based on the use of the linear polynomial basis and that of the quadratic polynomial basis. Some of the input and output data in this example are given in Table A.1, Appendix A.

In this table, the output data have been calculated when the point of interest is set to be the central point of the square domain, i.e. $\boldsymbol{x} = (0,0)$. It is clear from this table that the sum of the shape functions in both the case of using the linear polynomial basis and that of using the quadratic polynomial basis is equal to unity:

$$\sum_{I=1}^{n} \phi_I(\boldsymbol{x}) = 1 \qquad (3.27)$$

The above feature is referred to as the property of *partitions of unity* and is possessed by not only the MLS-based shape functions but also many other shape functions such as the RBF-based and MK-based shape functions, which will be demonstrated later in Sections 3.4.3 and 3.5.3. The significance of possessing such a property is that it allows for the reproduction of a constant field or rigid body moment.

Apart from the above results, further calculations have also been performed to derive the MLS-based shape functions and the corresponding first-order derivatives for a resolution of 51×51 uniformly distributed points. Here, it should be noted that the support domains used for these points are the same one, i.e. the square domain. The results corresponding to the central field node (which is one of the 5×5 field nodes not the 25×25 resolution nodes) are visualised in Fig. 3.5. As is evidently shown in this figure, both the MLS-based shape function and the first-order derivative are very smooth, with the former exhibiting a bell shape surface across the square domain and the latter showing an antisymmetric

shape with respect to the central point. In addition, the results obtained based on the linear polynomial basis resemble those based on the quadratic polynomial basis, except for the presence of higher peaks in the latter case. This means that both the linear polynomial basis and the quadratic polynomial basis are able to produce very smooth approximations.

(a) $\phi(x)$ based on linear polynomial

(b) $\partial\phi/\partial x$ based on linear polynomial

(c) $\phi(x)$ based on quadratic polynomial

(d) $\partial\phi/\partial x$ based on quadratic polynomial
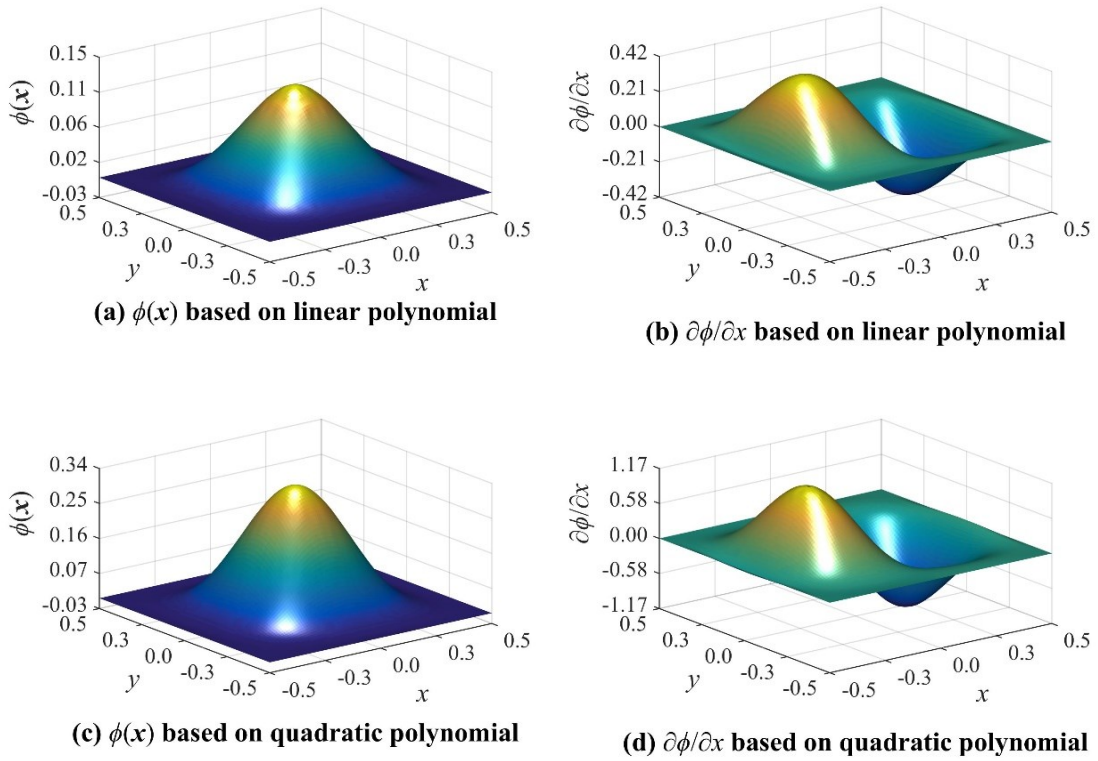
Figure 3.5: The MLS-based shape functions & *x*-derivatives at the central node
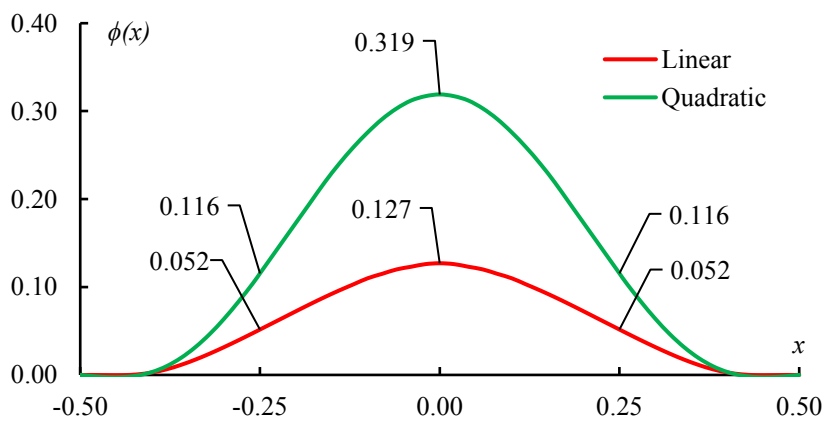
Figure 3.6: The MLS-based shape functions plotted on plane Y=0

To take a closer examination of the results presented in Fig. 3.5, the MLS-based shape functions are plotted on plane $Y = 0$, and the resulting curves are shown in Fig. 3.6. From

this figure, it can be seen that the MLS-based shape functions do not necessarily satisfy the following condition:

$$\phi_I(x = x_J) = \begin{cases} 1 & I = J \\ 0 & I \neq J \end{cases} \quad I = 1,2,\dots,n \tag{3.28}$$

The above feature is often termed as the Kronecker delta function property. The lack of such a property in the MLS-based shape functions is due to the fact that the field function of approximation in the MLS procedure is not required to pass through the nodal values. Therefore, it should be kept in mind that when using the MLS technique to enforce an essential boundary condition the displacements that will be actually prescribed may not be exactly equal to the designated values. Thus, additional treatments are often needed if an essential boundary condition needs to be enforced exactly.

3.4 RBF interpolation

In describing the MLS procedure, it has been assumed that the weighted moment matrix is invertible. However, it can be found by taking a closer examination that this assumption will fail if the number of the support nodes used is less than the number of components in the polynomial basis. Also, the reversibility of the weighted moment is dependent of the distribution of support nodes within the support domain. Therefore, one drawback of the MLS technique is that the weighted moment matrix can be singular. As demonstrated in the example in Section 3.2.3, another drawback of the MLS technique is that this type of shape functions does not possess the so-called Kronecker delta function property, which leads to a difficulty in exactly enforcing essential boundary conditions. A simple solution to avoid the above two problems is to replace the MLS technique with the RBF technique, as will be detailed in the following section.

3.4.1 RBF procedure

To illustrate the RBF procedure, consider again the problem domain defined in Section 3.3.1. In the RBF technique, the field function of a point interest is approximated based on radial basis functions, as follows:

$$u^h(x) = \sum_{I=1}^{n} r_I(x)\alpha_I = r^{\mathrm{T}}(x)\alpha \tag{3.29}$$

where n is the number of support nodes, and α_I is the unknown coefficient corresponding to the Ith radial basis function, $r_I(\boldsymbol{x})$:

$$\boldsymbol{r}^{\mathrm{T}}(\boldsymbol{x}) = \{r_1(\boldsymbol{x}) \quad r_2(\boldsymbol{x}) \quad \cdots \quad r_n(\boldsymbol{x})\} \tag{3.30}$$

$$\boldsymbol{\alpha}(\boldsymbol{x}) = \{\alpha_1(\boldsymbol{x}) \quad \alpha_2(\boldsymbol{x}) \quad \cdots \quad \alpha_n(\boldsymbol{x})\}^{\mathrm{T}} \tag{3.31}$$

where the Ith radial basis function, $r_I(\boldsymbol{x})$, is related to the distance between $\boldsymbol{x}$ and the Ith support node, which can be defined as follows:

$$d_I = \begin{cases} |x - x_I| & \text{1D} \\ \sqrt{(x - x_I)^2 + (y - y_I)^2} & \text{2D} \\ \sqrt{(x - x_I)^2 + (y - y_I)^2 + (z - z_I)^2} & \text{3D} \end{cases} \tag{3.32}$$

The commonly used RBFs include the multiquadric function (MQF), the Gaussian radial function (GRF), the thin plate spline function (TPSF) and the logarithmic radial basis function (LRBF). The general forms of these functions are defined as follows:

$$r_I(\boldsymbol{x}) = (a_0^2 + d_I^2)^q \quad \text{MQF} \tag{3.33}$$

$$r_I(\boldsymbol{x}) = \exp(-\theta d_I^2) \quad \text{GRF} \tag{3.34}$$

$$r_I(\boldsymbol{x}) = d_I^\eta \quad \text{TPSF} \tag{3.35}$$

$$r_I(\boldsymbol{x}) = d_I^\eta \log d_I \quad \text{LRFB} \tag{3.36}$$

where a_0, q, θ and η are numerical parameters controlling the shape and size of the radial basis function.

In the present work, we focus on the use of the MQF proposed by Hardy [159] since this type of MQF is widely used for surface fitting and approximating solutions. Such an MQF can be obtained by setting $q = 0.5$ in Eq. (3.33), as follows:

$$r_I(\boldsymbol{x}) = \sqrt{a_0^2 + d_I^2} \tag{3.37}$$

In this work, three scaling parameters are added into d_I to scale the radial basis function, as follows:

$$d_I = \begin{cases} |a_1(x - x_I)| & \text{1D} \\ \sqrt{a_1^2(x - x_I)^2 + a_2^2(y - y_I)^2} & \text{2D} \\ \sqrt{a_1^2(x - x_I)^2 + a_2^2(y - y_I)^2 + a_3^2(z - z_I)^2} & \text{3D} \end{cases} \tag{3.38}$$

where a_1, a_2 and a_3 are the scaling parameters. The purpose of using these parameters is to improve the flexibility of the RBF technique in terms of controlling the resulting shape functions and derivatives.

By applying Eq. (3.29) to all the n support nodes, a linear system of equations can be formed, as follows:

$$\boldsymbol{u} = \mathbf{R}\boldsymbol{\alpha} \tag{3.39}$$

where $\boldsymbol{u}$ is a vector collecting the nodal values of the n support nodes, $\boldsymbol{\alpha}$ is the vector consisting of the unknown coefficients and $\mathbf{R}$ refers to the RBF moment matrix:

$$\boldsymbol{u} = \{u_1 \quad u_2 \quad \cdots \quad u_n\}^{\mathrm{T}} \tag{3.40}$$

$$\boldsymbol{\alpha} = \{\alpha_1 \quad \alpha_2 \quad \cdots \quad \alpha_n\}^{\mathrm{T}} \tag{3.41}$$

$$\mathbf{R} = \begin{bmatrix} r_1(\boldsymbol{x}_1) & r_2(\boldsymbol{x}_1) & \cdots & r_n(\boldsymbol{x}_1) \\ r_1(\boldsymbol{x}_2) & r_2(\boldsymbol{x}_2) & \cdots & r_n(\boldsymbol{x}_2) \\ \vdots & \vdots & \ddots & \vdots \\ r_1(\boldsymbol{x}_n) & r_2(\boldsymbol{x}_n) & \cdots & r_n(\boldsymbol{x}_n) \end{bmatrix} \tag{3.42}$$

It should be noted that the radial basis functions are positively defined and thus the RBF moment matrix is invertible. Therefore, the unknown coefficients in Eq. (3.39) can be solved, as follows:

$$\boldsymbol{\alpha} = \mathbf{R}^{-1}\boldsymbol{u} \tag{3.43}$$

Substituting this equation back into Eq. (3.29) yields the RBF approximation of the field function, as follows:

$$u^h(\boldsymbol{x}) = \sum_{I=1}^{n}\left(\sum_{J=1}^{n} r_J(\boldsymbol{x})(\mathbf{R}^{-1})_{JI}\right)u_I = \sum_{I=1}^{n} \phi_I(\boldsymbol{x})u_I \tag{3.44}$$

or in the matrix form:

$$u^h(x) = r^{\mathrm{T}}(x)\mathbf{R}^{-1}u = \phi^{\mathrm{T}}(x)u \tag{3.45}$$

where $(\mathbf{R}^{-1})_{JI}$ is the JIth component of $\mathbf{R}^{-1}$, and ϕ is the vector consisting of the RBF-based shape functions:

$$\phi^{\mathrm{T}}(x) = \{\phi_1 \quad \phi_2 \quad \cdots \quad \phi_n\}^{\mathrm{T}} = r^{\mathrm{T}}(x)\mathbf{R}^{-1} \tag{3.46}$$

where $\phi_I(x)$ is the RBF-based shape function corresponding to the Ith support node, and it can be expanded as follows:

$$\phi_I(x) = \sum_{J=1}^{n} r_J(x)(\mathbf{R}^{-1})_{JI} \tag{3.47}$$

3.4.2 RBF shape function derivatives

It is evident from Eq. (3.42) that the RBF moment matrix is independent of x. Thus, the first-order and second-order partial derivatives of the RBF shape functions can be directly obtained by taking the derivatives of Eq. (3.46) and the resulting equation with respect to i and j, respectively, as follows:

$$\phi_{I,i}(x) = \sum_{J=1}^{n} r_{J,i}(x)(\mathbf{R}^{-1})_{JI} \tag{3.48}$$

$$\phi_{I,ij}(x) = \sum_{J=1}^{n} r_{J,ij}(x)(\mathbf{R}^{-1})_{JI} \tag{3.49}$$

where $r_{J,i}(x)$ and $r_{J,ij}(x)$ are the first-order and second-order partial derivatives of $r_J(x)$, and they can be explicitly expressed for the case of using the modified MQF, as follows:

$$r_{J,i}(x) = \frac{2qa_i^2\big((x)_i-(x_J)_i\big)}{a_0^2+d_I^2} r_J(x) \tag{3.50}$$

$$r_{J,ij}(x) = \frac{4q(q-1)a_i^2 a_j^2\big((x)_i-(x_J)_i\big)\big((x)_j-(x_J)_j\big)}{\big(a_0^2+d_I^2\big)^2} r_J(x) \tag{3.51}$$

3.4.3 An RBF example

An example of utilising the RBF technique has been also conducted to study the features possessed by this type of shape functions. This example is performed by using again the

2D domain described in Section 3.3.3. Results are calculated for both the case of using the MQF defined in Eq. (3.37) and that of using the GQF defined in Eq. (3.34) as the radial basis function. The parameters used in this example are $a_0 = 1$, $a_1 = 1$, $a_2 = 1$ and $\theta = 0.75$.

The input and output data for the case of the central point being the point of interest are given in Table A.2, Appendix A. It is clearly seen in this table that the sum of the shape functions at all field nodes is equal to unity, meaning that the RBF-based shape functions possess the property of partitions of unity. Also, it can be found that the shape function at the central field node is equal to unity, while those at the remaining field nodes are equal to zero. This suggests that the RBF-based shape functions also possess the Kronecker delta function property, which is essentially a result of the fact that the field function of approximation in the RBF procedure is required to pass through all the field nodes in the support domain.

(a) $\phi(x)$ based on MQF

(b) $\partial\phi/\partial x$ based on MQF

(c) $\phi(x)$ based on GQF

(d) $\partial\phi/\partial x$ based on GQF
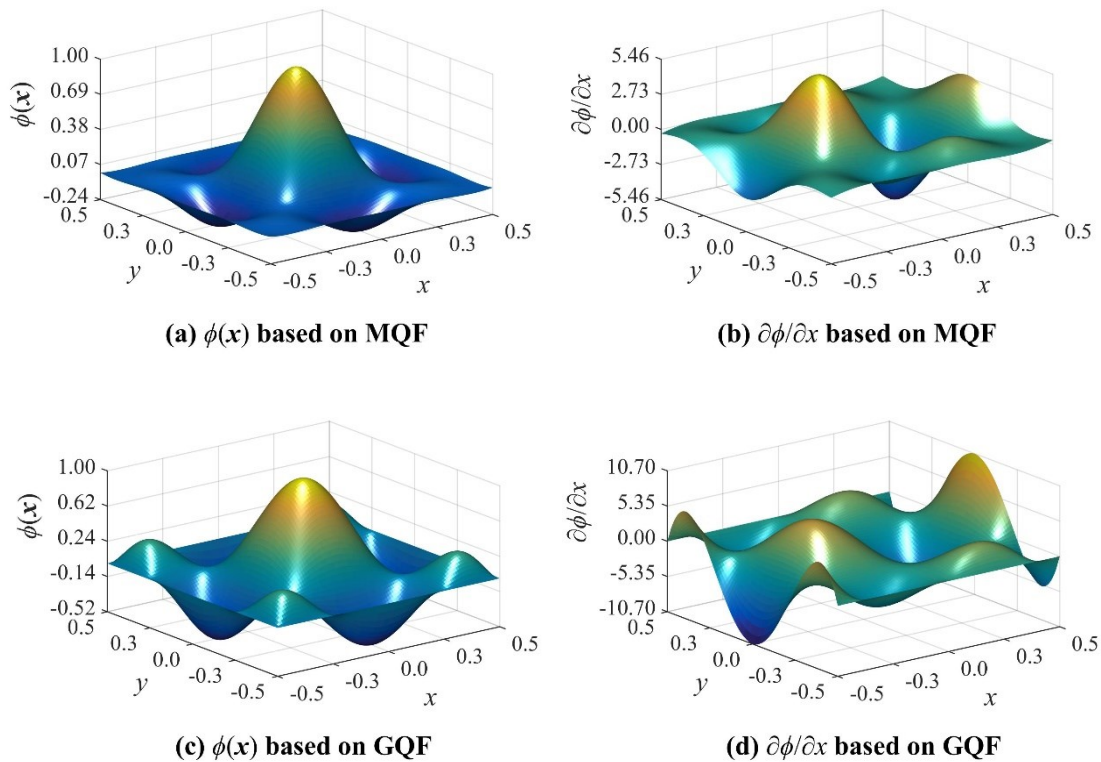
Figure 3.7: The RBF-based shape functions & x-derivatives at the central node

Similar to the MLS example, the shape functions and the x-derivatives corresponding to the central field node have been plotted with a resolution of 51×51 points for both the

case of using the MQF and that of using the GQF, as shown in Fig. 3.7. Here, it is evident that both the two cases are able to generate smooth shape functions and the first-order partial derivatives, with the latter case producing a higher degree of variations and thus a higher order of smoothness.
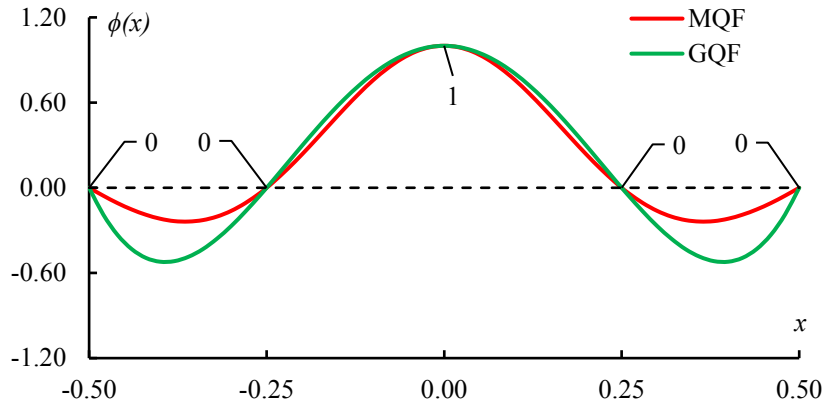
Figure 3.8: The RBF-based shape functions plotted on plane Y=0

Fig. 3.8 shows the shape function curves obtained by sectioning Figs. 3.7a and 3.7c using plane Y = 0. As is clearly shown in this figure, for both the case of using the MQF and that of using the GQF, the shape functions are equal to unity at the central field node and zero at all the other field nodes. This again confirms that the RBF-based functions possess the Kronecker delta function property, and thus the RBF technique can be used to avoid the problem in using the MLS technique to enforce essential boundary conditions.

3.5 MK interpolation

As demonstrated in the previous section, a solution to address the drawback of lacking the Kronecker delta function property in the MLS technique is to replace it with the RBF technique. Alternatively, this drawback can be effectively avoided by employing the MK technique. Such a technique was developed by Gu [160] from the kriging method, which is a geostatistical approach initially proposed by Krige [161] and formalised by Matheron [162] for spatial data interpolation. In this section, the MK procedure will be described and an MK-based example will be presented.

3.5.1 MK procedure

To illustrate the MK procedure, consider again the problem domain defined in Section 3.3.1. In the MK technique, the field function of a point of interest is approximated based on a combination of a polynomial interpolation and a stochastic process, as follows:

$$u^h(\boldsymbol{x}) = \sum_{J=1}^m p_J(\boldsymbol{x})\alpha_J + Z(\boldsymbol{x}) = \boldsymbol{p}^\mathrm{T}(\boldsymbol{x})\boldsymbol{\alpha} + Z(\boldsymbol{x}) \tag{3.52}$$

where $p_J(\boldsymbol{x})$ is the jth component of polynomial basis $\boldsymbol{p}^\mathrm{T}(\boldsymbol{x})$, which has m terms and is often chosen to be the complete basis given in Eq. (3.7); α_J is the unknown coefficient corresponding to $p_J(\boldsymbol{x})$ and yet to be determined; and $Z(\boldsymbol{x})$ is a function representing the realisation of a stochastic process that has a mean value of zero, a variance of σ^2, and a nonzero covariance defined by:

$$\mathrm{cov}\big[Z(\boldsymbol{x}_I), Z(\boldsymbol{x}_J)\big] = \sigma^2 \mathbf{G} \tag{3.53}$$

$$\mathbf{G} = \begin{bmatrix} 1 & G(\boldsymbol{x}_1, \boldsymbol{x}_2) & \cdots & G(\boldsymbol{x}_1, \boldsymbol{x}_n) \\ G(\boldsymbol{x}_2, \boldsymbol{x}_1) & 1 & \cdots & G(\boldsymbol{x}_2, \boldsymbol{x}_n) \\ \vdots & \vdots & \ddots & \vdots \\ G(\boldsymbol{x}_n, \boldsymbol{x}_1) & G(\boldsymbol{x}_n, \boldsymbol{x}_2) & \cdots & 1 \end{bmatrix} \tag{3.54}$$

where $\mathbf{G}$ is termed as the correlation matrix. The IJth component in this matrix, $G(\boldsymbol{x}_I, \boldsymbol{x}_J)$, is a correlation function relating to support nodes $\boldsymbol{x}_I$ and $\boldsymbol{x}_J$. Here, the GBF defined in Eq. (3.34) is modified to define this correlation function, as follows:

$$G(\boldsymbol{x}_I, \boldsymbol{x}_J) = \exp\big(-\theta d_{IJ}^2\big) \tag{3.55}$$

where θ is a parameter controlling the shape of the GBF, and the modification to this equation is made by introducing an free parameter, a_0, to d_{IJ}, which is thus defined as follows:

$$d_{IJ} = \begin{cases} a_0 + \left|a_1(x_I - x_J)\right| & \text{1D} \\[2mm] \sqrt{a_0^2 + a_1^2(x_I - x_J)^2 + a_2^2(y_I - y_J)^2} & \text{2D} \\[2mm] \sqrt{a_0^2 + a_1^2(x_I - x_J)^2 + a_2^2(y_I - y_J)^2 + a_3^2(z_I - z_J)^2} & \text{3D} \end{cases} \tag{3.56}$$

The use of $Z(\boldsymbol{x})$ produces a localised deviation in the approximation of the field function. Thus, a function of the mean squared error (MSE) is created to minimise such a deviation, as follows:

$$\text{MSE} = E[u^h(\boldsymbol{x}) - u(\boldsymbol{x})]^2 \tag{3.57}$$

By minimising this error under the unbiased constraint of $E[u^h(\boldsymbol{x})] = E[u(\boldsymbol{x})]$, the best linear unbiased prediction of $u(\boldsymbol{x})$ can be obtained [163], as follows:

$$u^h(\boldsymbol{x}) = \boldsymbol{p}^{\mathrm{T}}(\boldsymbol{x})\boldsymbol{\zeta} + \boldsymbol{g}^{\mathrm{T}}(\boldsymbol{x})\mathbf{G}^{-1}(\boldsymbol{u} - \mathbf{P}\boldsymbol{\zeta}) \tag{3.58}$$

where $\boldsymbol{p}^{\mathrm{T}}(\boldsymbol{x})$ is the polynomial basis defined in Eq. (3.7), $\boldsymbol{u}$ denotes the vector collecting the nodal values, and $\boldsymbol{g}^{\mathrm{T}}(\boldsymbol{x})$, $\mathbf{P}$ and $\boldsymbol{\zeta}$ are defined as follows:

$$\boldsymbol{g}^{\mathrm{T}}(\boldsymbol{x}) = \{g_1(\boldsymbol{x}) \quad g_2(\boldsymbol{x}) \quad ... \quad g_n(\boldsymbol{x})\} \tag{3.59}$$

$$\mathbf{P} = \begin{bmatrix} p_1(\boldsymbol{x}_1) & p_2(\boldsymbol{x}_1) & \cdots & p_m(\boldsymbol{x}_1) \\ p_1(\boldsymbol{x}_2) & p_2(\boldsymbol{x}_2) & \cdots & p_m(\boldsymbol{x}_2) \\ \vdots & \vdots & \ddots & \vdots \\ p_1(\boldsymbol{x}_n) & p_2(\boldsymbol{x}_n) & \cdots & p_m(\boldsymbol{x}_n) \end{bmatrix} \tag{3.60}$$

$$\boldsymbol{\zeta} = (\mathbf{P}^{\mathrm{T}}\mathbf{G}^{-1}\mathbf{P})^{-1}\mathbf{P}^{\mathrm{T}}\mathbf{G}^{-1}\boldsymbol{u} \tag{3.61}$$

where the Ith component of $\boldsymbol{g}^{\mathrm{T}}(\boldsymbol{x})$ is a correlation function defined by $g_I(\boldsymbol{x}) = G(\boldsymbol{x}, \boldsymbol{x}_I)$. To reorganise Eq. (3.58), the following notations are introduced, where $\mathbf{I}$ represents the identity matrix:

$$\mathbf{A} = (\mathbf{P}^{\mathrm{T}}\mathbf{G}^{-1}\mathbf{P})^{-1}\mathbf{P}^{\mathrm{T}}\mathbf{G}^{-1} \tag{3.62}$$

$$\mathbf{B} = \mathbf{G}^{-1}(\mathbf{I} - \mathbf{P}\mathbf{A}) \tag{3.63}$$

Based on the above notations, Eq. (3.58) can be rewritten into the following form, which is the MK approximation of the field function:

$$u^h(\boldsymbol{x}) = \sum_{I=1}^{n}\left(\sum_{J=1}^{m} p_J(\boldsymbol{x})(\mathbf{A})_{JI} + \sum_{K=1}^{n} g_K(\boldsymbol{x})(\mathbf{B})_{KI}\right)u_I = \sum_{I=1}^{n} \phi_I(\boldsymbol{x})u_I \tag{3.64}$$

or in the matrix form:

$$u^h(x) = (p^{\mathrm{T}}(x)\mathbf{A} + \mathbf{G}^{\mathrm{T}}(x)\mathbf{B})u = \phi^{\mathrm{T}}(x)u \tag{3.65}$$

where the symbols, $(\mathbf{A})_{JI}$ and $(\mathbf{B})_{KI}$, denotes the JIth and KIth components of $\mathbf{A}$ and $\mathbf{B}$, and ϕ is the vector consisting of the MK shape functions:

$$\phi^{\mathrm{T}}(x) = \{\phi_1 \quad \phi_2 \quad \cdots \quad \phi_n\}^{\mathrm{T}} = p^{\mathrm{T}}(x)\mathbf{A} + \mathbf{G}^{\mathrm{T}}(x)\mathbf{B} \tag{3.66}$$

where $\phi_I(x)$ is the MK shape function corresponding to the Ith support node, and it can be expressed as follows:

$$\phi_I(x) = \sum_{J=1}^{m} p_J(x)(\mathbf{A})_{JI} + \sum_{K=1}^{n} g_K(x)(\mathbf{B})_{KI} \tag{3.67}$$

3.5.2 MK shape function derivatives

Since $\mathbf{A}$ and $\mathbf{B}$ in Eq. (3.67) are independent of x, the first-order and second-order partial derivatives of the MK shape functions can be obtained directly by taking the derivatives of this equation and the resulting equation with respect to i and j respectively, as follows:

$$\phi_{I,i}(x) = \sum_{J=1}^{m} p_{J,i}(x)(\mathbf{A})_{JI} + \sum_{K=1}^{n} g_{K,i}(x)(\mathbf{B})_{KI} \tag{3.68}$$

$$\phi_{I,ij}(x) = \sum_{J=1}^{m} p_{J,ij}(x)(\mathbf{A})_{JI} + \sum_{K=1}^{n} g_{K,ij}(x)(\mathbf{B})_{KI} \tag{3.69}$$

where $p_{J,i}(x)$ and $p_{J,ij}(x)$ can be obtained easily based on the polynomial basis, and the first-order and second-order partial derivatives of $g_K(x)$ are defined by:

$$g_{K,i}(x) = -2\theta a_i^2((x)_i - (x_K)_i)g_K(x) \tag{3.70}$$

$$g_{K,ij}(x) = 4\theta^2 a_i^2 a_j^2((x)_i - (x_K)_i)\big((x)_j - (x_K)_j\big)g_K(x) \tag{3.71}$$

3.5.3 An MK example

To study the features possessed by the MK-based shape functions, an example of utilising the MK technique has been conducted on again the 2D domain described in Section 3.3.3. In this example, the parameters in the modified GQF are $\theta = 1$, $a_0 = 0$, $a_1 = 4$ and $a_2 = 4$. Results are calculated for both the case of using the linear polynomial basis and that of using the quadratic polynomial basis.

The input and output data for the case of the central point being the point of interest are presented in Table A.3, Appendix A. The data given in this table clearly suggest that the MK-based shape functions possess both the partitions of unity property and the Kronecker delta function property.

(a) $\phi(x)$ based on linear polynomial   **(b) $\partial\phi/\partial x$ based on linear polynomial**

(c) $\phi(x)$ based on quadratic polynomial   **(d) $\partial\phi/\partial x$ based on quadratic polynomial**
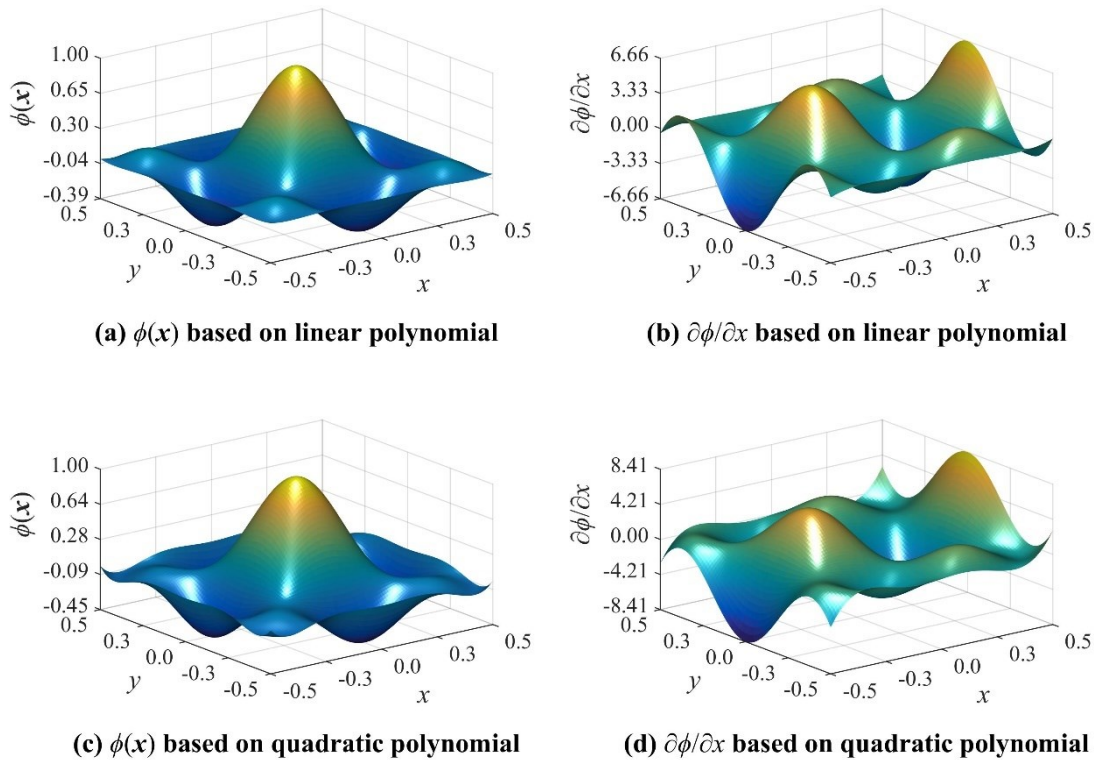
Figure 3.9: The MK-based shape functions & x-derivatives at the central node

Similar to the MLS and RBF example, the shape functions and the x-derivatives relating to the central field node have been plotted with a resolution of 51×51 points for both the case of using the linear polynomial basis and that of using the quadratic polynomial basis, as shown in Fig. 3.9. It is interesting to note that the results calculated based on the former case are very similar to those obtained based on the latter case, exhibiting a high degree of smoothness in both the shape functions and the x-derivatives.

Fig. 3.10 shows the shape functions obtained after sectioning Figs. 3.9a and 3.9c using plane $Y = 0$. The results shown in this figure once again confirm that the shape functions obtained using the MK technique possess the Kronecker delta function property. Thus, similar to the RBF technique, the MK technique can be utilised to address the problem in using the MLS technique to enforce essential boundary conditions.
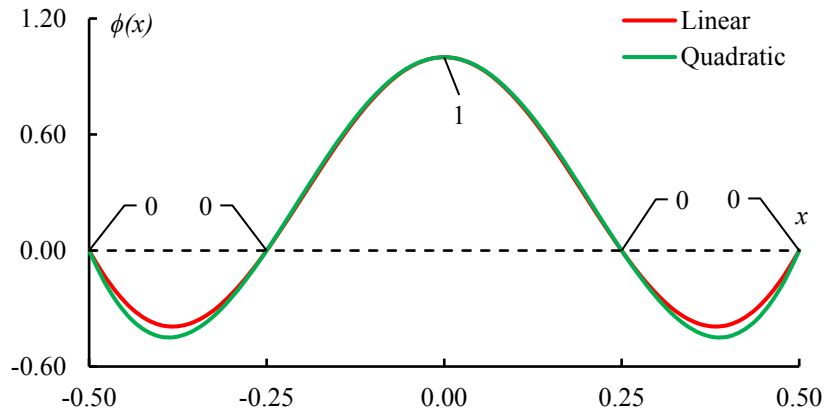
Figure 3.10: The MK-based shape functions plotted on plane Y=0

3.6 System equation formulation

3.6.1 Categorisation of meshfree methods

As discussed previously in the introduction of this chapter, engineering problems can be described often using governing equations such as PDEs. In many cases, obtaining the exact or analytical solution for a complex engineering is impractical. The only practical way is to use a numerical method to get an approximate solution. Among different types of numerical methods, meshfree methods are perhaps of the greatest potential as they are based on nodes only and do not require the use of elements. Based on the procedure for solving the governing equation, meshfree methods can be classified into three types, namely, the strong-form meshfree methods, the weak-form meshfree methods and the strong-weak form meshfree methods. In this section, the basic features, advantages and disadvantages of these methods will be briefly discussed.

In a general engineering problem, the governing equation and the equations for enforcing boundary and/or initial conditions are typically strong-form equations. In the strong-form meshfree methods, the above equations are directly satisfied at field nodes. Therefore, the functions for approximating field variables in the strong-form meshfree methods should have a sufficient degree of consistency such that they are differentiable up to the order of the governing equation. Currently, a wide variety of strong-form meshfree methods has been developed, such as the general FDM [164-167], the meshfree collocation methods [168-171] and the finite point method (FPM) [172-174]. The primary advantage of the

strong-form meshfree methods is that they are simple and computationally efficient, due to the fact that the governing equation is satisfied only at field nodes and no background mesh is required to perform integral operations over the problem domain. Therefore, these methods are truly meshfree. However, a critical issue in these methods is that the moment matrix formed during the construction of shape functions can be singular. In addition, to reach a reasonable accuracy, it is often required to use irregular field node distributions, which prevents these methods from being utilised to address the problems with derivative boundary conditions (DBCs). In general, this type of meshfree methods is less stable and less accurate compared to the weak-form meshfree methods.

In the weak-form meshfree methods, the governing equation is satisfied in an average sense, which is generally achieved by applying to the governing equation with an integral operation that is based on a physical or mathematical principle such as the variational principle and the weighted residual method. Due to the introduction of such an integral operation, these methods require a weaker consistency on the functions for approximating field variables and meanwhile are capable of producing very stable discretised system of equations. Thus, they are generally more accurate compared to the strong-form meshfree methods. However, introducing such an integral operation means that a background mesh is needed to discretise the problem domain simply for performing integral calculations, which makes these methods not truly meshfree. Based on the way of applying the integral operation to the governing equation, this type of meshfree methods can be further divided into the global and local weak-form meshfree methods. In the global weak-form meshfree methods, an integration operation is applied to the whole problem domain such that the governing equation is satisfied on the entire problem domain. Typical examples of the global weak-form meshfree methods include the element-free Galerkin method (EFGM) [157], the radial point interpolation method (RPIM) [175, 176] and the reproducing kernel particle method (RKPM) [177]. On the contrary, the local weak-form meshfree methods apply an integration operation to local domains so that the governing equation is locally satisfied. Examples of the local weak-form meshfree methods include the meshless local Petrov-Galerkin method (MLPGM) [178-180] and the local radial point interpolation method (LRPIM) [181, 182].

The meshfree methods that utilise both strong-form and weak-form formulations to obtain the discretised system equations are termed as the strong-weak form meshfree methods.

For instance, the meshfree method developed by Liu and Gu [183, 184] is a strong-weak form method, where a local weak-form formulation is performed for the field nodes near or on the boundaries with derivative boundary conditions, and a strong-form formulation is applied for all the other field nodes. Other examples of the strong-weak form methods include the smooth particle hydrodynamics methods (SPHMs) developed by Lucy [185] and Gingold and Monaghan [186]. In this type of methods, a weak-form operation (i.e. an integration operation) is applied for field variable approximation, while a strong-form operation is utilised to form the discretised system of equations. The main advantage of the strong-weak form meshfree methods is that they combine the stability of the weak-form methods and the efficiency of the strong-form methods. However, they are much more complex compared to the other two types of meshfree methods.

In this research, instead of using the other two types of meshfree methods, the weak-form meshfree methods have been selected for predicting both the elastic properties and the overall response of woven composites. One of the reasons for choosing the weak-form meshfree methods is that the weak-form formulation techniques such as the variational principle and the weighted residual method have been well-established and also widely used in the FEM. In addition, the weak-form meshfree methods are much more stable and accurate compared to the strong-form meshfree methods and much less complex than the strong-weak form meshfree methods. In the following two sections, the weak-form meshfree methods that have been selected in this thesis to predict the elastic properties and the overall response of woven composites will be described. For convenience, the two meshfree methods are termed as the standard weak-form meshfree method and the explicit weak-form meshfree method, respectively.

3.6.2 Standard weak-form meshfree method

3.6.2.1 Formulation of the discretised system of equations

The homogenisation of the elastic properties of woven composites is essentially a static problem of linear elasticity. If we denote the unit cell (UC) of homogenisation as Ω, and the boundary as Γ, the governing equation for the homogenisation of the elastic properties of woven composites and the equations for boundary conditions can be written as follows:

$$\text{Governing equation: } \mathbf{L}^{\mathrm{T}}\boldsymbol{\sigma} + \boldsymbol{b} = \mathbf{0} \text{ in } \Omega \qquad (3.72)$$

$$\text{Natural boundary condition: } \boldsymbol{\sigma}\boldsymbol{n} = \bar{\boldsymbol{t}} \text{ on } \Gamma_t \tag{3.73}$$

$$\text{Essential boundary condition: } \boldsymbol{u} = \bar{\boldsymbol{u}} \text{ on } \Gamma_u \tag{3.74}$$

where $\boldsymbol{\sigma}$ denotes the stress, $\boldsymbol{b}$ represents the external body force, $\boldsymbol{u}$ is the displacement, $\boldsymbol{n}$ stands for the unit outward normal to the natural boundary, $\bar{\boldsymbol{t}}$ is the traction prescribed to the natural boundary, $\bar{\boldsymbol{u}}$ denotes the displacement prescribed to the essential boundary, and $\mathbf{L}$ is the differential operator and is defined by:

$$\mathbf{L}^{\mathrm{T}} = \begin{bmatrix} \frac{\partial}{\partial x} & 0 & 0 & \frac{\partial}{\partial y} & 0 & \frac{\partial}{\partial z} \\ 0 & \frac{\partial}{\partial y} & 0 & \frac{\partial}{\partial x} & \frac{\partial}{\partial z} & 0 \\ 0 & 0 & \frac{\partial}{\partial z} & 0 & \frac{\partial}{\partial y} & \frac{\partial}{\partial x} \end{bmatrix} \tag{3.75}$$

Here, it should be noted that the external body force term in Eq. (3.72) should be set to zero in the homogenisation of the elastic properties of woven composites, owing to the fact that no body force will be prescribed to the UC of homogenisation. It is further noted that Eq. (3.74) is inadequate for describing a homogenisation that is performed based on the use of periodic boundary condition (PBC), where a displacement constraint is applied in the form of a displacement relation between two equivalent boundary nodes, see Eq. (2.79) or (2.80), rather than in the form of Eq. (3.74). Thus, a special treatment is needed to enforce the PBC, which will be addressed later in this section.

To solve Eq. (3.72), which is a strong-form equation, the minimum total potential energy principle can be employed to transform it into a weak-form equation, which leads to the formulation of the standard weak-form meshfree method, as follows. The minimum total potential energy principle dictates that the total potential energy is equal to the sum of the elastic strain energy and the potential energy or the work done the external forces:

$$\Pi = U + W = \int_\Omega \boldsymbol{\varepsilon}^{\mathrm{T}}\boldsymbol{\sigma}\,dV - \left(\int_\Omega \boldsymbol{u}^{\mathrm{T}}\boldsymbol{b}\,dV + \int_{\Gamma_t} \boldsymbol{u}^{\mathrm{T}}\bar{\boldsymbol{t}}\,dS \right) \tag{3.76}$$

In this equation, the minus sign indicates a loss of the potential energy when the force is displaced in its direction. At an equilibrium state, the total potential energy should be at a minimum, meaning that:

$$\delta\Pi = \delta U + \delta W = 0 \tag{3.77}$$

where the symbol, δ, denotes the first variation operator. Expanding the above equation produces the standard variational (i.e. weak-form) formulation, as follows:

$$\int_\Omega \delta\boldsymbol{\varepsilon}^{\mathrm{T}}\boldsymbol{\sigma}dV - \left(\int_\Omega \delta\boldsymbol{u}^{\mathrm{T}}\boldsymbol{b}dV + \int_{\Gamma_t} \delta\boldsymbol{u}^{\mathrm{T}}\bar{\boldsymbol{t}}dS\right) = 0 \qquad (3.78)$$

Since the integral operation in Eq. (3.77) is imposed on the whole problem domain Ω, a background mesh consisting of non-overlapping cells should be applied to partition the problem domain for the sake of performing numerical integrations. An example of using a background mesh to discretise a 2D general domain is shown in Fig. 3.11. It can be seen from this figure that the discretisation of the problem domain using background cells is independent of the way of discretising the problem using field nodes. This is because the former is made simply for conducting numerical integrations cell by cell. Technically, the shape of background cells can be arbitrary as far as they do not overlap with each other and there is no gap between any two adjacent cells. In addition, if a sufficient number of background cells is used, then the solution obtained should be independent of the type of background cells being used. Thus, it is often recommended to use background cells with simple shapes.

Background cells • Field nodes ✕ Integration points
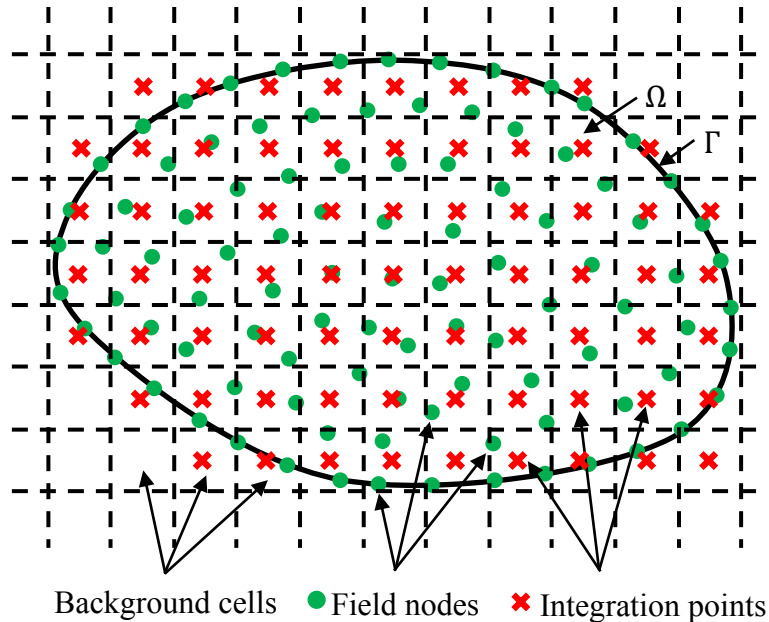
Figure 3.11: 2D example of a background mesh in weak-form meshfree methods

Assume that the whole problem domain is discretised with a set of field nodes that are numbered sequentially from 1 to N. For an integration point defined in the background

mesh, its displacement can be interpolated based on those of the field nodes within its local support domain, which can be achieved by applying a field function approximation technique, such as the MLS, RBF or MK techniques, as follows:

$$\boldsymbol{u}^h = \begin{Bmatrix} u \\ v \\ w \end{Bmatrix} = \begin{bmatrix} \phi_1 & 0 & 0 & \cdots & \phi_n & 0 & 0 \\ 0 & \phi_1 & 0 & \cdots & 0 & \phi_n & 0 \\ 0 & 0 & \phi_1 & \cdots & 0 & 0 & \phi_n \end{bmatrix} \begin{Bmatrix} u_1 \\ v_1 \\ \vdots \\ w_n \end{Bmatrix} = \boldsymbol{\Phi}\boldsymbol{u}^s \qquad (3.79)$$

where n is the number of the field nodes within the support domain, $\boldsymbol{\Phi}$ is a $3 \times 3n$ matrix consisting of shape functions, and $\boldsymbol{u}^s$ is a vector collecting the displacements of the local support nodes. An alternative form of this equation is as follows:

$$\boldsymbol{u}^h = \sum_{I=1}^{n} \begin{bmatrix} \phi_I & 0 & 0 \\ 0 & \phi_I & 0 \\ 0 & 0 & \phi_I \end{bmatrix} \begin{Bmatrix} u_I \\ v_I \\ w_I \end{Bmatrix} = \sum_{I=1}^{n} \boldsymbol{\Phi}_I \boldsymbol{u}_I \qquad (3.80)$$

where $\boldsymbol{\Phi}_I$ and $\boldsymbol{u}_I$ denote the shape function matrix and the displacement corresponding to field node I. Based on the strain-displacement relation, i.e. $\boldsymbol{\varepsilon} = \mathbf{L}\boldsymbol{u}^h$, and substituting Eq. (3,79) into this relation, the strain of the integration point can be obtained, as follows:

$$\boldsymbol{\varepsilon} = \mathbf{L}\boldsymbol{\Phi}\boldsymbol{u}^s = \begin{bmatrix} \frac{\partial \phi_1}{\partial x} & 0 & 0 & \cdots & \frac{\partial \phi_n}{\partial x} & 0 & 0 \\ 0 & \frac{\partial \phi_1}{\partial y} & 0 & \cdots & 0 & \frac{\partial \phi_n}{\partial y} & 0 \\ 0 & 0 & \frac{\partial \phi_1}{\partial z} & \cdots & 0 & 0 & \frac{\partial \phi_n}{\partial z} \\ \frac{\partial \phi_1}{\partial y} & \frac{\partial \phi_1}{\partial x} & 0 & \cdots & \frac{\partial \phi_n}{\partial y} & \frac{\partial \phi_n}{\partial x} & 0 \\ 0 & \frac{\partial \phi_1}{\partial z} & \frac{\partial \phi_1}{\partial y} & \cdots & 0 & \frac{\partial \phi_n}{\partial z} & \frac{\partial \phi_n}{\partial y} \\ \frac{\partial \phi_1}{\partial z} & 0 & \frac{\partial \phi_1}{\partial x} & \cdots & \frac{\partial \phi_n}{\partial z} & 0 & \frac{\partial \phi_n}{\partial x} \end{bmatrix} \begin{Bmatrix} u_1 \\ v_1 \\ w_1 \\ \vdots \\ u_n \\ v_n \\ w_n \end{Bmatrix} = \mathbf{B}\boldsymbol{u}^s \qquad (3.81)$$

alternatively:

$$\boldsymbol{\varepsilon} = \sum_{I=1}^{n} \begin{bmatrix} \frac{\partial \phi_I}{\partial x} & 0 & 0 & \frac{\partial \phi_I}{\partial y} & 0 & \frac{\partial \phi_I}{\partial z} \\ 0 & \frac{\partial \phi_I}{\partial y} & 0 & \frac{\partial \phi_I}{\partial x} & \frac{\partial \phi_I}{\partial z} & 0 \\ 0 & 0 & \frac{\partial \phi_I}{\partial z} & 0 & \frac{\partial \phi_I}{\partial y} & \frac{\partial \phi_I}{\partial x} \end{bmatrix}^{\mathrm{T}} \begin{Bmatrix} u_I \\ v_I \\ w_I \end{Bmatrix} = \sum_{I=1}^{n} \mathbf{B}_I \boldsymbol{u}_I \qquad (3.82)$$

where $\mathbf{B}$ is equal to $\mathbf{L\Phi}$, and $\mathbf{B}_I$ is equal to $\mathbf{L\Phi}_I$ and is often termed as the strain matrix corresponding to node I. By considering the constitutive relation of the integration point, its stress can be obtained, as follows:

$$\boldsymbol{\sigma} = \mathbf{C}\boldsymbol{\varepsilon} = \mathbf{CL\Phi}\boldsymbol{u}^s = \mathbf{CB}\boldsymbol{u}^s = \sum_{I=1}^{n} \mathbf{CL\Phi}_I \boldsymbol{u}_I = \sum_{I=1}^{n} \mathbf{CB}_I \boldsymbol{u}_I \qquad (3.83)$$

In this equation, $\mathbf{C}$ is the elasticity matrix, which has been defined in Eq. (2.5) for the isotropic polymer matrix and in Eqs. (2.13) and (2.54) for the transversely isotropic yarn material. By taking the first variation of Eq. (3.79) or (3.80) and substituting the resulting equation into Eq. (3.81), we can obtain:

$$\delta\boldsymbol{u}^h = \mathbf{\Phi}\delta\boldsymbol{u}^s = \sum_{I=1}^{n} \mathbf{\Phi}_I \delta\boldsymbol{u}_I \qquad (3.84)$$

$$\delta\boldsymbol{\varepsilon} = \mathbf{L}\delta\boldsymbol{u}^h = \mathbf{L\Phi}\delta\boldsymbol{u}^s = \mathbf{B}\delta\boldsymbol{u}^s = \sum_{I=1}^{n} \mathbf{B}_I \delta\boldsymbol{u}_I \qquad (3.85)$$

Based on Eqs. (3.83) and (3.85), the first term of Eq. (3.78) can be rewritten as follows:

$$\int_\Omega \delta\boldsymbol{\varepsilon}^\mathrm{T} \boldsymbol{\sigma} d\mathrm{V} = \int_\Omega (\mathbf{B}\delta\boldsymbol{u}^s)^\mathrm{T} \mathbf{CB}\boldsymbol{u}^s d\mathrm{V}$$

$$= \int_\Omega \left(\sum_{I=1}^{n} \mathbf{B}_I \delta\boldsymbol{u}_I\right)^\mathrm{T} \sum_{J=1}^{n} \mathbf{CB}_J \boldsymbol{u}_J d\mathrm{V}$$

$$= \int_\Omega \sum_{I=1}^{n} \sum_{J=1}^{n} \delta\boldsymbol{u}_I^\mathrm{T} \left(\mathbf{B}_I \mathbf{CB}_J\right) \boldsymbol{u}_J d\mathrm{V} \qquad (3.86)$$

where the subscripts, I and J, represent the Ith and Jth field nodes and are defined based on the local numbering sequence of the support domain (i.e. 1 to n). Since the numbers representing the field nodes in a support domain can overlap with those denoting the field nodes in another support domain. To avoid this problem, the global numbering sequence defined previously (i.e. 1 to N) can be used to replace the local numbering sequence such that each field node is labelled using a unique number. Since in Eq. (3.86) the integration operation can be moved within the summation operations, Eq. (3.86) can be rewritten into the following form:

$$\int_\Omega \delta\boldsymbol{\varepsilon}^\mathrm{T} \boldsymbol{\sigma} d\mathrm{V} = \int_\Omega \sum_{I=1}^{n} \sum_{J=1}^{n} \delta\boldsymbol{u}_I^\mathrm{T} \left(\mathbf{B}_I \mathbf{CB}_J\right) \boldsymbol{u}_J d\mathrm{V}$$

$$= \sum_{I=1}^{N} \sum_{J=1}^{N} \delta\boldsymbol{u}_I^\mathrm{T} \mathbf{K}_{IJ} \boldsymbol{u}_J \qquad (3.87)$$

where $\mathbf{K}_{IJ}$ is often termed as the nodal stiffness matrix and is defined by:

$$\mathbf{K}_{IJ} = \int_{\Omega}(\mathbf{B}_I \mathbf{C} \mathbf{B}_J)d\mathrm{V} \tag{3.88}$$

The right-hand side of Eq. (3.87) can be expanded and rewritten into the following matrix form:

$$\sum_{I=1}^{N}\sum_{J=1}^{N}\delta\boldsymbol{u}_I^{\mathrm{T}}\mathbf{K}_{IJ}\boldsymbol{u}_J = \delta\boldsymbol{U}^{\mathrm{T}}\mathbf{K}\boldsymbol{U} \tag{3.89}$$

where $\boldsymbol{U}$ is a vector consisting of the displacement of all field nodes, $\delta\boldsymbol{U}$ refers to the first variation of $\boldsymbol{U}$, and $\mathbf{K}$ is the global stiffness matrix:

$$\delta\boldsymbol{U}^{\mathrm{T}} = \{\delta\boldsymbol{u}_1 \quad \delta\boldsymbol{u}_2 \quad \cdots \quad \delta\boldsymbol{u}_N\} \tag{3.90}$$

$$\boldsymbol{U} = \{\boldsymbol{u}_1 \quad \boldsymbol{u}_2 \quad \cdots \quad \boldsymbol{u}_N\}^{\mathrm{T}} \tag{3.91}$$

$$\mathbf{K} = \begin{Bmatrix} \mathbf{K}_{11} & \mathbf{K}_{12} & \cdots & \mathbf{K}_{1N} \\ \mathbf{K}_{21} & \mathbf{K}_{22} & \cdots & \mathbf{K}_{2N} \\ \vdots & \vdots & \ddots & \vdots \\ \mathbf{K}_{N1} & \mathbf{K}_{N2} & \cdots & \mathbf{K}_{NN} \end{Bmatrix} \tag{3.92}$$

Based on the above, the first term of Eq. (3.78) can be finally rewritten into the following form:

$$\int_{\Omega}\delta\boldsymbol{\varepsilon}^{\mathrm{T}}\boldsymbol{\sigma}d\mathrm{V} = \delta\boldsymbol{U}^{\mathrm{T}}\mathbf{K}\boldsymbol{U} \tag{3.93}$$

By considering Eq. (3.84) and following a similar procedure for obtaining Eq. (3.93), the second and third terms of Eq. (3.78) can be rewritten as follows:

$$\int_{\Omega}\delta\boldsymbol{u}^{\mathrm{T}}\boldsymbol{b}d\mathrm{V} = \delta\boldsymbol{U}^{\mathrm{T}}\boldsymbol{F}^{\mathrm{b}} \tag{3.94}$$

$$\int_{\Omega}\delta\boldsymbol{u}^{\mathrm{T}}\bar{\boldsymbol{t}}d\mathrm{V} = \delta\boldsymbol{U}^{\mathrm{T}}\boldsymbol{F}^{\mathrm{t}} \tag{3.95}$$

where $\boldsymbol{F}^{\mathrm{b}}$ and $\boldsymbol{F}^{\mathrm{t}}$ denote the global body force vector and the global traction force vector, and are defined by the following equations respectively:

$$\boldsymbol{F}^{\mathrm{b}} = \{\boldsymbol{F}_1^{\mathrm{b}} \quad \boldsymbol{F}_2^{\mathrm{b}} \quad \cdots \quad \boldsymbol{F}_N^{\mathrm{b}}\}^{\mathrm{T}} \tag{3.96}$$

$$\boldsymbol{F}^{\mathrm{t}} = \{\boldsymbol{F}_1^{\mathrm{t}} \quad \boldsymbol{F}_2^{\mathrm{t}} \quad \cdots \quad \boldsymbol{F}_N^{\mathrm{t}}\}^{\mathrm{T}} \tag{3.97}$$

where

$$F_I^{\mathrm{b}} = \int_\Omega \mathbf{\Phi}_I \boldsymbol{b} d\mathrm{V} \tag{3.98}$$

$$F_I^{\mathrm{t}} = \int_\Omega \mathbf{\Phi}_I \bar{\boldsymbol{t}} d\mathrm{V} \tag{3.99}$$

Substituting Eqs. (3.93) – (3.95) into Eq. (3.78) yields:

$$\delta \boldsymbol{U}^{\mathrm{T}} \mathbf{K} \boldsymbol{U} = \delta \boldsymbol{U}^{\mathrm{T}} \left(\boldsymbol{F}^{\mathrm{b}} + \boldsymbol{F}^{\mathrm{t}} \right) \tag{3.100}$$

Since the first variation of the global displacement, i.e. $\delta \boldsymbol{U}$, is arbitrary, Eq. (3.100) can be satisfied only if:

$$\mathbf{K} \boldsymbol{U} = \boldsymbol{F}^{\mathrm{b}} + \boldsymbol{F}^{\mathrm{t}} = \boldsymbol{F}^{\mathrm{e}} \tag{3.101}$$

where $\boldsymbol{F}^{\mathrm{e}}$ represents the global external force vector.

Eq. (3.101) is the final form of the discretised system of equations in the standard weak-form meshfree method. If it is used to predict the elastic properties of woven composites, all components in $\mathbf{K}$, $\boldsymbol{F}_I^{\mathrm{b}}$ and $\boldsymbol{F}_I^{\mathrm{t}}$ can be directly calculated by using a proper integration scheme such as the Gauss-Legendre quadrature. Then, the displacement of all field nodes, i.e. $\boldsymbol{U}$, can be obtained using a suitable algorithm such as the Gaussian elimination method. After obtaining $\boldsymbol{U}$, the strains and consequently the stresses of all integration points can be calculated using Eqs. (3.82) and (3.83), respectively.

3.6.2.2 Enforcement of boundary conditions

For traction boundary conditions, which are explicitly defined in the form of Eq. (3.73), they have been naturally implemented during the formulation of the discretised system of equations. Therefore, no treatment is needed to enforce this type of boundary conditions. In terms of essential boundary conditions, they can be defined either explicitly in the form of Eq. (3.74) or implicitly in a PBC form, see Eq. (2.79) or (2.80). For the former case, they can be enforced by modifying the discretised system of equations as follows. Assume that a fixed displacement is prescribed to the ith component of the global displacement:

$$u_i = \bar{u}_i \tag{3.102}$$

The above condition can be exactly enforced by modifying the global stiffness matrix and the global force vector into the following forms, respectively:

$$
\mathbf{K} = \left\{
\begin{array}{ccccccc}
k_{11} & \cdots & k_{1(i-1)} & k_{1i} & k_{1(i+1)} & \cdots & k_{1(3N)} \\
\vdots & \ddots & \vdots & \vdots & \vdots & \ddots & \vdots \\
k_{(i-1)1} & \cdots & k_{(i-1)(i-1)} & k_{(i-1)i} & k_{(i-1)(i+1)} & \cdots & k_{(i-1)(3N)} \\
0 & \cdots & 0 & 1 & 0 & \cdots & 0 \\
k_{(i+1)1} & \cdots & k_{(i+1)(i-1)} & k_{(i+1)i} & k_{(i+1)(i+1)} & \cdots & k_{(i+1)(3N)} \\
\vdots & \ddots & \vdots & \vdots & \vdots & \ddots & \vdots \\
k_{(3N)1} & \cdots & k_{(3N)(i-1)} & k_{(3N)i} & k_{(3N)(i+1)} & \cdots & k_{(3N)(3N)}
\end{array}
\right\}
\tag{3.103}
$$

$$
\boldsymbol{F}^{\mathrm{e}} = \{F_1 \quad \cdots \quad F_{(i-1)} \quad \bar{u}_i \quad F_{(i+1)} \quad \cdots \quad F_{(3N)}\}^{\mathrm{T}}
\tag{3.104}
$$

For the PBC-based essential boundary conditions, see Eq. (2.79) or (2.80), they cannot be enforced directly since they present in the form of a displacement relation between two equivalent nodes. In this work, the displacement constraint elimination method [147] is extended to enforce this type of boundary conditions. It should be noted that the generic form of PBC, see Eq. (2.80), will become the standard form of PBC, see Eq. (2.79), if the load reversal factor is set to be unity, $\gamma=1$, and the transformation matrix is set to be the identity matrix, $\mathbf{T} = \mathbf{I}_0$. Thus, the enforcement of the PBC-based essential boundary conditions will be addressed based on the generic form of PBC.

The constraint elimination method is based on a division of all field nodes in the problem domain into three subsets, namely, the internal nodes, i.e. $\boldsymbol{x}_{Ii}$ $(I = 1, \ldots, n_i)$, the nodes on the negative boundary, i.e. $\boldsymbol{x}_{J-}$ $(J = 1, \ldots, n_-)$, and the nodes on the positive boundary, i.e. $\boldsymbol{x}_{K+}$ $(K = 1, \ldots, n_+)$. Then, the three subsets of field nodes are numbered sequentially, forming a set-based numbering sequence. Based this numbering sequence, the originally defined global displacement vector is reorganised such that it consists sequentially of an internal displacement vector, which collects the displacements of the internal nodes, i.e. $\boldsymbol{U}_i$, a negative displacement vector, which collects the displacements of the field nodes on the negative boundary, i.e. $\boldsymbol{U}_-$, and a positive displacement vector, which collects the displacements of the field nodes on the positive boundary, i.e. $\boldsymbol{U}_+$, as follows:

$$
\boldsymbol{U} = \{\boldsymbol{U}_i \quad \boldsymbol{U}_- \quad \boldsymbol{U}_+\}^{\mathrm{T}}
\tag{3.105}
$$

Similarly, the originally defined global stiffness matrix, $\mathbf{K}$, and global external force, $\boldsymbol{F}^{\mathrm{e}}$, can be reorganised, and consequently the discretised system of equations can be rewritten as follows:

$$\begin{bmatrix} \mathbf{K}_{ii} & \mathbf{K}_{i-} & \mathbf{K}_{i+} \\ \mathbf{K}_{-i} & \mathbf{K}_{--} & \mathbf{K}_{-+} \\ \mathbf{K}_{+i} & \mathbf{K}_{+-} & \mathbf{K}_{++} \end{bmatrix} \begin{Bmatrix} \boldsymbol{U}_i \\ \boldsymbol{U}_- \\ \boldsymbol{U}_+ \end{Bmatrix} = \begin{Bmatrix} \boldsymbol{F}_i^{\mathrm{e}} \\ \boldsymbol{F}_-^{\mathrm{e}} \\ \boldsymbol{F}_+^{\mathrm{e}} \end{Bmatrix} \tag{3.106}$$

If we denote $\gamma\mathbf{T}$ in Eq. (2.80) as $\mathbf{T}_\gamma$, the positive and negative displacement vectors can be related to each other as follows:

$$\boldsymbol{U}_+ = \widetilde{\mathbf{T}}\boldsymbol{U}_- + \boldsymbol{\xi} \tag{3.107}$$

where $\boldsymbol{\xi}$ is a vector denoting the difference between $\boldsymbol{U}_+$ and $\widetilde{\mathbf{T}}\boldsymbol{U}_-$ and can be calculated based on the macroscopic strain applied to the UC of homogenisation, and $\widetilde{\mathbf{T}}$ is a matrix collecting all the $\mathbf{T}_\gamma$ associated with each pair of equivalent points. Substituting the above relation into Eq. (3.106), the discretised system of equations can be rearranged into:

$$\widetilde{\mathbf{K}}\widetilde{\boldsymbol{U}} = \widetilde{\boldsymbol{F}}^{\mathrm{e}} \tag{3.108}$$

where

$$\widetilde{\mathbf{K}} = \begin{bmatrix} \mathbf{K}_{ii} & \mathbf{K}_{i-} + \mathbf{K}_{i+}\widetilde{\mathbf{T}} \\ (\mathbf{K}_{-i} + \mathbf{K}_{+i}) & \mathbf{K}_{--} + \mathbf{K}_{+-} + (\mathbf{K}_{-+} + \mathbf{K}_{++})\widetilde{\mathbf{T}} \end{bmatrix} \tag{3.109}$$

$$\widetilde{\mathbf{U}} = \begin{Bmatrix} \boldsymbol{U}_i \\ \boldsymbol{U}_- \end{Bmatrix} \tag{3.110}$$

$$\widetilde{\boldsymbol{F}}^{\mathrm{e}} = \begin{Bmatrix} \boldsymbol{F}_i^{\mathrm{e}} - \mathbf{K}_{i+}\boldsymbol{\xi} \\ \boldsymbol{F}_-^{\mathrm{e}} + \boldsymbol{F}_+^{\mathrm{e}} - (\mathbf{K}_{-+} + \mathbf{K}_{++})\boldsymbol{\xi} \end{Bmatrix} \tag{3.111}$$

It should be noted that no external force will be prescribed in homogenising the elastic properties of woven composites. Therefore, the external force components in Eq. (3.111) vanish, leading to:

$$\widetilde{\boldsymbol{F}}^{\mathrm{e}} = \begin{Bmatrix} -\mathbf{K}_{i-}\boldsymbol{\xi} \\ -(\mathbf{K}_{-+} + \mathbf{K}_{++})\boldsymbol{\xi} \end{Bmatrix} \tag{3.112}$$

Since $\widetilde{\mathbf{K}}$ and $\widetilde{F}^e$ are known for a given problem, the reorganised displacement vector, $\widetilde{U}$, and thus the negative displacement vector, U_-, can be solved. By utilising Eq. (3.107), the positive displacement vector, U_+, can also be calculated.

3.6.3 Explicit weak-form meshfree method

3.6.3.1 Formulation of the discretised system of equations

In predicting the overall response of woven composites based on the UC methodology, a history of macroscopic strains needs to be enforced to the UC for the sake of calculating the history of the volume average stresses of the UC. The suggests that the prediction of the overall response of woven composites is essentially a dynamic problem, with the time-dependent macroscopic strains prescribed to the boundary acting as the external dynamic loading. If we denote the UC domain of homogenisation as Ω, and the boundary as Γ, the governing equation for the prediction of the overall response of woven composites and the equations for boundary and initial conditions can be written as follows:

$$\text{Governing equation: } \mathbf{L}^T \boldsymbol{\sigma}(t) + \boldsymbol{b}(t) = \rho \ddot{\boldsymbol{u}}(t) \text{ in } \Omega \qquad (3.113)$$

$$\text{Natural boundary condition: } \boldsymbol{\sigma}(t)\boldsymbol{n} = \bar{\boldsymbol{t}}(t) \text{ on } \Gamma_t \qquad (3.114)$$

$$\text{Essential boundary condition: } \boldsymbol{u}(t) = \bar{\boldsymbol{u}}(t) \text{ on } \Gamma_u \qquad (3.115)$$

$$\text{Initial velocity condition: } \boldsymbol{v}(t = 0) = \boldsymbol{v}_0 \text{ in } \Omega \qquad (3.116)$$

where ρ is the density of material, $\dot{\boldsymbol{u}}$ and $\ddot{\boldsymbol{u}}$ denote the velocity and acceleration, and all the other symbols have the same meaning as those in Eqs. (3.72) – (3.74). Here, it should be noted that the boundary condition given in Eq. (3.115) is not adequate for describing the problem of the overall response prediction of woven composites if a time-dependent PBC is applied, which will be addressed later.

To solve Eq. (3.113), which is a strong-form equation, Hamilton's principle can be used to transform it into a weak-form equation, which leads to the formulation of the explicit weak-form meshfree method, as follows. For a deformation body, Hamilton's principle states that the most accurate solution of all the admissible histories of displacement is a solution of the following equation:

$$\delta \int_{t_1}^{t_2} \mathcal{L} dt = 0 \tag{3.117}$$

alternatively,

$$\int_{t_1}^{t_2} \delta \mathcal{L} dt = 0 \tag{3.118}$$

where t_1 and t_2 denote the starting and ending times of the dynamic event, and $\mathcal{L}$ refers to a Lagrangian function defined based on a set of time histories of displacement and is defined as follows:

$$\mathcal{L} = T - \Pi + W \tag{3.119}$$

where T is the kinematic energy, Π is the potential or elastic strain energy, and W is the work done by external force:

$$T = \frac{1}{2} \int_{\Omega} \rho \dot{\boldsymbol{u}}^{\mathrm{T}} \dot{\boldsymbol{u}} dV \tag{3.120}$$

$$\Pi = \frac{1}{2} \int_{\Omega} \boldsymbol{\varepsilon}^{\mathrm{T}} \boldsymbol{\sigma} dV \tag{3.121}$$

$$W = \int_{\Omega} \boldsymbol{u}^{\mathrm{T}} \boldsymbol{b} dV + \int_{\Gamma_t} \boldsymbol{u}^{\mathrm{T}} \bar{\boldsymbol{t}} dS \tag{3.122}$$

By taking the first variations of Eqs. (3.121) and (3.122), we can obtain the following two equations:

$$\delta \Pi = \frac{1}{2} \delta \int_{\Omega} \boldsymbol{\varepsilon}^{\mathrm{T}} \boldsymbol{\sigma} dV = \frac{1}{2} \delta \int_{\Omega} \boldsymbol{\varepsilon}^{\mathrm{T}} \mathbf{C} \boldsymbol{\varepsilon} dV = \int_{\Omega} \delta \boldsymbol{\varepsilon}^{\mathrm{T}} \mathbf{C} \boldsymbol{\varepsilon} dV \tag{3.123}$$

$$\delta W = \delta \int_{\Omega} \boldsymbol{u}^{\mathrm{T}} \boldsymbol{b} dV + \delta \int_{\Gamma_t} \boldsymbol{u}^{\mathrm{T}} \bar{\boldsymbol{t}} dS = \int_{\Omega} \delta \boldsymbol{u}^{\mathrm{T}} \boldsymbol{b} dV + \int_{\Gamma_t} \delta \boldsymbol{u}^{\mathrm{T}} \bar{\boldsymbol{t}} dS \tag{3.124}$$

Since Eq. (3.123) is actually the first term of Eq. (3.78), and Eq. (3.124) is the sum of the second and third terms of Eq. (3.78), we can directly get the following two equations:

$$\delta \Pi = \int_{\Omega} \delta \boldsymbol{\varepsilon}^{\mathrm{T}} \mathbf{C} \boldsymbol{\varepsilon} dV = \delta \boldsymbol{U}^{\mathrm{T}} \boldsymbol{F}^{\mathrm{i}} \tag{3.125}$$

$$\delta W = \int_{\Omega} \delta \boldsymbol{u}^{\mathrm{T}} \boldsymbol{b} dV + \int_{\Gamma_t} \delta \boldsymbol{u}^{\mathrm{T}} \bar{\boldsymbol{t}} dS = \delta \boldsymbol{U}^{\mathrm{T}} (\boldsymbol{F}^{\mathrm{b}} + \boldsymbol{F}^{\mathrm{t}}) = \delta \boldsymbol{U}^{\mathrm{T}} \boldsymbol{F}^{\mathrm{e}} \tag{3.126}$$

where $\boldsymbol{F}^{\mathrm{i}}$ stands for the internal force.

In terms of the kinematic energy, its first variation can be expressed as:

$$\delta T = \frac{1}{2}\delta \int_{\Omega} \rho \dot{\boldsymbol{u}}^{\mathrm{T}}\dot{\boldsymbol{u}}dV = \int_{\Omega} \rho \delta \dot{\boldsymbol{u}}^{\mathrm{T}}\dot{\boldsymbol{u}}dV \tag{3.127}$$

The velocity vector in the above equation can be approximated in a similar manner as that for displacement, as shown in Eq. (3.80). Therefore, we can obtain:

$$\dot{\boldsymbol{u}}^{h} = \sum_{I=1}^{n}\begin{bmatrix} \phi_I & 0 & 0 \\ 0 & \phi_I & 0 \\ 0 & 0 & \phi_I \end{bmatrix}\begin{Bmatrix} \dot{u}_I \\ \dot{v}_I \\ \dot{w}_I \end{Bmatrix} = \sum_{I=1}^{n}\boldsymbol{\Phi}_I\dot{\boldsymbol{u}}_I = \boldsymbol{\Phi}\dot{\boldsymbol{u}}^{\mathrm{s}} \tag{3.128}$$

By taking the first variation of $\dot{\boldsymbol{u}}^{h}$, we have $\delta\dot{\boldsymbol{u}}^{h} = \delta(\sum_{I=1}^{n}\boldsymbol{\Phi}_I\dot{\boldsymbol{u}}_I) = \boldsymbol{\Phi}\delta\dot{\boldsymbol{u}}^{\mathrm{s}}$. Therefore, the integrand of the right side of Eq. (3.127) can be approximated as follows:

$$\rho\delta\dot{\boldsymbol{u}}^{\mathrm{T}}\dot{\boldsymbol{u}} = \sum_{I=1}^{n}\sum_{J=1}^{n}\rho\delta(\boldsymbol{\Phi}_I\dot{\boldsymbol{u}}_I)^{\mathrm{T}}\boldsymbol{\Phi}_J\dot{\boldsymbol{u}}_J = \sum_{I=1}^{n}\sum_{J=1}^{n}\delta\dot{\boldsymbol{u}}_I^{\mathrm{T}}(\rho\boldsymbol{\Phi}_I^{\mathrm{T}}\boldsymbol{\Phi}_J)\dot{\boldsymbol{u}}_J \tag{3.129}$$

If the global numbering sequence is used instead of the local numbering sequence, Eq. (3.129) can be rewritten into the following form:

$$\rho\delta\dot{\boldsymbol{u}}^{\mathrm{T}}\dot{\boldsymbol{u}} = \sum_{I=1}^{N}\sum_{J=1}^{N}\delta\dot{\boldsymbol{u}}_I^{\mathrm{T}}(\rho\boldsymbol{\Phi}_I^{\mathrm{T}}\boldsymbol{\Phi}_J)\dot{\boldsymbol{u}}_J \tag{3.130}$$

Substituting Eq. (3.130) into Eq. (3.127) yields:

$$\delta T = \sum_{I=1}^{N}\sum_{J=1}^{N}\delta\dot{\boldsymbol{u}}_I^{\mathrm{T}}\mathbf{M}_{IJ}\dot{\boldsymbol{u}}_J = \delta\dot{\boldsymbol{U}}^{\mathrm{T}}\mathbf{M}\dot{\boldsymbol{U}} \tag{3.131}$$

where $\dot{\boldsymbol{U}}$ is a vector collecting the velocities of all field nodes in the problem domain, and $\mathbf{M}_{IJ}$ and $\mathbf{M}$ denote the nodal mass matrix and the global mass matrix, which are defined by:

$$\mathbf{M}_{IJ} = \int_{\Omega}\rho\boldsymbol{\Phi}_I^{\mathrm{T}}\boldsymbol{\Phi}_J dV \tag{3.132}$$

$$\mathbf{M} = \begin{Bmatrix} \mathbf{M}_{11} & \mathbf{M}_{12} & \cdots & \mathbf{M}_{1N} \\ \mathbf{M}_{21} & \mathbf{M}_{22} & \cdots & \mathbf{M}_{2N} \\ \vdots & \vdots & \ddots & \vdots \\ \mathbf{M}_{N1} & \mathbf{M}_{N2} & \cdots & \mathbf{M}_{NN} \end{Bmatrix} \tag{3.133}$$

Substituting Eqs. (3.125), (3.126) and (3.131) into Eq. (3.118) produces:

$$\int_{t_1}^{t_2}\left(\delta\dot{\boldsymbol{U}}^{\mathrm{T}}\mathbf{M}\dot{\boldsymbol{U}} - \delta\boldsymbol{U}^{\mathrm{T}}\boldsymbol{F}^{\mathrm{i}} + \delta\boldsymbol{U}^{\mathrm{T}}\boldsymbol{F}^{\mathrm{e}}\right)dt = 0 \tag{3.134}$$

Since the variation and the differentiation operations are interchangeable, the variation of the velocity vector can be rewritten as follows:

$$\delta\dot{\boldsymbol{U}}^{\mathrm{T}} = \delta\left(\frac{d\boldsymbol{U}^{\mathrm{T}}}{dt}\right) = \frac{d}{dt}\left(\delta\boldsymbol{U}^{\mathrm{T}}\right) \tag{3.135}$$

Based on the above equation, the left side of Eq. (3.134) can be integrated by parts, as follows:

$$\int_{t_1}^{t_2}\delta\dot{\boldsymbol{U}}^{\mathrm{T}}\mathbf{M}\dot{\boldsymbol{U}}dt = \delta\boldsymbol{U}^{\mathrm{T}}\mathbf{M}\dot{\boldsymbol{U}}\Big|_{t_1}^{t_2} - \int_{t_1}^{t_2}\delta\boldsymbol{U}^{\mathrm{T}}\mathbf{M}\ddot{\boldsymbol{U}}dt \tag{3.136}$$

Since the first term of the right side of Eq. (3.136) vanishes due to $\delta\boldsymbol{U}^{\mathrm{T}}|_{t_1} = \delta\boldsymbol{U}^{\mathrm{T}}|^{t_2} = 0$, Eq. (3.136) can be simplified into the following form:

$$\int_{t_1}^{t_2}\delta\dot{\boldsymbol{U}}^{\mathrm{T}}\mathbf{M}\dot{\boldsymbol{U}}dt = -\int_{t_1}^{t_2}\delta\boldsymbol{U}^{\mathrm{T}}\mathbf{M}\ddot{\boldsymbol{U}}dt \tag{3.137}$$

Substituting this equation into Eq. (3.134) gives:

$$\int_{t_1}^{t_2}\delta\dot{\boldsymbol{U}}^{\mathrm{T}}\left(-\mathbf{M}\ddot{\boldsymbol{U}} - \boldsymbol{F}^{\mathrm{i}} + \boldsymbol{F}^{\mathrm{e}}\right)dt = 0 \tag{3.138}$$

In Eq. (3.138), the first variation of the displacement vector, i.e. $\delta\dot{\boldsymbol{U}}^{\mathrm{T}}$, is arbitrary. Thus, the only condition satisfying the above equation is:

$$\mathbf{M}\ddot{\boldsymbol{U}} + \boldsymbol{F}^{\mathrm{i}} = \boldsymbol{F}^{\mathrm{e}} \tag{3.139}$$

The above equation is the final form of the discretised system of equations in the explicit weak-form meshfree method. It is interesting to note that the above-discretised system of equations has exactly the same form as that formulated based on the FEM. Thus, it should be borne in mind that the quantities in this equation, i.e. $\mathbf{M}$, $\boldsymbol{F}^{\mathrm{i}}$, and $\boldsymbol{F}^{\mathrm{e}}$, are obtained based on meshfree shape functions. In this research, the explicit central difference method has been utilised to solve the meshfree-based discretised system of equations, which will be briefly introduced in the following section.

3.6.3.2 Meshfree explicit time integration

In the explicit central difference method, the equations of motion are explicitly integrated using the following rules:

$$\ddot{\boldsymbol{U}}^{(n)} = \mathbf{M}^{-1}\left(\boldsymbol{F}^{\mathrm{e}(n)} - \boldsymbol{F}^{\mathrm{i}(n)}\right) \tag{3.140}$$

$$\dot{\boldsymbol{U}}^{(n+\frac{1}{2})} = \dot{\boldsymbol{U}}^{(n-\frac{1}{2})} + \frac{\Delta t^{(n+1)}+\Delta t^{(n)}}{2}\ddot{\boldsymbol{U}}^{(n)} \tag{3.141}$$

$$\boldsymbol{U}^{(n+1)} = \boldsymbol{U}^{(n)} + \Delta t^{(n+1)}\dot{\boldsymbol{U}}^{(n+\frac{1}{2})} \tag{3.142}$$

where the superscripts represent the time steps, and Δt is the time increment. The above integration rules are explicit in that the calculation of the displacement at the current step can be advanced by using the acceleration at the previous step, the velocity at the previous half step and the displacement at the previous step.

It should be noted that the calculation of the inverse of the global mass matrix, as well as the multiplication of the inverse with the force vectors, are computationally expressive, particularly for the problems with high degrees of freedom. To improve the efficiency of the solution procedure, the global mass matrix (which is often termed as the consistent mass matrix) can be lumped into a diagonal mass matrix, which is denoted using $\mathbf{M}_{\mathrm{L}}$. The mass lumping made to the consistent mass matrix can be achieved by using the commonly used row-sum technique, as follows:

$$(\mathbf{M}_{\mathrm{L}})_{II} = \sum_{I=1}^{3N} \mathrm{M}_{IJ} \tag{3.143}$$

where $(\mathbf{M}_{\mathrm{L}})_{II}$ denotes the Ith diagonal element of the lumped mass matrix, and M_{IJ} is a component of the consistent mass matrix.

The mass lumping operation described above has been widely used and considered as a necessary strategy in the explicit FEM. Although there is still very little theory formally justifying the use of such a strategy, its combination with the explicit central difference method can generally produce stable and reasonably accurate solutions. However, it must be noted that the lumping operation alters the consistent mass matrix in a way that most of the mass is lumped to the field nodes corresponding to the diagonal elements of the lumped mass matrix. This effect can get increasingly evident if high-orders of integration

are applied to obtain the mass matrix, leading to distortions in the accelerations that will be calculated. Thus, high-order integrations should be avoided if the lumping strategy is applied for the sake of efficiency.

From Eqs. (3.140) – (3.142), it can be seen that the velocities are calculated only at half time steps. If the velocity at the current step needs to be obtained, the following equation can be employed:

$$\dot{U}^{(n+1)} = \dot{U}^{(n+\frac{1}{2})} + \frac{1}{2}\Delta t^{(n+1)}\ddot{U}^{(n+1)} \tag{3.144}$$

It should be further noted that the explicit central difference method is not a self-starting method. To enable the calculation to be advanced automatically, the velocities at steps $\left(-\frac{1}{2}\right)$ and $\left(+\frac{1}{2}\right)$ need to be predefined. By replacing n in Eq. (3.144) with -1, the velocity at time step $\left(-\frac{1}{2}\right)$ can be determined, as follows:

$$\dot{U}^{(-\frac{1}{2})} = \dot{U}^{(0)} - \frac{1}{2}\Delta t^{(0)}\ddot{U}^{(0)} \tag{3.145}$$

By replacing n in Eq. (3.141) with 0 and considering Eq. (3.145), the velocity at time step $\left(+\frac{1}{2}\right)$ can be determined, as follows:

$$\dot{U}^{(+\frac{1}{2})} = \dot{U}^{(0)} + \frac{1}{2}\Delta t^{(1)}\ddot{U}^{(0)} \tag{3.146}$$

3.6.3.3 Enforcement of boundary conditions

The essential boundary conditions in the homogenisation of the overall response of woven composites can be prescribed either explicitly in the form of Eq. (3.115) or implicitly in a PBC form. For the former case, they can be enforced directly in Eq. (3.142), and thus no further treatment is needed. In terms of the PBC-based essential boundary conditions, since they present in the form of displacement relations between each pair of equivalent boundary nodes, they should be enforced using the displacement constraint elimination method. However, it should be noted that the homogenisation of the overall response of woven composites requires applying a history of PBCs. This suggests that the PBC in this case is time-dependent and can be described using the following equation:

$$u(x^A, t) - \gamma \mathbf{T} u(x^{\bar{A}}, t) = -\langle \varepsilon(t) \rangle \mathbf{T} \lambda \quad \forall x^{\bar{A}} \in \Gamma^- \ \& \ \forall x^A \in \Gamma^+ \tag{3.147}$$

To enforce the above time-dependent PBC, the constraint elimination method described in Section 3.6.2 is extended as follows. Again, the original numbering sequence of field nodes is reorganised based on a division of all field nodes in the problem domain into the internal field nodes, i.e. $\boldsymbol{x}_{Ii}$ ($I = 1, \ldots, n_i$), the field nodes on the negative boundary, i.e. $\boldsymbol{x}_{J-}$ ($J = 1, \ldots, n_-$), and the field nodes on the positive boundary, i.e. $\boldsymbol{x}_{K+}$ ($K = 1, \ldots, n_+$). Based on the modified numbering sequence, the basic equations for the explicit central difference method can be rewritten as follows, where the diagonal lumped mass matrix is used instead of the consistent mass matrix:

$$\begin{Bmatrix} \ddot{\boldsymbol{U}}_i^{(n)} \\ \ddot{\boldsymbol{U}}_-^{(n)} \\ \ddot{\boldsymbol{U}}_+^{(n)} \end{Bmatrix} = \begin{bmatrix} (\mathbf{M}_\mathrm{L})_{ii}^{-1} & \mathbf{0} & \mathbf{0} \\ \mathbf{0} & (\mathbf{M}_\mathrm{L})_{--}^{-1} & \mathbf{0} \\ \mathbf{0} & \mathbf{0} & (\mathbf{M}_\mathrm{L})_{++}^{-1} \end{bmatrix} \left(\begin{Bmatrix} \boldsymbol{F}_i^{\mathrm{e}(n)} \\ \boldsymbol{F}_-^{\mathrm{e}(n)} \\ \boldsymbol{F}_+^{\mathrm{e}(n)} \end{Bmatrix} - \begin{Bmatrix} \boldsymbol{F}_i^{\mathrm{i}(n)} \\ \boldsymbol{F}_-^{\mathrm{i}(n)} \\ \boldsymbol{F}_+^{\mathrm{i}(n)} \end{Bmatrix} \right) \tag{3.148}$$

$$\begin{Bmatrix} \dot{\boldsymbol{U}}_i^{\left(n+\frac{1}{2}\right)} \\ \dot{\boldsymbol{U}}_-^{\left(n+\frac{1}{2}\right)} \\ \dot{\boldsymbol{U}}_+^{\left(n+\frac{1}{2}\right)} \end{Bmatrix} = \begin{Bmatrix} \dot{\boldsymbol{U}}_i^{\left(n-\frac{1}{2}\right)} \\ \dot{\boldsymbol{U}}_-^{\left(n-\frac{1}{2}\right)} \\ \dot{\boldsymbol{U}}_+^{\left(n-\frac{1}{2}\right)} \end{Bmatrix} + \frac{\Delta t^{(n)} + \Delta t^{(n+1)}}{2} \begin{Bmatrix} \ddot{\boldsymbol{U}}_i^{(n)} \\ \ddot{\boldsymbol{U}}_-^{(n)} \\ \ddot{\boldsymbol{U}}_+^{(n)} \end{Bmatrix} \tag{3.149}$$

$$\begin{Bmatrix} \boldsymbol{U}_i^{(n+1)} \\ \boldsymbol{U}_-^{(n+1)} \\ \boldsymbol{U}_+^{(n+1)} \end{Bmatrix} = \begin{Bmatrix} \boldsymbol{U}_i^{(n)} \\ \boldsymbol{U}_-^{(n)} \\ \boldsymbol{U}_+^{(n)} \end{Bmatrix} + \Delta t^{(n+1)} \begin{Bmatrix} \dot{\boldsymbol{U}}_i^{\left(n+\frac{1}{2}\right)} \\ \dot{\boldsymbol{U}}_-^{\left(n+\frac{1}{2}\right)} \\ \dot{\boldsymbol{U}}_+^{\left(n+\frac{1}{2}\right)} \end{Bmatrix} \tag{3.150}$$

Based on Eq. (3.147), we can assume:

$$\boldsymbol{U}_+^{(n)} = \widetilde{\mathbf{T}} \boldsymbol{U}_-^{(n)} + \boldsymbol{\xi}^{(n)} \tag{3.151}$$

$$\boldsymbol{U}_+^{(n+1)} = \widetilde{\mathbf{T}} \boldsymbol{U}_-^{(n+1)} + \boldsymbol{\xi}^{(n+1)} \tag{3.152}$$

where $\boldsymbol{\xi}^{(n)}$ and $\boldsymbol{\xi}^{(n+1)}$ denote the differences between $\boldsymbol{U}_+$ and $\widetilde{\mathbf{T}} \boldsymbol{U}_-$ at time steps n and $n + 1$, and $\widetilde{\mathbf{T}}$ has been defined in Eq. (3.107). Substituting the above two equations into Eq. (3.150), we can obtain:

$$\dot{\boldsymbol{U}}_+^{\left(n+\frac{1}{2}\right)} = \widetilde{\mathbf{T}} \dot{\boldsymbol{U}}_-^{\left(n+\frac{1}{2}\right)} + \dot{\boldsymbol{\xi}}^{\left(n+\frac{1}{2}\right)} \tag{3.153}$$

where

$$\dot{\xi}^{\left(n+\frac{1}{2}\right)} = \frac{\left(\xi^{(n+1)} - \xi^{(n)}\right)}{\Delta t^{(n+1)}} \tag{3.154}$$

Replacing n in Eq. (3.153) with $n-1$ produces:

$$\dot{U}_+^{\left(n-\frac{1}{2}\right)} = \widetilde{\mathbf{T}} \dot{U}_-^{\left(n-\frac{1}{2}\right)} + \dot{\xi}^{\left(n-\frac{1}{2}\right)} \tag{3.155}$$

where

$$\dot{\xi}^{\left(n-\frac{1}{2}\right)} = \frac{\left(\xi^{(n)} - \xi^{(n-1)}\right)}{\Delta t^{(n)}} \tag{3.156}$$

Substituting Eqs. (3.153) and (3.155) into Eq. (3.149), we can obtain:

$$\ddot{U}_+^{(n)} = \widetilde{\mathbf{T}} \ddot{U}_-^{(n)} + \ddot{\xi}^{(n)} \tag{3.157}$$

where

$$\ddot{\xi}^{(n)} = \frac{2\left(\dot{\xi}^{\left(n+\frac{1}{2}\right)} - \dot{\xi}^{\left(n-\frac{1}{2}\right)}\right)}{\Delta t^{(n)} + \Delta t^{(n+1)}} \tag{3.158}$$

Substituting Eq. (3.157) into Eq. (3.148), the following equation can be obtained after performing some mathematical manipulations:

$$\widetilde{\ddot{U}}^{(n)} = \widetilde{\mathbf{M}}^{-1}\left(\widetilde{F}^{\mathrm{e}(n)} - \widetilde{F}^{\mathrm{i}(n)}\right) \tag{3.159}$$

where

$$\widetilde{\ddot{U}}^{(n)} = \left\{\ddot{U}_i^{(n)} \quad \ddot{U}_-^{(n)}\right\}^{\mathrm{T}} \tag{3.160}$$

$$\widetilde{\mathbf{M}}^{-1} = \begin{bmatrix} (\mathbf{M}_{\mathrm{L}})_{ii} & \mathbf{O} \\ \mathbf{O} & (\mathbf{M}_{\mathrm{L}})_{--} + (\mathbf{M}_{\mathrm{L}})_{++}\widetilde{\mathbf{T}} \end{bmatrix}^{-1} \tag{3.161}$$

$$\widetilde{F}^{\mathrm{e}(n)} = \left\{ \begin{matrix} F_i^{\mathrm{e}(n)} \\ F_-^{\mathrm{e}(n)} + F_+^{\mathrm{e}(n)} - (\mathbf{M}_{\mathrm{L}})_{++}\ddot{\xi}^{(n)} \end{matrix} \right\} \tag{3.162}$$

$$\widetilde{\boldsymbol{F}}^{\mathrm{i}(n)} = \begin{bmatrix} \boldsymbol{F}_i^{\mathrm{i}(n)} \\ \boldsymbol{F}_-^{\mathrm{i}(n)} + \boldsymbol{F}_+^{\mathrm{i}(n)} \end{bmatrix} \tag{3.163}$$

Since no external force will be prescribed when predicting the overall response of woven composites, the external force components in Eq. (3.162) vanish, leading to:

$$\widetilde{\boldsymbol{F}}^{\mathrm{e}(n)} = \begin{Bmatrix} \mathbf{0} \\ -(\mathbf{M}_{\mathrm{L}})_{++} \ddot{\boldsymbol{\xi}}^{(n)} \end{Bmatrix} \tag{3.164}$$

From Eqs. (3.149) and (3.150), we can also obtain:

$$\widetilde{\boldsymbol{U}}^{\left(n+\frac{1}{2}\right)} = \widetilde{\boldsymbol{U}}^{\left(n-\frac{1}{2}\right)} + \frac{\Delta t^{(n)} + \Delta t^{(n+1)}}{2} \widetilde{\ddot{\boldsymbol{U}}}^{(n)} \tag{3.165}$$

$$\widetilde{\boldsymbol{U}}^{(n+1)} = \widetilde{\boldsymbol{U}}^{(n)} + \Delta t^{(n+1)} \widetilde{\dot{\boldsymbol{U}}}^{\left(n+\frac{1}{2}\right)} \tag{3.166}$$

where

$$\widetilde{\boldsymbol{U}}^{\left(n-\frac{1}{2}\right)} = \left\{ \dot{\boldsymbol{U}}_i^{\left(n-\frac{1}{2}\right)} \quad \dot{\boldsymbol{U}}_-^{\left(n-\frac{1}{2}\right)} \right\}^{\mathrm{T}} \tag{3.167}$$

$$\widetilde{\boldsymbol{U}}^{(n)} = \left\{ \boldsymbol{U}_i^{(n)} \quad \boldsymbol{U}_-^{(n)} \right\}^{\mathrm{T}} \tag{3.168}$$

Eqs. (3.159), (3.165) and (3.166) are the final equations for enforcing the PBC defined in Eq. (3.147). Solving these equations and considering Eqs. (3.152), (3.153) and (3.157), all the components of the global displacement vector, the global velocity vector and the acceleration vectors can be calculated.

3.7 Summary

In this chapter, the background knowledge and basic concepts associated with meshfree methods were firstly introduced. Then, the formulation procedures for three commonly used shape function construction techniques, i.e. MLS, RBF and MK, were detailed in combination with examples of calculating shape functions using these techniques. These examples suggest that the RBF-based and MK-based shape functions possess both the property of partitions of unity and the Kronecker delta function property, while the MLS-

based shape functions possess only the property of partitions of unity. At the end of this chapter, the formulation procedures for both the standard weak-form meshfree method and the explicit weak-form meshfree method were described, and the basic equations for enforcing the PBC-based essential boundary conditions within the two meshfree methods were formulated.

CHAPTER 4: ELASTIC PROPERTY HOMOGENISATION

4.1 Introduction

4.1.1 Unit cell identification and domain reduction

In the micromechanical homogenisation of woven composites, the representative region that is used to perform a homogenisation is termed as a unit cell (UC). In general, a full-size UC is defined as the smallest region such that the entire composite structure can be reconstructed from translational copies of it, without using rotational and/or reflectional symmetries [187]. This suggests that the choice of a UC for woven composites is not unique, but with many possibilities.
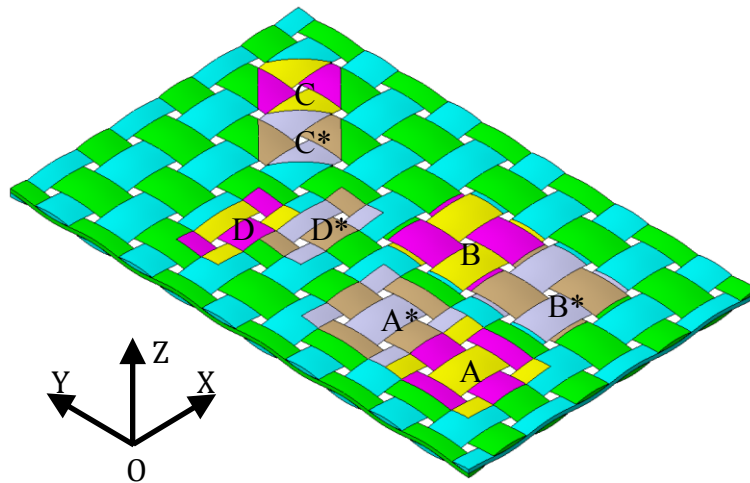
Figure 4.1: Typical plain woven composites and its possible UCs

Fig. 4.1 shows some of the possible UCs in typical plain woven composites. In this figure, the matrix has been set to be transparent in order to reveal the internal architecture. The same treatment will be applied if appropriate for presenting the internal architectures of other types of woven composites throughout this thesis. Clearly, each of the highlighted

regions in this figure can be defined as a UC, owing to the fact the composite structure can be reconstructed based on translations copies of any of these regions. In addition, this figure suggests that different types of UCs do not necessarily have the same size, but with the size of the UC being dependent of the translation symmetry applied to obtain the UC. For example, the size of UC "A" is the same as that of UC "B", which is because the translational symmetries used in the two cases, i.e. those from A to A* and B to B*, are parallel to the global coordinate system (GCS) of the composite material, i.e. OXYZ. On the other hand, the size of UC "C" or "D" is smaller than that of UC "A" as a result of utilising non-parallel translational symmetries in obtaining UC "C" or "D". Furthermore, it is worth noting that a UC should be defined such that it facilitates the homogenisation analysis that is to be performed. For instance, UC "A", "B" or "D" is well-suited for homogenising the elastic properties in the warp and weft directions, while UC "C" is only suitable to predict the properties in off-axis directions, e.g. 45° to the warp direction. For convenience, the UCs that are similar to UC "A" will be referred to as *normal* UCs, while those similar to UC "C" will be termed as *off-axis* UCs in the rest of this thesis.
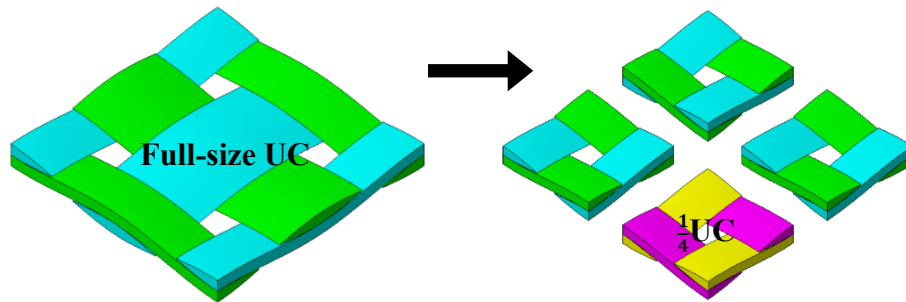
(a) Full-size UC to $\frac{1}{4}$UC by using reflectional symmetries
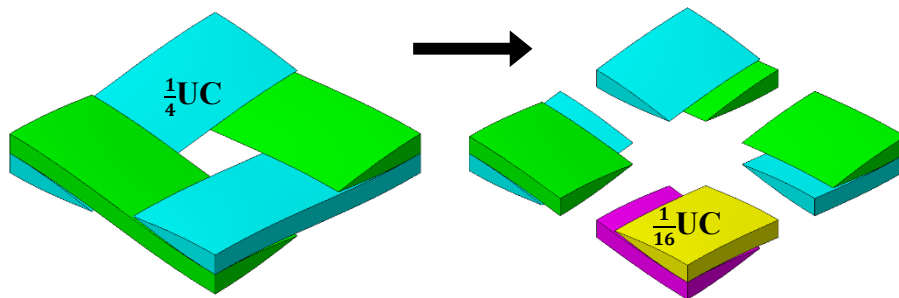
(b) $\frac{1}{4}$UC to $\frac{1}{16}$UC by using reflectional & rotational symmetries

Figure 4.2: Domain reduction for plain woven composites

Clearly, the highly complex internal architecture of woven composites often requires an excessive modelling time and a high computational cost even at the level of full-size UC. Thus, it is always desirable to exploit all possible symmetries of the woven composites of investigation to reduce the size of the domain of homogenisation. The symmetries that can be exploited in woven composites consist of translation, rotation, reflection and a combination of these symmetries. Fig. 4.2 shows a typical procedure for exploiting all possible symmetries in plain woven composites from a full-size UC to the smallest UC, which is comprised of two steps. Firstly, the full-size UC can be quartered by exploiting the reflectional symmetries, leading to a $\frac{1}{4}$UC. Secondly, the $\frac{1}{4}$UC can be further reduced by considering both the reflectional and rotational symmetries, leading to a $\frac{1}{16}$UC, which is a UC that cannot be further exploited.

The above example suggests that there will be different sizes of UCs involved in reducing the domain of woven composites. For clarity, the following definitions are introduced and will be utilised hereafter in this thesis. A domain region that is obtained after exploiting partially or fully the symmetries of a full-size UC will be referred to as a *reduced unit cell* (rUC), and an rUC will be termed as a *minimum unit cell* (mUC) if there is no symmetry that can be further exploited. Based on the above definitions, we can see in Fig. 4.2 that both the $\frac{1}{4}$UC and $\frac{1}{16}$UC are rUCs, while only the $\frac{1}{16}$UC is an mUC. For simplicity, all woven composite geometry models developed in the present research are mUCs.

It should be noted that if a homogenisation of woven composites is conducted using a full-size UC, which is derived based on translational symmetries only, the standard form of PBC, as defined in Eq. (2.79), can be applied directly to enforce boundary conditions. However, if an rUC or mUC is used, the standard form of PBC cannot be applied since this type of PBC is formulated based on a full-size UC, rather than on an rUC or mUC, which can be obtained only after exploiting at least a non-translational symmetry. Thus, enforcing boundary conditions for an rUC or mUC must be performed in accordance with the reduction operations used to obtain the rUC or mUC. Algorithms for deriving the PBC of rUCs or mUCs of woven composites can be found in Li *et al.* [188], Whitcomb and co-workers [189, 190], De Carvalho *et al.* [191]. In this research, the algorithm developed by De Carvalho *et al.* [191] has been utilised to derive boundary conditions for woven composites, and it will be described in detail in Section 4.5.

4.1.2 General assumptions

To model the internal architecture of woven composites as accurate as possible, a number of plain woven carbon fibre-reinforced polymer (CFRP) composite specimens has been fabricated based on EP121-C15-53 prepreg supplied by Gurit Ltd to observe the cross-section and waviness of yarns. The woven fabric in this prepreg is made from 3k HTA40 carbon fibres and has an areal density of $193g/m^2$. The fabric is pre-impregnated with a 53% EP121 resin matrix, which is a toughened self-extinguishing epoxy resin. Hereafter in this thesis, this composite material will be used for predicting the elastic properties and the overall response. For convenience, it is denoted as EP121-C15-53 composites.
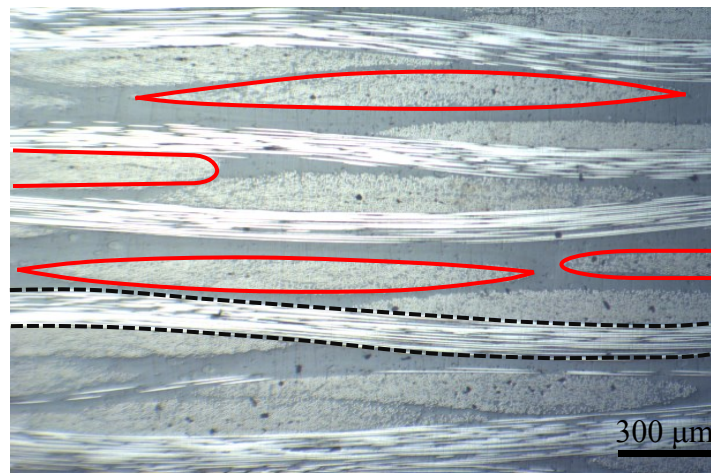
(a) Micrograph at 25x magnification
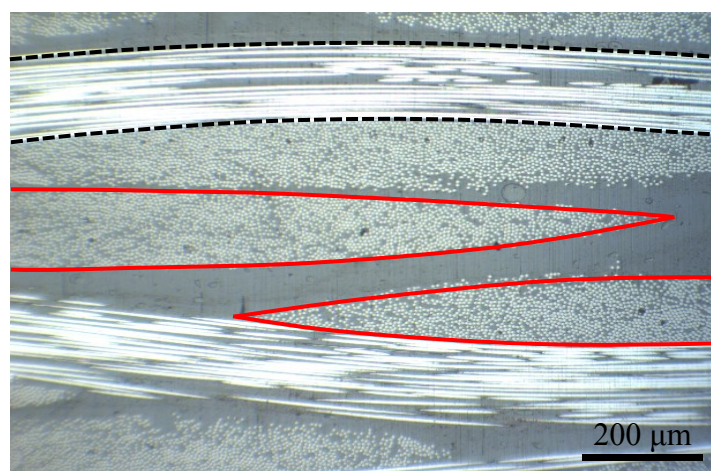
(b) Micrograph at 100x magnification

Figure 4.3: Micrographs of typical plain woven composites

Fig. 4.3 shows two micrographs of this composite material at different magnifications. An initial observation of the two micrographs suggests that although the cross-sections of the yarns exhibit in different shapes (see the areas highlighted using solid curves), the dominant ones are lenticular. Thus, it is assumed that the cross-section of a general yarn in woven composites can be fitted using simple functions, such as cosine functions. Fig. 4.4 shows the result of using cosine functions to fit the cross-sections of the yarns in the specimens. Here, it should be noted that the data points representing the cross-sections have been translated such that all cross-sections are centred at the same point for the sake of easy comparison. From this figure, it is established that the cross-section of a general yarn in woven composites can be described using cosine functions.

The figure shows a plot with a fitted lenticular cross-section. The equation shown is:

$$y = 0.14 + 0.07\left\{1 \pm \cos\left(\frac{\pi}{1.8}x\right)\right\}$$

with legend: Formulated, Measured #1, Measured #2, Measured #3, Measured #4, Measured #5. Axes: Z (mm) vertical, X (mm) horizontal.
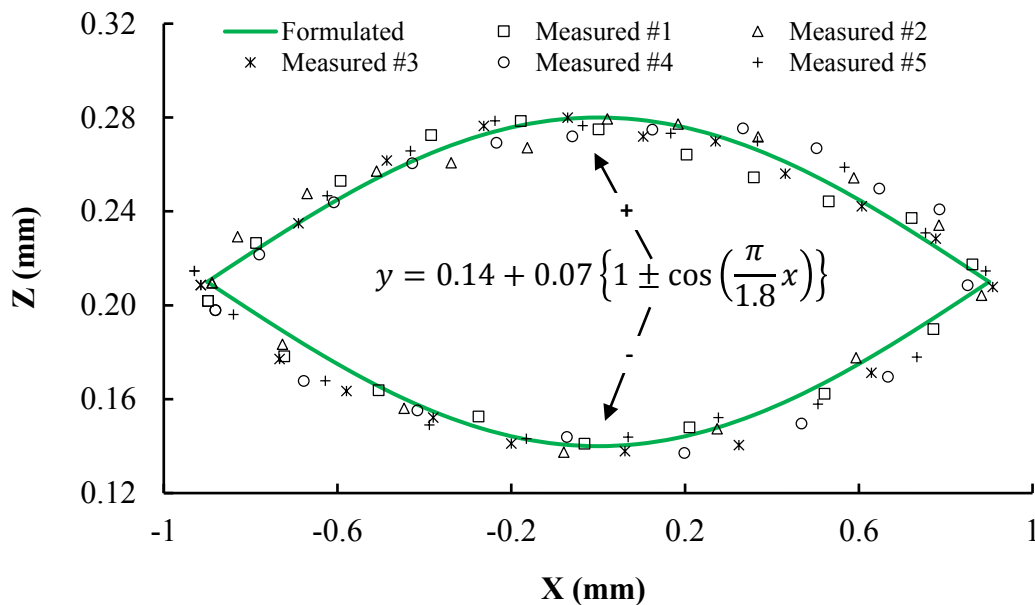
Figure 4.4: Yarn's cross-section fitted by using cosine functions

In addition to the above observation, it can be found in Fig. 4.3 that the yarns in this type of composite material have a wave-like shape in the fibre direction, as highlighted in the figure using dashed curves. Furthermore, it can be seen that the thickness of each yarn is almost constant across the whole yarn. Based on these findings, it is assumed that the waviness of a general yarn in woven composites can be largely described using cosine functions. A subsequent curve fitting, as shown in Fig. 4.4, confirms the feasibility of such an assumption.

The figure shows a plot with Z (mm) on the vertical axis (ranging from -0.02 to 0.18) and Y (mm) on the horizontal axis (ranging from -1.2 to 3.3). It includes curves and measured data points with the legend: Formulated, Measured #1, Measured #2, Measured #3, Measured #4, Measured #5. The equation annotated is:

$$z = 0.07 \left(1 - \cos \frac{\pi x}{2} \right)$$
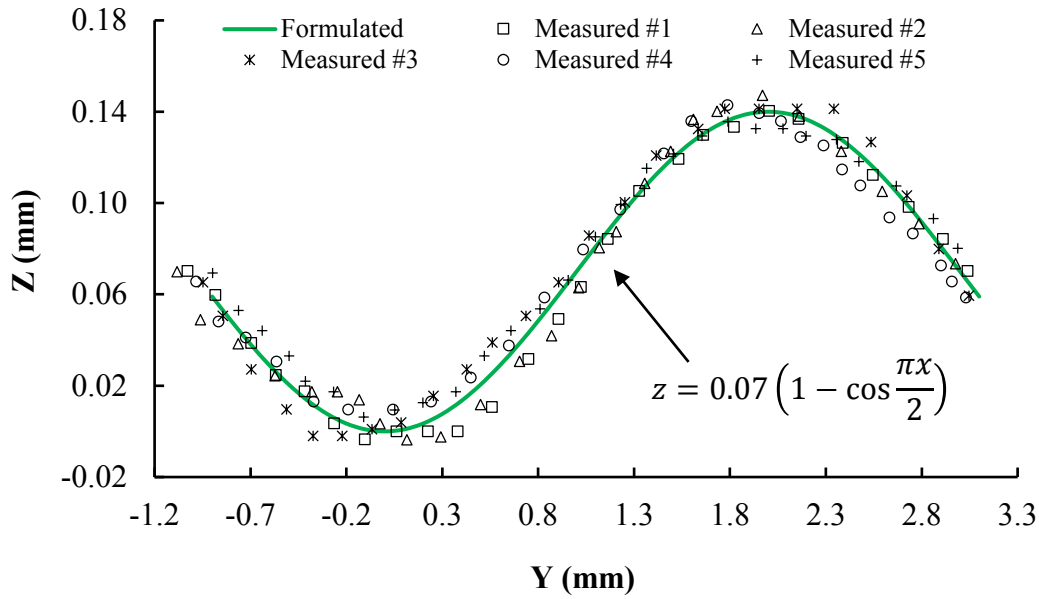
Figure 4.5: Yarn's waviness fitted using cosine functions

Based on the above observations and curve fittings, the general assumptions made in the present research to model the internal architecture of woven composites are summarised as follows:

1) The cross-section of a general yarn in woven composites can be described using simple functions such cosine functions;

2) The waviness of a general yarn in woven composites can be fitted using simple functions such as cosine functions;

3) Each yarn in woven composites has a constant cross-sectional shape across the whole yarn.

4.1.3 Further assumptions

In structural application of woven composites, a woven composite structure is fabricated typically by stacking a number of plies or layers together to form the whole thickness of the structure. Depending on the mechanical performance required, the direction of a ply can be parallel or at an angle to that of another ply. Additionally, composite plies can be stacked together based on simple stacking, symmetrical stacking and/or a combination of them. Examples of simple and symmetrical stacking are shown in Fig. 4.6.

The many possible combinations of composite stacking and ply orientation complicates the development of predictive models for woven composites. Thus, the present research focuses on developing predictive models for the woven composites with simple stacking and the same ply orientation. This means that only a layer of woven composites is needed to identify UCs as translation is the unique type of symmetry in the through-the-thickness direction in such type of woven composites. Also, for simplicity, manufacturing defects, such as inter-ply shifting, yarn nesting and fibre misalignment, will not be considered in developing geometry models for woven composites. Furthermore, a perfect bonding is assumed, avoiding the effort needed to model the interface between the polymer matrix and the yarn material.
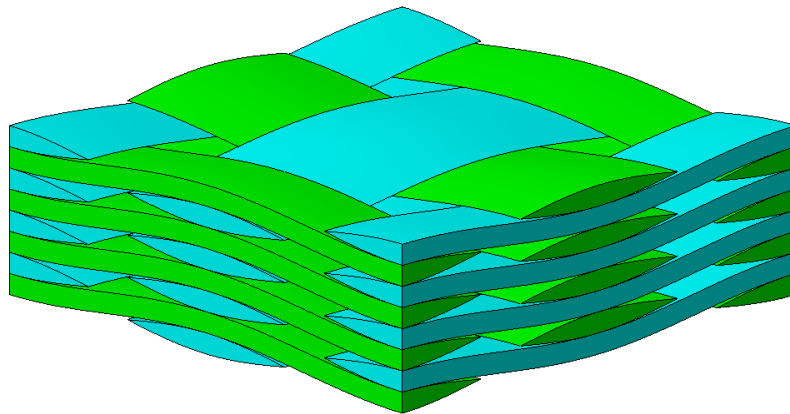
(a) Plain woven composites based on simple stacking
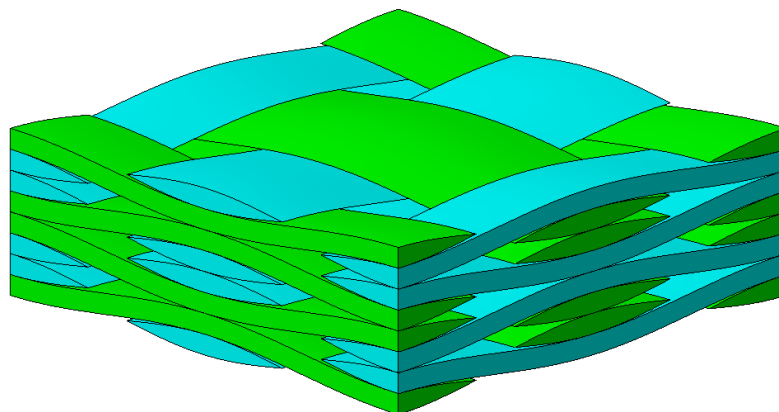
(b) Plain woven composites based on symmetrical stacking

Figure 4.6: Two typical stacking methods in woven composites

4.1.4 Definitions and notations
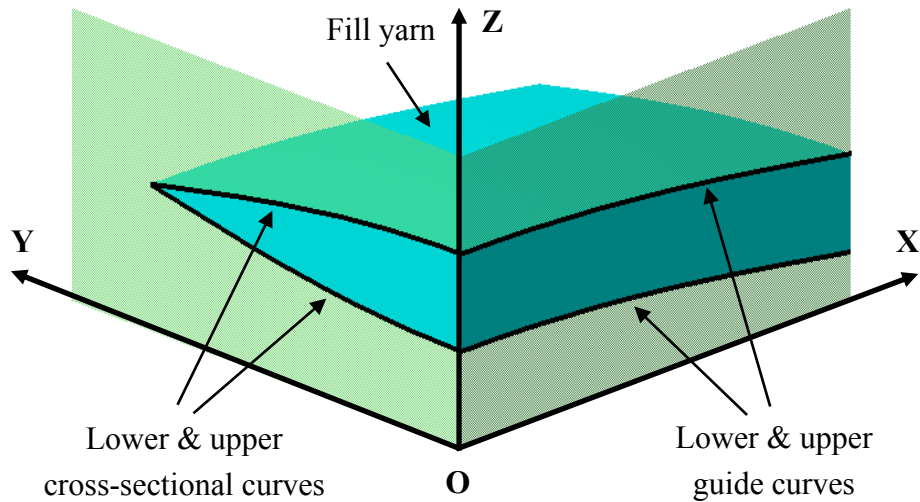
Figure 4.7: Definitions for the feature curves of a typical yarn

To simplify the description of the UC models, which will be presented in the following sections, the following definitions are introduced for describing yarns. Firstly, the lower and upper curves of the intersection between a yarn and a plane that is perpendicular to the fibre direction are referred to as the *lower cross-sectional curve* and the *upper cross-sectional curve*, see Fig. 4.7. Secondly, the lower and upper curves of the intersection between a yarn and a plane that is parallel to the fibre direction are termed as the *lower guide curve* and the *upper guide curve*, see Fig. 4.7. To systematically and accurately quote a feature curve, the following notation strategy is employed:

$$\Sigma_{①②③}$$

Σ   This symbol is to suggest based on which coordinate a feature curve is described. For example, if a curve is described in the form of $z = f(x, y)$, this symbol should be "z".

①   This subscript is to suggest to which type of yarn a curve belongs, and it should be filled with the first letter of yarn's name. For example, if a curve belongs the warp, fill or binder yarn, this subscript is filled with "w", "f" or "b". It should be noted that there could be more than one yarn of the same type even in a single UC model. In such a case, this subscript should be filled with a letter followed by a

number. For instance, subscripts "w1" and "f2" stand for the first warp yarn and the second fill yarn, respectively.

② This subscript is to suggest the relative location of the curve being described. It should be filled with letter "l" if it is a lower curve; otherwise, letter "u" should be used to denote an upper curve.

③ This subscript is to the type of a curve being described. This subscript should be filled with letter "c" if it is a cross-sectional curve; otherwise, letter "g" should be used to denote a guide curve.

Based on the above notation strategy, the notation of z_{wlc} suggests that the curve being described is the lower cross-sectional curve of the warp yarn. Similarly, the notation of z_{f2ug} suggests that it is the upper guide curve of the second fill yarn.

4.2 Normal mUC for plain woven composites

(a) Model I: lenticular cross-section   (b) Model II: elliptical cross-section
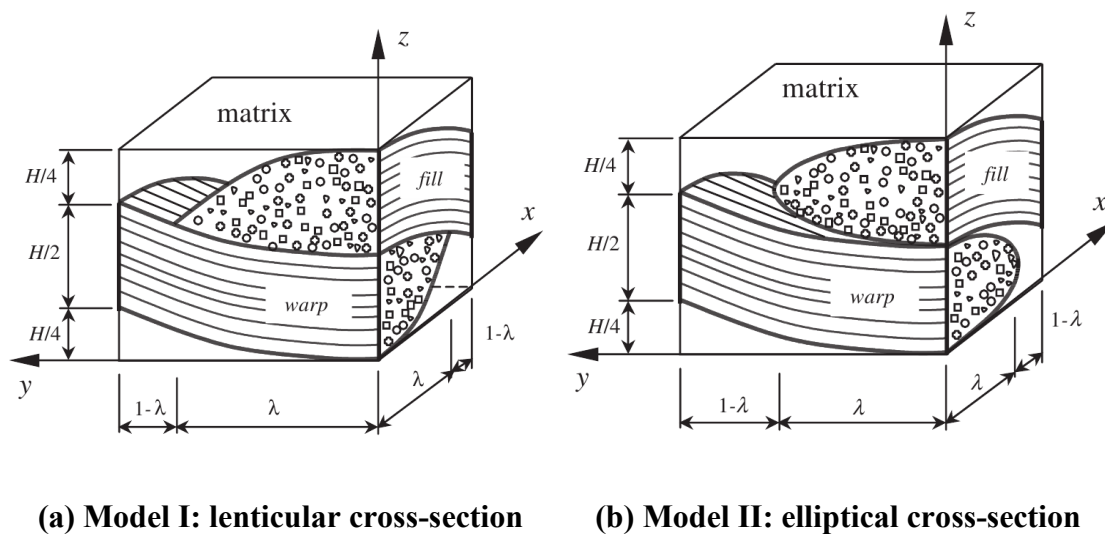
Figure 4.8: Plain woven composite UCs developed by Wen and Aliabadi [94]

The plain woven composite UC model proposed in the present research is improved from those originally developed by Wen and Aliabadi [94] for predicting the elastic properties of plain woven composites, as shown in Fig. 4.8. In their first model, the cross-section of a yarn was modelled as a lenticular shape with one cross-sectional curve described using a cosine function and the other using a quadratic function. Such an assumption, however,

leads to an asymmetrical cross-section. Although this problem was properly addressed in their second model by using an elliptical cross-section, the combination of using elliptical functions to describe the cross-section and using cosine functions to describe the waviness causes another problem, which is that the lower surface of the fill yarn is even lower than the upper surface of the warp yarn in the vicinity of the expected coincidence point of the two yarns, i.e. $x = (0, 0, H/2)$.
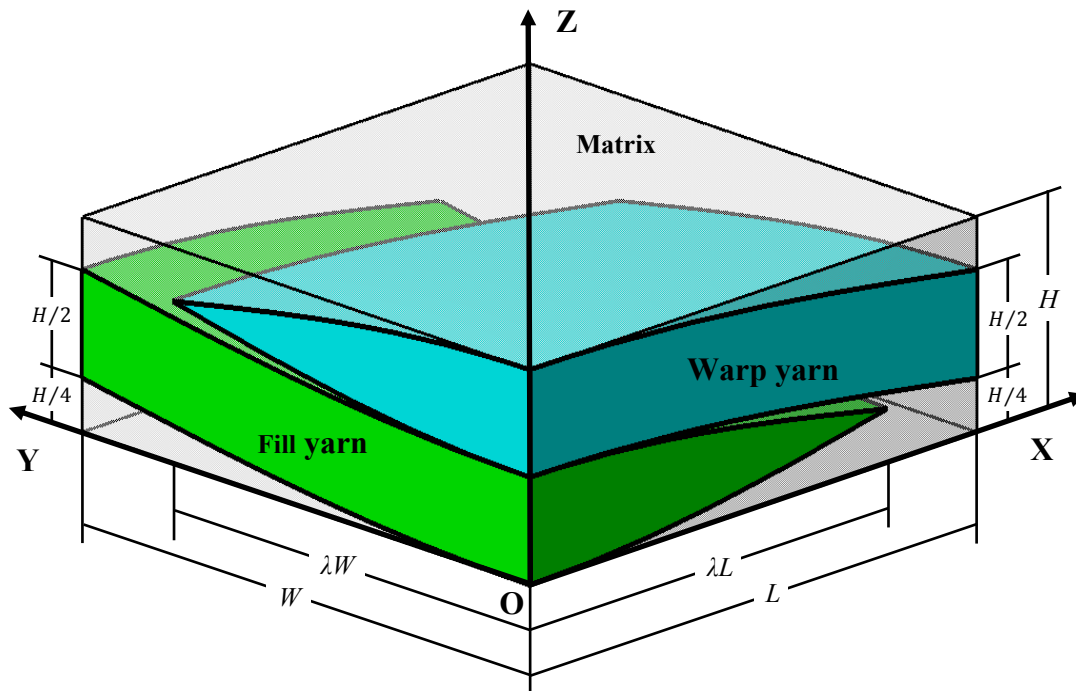
Figure 4.9: The improved mUC model for plain woven composites

To avoid the above two problems and follow the assumption given in Section 4.1, cosine functions are used to describe both the cross-section and waviness of the yarns of plain woven composites. Fig. 4.9 shows the improved model, which is a normal mUC obtained after performing the domain reduction operations illustrated in Fig. 4.2. Compared to the models shown in Fig. 4.8, two extra parameters, L and W, which stand for the length and width of the UC, are utilised here to improve the flexibility of accommodating this model for plain woven composites with different fabric sizes. Similar to the original models, a dimensionless parameter, λ, which is defined as the ratio of the half width of the warp (λW) or fill yarn (λL) to the width (W) or length (L) of the UC, is utilised to control the width of the yarns. In addition, the warp and fill yarns are assumed to have a maximum

thickness of $H/2$. It is further assumed that each yarn can be constructed by sweeping its cross-section along the corresponding guide curves.

4.2.1 Warp yarn $(0 \leq y \leq \lambda W)$
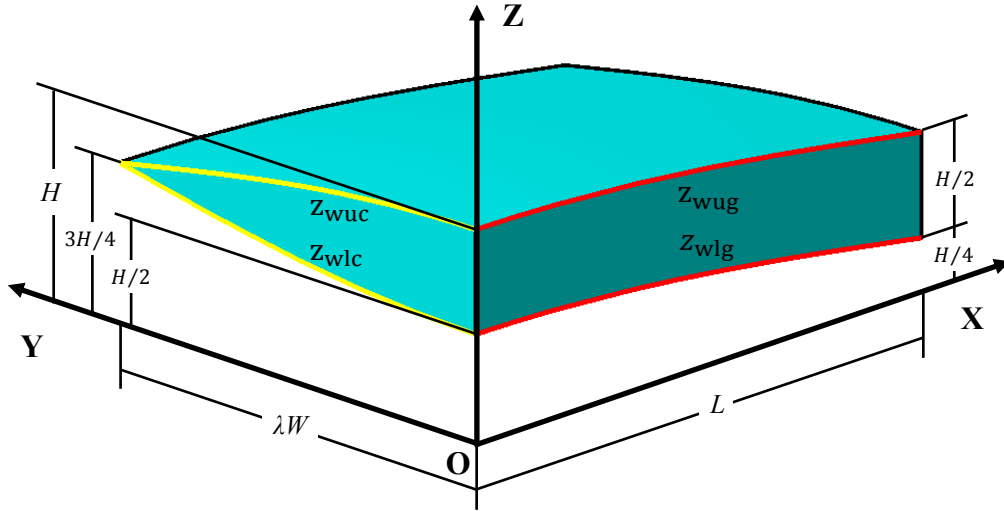
Figure 4.10: The warp yarn of the improved mUC for plain woven composites

According to the assumptions in Section 4.1 and the geometry configuration shown in Fig. 4.10, the lower and upper cross-sectional and guide curves can be described using the following four equations, respectively:

$$z_{\text{wlc}} = \frac{3H}{4} - \frac{H}{4}\cos\frac{\pi y}{2\lambda W} \tag{4.1}$$

$$z_{\text{wuc}} = \frac{3H}{4} + \frac{H}{4}\cos\frac{\pi y}{2\lambda W} \tag{4.2}$$

$$z_{\text{wlg}} = \frac{H}{4} + \frac{H}{4}\cos\frac{\pi x}{2L} \tag{4.3}$$

$$z_{\text{wug}} = \frac{3H}{4} + \frac{H}{4}\cos\frac{\pi x}{2L} \tag{4.4}$$

Based on the above four equations, the lower and upper surfaces of the warp yarn can be described using the following two equations:

$$z_{\text{warp}}^{\text{lower}} = z_{\text{wlc}} + z_{\text{wlg}} - \frac{H}{2} = \frac{H}{4}\left(2 + \cos\frac{\pi x}{2L} - \cos\frac{\pi y}{2\lambda W}\right) \tag{4.5}$$

$$z_{\text{warp}}^{\text{upper}} = z_{\text{wuc}} + z_{\text{wlg}} - H = \frac{H}{4}\left(2 + \cos\frac{\pi x}{2L} + \cos\frac{\pi y}{2\lambda W}\right) \tag{4.6}$$

By taking the partial derivative of Eq. (4.5) or (4.6) with respect to x, the waviness or the undulation angle of any material point on the warp yarn with respect to the XOY plane can be determined, as follows:

$$\theta_{\text{warp}} = \tan^{-1}\left(\frac{\partial z_{\text{warp}}^{\text{lower}}}{\partial x}\right) = \tan^{-1}\left(-\frac{\pi H}{8L}\sin\frac{\pi x}{2L}\right) \tag{4.7}$$

4.2.2 Fill yarn $(0 \le x \le \lambda L)$
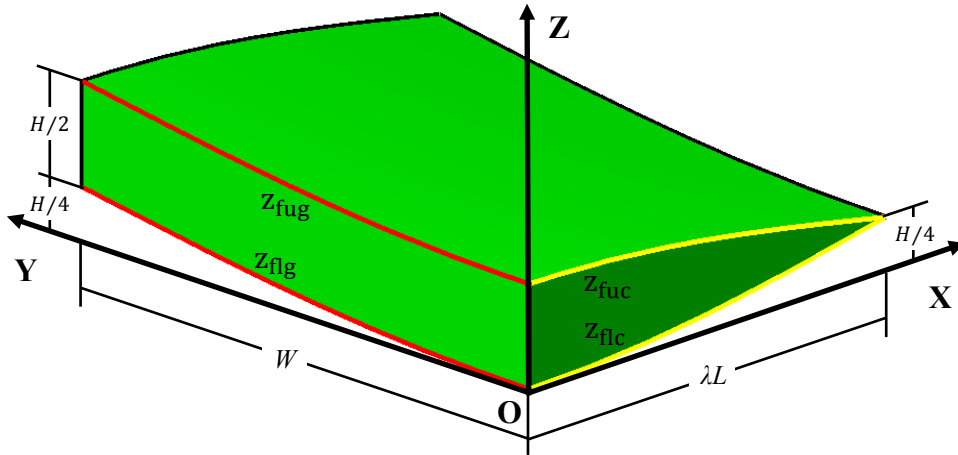
Figure 4.11: The fill yarn of the improved mUC for plain woven composites

Similar to the warp yarn, the equations for describing the lower and upper cross-sectional and guide curves of the fill yarn, as highlighted in Fig. 4.11, can be obtained, as follows:

$$z_{\text{flc}} = \frac{H}{4} - \frac{H}{4}\cos\frac{\pi x}{2\lambda L} \tag{4.8}$$

$$z_{\text{fuc}} = \frac{H}{4} + \frac{H}{4}\cos\frac{\pi x}{2\lambda L} \tag{4.9}$$

$$z_{\text{flg}} = \frac{H}{4} - \frac{H}{4}\cos\frac{\pi y}{2W} \tag{4.10}$$

$$z_{\text{fug}} = \frac{3H}{4} - \frac{H}{4}\cos\frac{\pi y}{2W} \tag{4.11}$$

Based on the above four equations, the lower and upper surfaces of the fill yarn can be described using the following two equations:

$$z_{\text{fill}}^{\text{lower}} = z_{\text{flc}} + z_{\text{flg}} = \frac{H}{4}\left(2 - \cos\frac{\pi x}{2\lambda L} - \cos\frac{\pi y}{2W}\right) \tag{4.12}$$

$$z_{\text{fill}}^{\text{upper}} = z_{\text{fug}} + z_{\text{fuc}} - \frac{H}{2} = \frac{H}{4}\left(2 + \cos\frac{\pi x}{2\lambda L} - \cos\frac{\pi y}{2W}\right) \tag{4.13}$$

By taking the partial derivative of Eq. (4.12) or (4.13) with respect to y, the waviness or the undulation angle of any material point on the fill yarn with respect to the XOY plane can be determined, as follows:

$$\theta_{\text{fill}} = \tan^{-1}\left(\frac{\partial z_{\text{fill}}^{\text{lower}}}{\partial y}\right) = \tan^{-1}\left(\frac{\pi H}{8W}\sin\frac{\pi y}{2W}\right) \tag{4.14}$$

Based on the above equations, the volume of the warp yarn, the volume of the fill yarn and the overall yarn volume fraction can be calculated, as follows:

$$V_{\text{warp}} = L\int_0^{\lambda W}(z_{\text{wuc}} - z_{\text{wlc}})dx = \frac{\lambda LWH}{\pi} \tag{4.15}$$

$$V_{\text{fill}} = W\int_0^{\lambda L}(z_{\text{fuc}} - z_{\text{flc}})dx = \frac{\lambda LWH}{\pi} \tag{4.16}$$

$$v_{\text{yarn}} = \left(V_{\text{warp}} + V_{\text{fill}}\right)/V_{\text{cell}} = \frac{2\lambda}{\pi} \tag{4.17}$$

4.2.3 Choice of parameter λ
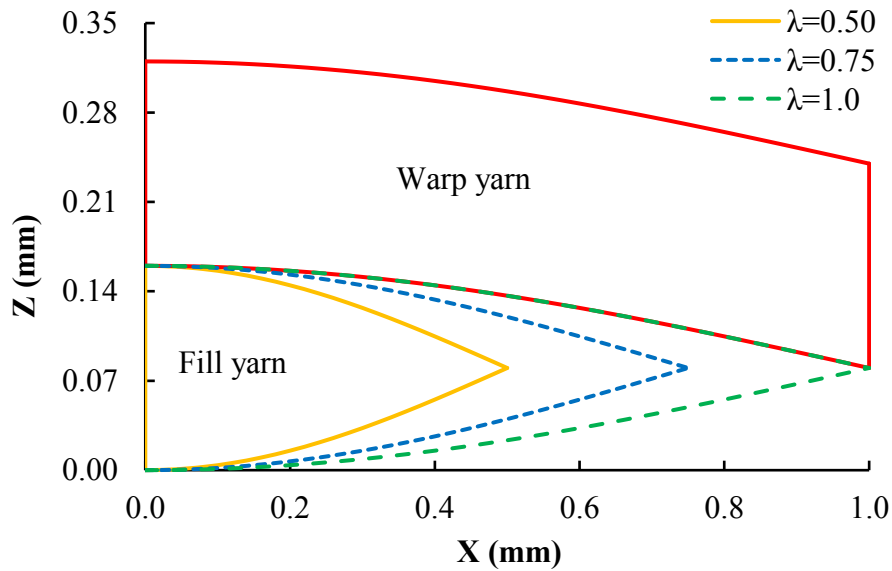
Figure 4.12: Variation of on the shape and size of the yarn

It should be noted that the dimensionless parameter, λ, must satisfy the condition of $0 < \lambda \leq 1$ since the widths of the yarns must be no larger than the corresponding dimensions

of the UC, i.e. $\lambda W \leq W$ or $\lambda L \leq L$. Fig. 4.12 shows the variation of λ on the shape and size of the cross-section of the fill yarn. It is evident from this figure that the width of the fill yarn increases as the value of λ is increased. In addition, when the value of λ reaches its upper limit (i.e. 1.0), the upper cross-sectional curve of the fill yarn coincides with the lower guide curve of the warp yarn.

4.3 Normal mUC for 2/2 twill woven composites

The UC developed for 2/2 twill woven composites is shown in Fig. 4.13. This model is a normal mUC obtained after performing the three-step reduction operations illustrated in Fig. 4.14. Firstly, a single layer of twill woven composites is quartered after exploiting its translational symmetries, leading to a full-size UC. Secondly, by using the reflectional and rotational symmetries, the full-size UC is quartered into a $\frac{1}{4}$UC. Finally, exploiting the symmetries in the $\frac{1}{4}$UC leads to a $\frac{1}{16}$UC, which is the mUC shown in Fig. 4.13.
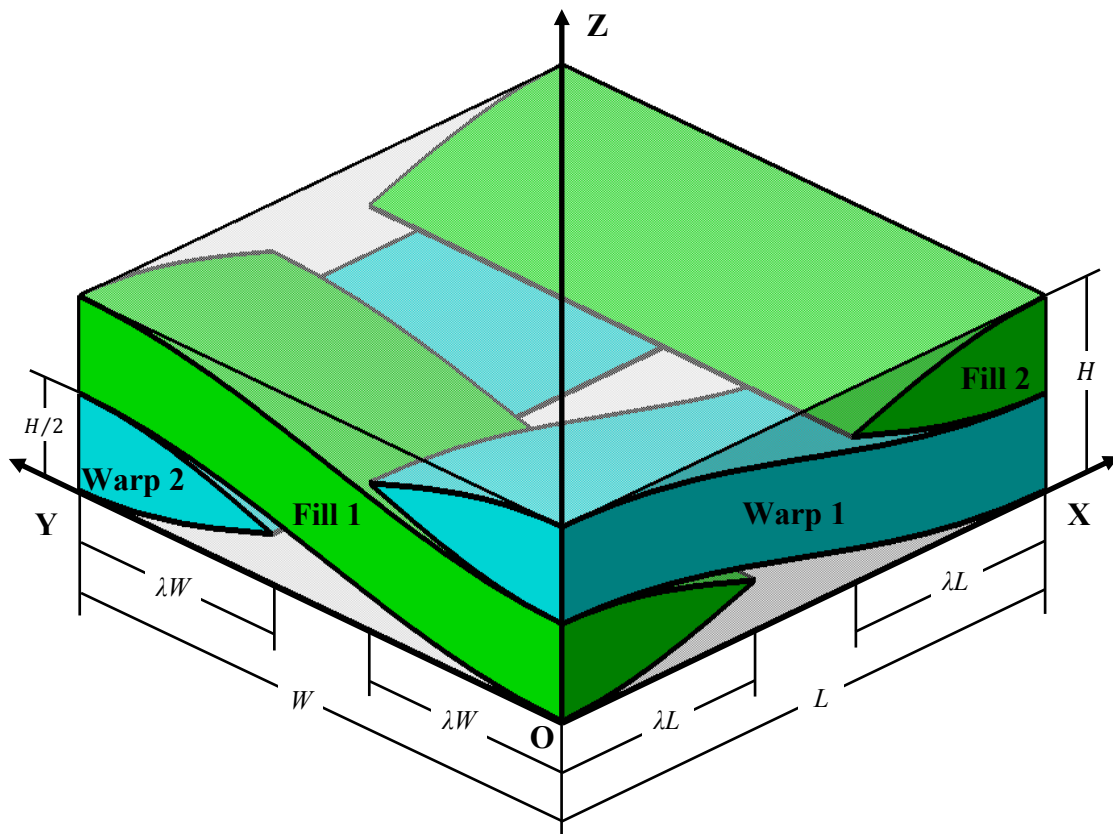
Figure 4.13: The proposed mUC model for 2/2 twill woven composites
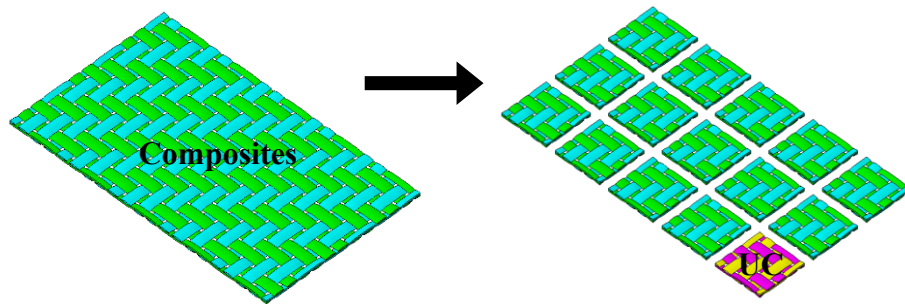
(a) Composite ply to full-size UC by using translational symmetries
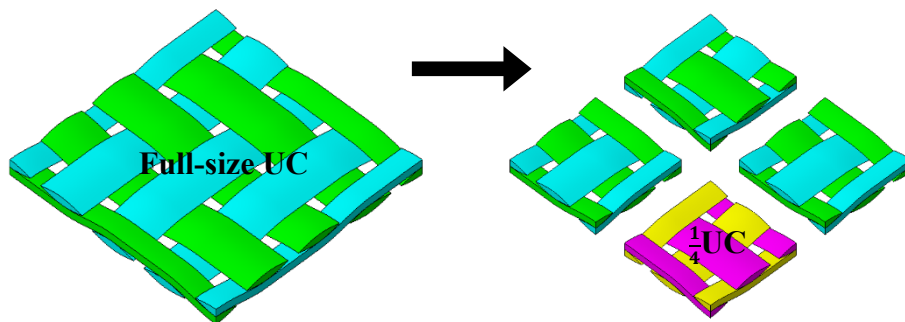
(b) Full-size UC to $\frac{1}{4}$UC by using reflectional and rotational symmetries
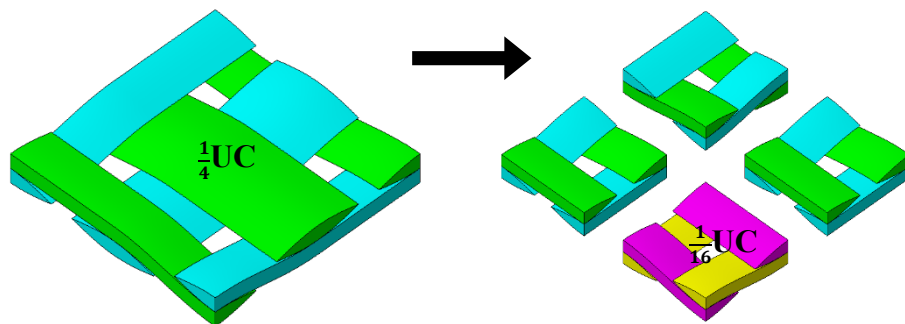
(c) $\frac{1}{4}$UC to $\frac{1}{16}$UC by using reflectional and rotational symmetries

Figure 4.14: Domain reduction for 2/2 twill woven composites

The geometry configuration of the mUC model for twill woven composites is shown in Fig. 4.13. In this figure, L, W and H stand for the length, width and height of the UC, and the dimensionless parameter, λ, is defined as the ratio of the half width of the warp yarns (λW) or the fill yarns (λL) to the width (W) or length (L) of the UC. To prevent any interpenetration between adjacent yarns, the dimensionless parameter should be no larger than 0.5. In addition, all the yarns are assumed to have a maximum thickness of $H/2$.

4.3.1 Warp yarn 1 ($0 \leq y \leq \lambda W$)

Based on the assumptions in Section 4.1 and the geometry configuration shown in Fig. 4.13, the lower and upper cross-sectional and guide curves of warp yarn 1, as shown in Fig. 4.15, can be described using the following equations:

$$z_{\text{w1lc}} = \frac{3H}{4} - \frac{H}{4}\cos\frac{\pi y}{2\lambda W} \tag{4.18}$$

$$z_{\text{w1uc}} = \frac{3H}{4} + \frac{H}{4}\cos\frac{\pi y}{2\lambda W} \tag{4.19}$$

$$z_{\text{w1lg}} = \frac{H}{4} + \frac{H}{4}\cos\frac{\pi x}{L} \tag{4.20}$$

$$z_{\text{w1ug}} = \frac{3H}{4} + \frac{H}{4}\cos\frac{\pi x}{L} \tag{4.21}$$
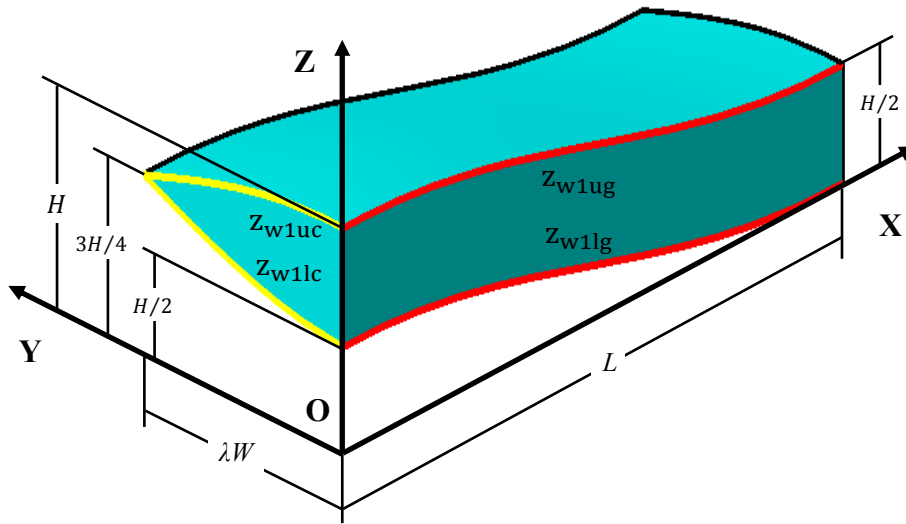
Figure 4.15: Warp yarn 1 of the proposed mUC for twill woven composites

By considering the above four equations, the equations for describing the lower and upper surfaces of warp yarn 1 can be obtained, as follows:

$$z_{\text{warp1}}^{\text{lower}} = z_{\text{w1lg}} + z_{\text{w1lc}} - \frac{H}{2} = \frac{H}{4}\left(2 + \cos\frac{\pi x}{L} - \cos\frac{\pi y}{2\lambda W}\right) \tag{4.22}$$

$$z_{\text{warp1}}^{\text{upper}} = z_{\text{w1ug}} + z_{\text{w1uc}} - H = \frac{H}{4}\left(2 + \cos\frac{\pi x}{L} + \cos\frac{\pi y}{2\lambda W}\right) \tag{4.23}$$

98

By taking the partial derivative of Eq. (4.22) or (4.23) with respect to x, the waviness or the undulation angle of any material point on warp yarn 1 with respect to the XOY plane can be determined, as follows:

$$\theta_{\text{warp1}} = \tan^{-1}\left(\frac{\partial z_{\text{warp1}}^{\text{lower}}}{\partial x}\right) = \tan^{-1}\left(-\frac{\pi H}{4L}\sin\frac{\pi x}{L}\right) \tag{4.24}$$

4.3.2 Warp yarn 2 ($W\text{-}\lambda W \leq y \leq W$)

The geometry configuration of the second warp yarn is illustrated in Fig. 4.16, where the $X^1O^1Z^1$ plane denotes plane $Y = W - \lambda W$. It can be seen from this figure that there is no presence of waviness in this yarn. This indicates that the equations for describing the lower and upper surfaces are essentially those for describing the lower and upper cross-sectional curves, as follows:

$$z_{\text{warp2}}^{\text{lower}} = z_{\text{w2lc}} = \frac{H}{4} - \frac{H}{4}\cos\left(\frac{\pi y}{2\lambda W} - \frac{\pi}{2\lambda}\right) \tag{4.25}$$

$$z_{\text{warp2}}^{\text{upper}} = z_{\text{w2uc}} = \frac{H}{4} + \frac{H}{4}\cos\left(\frac{\pi y}{2\lambda W} - \frac{\pi}{2\lambda}\right) \tag{4.26}$$
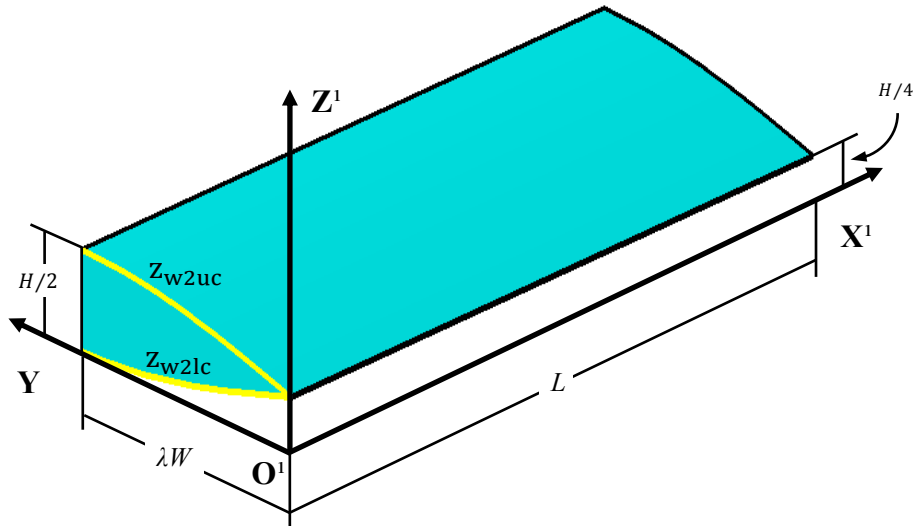
Figure 4.16: Warp yarn 2 of the proposed mUC for twill woven composites

4.3.3 Fill yarn 1 ($0 \leq x \leq \lambda L$)

Similar to warp yarn 1, the lower and upper cross-sectional and guide curves of fill yarn 1, as shown in Fig. 4.17, can be described using the following four equations:
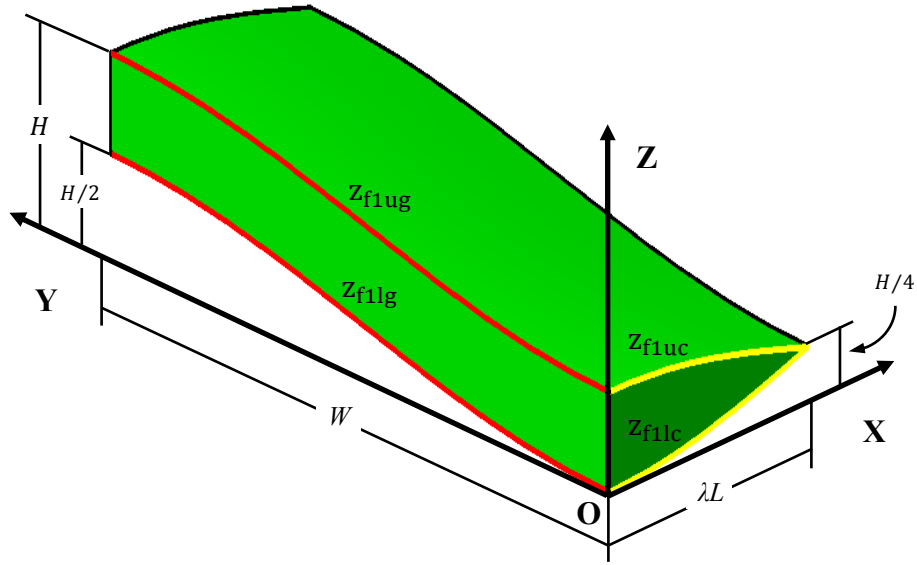
Figure 4.17: Fill yarn 1 of the proposed mUC for twill woven composites

$$z_{\text{f1lc}} = \frac{H}{4} - \frac{H}{4}\cos\frac{\pi x}{2\lambda L} \tag{4.27}$$

$$z_{\text{f1uc}} = \frac{H}{4} + \frac{H}{4}\cos\frac{\pi x}{2\lambda L} \tag{4.28}$$

$$z_{\text{f1lg}} = \frac{H}{4} - \frac{H}{4}\cos\frac{\pi y}{W} \tag{4.29}$$

$$z_{\text{f1ug}} = \frac{3H}{4} - \frac{H}{4}\cos\frac{\pi y}{W} \tag{4.30}$$

By combining the above four equations, the equations for describing the lower and upper surfaces of fill yarn 1 can be derived, as follows:

$$z_{\text{fill1}}^{\text{lower}} = z_{\text{f1lg}} + z_{\text{f1lc}} = \frac{H}{4}\left(2 - \cos\frac{\pi x}{2\lambda L} - \cos\frac{\pi y}{W}\right) \tag{4.31}$$

$$z_{\text{fill1}}^{\text{upper}} = z_{\text{f1ug}} + z_{\text{f1uc}} - \frac{H}{2} = \frac{H}{4}\left(2 + \cos\frac{\pi x}{2\lambda L} - \cos\frac{\pi y}{W}\right) \tag{4.32}$$

By taking the partial derivative of Eq. (4.31) or (4.32) with respect to y, the waviness or the undulation angle of any material point on fill yarn 1 with respect to the XOY plane can be determined as follows:

$$\theta_{\text{fill1}} = \tan^{-1}\left(\frac{\partial z_{\text{fill1}}^{\text{lower}}}{\partial y}\right) = \tan^{-1}\left(\frac{\pi H}{4W}\sin\frac{\pi y}{W}\right) \tag{4.33}$$

100

4.3.4 Fill yarn 2 (L-λL ≤ x ≤ L)
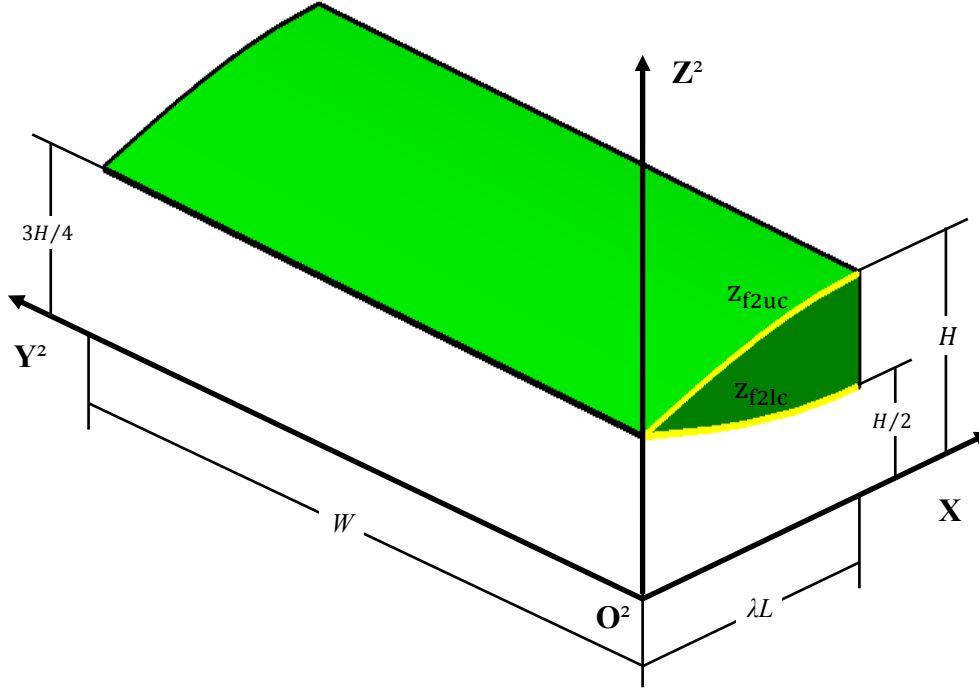
Figure 4.18: Fill yarn 2 of the proposed mUC for twill woven composites

In terms of the second fill yarn, as shown in Fig. 4.18, where the $X^2O^2Z^2$ plane denotes plane $X = L - \lambda L$, there is again no presence of waviness in this yarn. Thus, its lower and upper surfaces can be described directly using the equations for describing the lower and upper cross-sectional curves on the $X\,O^2Z^2$ plane, as follows:

$$z_{\text{fill2}}^{\text{lower}} = z_{\text{f2lc}} = \frac{3H}{4} - \frac{H}{4}\cos\left(\frac{\pi x}{2\lambda L} - \frac{\pi}{2\lambda}\right) \tag{4.34}$$

$$z_{\text{fill2}}^{\text{upper}} = z_{\text{f2uc}} = \frac{3H}{4} + \frac{H}{4}\cos\left(\frac{\pi x}{2\lambda L} - \frac{\pi}{2\lambda}\right) \tag{4.35}$$

Based on the above equations, the volumes of the warp yarns, the volumes of the fill yarns and the overall yarn volume fraction can be calculated, as follows:

$$V_{\text{warp2}} = V_{\text{warp1}} = L \int_0^{\lambda W}(z_{\text{w1uc}} - z_{\text{w1lc}})dx = \frac{\lambda LWH}{\pi} \tag{4.36}$$

$$V_{\text{fill2}} = V_{\text{fill1}} = W \int_0^{\lambda L}(z_{\text{f1uc}} - z_{\text{f1lc}})dx = \frac{\lambda LWH}{\pi} \tag{4.37}$$

$$v_{\text{yarn}} = \left(V_{\text{warp1}} + V_{\text{warp2}} + V_{\text{fill1}} + V_{\text{fill2}}\right)/V_{\text{cell}} = \frac{4\lambda}{\pi} \tag{4.38}$$

4.4 Normal mUC for 3D woven composites
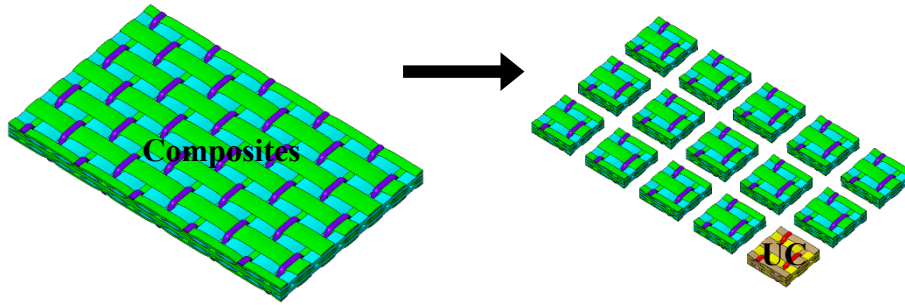
(a) Composite ply to full-size UC by using translational symmetries only
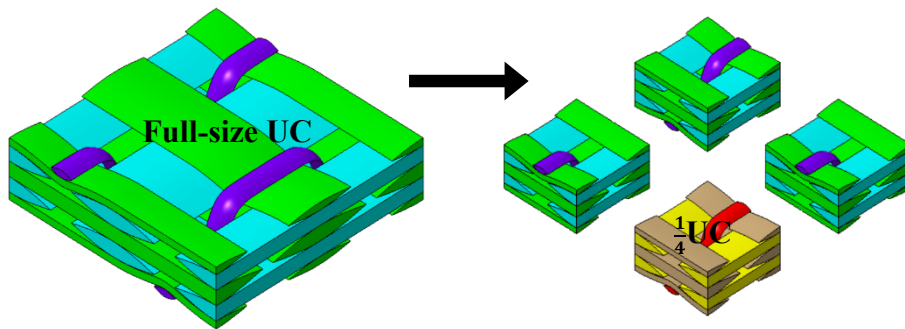
(b) Full-size UC to $\frac{1}{4}$UC by using reflectional symmetries only
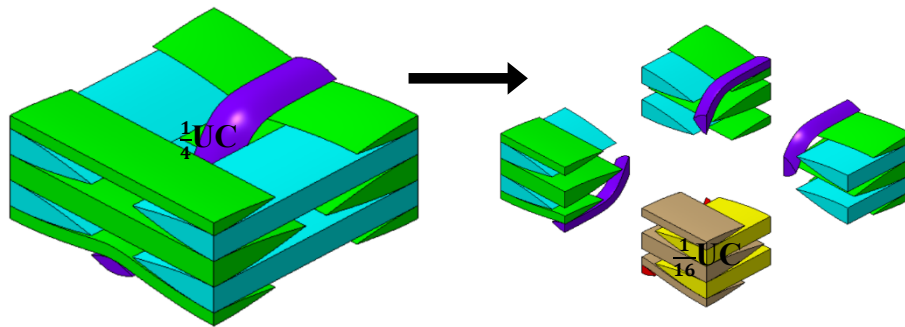
(c) $\frac{1}{4}$UC → $\frac{1}{16}$UC by using reflectional and rotational symmetries

Figure 4.19: Domain reduction for 3D orthogonal woven composites

For three-dimensional (3D) orthogonal woven composites, the mUC can be derived after performing the domain reduction operations demonstrated in Fig. 4.19. Specifically, a full-size UC is firstly obtained by exploiting the translational symmetries in the composite ply. Secondly, the full-size UC can be reduced based on its reflectional and rotational

symmetries, which leads to a $\frac{1}{4}$UC. Finally, exploiting both the reflectional and rotational symmetries of the $\frac{1}{4}$UC yields a $\frac{1}{16}$UC, which is the mUC model that will be used to model the geometry of 3D orthogonal woven composites.

At the level of mUC, Li *et al.* [145] developed a sophisticated model for predicting the elastic properties of 3D orthogonal woven composites. In their model, as shown in Fig. 4.20, the cross-sections of the two warp yarns and the middle fill yarn, which are straight within the mUC, were assumed to be elliptical. For the lowest and highest fill yarns, they were modelled by utilising an arctangent function to describe one of the cross-sectional curves and a parabolic function to describe the other. In addition, the lowest fill yarn was assumed to be comprised of a straight part and a wavy part, with the waviness of the wavy part being described using a sine function. In terms of the binder yarn, its cross-section was assumed to be elliptical, and the waviness of the middle guide curve was described using an arctangent function.
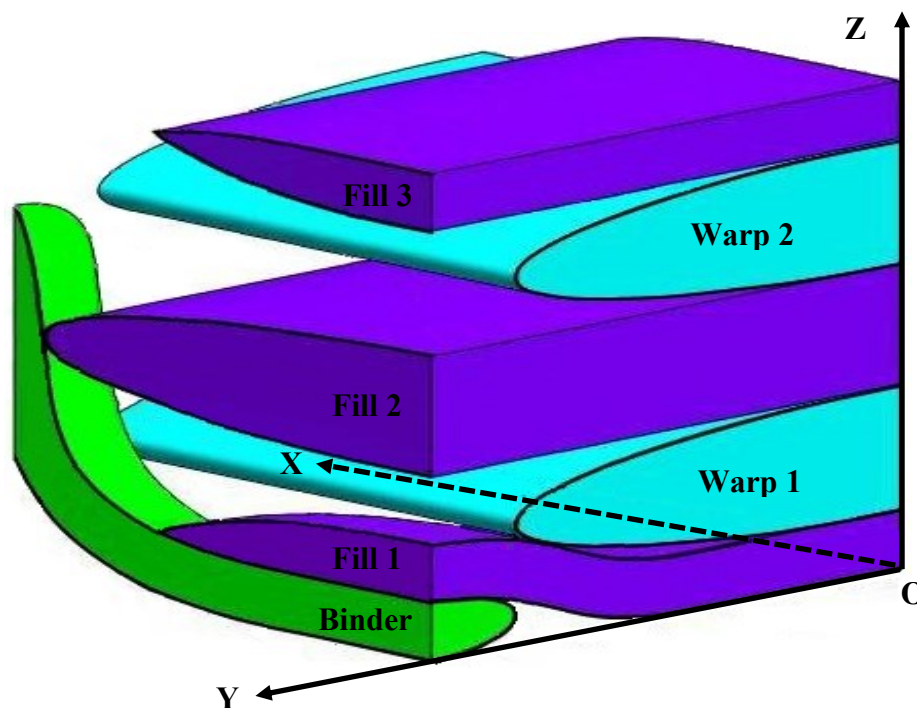
Figure 4.20: An mUC for 3D orthogonal woven composites (by Li *et al.* [145])

A small drawback of the above mUC model is that the use of different types of functions to describe the lower and upper cross-sectional curves of the lowest and highest fill yarns creates asymmetrical cross-sections, which is technically undesirable. In addition, this

UC model does not permit space between the adjacent yarns in the warp direction. For example, no space was assumed between the binder yarn and fill yarn 2. A problem of such a design is that it reduces the flexibility of accommodating the mUC model for the 3D woven composites with loose weave pattern. Furthermore, for the sake of the lowest fill yarn interlacing with warp yarn 1 and the binder yarn, the use of a straight part and a wavy part produces a pocket between the fill yarn and warp yarn 1, which is obviously undesirable. Finally, the equations defined for the binder yarn produce lower values of the thickness in the regions with high waviness. A consequence of such a design is the presence of a high variation in the cross-section of the binder yarn, leaving the assumption of a constant cross-sectional shape being not satisfied exactly.
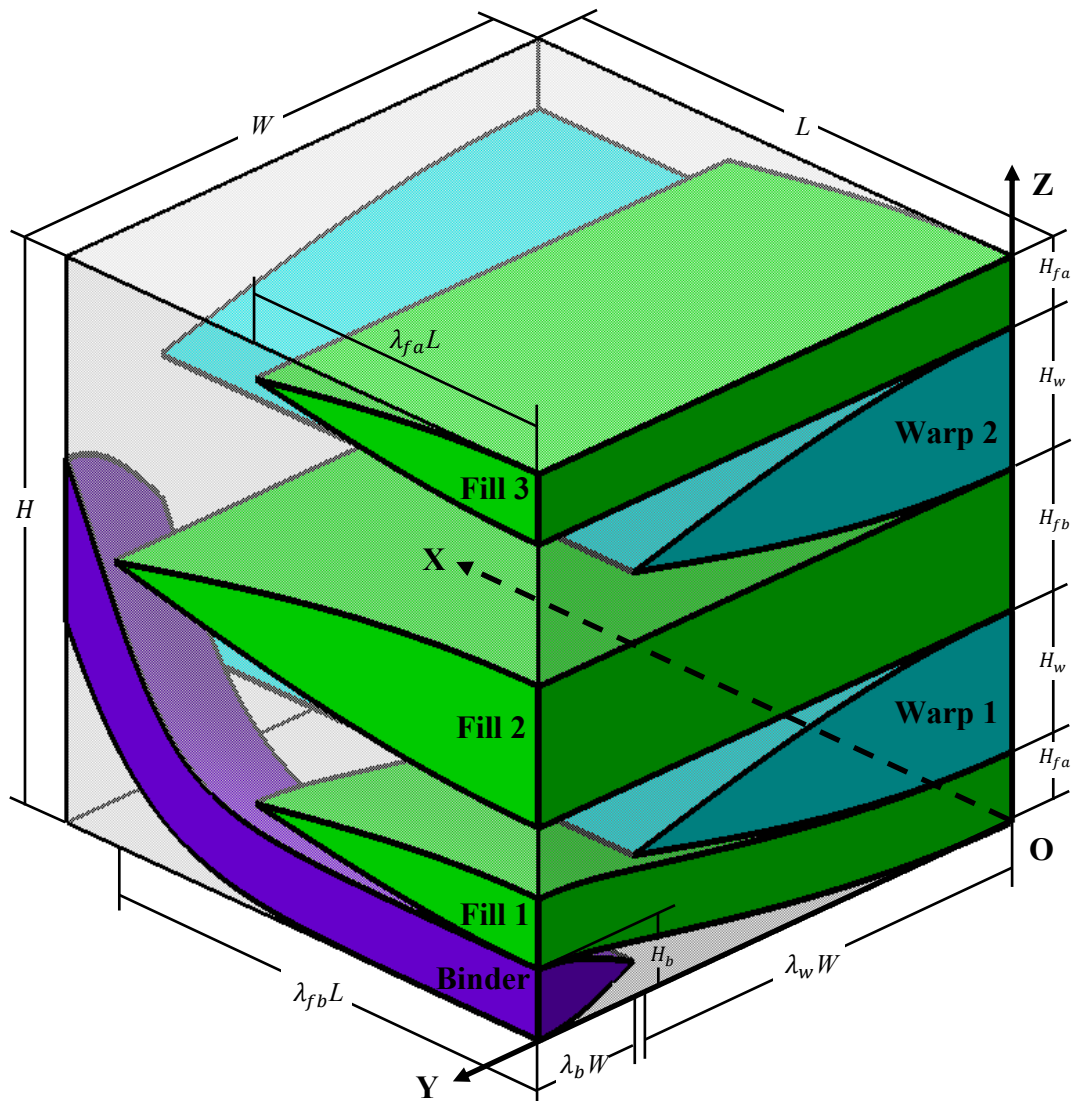
Figure 4.21: The improved mUC model for 3D orthogonal woven composites

In the present research, an improved mUC has been developed to avoid the drawbacks discussed above. In the improved model, as demonstrated in Fig. 4.21, the problem of asymmetrical cross-sections is avoided by using cosine functions to describe both the lower and upper cross-sectional curves of all the yarns. In addition, four coefficients, λ_w, λ_{fa}, λ_{fb} and λ_b, the meaning of which will be listed later at the end of this paragraph, are utilised to improve the flexibility of the mUC in terms of forming gaps between adjacent yarns if needed. Furthermore, in order to avoid the problem of creating a pocket between the lowest fill yarn and warp yarn 1, the lowest fill yarn is assumed to consist of two wavy parts that match with both the binder yarn and warp yarn 1, respectively. In terms of the binder yarn, its waviness is described based on the middle guide curve using a hyperbolic tangent function, and the requirement of a constant cross-sectional shape is ensured by including a coordinate-dependent term when developing the equations for describing the lower and upper guide curves, which will be addressed later. To be concise, the meanings of the symbols in Fig. 4.21 are summarised as follows:

$L \rightarrow$ Overall length of the mUC

$W \rightarrow$ Overall width of the mUC

$H \rightarrow$ Overall height of the mUC

$\lambda_w \rightarrow$ The ratio of the half width ($\lambda_w W$) of warp yarn 1 or 2 to W

$\lambda_{fa} \rightarrow$ The ratio of the half width ($\lambda_{fa} L$) of fill yarn 1 or 3 to L

$\lambda_{fb} \rightarrow$ The ratio of the half width ($\lambda_{fb} L$) of fill yarn 2 to L

$\lambda_b \rightarrow$ The ratio of the half width ($\lambda_b W$) of the binder yarn to W

$H_w \rightarrow$ The maximum thickness of warp yarn 1 or 2

$H_{fa} \rightarrow$ The maximum thickness of fill yarn 1 or 3

$H_{fb} \rightarrow$ The maximum thickness of fill yarn 2

$H_b \rightarrow$ The maximum thickness of the binder yarn

4.4.1 Warp yarn 1 ($0 \leq y \leq \lambda_w W$)
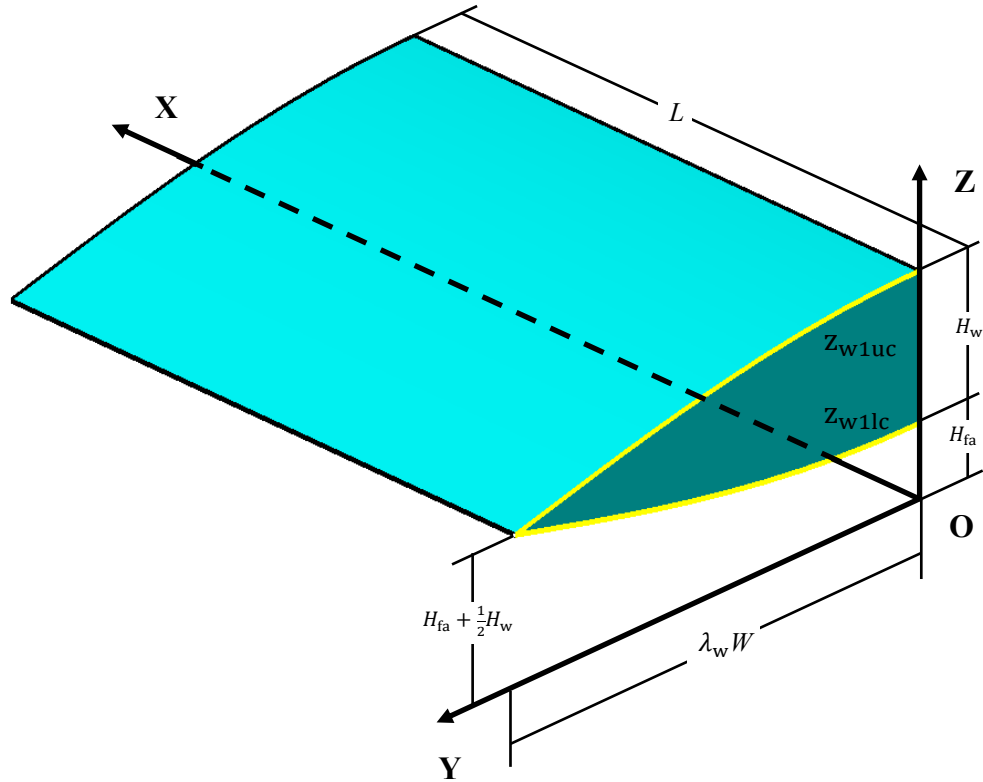
Figure 4.22: Warp yarn 1 of the improved mUC for 3D woven composites

The lower warp yarn (i.e. warp yarn 1) of the mUC is a straight yarn, as shown in Fig. 4.22. Therefore, its lower and upper surfaces can be described directly using the lower and upper cross-sectional curves, as follows:

$$z_{\text{warp1}}^{\text{lower}} = z_{\text{w1lc}} = H_{\text{fa}} + \frac{H_w}{2} - \frac{H_w}{2}\cos\left(\frac{\pi y}{2\lambda_w W}\right) \tag{4.39}$$

$$z_{\text{warp1}}^{\text{upper}} = z_{\text{w1uc}} = H_{\text{fa}} + \frac{H_w}{2} + \frac{H_w}{2}\cos\left(\frac{\pi y}{2\lambda_w W}\right) \tag{4.40}$$

4.4.2 Warp yarn 2 ($0 \leq y \leq \lambda_w W$)

The upper warp yarn (i.e. warp yarn 2) is also a straight one, as shown in Fig. 4.23, where $H_t = H_{\text{fb}} + H_w$. Again, its surfaces can be described based on the cross-sectional curves. However, since it has exactly the same geometry as warp yarn 1 and can be treated as a result of translating warp yarn 1 for a distance of H_t in the Z direction, its lower and upper surfaces can be described directly as follows:

$$z_{\text{warp2}}^{\text{lower}} = z_{\text{w2lc}} = H_{\text{fa}} + H_{\text{fb}} + \frac{3H_{\text{w}}}{2} - \frac{H_{\text{w}}}{2}\cos\left(\frac{\pi y}{2\lambda_{\text{w}}W}\right) \qquad (4.41)$$

$$z_{\text{warp2}}^{\text{upper}} = z_{\text{w2uc}} = H_{\text{fa}} + H_{\text{fb}} + \frac{3H_{\text{w}}}{2} + \frac{H_{\text{w}}}{2}\cos\left(\frac{\pi y}{2\lambda_{\text{w}}W}\right) \qquad (4.42)$$
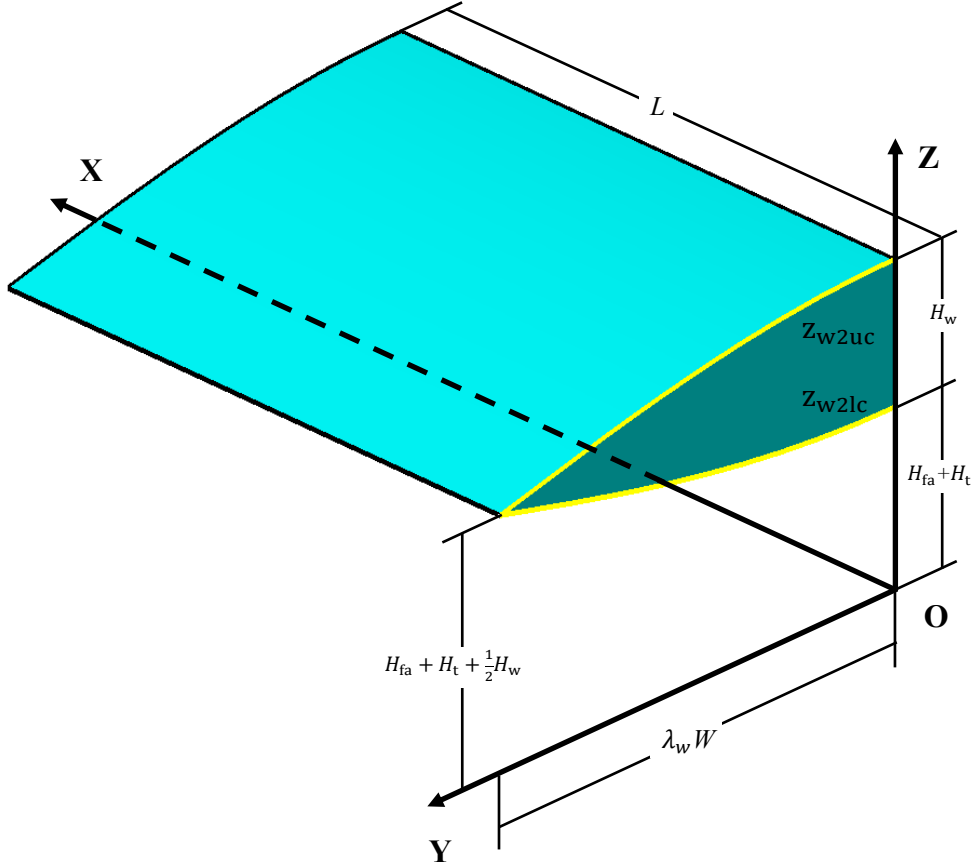
Figure 4.23: Warp yarn 2 of the improved mUC for 3D woven composites

4.4.3 Fill yarn 1 ($0 \leq x \leq \lambda_{\text{fa}}L$)

For the lowest fill yarn (i.e. fill yarn 1), as highlighted in Fig. 4.24, it consists of two wavy parts, which should be described separately. However, as the yarn has been assumed to have a constant cross-sectional shape, the lower and upper cross-sectional curves of both parts on plane $Y = W$ can be described using the same set of equations, as follows:

$$z_{\text{f1lc}} = H_{\text{b}} + \frac{H_{\text{fa}}}{2} - \frac{H_{\text{fa}}}{2}\cos\left(\frac{\pi x}{2\lambda_{\text{fa}}L}\right) \qquad (4.43)$$

$$z_{\text{f1uc}} = H_{\text{b}} + \frac{H_{\text{fa}}}{2} + \frac{H_{\text{fa}}}{2}\cos\left(\frac{\pi x}{2\lambda_{\text{fa}}L}\right) \qquad (4.44)$$
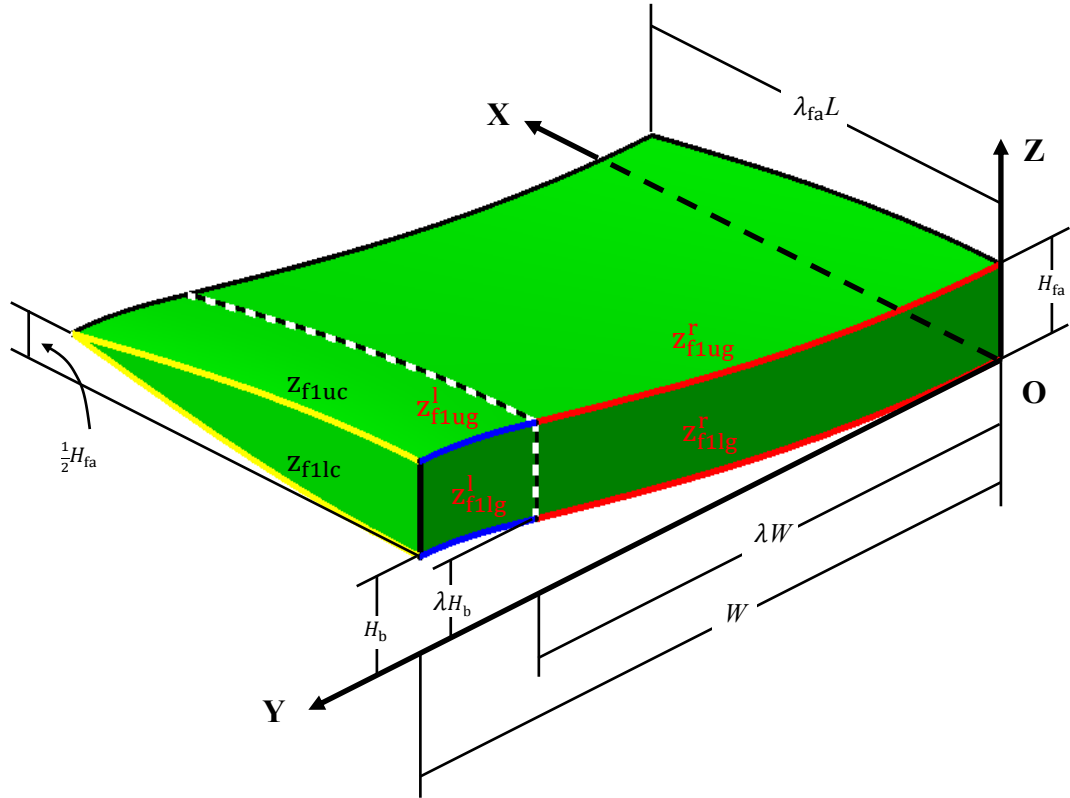
Figure 4.24: Fill yarn 1 of the improved mUC for 3D woven composites

To describe the surfaces of both parts of fill yarn 1, the waviness of each part and the ratio of the length of each part to that of the whole yarn need to be determined. In this work, the division of this yarn is controlled by a dimensionless parameter, λ. It is assumed that the right wavy part has a length of λW and a guide curve height of λH_b, and the left wavy part has a length of $(1 - \lambda)W$ and a guide curve height of $(1 - \lambda)H_b$, as shown in Fig. 4.24. To ensure a smooth transition from the right wavy part to the left wavy part and at the same time to maintain a reasonable match of fill yarn 1 with both the warp and binder yarns, it is further assumed that the ratio of the length of the right wavy part to that of the left wavy part is equal to the ratio of the width of warp yarn 1 to that of the binder yarn, which leads to the following relation:

$$\frac{\lambda W}{(1-\lambda)W} = \frac{\lambda_w W}{\lambda_b W} \tag{4.45}$$

Solving this equation yields the value of the dimensionless parameter:

$$\lambda = \frac{\lambda_w}{\lambda_b + \lambda_w} \tag{4.46}$$

4.4.3.1 Right wavy part of fill yarn 1 ($0 \leq y \leq \lambda W$)

Based on the above assumptions and those in Section 4.1, the equations for describing the lower and upper guide curves of the right wavy part can be obtained, as follows:

$$z^{r}_{f1lg} = \lambda H_{b} - \lambda H_{b} \cos\left(\frac{\pi y}{2\lambda W}\right) \tag{4.47}$$

$$z^{r}_{f1ug} = H_{fa} + \lambda H_{b} - \lambda H_{b} \cos\left(\frac{\pi y}{2\lambda W}\right) \tag{4.48}$$

By combining the above two equations with Eqs. (4.43) and (4.44), the lower and upper surfaces of the right wavy part of fill yarn 1 can be described, as follows:

$$z^{r,lower}_{fill1} = z_{f1lc} + z^{r}_{f1lg} - H_{b} \tag{4.49}$$

$$z^{r,upper}_{fill1} = z_{f1uc} + z^{r}_{f1ug} - (H_{fa} + H_{b}) \tag{4.50}$$

Expanding the above two equations gives:

$$z^{r,lower}_{fill1} = \frac{H_{fa}}{2} + \lambda H_{b} - \frac{H_{fa}}{2} \cos\left(\frac{\pi x}{2\lambda_{fa}L}\right) - \lambda H_{b} \cos\left(\frac{\pi y}{2\lambda W}\right) \tag{4.51}$$

$$z^{r,upper}_{fill1} = \frac{H_{fa}}{2} + \lambda H_{b} + \frac{H_{fa}}{2} \cos\left(\frac{\pi x}{2\lambda_{fa}L}\right) - \lambda H_{b} \cos\left(\frac{\pi y}{2\lambda W}\right) \tag{4.52}$$

By taking the partial derivative of Eq. (4.51) or (4.52) with respect to y, the waviness or the undulation angle of any material point on the right wavy part of fill yarn 1 with respect to the XOY plane can be determined, as follows:

$$\theta^{r}_{fill1} = \tan^{-1}\left(\frac{\partial z^{r,lower}_{fill1}}{\partial y}\right) = \tan^{-1}\left(\frac{\pi H_{b}}{2W} \sin\left(\frac{\pi y}{2\lambda W}\right)\right) \tag{4.53}$$

4.4.3.2 Left wavy part of fill yarn 1 ($\lambda W \leq y \leq W$)

Similarly, the equations for describing the lower and upper guide curves of the left wavy part can be formulated, as follows:

$$z^{l}_{f1lg} = \lambda H_{b} + (1-\lambda)H_{b} \cos\left(\frac{\pi(y-W)}{2(1-\lambda)W}\right) \tag{4.54}$$

$$z^{l}_{f1ug} = H_{fa} + \lambda H_{b} + (1-\lambda)H_{b} \cos\left(\frac{\pi(y-W)}{2(1-\lambda)W}\right) \tag{4.55}$$

By combining the above two equations with Eqs. (4.43) and (4.44), the lower and upper surfaces of the left wavy part of fill yarn 1 can be described, as follows:

$$z_{\text{fill1}}^{\text{l,lower}} = z_{\text{f1lc}} + z_{\text{f1lg}}^{\text{l}} - H_{\text{b}} \tag{4.56}$$

$$z_{\text{fill1}}^{\text{l,upper}} = z_{\text{f1uc}} + z_{\text{f1ug}}^{\text{l}} - (H_{\text{fa}} + H_{\text{b}}) \tag{4.57}$$

Expanding the above two equations gives:

$$z_{\text{fill1}}^{\text{l,lower}} = \frac{H_{\text{fa}}}{2} + \lambda H_{\text{b}} - \frac{H_{\text{fa}}}{2}\cos\left(\frac{\pi x}{2\lambda_{\text{fa}}L}\right) + (1-\lambda)H_{\text{b}}\cos\left(\frac{\pi(y-W)}{2(1-\lambda)W}\right) \tag{4.58}$$

$$z_{\text{fill1}}^{\text{l,upper}} = \frac{H_{\text{fa}}}{2} + \lambda H_{\text{b}} + \frac{H_{\text{fa}}}{2}\cos\left(\frac{\pi x}{2\lambda_{\text{fa}}L}\right) + (1-\lambda)H_{\text{b}}\cos\left(\frac{\pi(y-W)}{2(1-\lambda)W}\right) \tag{4.59}$$

By taking the partial derivative of Eq. (4.58) or (4.59) with respect to y, the waviness or the undulation angle of any material point on the left wavy part of fill yarn 1 with respect to the XOY plane can be determined as follows:

$$\theta_{\text{fill1}}^{\text{l}} = \tan^{-1}\left(\frac{\partial z_{\text{fill1}}^{\text{l,lower}}}{\partial y}\right) = \tan^{-1}\left(-\frac{\pi H_{\text{b}}}{2W}\sin\left(\frac{\pi(y-W)}{2(1-\lambda)W}\right)\right) \tag{4.60}$$

4.4.3.3 Comparison with the original formulation

In order to demonstrate the improvement that has been achieved in modelling fill yarn 1, the intersections of fill yarn 1, warp yarn 1 and the binder yarn with the YOZ plane are visualised in Fig. 4.25a, where the intersection of the binder yarn with the plane is plotted based on Eqs. (4.65) and (4.66), which will be presented later in Section 4.4.6. For comparison, the intersections based on the formulation developed by Li *et al.* [145] are also drawn and shown in Fig. 4.25b. It should be noted that the same set of parameters was used to generate the figures, and the parameters were $W = 2.54$, $H_{\text{b}} = 0.292$, $H_{\text{fa}} = 0.292$, $H_{\text{w}} = 0.637$, $\lambda_{\text{w}}W = 2.086$ and $\lambda_{\text{b}}W = 0.454$.

As is clearly shown in Fig. 4.25, the improved formulation is able to produce a smoother transition in the waviness of fill yarn 1, compared to the original formulation. More importantly, the undesirable pocket between the fill yarn and the warp yarn has been successfully eliminated by using the improved formulation.
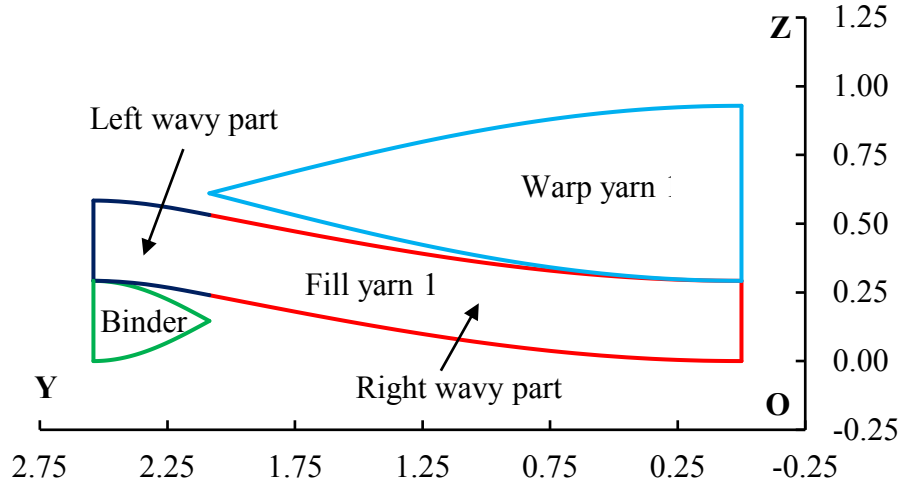
(a) Intersections plotted based on the improved formulation
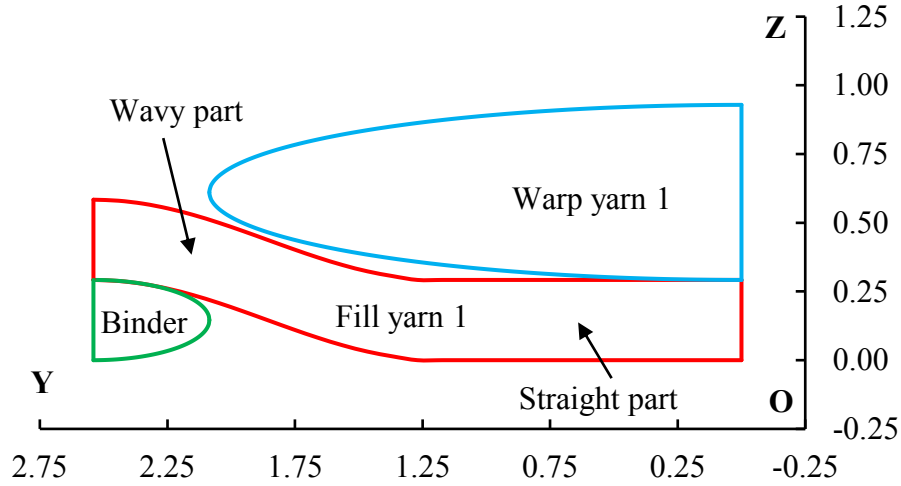
(b) Intersections drawn based on the formulation by Li *et al.* [145]

Figure 4.25: Comparison of the intersections of the two formulations

4.4.4 Fill yarn 2 $(0 \leq x \leq \lambda_{fb}L)$

The middle fill yarn (i.e. fill yarn 2) is a straight yarn, as shown in Fig. 4.26. Therefore, its lower and upper surfaces can be described directly using the equations for the lower and upper cross-sectional curves, as follows:

$$z_{fill2}^{lower} = z_{f2lc} = H_{fa} + H_w + \frac{H_{fb}}{2} - \frac{H_{fb}}{2}\cos\left(\frac{\pi x}{2\lambda_{fb}L}\right) \tag{4.61}$$

$$z_{fill2}^{upper} = z_{f2uc} = H_{fa} + H_w + \frac{H_{fb}}{2} + \frac{H_{fb}}{2}\cos\left(\frac{\pi x}{2\lambda_{fb}L}\right) \tag{4.62}$$

111
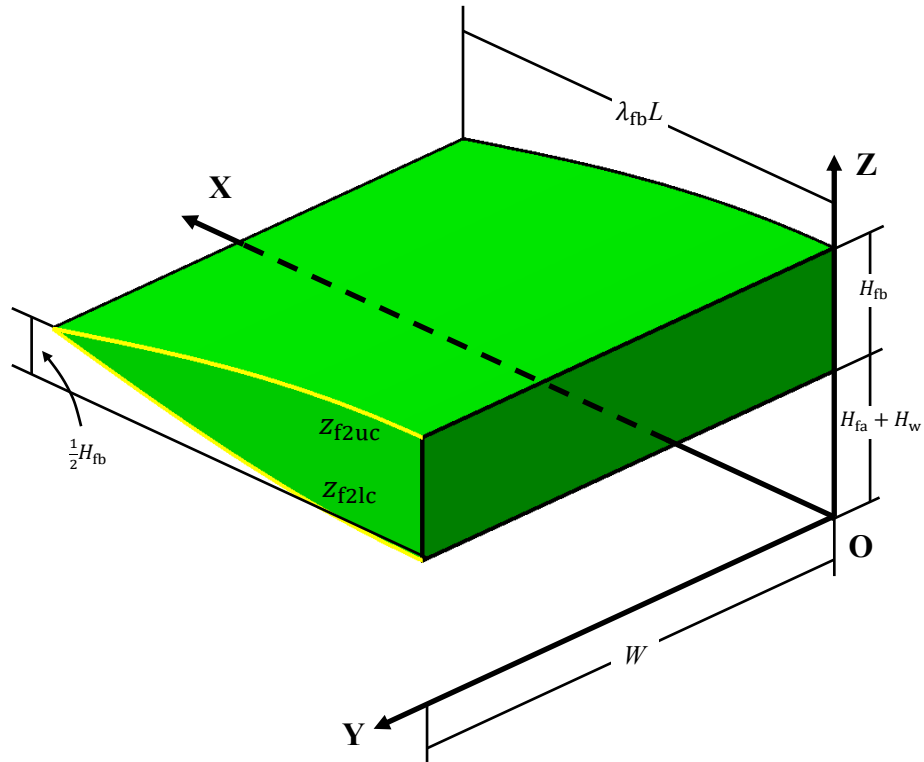
Figure 4.26: Fill yarn 2 of the improved mUC for 3D woven composites
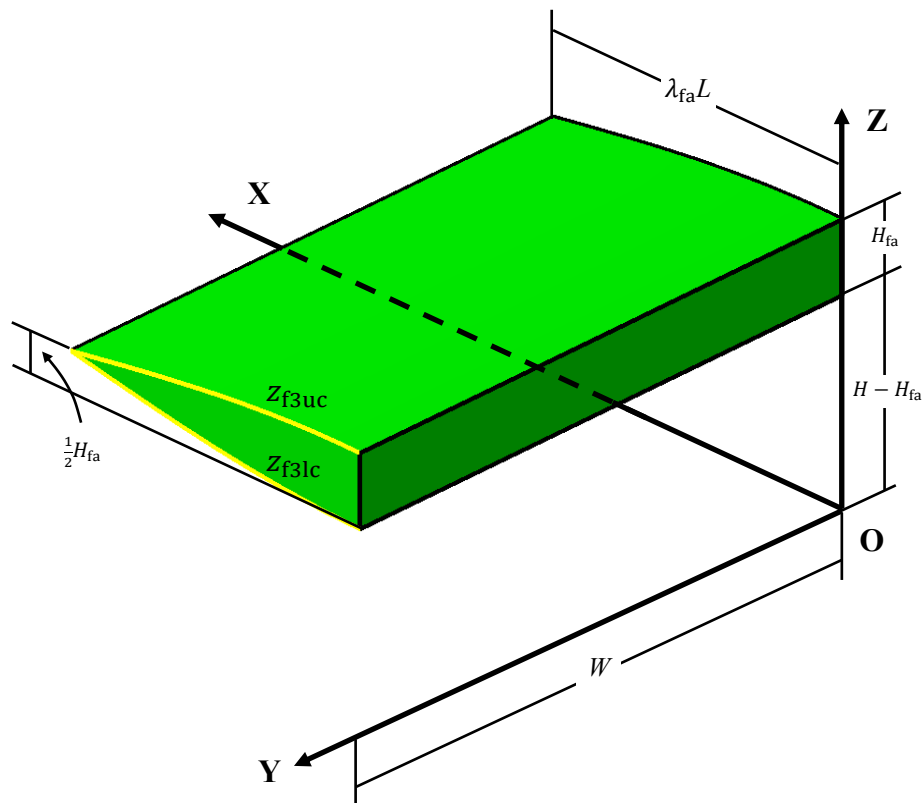
Figure 4.27: Fill yarn 3 of the improved mUC for 3D woven composites

4.4.5 Fill yarn 3 ($0 \leq x \leq \lambda_{fa}L$)

The highest fill yarn (i.e. fill yarn 3) is also a straight yarn, as shown Fig. 4.27. Thus, the lower and upper surfaces of this yarn can be described using the equations for the lower and upper cross-sectional curves, as follows:

$$z_{fill3}^{lower} = z_{f3lc} = H - \frac{H_{fa}}{2} - \frac{H_{fa}}{2} \cos\left(\frac{\pi x}{2\lambda_{fa}L}\right) \tag{4.63}$$

$$z_{fill3}^{upper} = z_{f3uc} = H - \frac{H_{fa}}{2} + \frac{H_{fa}}{2} \cos\left(\frac{\pi x}{2\lambda_{fa}L}\right) \tag{4.64}$$

4.4.6 Binder yarn ($W - \lambda_b W \leq y \leq W$)

According to the assumptions in Section 4.1 and the geometry configuration shown in Fig. 4.28, where the $X^1O^1Z^1$ plane stands for plane $Y = W$, the lower and upper cross-sectional curves of the binder yarn can be described as follows:

$$z_{blc} = \frac{H_b}{2} - \frac{H_b}{2} \cos\left(\frac{\pi(y-W)}{2\lambda_b W}\right) \tag{4.65}$$

$$z_{buc} = \frac{H_b}{2} + \frac{H_b}{2} \cos\left(\frac{\pi(y-W)}{\lambda_b W}\right) \tag{4.66}$$
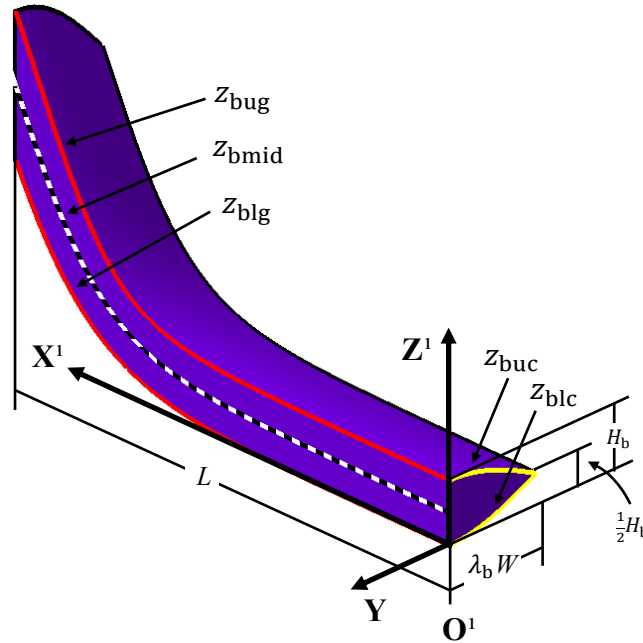
Figure 4.28: Binder yarn of the improved mUC for 3D woven composites

To facilitate the description of the waviness of the binder yarn, an extended binder yarn has been constructed based on the binder yarn shown in Fig. 4.28. In the extended yarn, as shown in Fig. 4.29, the extended part is a copy of the original part after performing a rotation of 180° with respect to the Y^1 axis. Clearly, in 3D orthogonal woven composites, the binder yarn is designed to bind warp and fill yarns together in the form of switching itself from one side of the ply to the other, as indicated in Fig. 4.29 or more clearly in Fig. 4.19. Such a switch requires the binder yarn to have a waviness with a significant variation in the middle region and minor variations in the remaining areas, suggesting that the initial assumption of simply utilising a cosine function to model the waviness of the whole yarn would be impossible in this case.
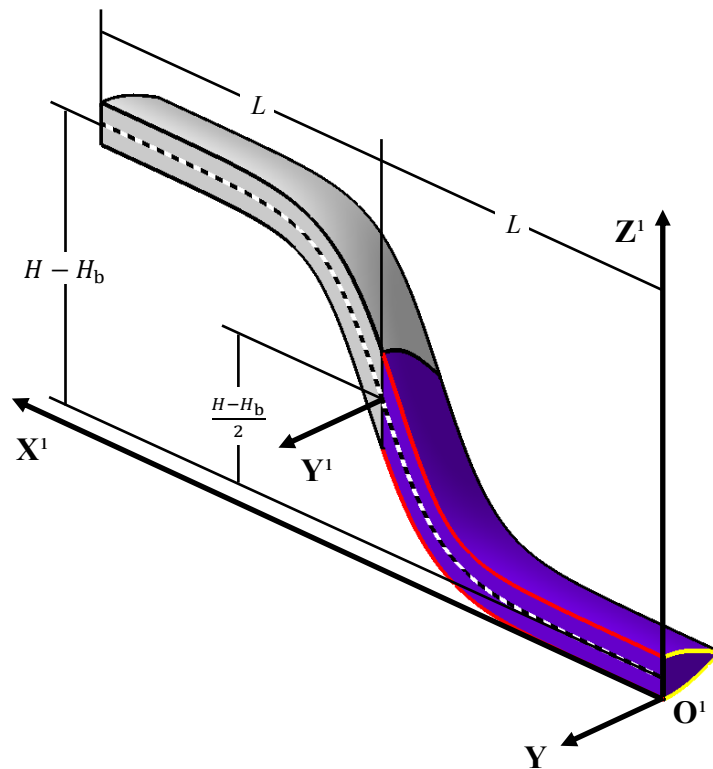
Figure 4.29: Extended binder yarn of the improved mUC

In this research, it is assumed that the waviness of the binder yarn can be described using a hyperbolic function as this type of function is capable of producing significant variation in the middle region and becoming flat in the remaining areas. Based on this assumption and the geometry configuration shown in Fig. 4.29, the following equation is proposed to describe the middle guide curve of the extended binder yarn:

$$z_{bmid} = \frac{H}{2} + m_0 \tanh[s_0(x - L)] \qquad (4.67)$$

where s_0 is a parameter used to control the rate of the function reaching its limit values and thus to fit the waviness of the binder yarn (an example showing how this parameter controls the shape or waviness of a binder yarn is given in Fig. 4.30), and m_0 is a scaling parameter defined such that the value of z_{bmid} exactly equals $H_b/2$ if $x = 0$ or equals $H - H_b/2$ if $x = 2L$, and it is determined as follows:

$$m_0 = \frac{H - H_b}{2 \tanh(s_0 L)} \qquad (4.68)$$
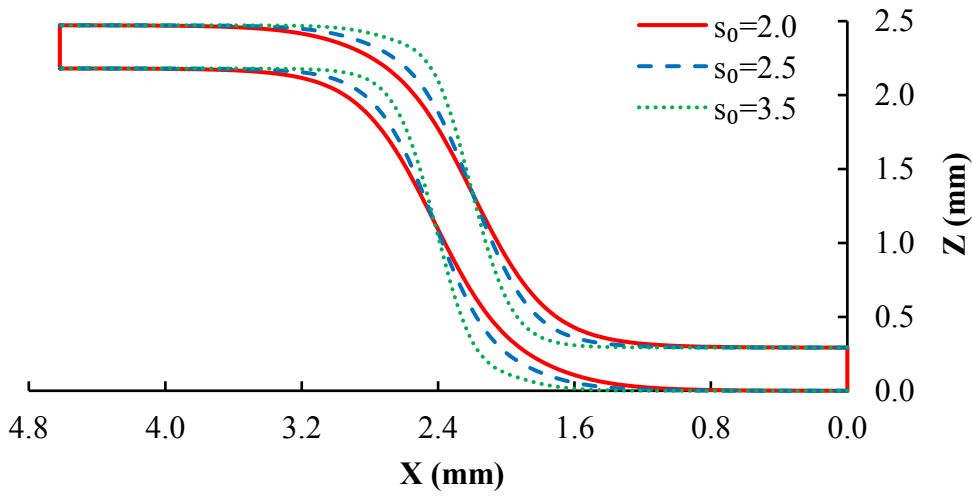
Figure 4.30: Variation in the waviness of a binder yarn on the value of s_0

Since the binder yarn shown in Fig. 4.28 is a part of the extended yarn, its waviness can also be described using Eq. (4.67). Therefore, by taking the derivative of Eq. (4.67) with respect to x, the waviness or the undulation angle of any material point on the binder yarn with respect to the XOY plane can be approximated, as follows:

$$\theta_{binder} = \frac{dz_{bmid}}{dx} = \tan^{-1}\{m_0 s_0\{1 - \tanh^2[s_0(x - L)]\}\} \qquad (4.69)$$

It should be noted that the binder yarn has been assumed to have a constant cross-sectional shape across the whole yarn. This suggests that both the lower and upper guide curves of the binder yarn should have the same distance from the middle guide curve, i.e. $H_b/2$. Thus, the equations for describing the two guide curves can be defined, as follows:

$$z_{\text{blg}} = z_{\text{bmid}} - \left|\frac{H_b}{2\sin\theta_0}\right| = \frac{H}{2} + m_0 \tanh[s_0(x - L)] - \left|\frac{H_b}{2\sin\theta_0}\right| \tag{4.70}$$

$$z_{\text{bug}} = z_{\text{bmid}} + \left|\frac{H_b}{2\sin\theta_0}\right| = \frac{H}{2} + m_0 \tanh[s_0(x - L)] + \left|\frac{H_b}{2\sin\theta_0}\right| \tag{4.71}$$

where

$$\theta_0 = -\tan^{-1}\left[\frac{1}{\tan(\theta_{\text{binder}})}\right] = -\tan^{-1}\left\{\frac{1}{m_0 s_0\{1 - \tanh^2[s_0(x - L)]\}}\right\} \tag{4.72}$$

Here, in Eq. (4.70) or Eq. (4.71), the use of the last term ensures the maximum thickness of the binder yarn at any cross-section exactly equalling H_b and thus ensures the binder yarn having a constant cross-sectional shape across the whole yarn.

Based on the above two equations and those defined for describing the lower and upper cross-sectional curves, i.e. Eqs. (4.65) and (4.66), the lower and upper surfaces of the binder yarn can be described, as follows:

$$z_{\text{binder}}^{\text{lower}} = z_{\text{blg}} + z_{\text{blc}} \tag{4.73}$$

$$z_{\text{binder}}^{\text{upper}} = z_{\text{bug}} + z_{\text{buc}} - H_b \tag{4.74}$$

Expanding the above two equations yields the explicit forms of equations for describing the surfaces of the binder yarn, as follows:

$$z_{\text{binder}}^{\text{lower}} = \frac{H}{2} + \frac{H_b}{2} - \frac{H_b}{2}\cos\left(\frac{\pi(y - W)}{2\lambda_b W}\right) + m_0 \tanh[s_0(x - L)] - \left|\frac{H_b}{2\sin\theta_0}\right| \tag{4.75}$$

$$z_{\text{binder}}^{\text{upper}} = \frac{H}{2} - \frac{H_b}{2} + \frac{H_b}{2}\cos\left(\frac{\pi(y - W)}{2\lambda_b W}\right) + m_0 \tanh[s_0(x - L)] + \left|\frac{H_b}{2\sin\theta_0}\right| \tag{4.76}$$

4.5 Derivation of boundary conditions

4.5.1 Introduction

Apart from identifying a UC and modelling the internal architecture, which have been covered previously in this chapter, one key issue to be addressed in the micromechanical homogenisation of the elastic properties or the overall response of woven composites is to derive the boundary condition for the UC of homogenisation. However, it should be

noted that the UC models proposed in this work are rUCs or specifically mUCs, which are identified by exploiting not only translational but also non-translational symmetries, such as rotation and reflection. This indicates that the standard form of PBC is applicable only at the level of full-size UC but inapplicable at the level of rUC or mUC since this form of PBC is formulated based on translational periodicity only, as detailed in Section 2.5, Chapter 2.

The approaches for deriving the PBC of woven composites at the level of rUC or mUC have been well established, and they can be largely classified into two types, namely, the multi-step approach and the equivalence approach. In the former approach, the boundary condition of an rUC is deduced step by step from that of the full-size UC in accordance with the symmetry operations that have been utilised to obtain the rUC from the full-size UC. An exhaustive example of utilising such an approach can be found in Li *et al.* [188], where the boundary conditions of rUCs of plain woven composites were calculated step by step and summarised for each loading condition.

On the other hand, the equivalence approach is a one-step method as it formulates generic equations based on which the boundary condition of either a full-size UC or an rUC can be calculated. This approach was first proposed by Whitcomb *et al.* [190] based on the concept of *Equivalent Coordinate System* (ECS), which was applied to establish relations between the geometry and mechanics quantities (i.e. coordinate, displacement, stress and strain) of two adjacent subdomains and thus to derive the boundary condition for the UC of homogenisation. This approach was later extended by Tang and Whitcomb [189] and De Carvalho *et al.* [191], leading to very generic forms of equations for determining the boundary condition of woven composites at the level of rUC. In this research, the generic equations developed by De Carvalho *et al.* [191] have been utilised to derive the boundary conditions for the mUCs presented in this thesis, and these equations will be detailed in the following section, for completeness.

4.5.2 The equivalence approach

The equivalence approach developed by De Carvalho *et al.* [191] is based on 4 concepts, i.e., physical equivalence, loading equivalence, periodicity and subdomain admissibility. To clearly illustrate how this approach can be used to derive PBCs for woven composites the concepts of physical equivalence, loading equivalence and subdomain admissibility

will be firstly introduced in this section. Here, the concept of periodicity will not be discussed since it has been actually covered at the beginning of this chapter. After that, the theoretical procedure for deducing the generic equations will be detailed. Finally, the basic steps of using the equivalence approach to derive PBCs will be summarised at the end of this section.

4.5.2.1 Physical equivalence

Consider a general domain. Assume that in the general domain there is a subdomain, D, bounded by a boundary, and that there are n physical properties which are defined in the local coordinate system (LCS) of D, i.e. $O_D xyz$, in a tensor form of $\boldsymbol{p}_D^i$, $i \in \{1, 2, \dots, n\}$. Then, two subdomains, D and $\overline{D}$, are treated as physically equivalent, i.e. $D \cong \overline{D}$, if for each point, A, in subdomain D there is an equivalent point, $\overline{A}$, in subdomain $\overline{D}$ such that for each physical property i the following condition holds [191]:

$$\boldsymbol{x}_D^A = \boldsymbol{x}_{\overline{D}}^{\overline{A}} \ \cap \ \boldsymbol{p}_D^i(A) = \boldsymbol{p}_{\overline{D}}^i(\overline{A}) \tag{4.77}$$

where $\boldsymbol{x}_D^A$ and $\boldsymbol{x}_{\overline{D}}^{\overline{A}}$ are the coordinates of the equivalent points in the LCSs attached to subdomains D and $\overline{D}$, respectively.
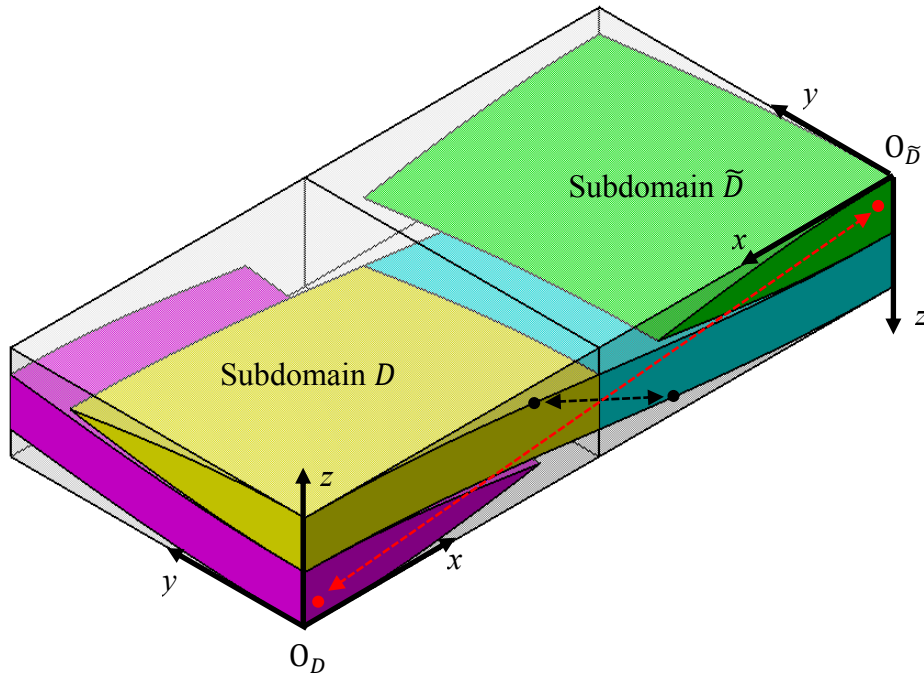
Figure 4.31: Physically equivalent subdomains in plain woven composites

An example of two physically equivalent subdomains is illustrated by using two subcells of plain woven composites, as shown in Fig. 4.31. It can be clearly seen in the figure that for every point in the left subcell there is a geometrically equivalent point in the right subcell, and the physical properties (e.g. material properties or orientation) of a point in the left subcell are identical to those of the equivalent point in the right subcell.

According to Eq. (4.77), the coordinate vectors of two equivalent points, A and $\bar{A}$, in their own LCSs are equal to each other. Based on this, the coordinates of two equivalent points can be related in the same LCS, as follows:

$$x_D^A = \mathbf{T}\left(x_D^{\bar{A}} - x_D^{O_{\bar{D}}}\right) \tag{4.78}$$

where $\mathbf{T}$ denotes the matrix for transforming from the LCS of the equivalent subdomain $\bar{D}$ to that of subdomain D, and $x_D^{\bar{A}}$ are $x_D^{O_{\bar{D}}}$ stands for the position vector of point $\bar{A}$ and that of the origin of the LCS of subdomain $\bar{D}$, i.e. point $O_{\bar{D}}$, in the LCS of subdomain D.

4.5.2.2 Loading equivalence

The concept of loading equivalence was originally proposed by Tang and Whitcomb [189]. It is utilised to correlate the stress and strain of a subdomain with those of the equivalent subdomain. Specifically, two physically equivalent subdomains, D and $\bar{D}$, are treated as loading equivalent if the stress and strain of each point in D and those of the equivalent point in $\bar{D}$ can be related using the following equations:

$$\sigma_D^A = \gamma \sigma_{\bar{D}}^{\bar{A}} \tag{4.79}$$

$$\varepsilon_D^A = \gamma \varepsilon_{\bar{D}}^{\bar{A}} \tag{4.80}$$

where γ is referred to as the load reversal factor and must be equal to 1 or -1.

4.5.2.3 Subdomain admissibility

As suggested in [191], not all physically equivalent subdomains can be employed to homogenise the properties of a periodic material. Given that the volume average strain is a homogenised quantity and thus should be independent of the subdomain that is chosen to perform the homogenisation, the sufficient condition for a subdomain being admissible

for a homogenisation is that the value of the volume average strain calculated based on this subdomain in a given coordinate system is equal to that calculated based on any other subdomain in the same coordinate system. Using this condition and the general relation between the volume average strains of two equivalent subdomains, as detailed in Eq. (10) in [191], it can be concluded that the necessary and sufficient condition for a subdomain being admissible is that the following condition must be satisfied:

$$\langle \boldsymbol{\varepsilon} \rangle_D^D = \gamma_i \mathbf{T}_i \langle \boldsymbol{\varepsilon} \rangle_D^{\overline{D}_i} \mathbf{T}_i^{\mathrm{T}} \tag{4.81}$$

where $\langle \boldsymbol{\varepsilon} \rangle_D^D$ is the volume average strain of subdomain D calculated in its LCS; $\langle \boldsymbol{\varepsilon} \rangle_D^{\overline{D}}$ is the volume average strain of any other subdomain, $\overline{D}_i$, derived in the LCS of subdomain D; and γ_i and $\mathbf{T}_i$ denotes the load reversal factor and the transformation matrix between subdomains D and $\overline{D}_i$.

The admissibility condition defined above indicates that not all combinations of loading conditions are admissible. Therefore, before conducting a homogenisation, all admissible loading cases of the subdomain of homogenisation must be determined, the procedure of which can be illustrated as follows. Consider two equivalent subdomains, D and $\overline{D}$, with D being the subdomain of homogenisation and the transformation matrix between the two equivalent subdomains being:

$$\mathbf{T} = \begin{bmatrix} a & 0 & 0 \\ 0 & b & 0 \\ 0 & 0 & c \end{bmatrix}$$

Here, it is should be noted that the diagonal elements in the transformation matrix have to be 1 or -1. By utilising the relations of $a^2 = 1$, $b^2 = 1$ and $c^2 = 1$ and substituting the transformation matrix into Eq. (4.81), it yields the following equation:

$$\begin{bmatrix} \langle \varepsilon_{11} \rangle & \langle \varepsilon_{12} \rangle & \langle \varepsilon_{13} \rangle \\ \langle \varepsilon_{21} \rangle & \langle \varepsilon_{22} \rangle & \langle \varepsilon_{23} \rangle \\ \langle \varepsilon_{31} \rangle & \langle \varepsilon_{32} \rangle & \langle \varepsilon_{33} \rangle \end{bmatrix} = \gamma \begin{bmatrix} \langle \varepsilon_{11} \rangle & ab\langle \varepsilon_{12} \rangle & ac\langle \varepsilon_{13} \rangle \\ ab\langle \varepsilon_{21} \rangle & \langle \varepsilon_{22} \rangle & bc\langle \varepsilon_{23} \rangle \\ ac\langle \varepsilon_{31} \rangle & bc\langle \varepsilon_{32} \rangle & \langle \varepsilon_{33} \rangle \end{bmatrix} \tag{4.82}$$

The above equation is essentially an explicit form of Eq. (4.81). By solving this equation, all admissible loading cases, as well as the load reversal factors, can be determined. For example, if we assume that $a = -1$, $b = 1$ and $c = -1$, Eq. (4.82) becomes:

$$\begin{bmatrix} \langle \varepsilon_{11} \rangle & \langle \varepsilon_{12} \rangle & \langle \varepsilon_{13} \rangle \\ \langle \varepsilon_{21} \rangle & \langle \varepsilon_{22} \rangle & \langle \varepsilon_{23} \rangle \\ \langle \varepsilon_{31} \rangle & \langle \varepsilon_{32} \rangle & \langle \varepsilon_{33} \rangle \end{bmatrix} = \gamma \begin{bmatrix} \langle \varepsilon_{11} \rangle & -\langle \varepsilon_{12} \rangle & \langle \varepsilon_{13} \rangle \\ -\langle \varepsilon_{21} \rangle & \langle \varepsilon_{22} \rangle & -\langle \varepsilon_{23} \rangle \\ \langle \varepsilon_{31} \rangle & -\langle \varepsilon_{32} \rangle & \langle \varepsilon_{33} \rangle \end{bmatrix}$$

Considering that a load reversal factor has to be 1 or -1, the solutions of the above equation can be easily obtained, as follows:

Solution 1: $\gamma = 1$ and $\langle \varepsilon_{12} \rangle = \langle \varepsilon_{21} \rangle = \langle \varepsilon_{23} \rangle = \langle \varepsilon_{32} \rangle = 0$

Solution 2: $\gamma = -1$ and $\langle \varepsilon_{11} \rangle = \langle \varepsilon_{22} \rangle = \langle \varepsilon_{33} \rangle = \langle \varepsilon_{13} \rangle = \langle \varepsilon_{31} \rangle = 0$

The above solutions indicate that there are only two admissible loading cases, and any other combinations of loadings cannot be applied to perform the homogenisation:

Admissible loading case 1: $\gamma = 1$ and $\begin{bmatrix} \langle \sigma_{11} \rangle & 0 & \langle \sigma_{13} \rangle \\ 0 & \langle \sigma_{22} \rangle & 0 \\ \langle \sigma_{31} \rangle & 0 & \langle \sigma_{31} \rangle \end{bmatrix}$

Admissible loading case 2: $\gamma = -1$ and $\begin{bmatrix} 0 & \langle \sigma_{12} \rangle & 0 \\ \langle \sigma_{12} \rangle & 0 & \langle \sigma_{23} \rangle \\ 0 & \langle \sigma_{32} \rangle & 0 \end{bmatrix}$

4.5.2.4 Generic equations for enforcing PBC

Based on the concepts discussed above, the standard form of PBC, as shown in Eq. (2.79), can be transformed into the generic form of PBC [191], which is an appropriate form for applying PBCs at the level of rUC or mUC. For the sake of clearly illustrating the specific procedure for enforcing this form of PBC, the derivation procedure of the basic equations is summarised as follows.

The derivation of the basic equations is based on two adjacent, physically equivalent and loading equivalent subdomains, D and $\overline{D}$. By using the physical equivalence between the two subdomains, we have that if a point, $\overline{A}$, that belongs to subdomain $\overline{D}$ is chosen on the shared boundary of the two subdomains, then its equivalent point, A, will be also on the boundary of subdomain D. In other words, both point $\overline{A}$ and point A are located on the boundary of subdomain D. Therefore, according to Eq. (2.70a), the displacements of the two equivalent points in the LCS of subdomain D can be expressed using the following two equations, respectively:

$$\boldsymbol{u}(A) = \langle\boldsymbol{\varepsilon}\rangle\boldsymbol{x}^A + \boldsymbol{u}^*(A) \tag{4.83}$$

$$\boldsymbol{u}(\bar{A}) = \langle\boldsymbol{\varepsilon}\rangle\boldsymbol{x}^{\bar{A}} + \boldsymbol{u}^*(\bar{A}) \tag{4.84}$$

Here, all quantities are evaluated in the same LCS (i.e. the LCS of D) and the subscripts denoting the reference coordinate system have been removed for simplicity. According to [192], the oscillatory parts in the above equations can be correlated using:

$$\boldsymbol{u}^*(A) = \gamma\mathbf{T}\boldsymbol{u}^*(\bar{A}) \tag{4.85}$$

Based on this relation, the oscillatory parts can be cancelled by firstly multiplying $\gamma\mathbf{T}$ to Eq. (4.84) and then subtracting the resulting equation from Eq. (4.83), leading to:

$$\boldsymbol{u}(A) - \gamma\mathbf{T}\boldsymbol{u}(\bar{A}) = (\langle\boldsymbol{\varepsilon}\rangle\mathbf{T} - \gamma\mathbf{T}\langle\boldsymbol{\varepsilon}\rangle)\boldsymbol{x}^{\bar{A}} - \langle\boldsymbol{\varepsilon}\rangle\mathbf{T}\boldsymbol{x}^{O_{\bar{D}}} \tag{4.86}$$

By considering the admissibility condition, as given in Eq. (4.81), we can get the relation of $\langle\boldsymbol{\varepsilon}\rangle\mathbf{T} - \gamma\mathbf{T}\langle\boldsymbol{\varepsilon}\rangle = \mathbf{0}$. Therefore, Eq. (4.86) can be simplified into:

$$\boldsymbol{u}(A) - \gamma\mathbf{T}\boldsymbol{u}(\bar{A}) = -\langle\boldsymbol{\varepsilon}\rangle\mathbf{T}\boldsymbol{x}^{O_{\bar{D}}} \tag{4.87}$$

This equation is the generic form of PBC equation, and it can be used to derive PBCs for not only rUCs or mUCs but also full-size UCs. Here, it should be noted that the standard form of PBC equation, as given in Eq. (2.79), is a special case of the above equation since the former can be derived by applying into the latter with the configurations associated with translation, i.e. $\mathbf{T} = \mathbf{I}$ and $\gamma = 1$, where $\mathbf{I}$ is the identity matrix.

4.5.2.5 Application procedure

The specific procedure for using the equivalence approach to derive PBCs for an rUC or mUC involves four steps:

1) Identify all adjacent and physically equivalent subdomains for the UC domain of homogenisation and determine the position vector of the origin of each subdomain in the LCS of the UC;

2) Determine the transformation matrix associated with the transformation between each pair of equivalent subdomains and calculate the coordinates of all equivalent points on the boundary of the UC by using Eq. (4.78);

3) Identify all admissible loading cases by using the admissibility condition, as given in Eq. (4.81) or (4.82) and determine the load reversal factor relating to each pair of equivalent subdomains;

4) For each pair of equivalent points, calculate the constraint that should be enforced according to the generic form of PBC equation, i.e. Eq. (4.87), for each prescribed admissible loading case.

4.5.3 PBCs for normal plain woven composites
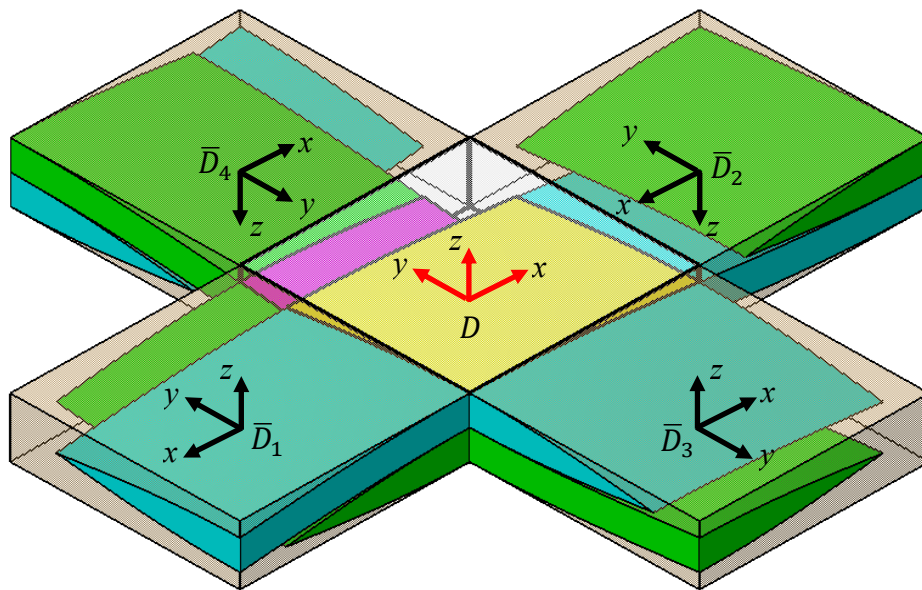
Figure 4.32: Normal mUC & adjacent subdomains of plain woven composites

The equivalence approach has been utilised to obtain the PBCs for all mUCs presented in this thesis. In this section, the PBCs for the normal mUC of plain woven composites will be derived. Fig. 4.32 shows the normal mUC of plain woven composites (denoted as D), as well as four adjacent and physically equivalent subdomains (denoted as $\overline{D}_1$, $\overline{D}_2$, $\overline{D}_3$ and $\overline{D}_4$). Here, it should be noted that the origin of each LCS is positioned such that it coincides with the centre of the associated subdomain. In addition, there should be two more subdomains, $\overline{D}_5$ and $\overline{D}_6$, with one of them being under the mUC and the other being above. However, they have been excluded from this figure for the sake of revealing the mUC on one hand. On the other hand, the present work focuses on the woven composites with simply stacking, which means that the boundary conditions on the lower and upper surfaces of an mUC of this category of woven composites can be directly derived based

on the standard form of PBC equation, without using the equivalent approach, due to the fact that the upper and lower subdomains are translational copies of the mUC.

Table 4.1: Relations between normal plain woven mUC & adjacent subdomains

	$\bar{D}_1$	$\bar{D}_2$	$\bar{D}_3$	$\bar{D}_4$
T_i	$\begin{bmatrix} -1 & 0 & 0 \\ 0 & 1 & 0 \\ 0 & 0 & 1 \end{bmatrix}$	$\begin{bmatrix} -1 & 0 & 0 \\ 0 & 1 & 0 \\ 0 & 0 & -1 \end{bmatrix}$	$\begin{bmatrix} 1 & 0 & 0 \\ 0 & -1 & 0 \\ 0 & 0 & 1 \end{bmatrix}$	$\begin{bmatrix} 1 & 0 & 0 \\ 0 & -1 & 0 \\ 0 & 0 & -1 \end{bmatrix}$
$x^{O_{\bar{D}_i}}$	$\begin{bmatrix} -L \\ 0 \\ 0 \end{bmatrix}$	$\begin{bmatrix} L \\ 0 \\ 0 \end{bmatrix}$	$\begin{bmatrix} 0 \\ -W \\ 0 \end{bmatrix}$	$\begin{bmatrix} 0 \\ W \\ 0 \end{bmatrix}$
$x^{\bar{A}_i}$	$\begin{bmatrix} -\frac{L}{2} \\ -\frac{W}{2} \le y \le \frac{W}{2} \\ -\frac{H}{2} \le z \le \frac{H}{2} \end{bmatrix}$	$\begin{bmatrix} \frac{L}{2} \\ -\frac{W}{2} \le y \le \frac{W}{2} \\ -\frac{H}{2} \le z \le \frac{H}{2} \end{bmatrix}$	$\begin{bmatrix} -\frac{L}{2} \le x \le \frac{L}{2} \\ -\frac{W}{2} \\ -\frac{H}{2} \le z \le \frac{H}{2} \end{bmatrix}$	$\begin{bmatrix} -\frac{L}{2} \le x \le \frac{L}{2} \\ \frac{W}{2} \\ -\frac{H}{2} \le z \le \frac{H}{2} \end{bmatrix}$
x^{A_i}	$\begin{bmatrix} -\frac{L}{2} \\ y^{\bar{A}} \\ z^{\bar{A}} \end{bmatrix}$	$\begin{bmatrix} \frac{L}{2} \\ y^{\bar{A}} \\ -z^{\bar{A}} \end{bmatrix}$	$\begin{bmatrix} x^{\bar{A}} \\ -\frac{W}{2} \\ z^{\bar{A}} \end{bmatrix}$	$\begin{bmatrix} x^{\bar{A}} \\ \frac{W}{2} \\ -z^{\bar{A}} \end{bmatrix}$

Given that all equivalent subdomains of the mUC have been identified, the transformation matrices, the origin position vectors of all equivalent subdomains, and the coordinates of all equivalent points on the boundary of the mUC can be calculated, as summarised in Table 4.1. After obtaining the geometry relations between the mUC and its adjacent and physically equivalent subdomains, the procedure described in Section 4.5.2.3 can be applied to determine all admissible loading cases and the relating load reversal factors, as listed in Table 4.2. Here, it is shown that there are four loading cases that should be treated independently in the homogenisation of plain woven composites.

Based on the quantities obtained above and Eq. (4.87), the PBC that should be applied to each pair of equivalent boundary nodes for each admissible loading case can be calculated, as summarised in Tables B.1 – B.4, Appendix B. Here, it should be noted that the shared surface between the mUC and an equivalent subdomain has been denoted using S_i, $i \in \{1, 2, 3, 4, 5, 6\}$. Also, the equations marked with strikethroughs should not be considered since each of these equations correlates a point with the point itself, creating a redundant displacement constraint in the form of $u_j(A) - u_j(A) = 0$, $j \in \{1, 2, 3\}$. Furthermore, for

the points located on the edges or vertices of the mUC, redundant equations may also be produced as they are shared by two or more surfaces. To eliminate redundant constraints, the technique described in [188] can be utilised. It should be further noted that the PBCs listed in Appendix B, including those for twill and 3D woven composites, are obtained based on such an LCS with its origin located at the centre of the mUC. Therefore, these PBCs need to be transformed back to the LCS that has been used to develop the analytical equations for describing the internal architecture of the mUC.

Table 4.2: Admissible loading cases of normal plain woven composites

	$\{\gamma_1 \quad \gamma_2 \quad \gamma_3 \quad \gamma_4\}$	Admissible loading
Case 1	$\{1 \quad 1 \quad 1 \quad 1\}$	$\begin{bmatrix} \langle\sigma_{11}\rangle & 0 & 0 \\ 0 & \langle\sigma_{22}\rangle & 0 \\ 0 & 0 & \langle\sigma_{33}\rangle \end{bmatrix}$
Case 2	$\{-1 \quad -1 \quad -1 \quad -1\}$	$\begin{bmatrix} 0 & \langle\sigma_{12}\rangle & 0 \\ \langle\sigma_{21}\rangle & 0 & 0 \\ 0 & 0 & 0 \end{bmatrix}$
Case 3	$\{1 \quad -1 \quad -1 \quad 1\}$	$\begin{bmatrix} 0 & 0 & 0 \\ 0 & 0 & \langle\sigma_{23}\rangle \\ 0 & \langle\sigma_{32}\rangle & 0 \end{bmatrix}$
Case 4	$\{-1 \quad 1 \quad 1 \quad -1\}$	$\begin{bmatrix} 0 & 0 & \langle\sigma_{13}\rangle \\ 0 & 0 & 0 \\ \langle\sigma_{31}\rangle & 0 & 0 \end{bmatrix}$

4.5.4 PBCs for normal twill woven composites

The procedure for utilising the equivalence approach to obtain the PBCs for the mUC of twill woven composites is similar to that for the case of plain woven composites. Fig. 4.33 shows the mUC (denoted as D) of twill woven composites, as well as its adjacent and physically equivalent subdomains (denoted as $\bar{D}_1, \bar{D}_2, \bar{D}_3$ and $\bar{D}_4$). Again, the lower and upper subdomains (i.e. $\bar{D}_5$ and $\bar{D}_6$) have been removed to reveal the mUC. Based on this figure, the geometry relations between the mUC and its equivalent subdomains are determined, as given in Table 4.3. Then, by enforcing the admissibility condition, as given in Eq. (4.81) or (4.82), all admissible loading cases are identified and the relating load reversal factors are obtained, as shown in Table 4.4. Here, it is shown that there are only two loading cases that should be treated independently. Finally, based on the quantities

calculated above and Eq. (4.87), the PBC that should be applied to each pair of equivalent boundary nodes for each admissible loading case for the normal mUC of twill woven composites can be derived, as summarised in Tables B.5 and B.6, Appendix B.
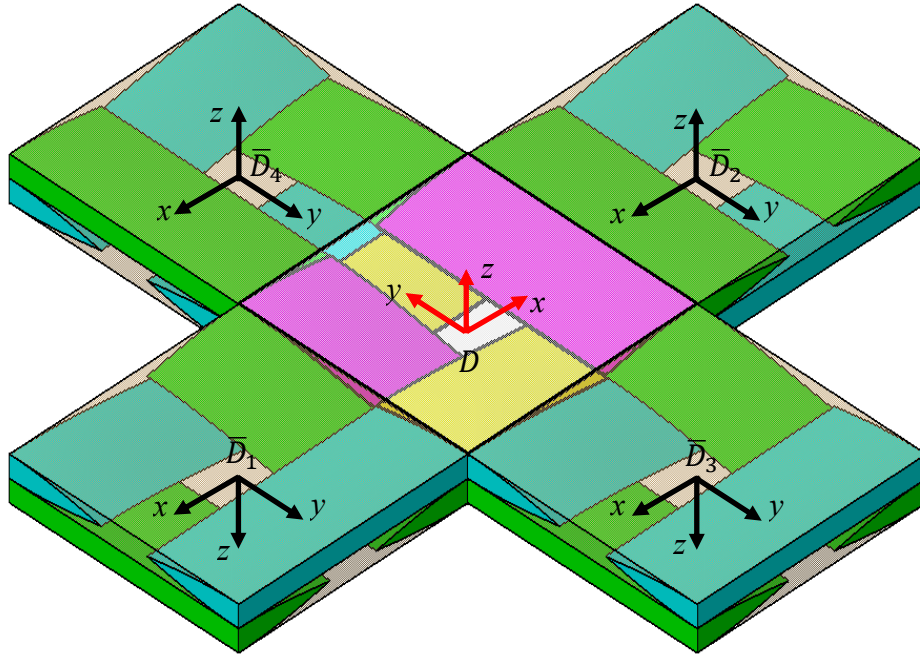
Figure 4.33: Normal mUC & adjacent subdomains of twill woven composites

Table 4.3: Relations between normal twill woven mUC & adjacent subdomains

	$\overline{D}_1$	$\overline{D}_2$	$\overline{D}_3$	$\overline{D}_4$
$\boldsymbol{T}_i$	$\begin{bmatrix} -1 & 0 & 0 \\ 0 & -1 & 0 \\ 0 & 0 & -1 \end{bmatrix}$	$\begin{bmatrix} -1 & 0 & 0 \\ 0 & -1 & 0 \\ 0 & 0 & 1 \end{bmatrix}$	$\begin{bmatrix} -1 & 0 & 0 \\ 0 & -1 & 0 \\ 0 & 0 & -1 \end{bmatrix}$	$\begin{bmatrix} -1 & 0 & 0 \\ 0 & -1 & 0 \\ 0 & 0 & 1 \end{bmatrix}$
$\boldsymbol{x}^{O_{\overline{D}_i}}$	$\begin{bmatrix} -L \\ 0 \\ 0 \end{bmatrix}$	$\begin{bmatrix} L \\ 0 \\ 0 \end{bmatrix}$	$\begin{bmatrix} 0 \\ -W \\ 0 \end{bmatrix}$	$\begin{bmatrix} 0 \\ W \\ 0 \end{bmatrix}$
$\boldsymbol{x}^{\bar{A}_i}$	$\begin{bmatrix} -\frac{L}{2} \\ -\frac{W}{2} \le y \le \frac{W}{2} \\ -\frac{H}{2} \le z \le \frac{H}{2} \end{bmatrix}$	$\begin{bmatrix} \frac{L}{2} \\ -\frac{W}{2} \le y \le \frac{W}{2} \\ -\frac{H}{2} \le z \le \frac{H}{2} \end{bmatrix}$	$\begin{bmatrix} -\frac{L}{2} \le x \le \frac{L}{2} \\ -\frac{W}{2} \\ -\frac{H}{2} \le z \le \frac{H}{2} \end{bmatrix}$	$\begin{bmatrix} -\frac{L}{2} \le x \le \frac{L}{2} \\ \frac{W}{2} \\ -\frac{H}{2} \le z \le \frac{H}{2} \end{bmatrix}$
$\boldsymbol{x}^{A_i}$	$\begin{bmatrix} -\frac{L}{2} \\ -y^{\bar{A}} \\ -z^{\bar{A}} \end{bmatrix}$	$\begin{bmatrix} \frac{L}{2} \\ -y^{\bar{A}} \\ z^{\bar{A}} \end{bmatrix}$	$\begin{bmatrix} -x^{\bar{A}} \\ -\frac{W}{2} \\ -z^{\bar{A}} \end{bmatrix}$	$\begin{bmatrix} -x^{\bar{A}} \\ \frac{W}{2} \\ z^{\bar{A}} \end{bmatrix}$

Table 4.4: Admissible loading cases of normal twill woven composites

	$\{\gamma_1 \quad \gamma_2 \quad \gamma_3 \quad \gamma_4\}$	Admissible loading
Case 1	$\{1 \quad 1 \quad 1 \quad 1\}$	$\begin{bmatrix} \langle\sigma_{11}\rangle & \langle\sigma_{12}\rangle & 0 \\ \langle\sigma_{21}\rangle & \langle\sigma_{22}\rangle & 0 \\ 0 & 0 & \langle\sigma_{33}\rangle \end{bmatrix}$
Case 2	$\{1 \quad -1 \quad 1 \quad -1\}$	$\begin{bmatrix} 0 & 0 & \langle\sigma_{13}\rangle \\ 0 & 0 & \langle\sigma_{23}\rangle \\ \langle\sigma_{31}\rangle & \langle\sigma_{32}\rangle & 0 \end{bmatrix}$

4.5.5 PBCs for normal 3D orthogonal woven composites
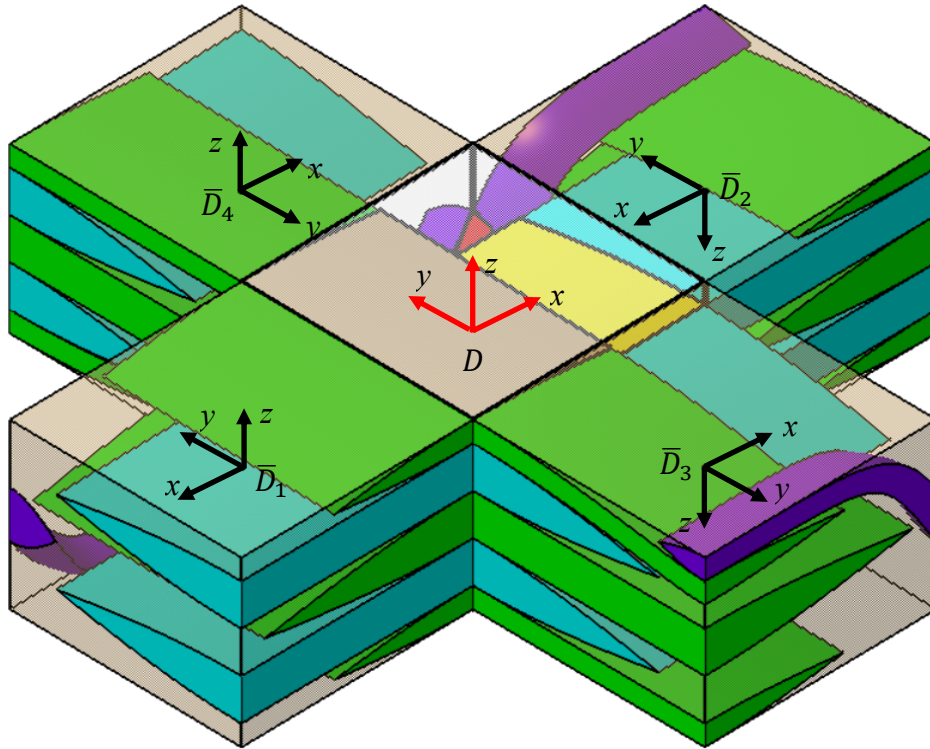
Figure 4.34: Normal mUC and adjacent subdomains of 3D woven composites

In terms of the PBCs for the mUC of 3D woven composites, they can be derived using a similar procedure to that for the case of plain or twill woven composites. However, after identifying the adjacent and physically equivalent subdomains for the mUC of 3D woven composites, as shown in Fig. 4.34 or Table 4.5, it can be found that the geometry relations between the mUC and its equivalent subdomains are different from those in the case of plain or twill woven composites. Thus, the admissible loading cases should be calculated

independently, as summarised in Table 4.6. Based on the results given in Tables 4.5 and 4.6, the PBCs for the normal mUC of 3D woven composites can be derived, as listed in Tables B.7 – B.10, Appendix B.

Table 4.5: Relations between normal 3D woven mUC & adjacent subdomains

	$\overline{D}_1$	$\overline{D}_2$	$\overline{D}_3$	$\overline{D}_4$
T_i	$\begin{bmatrix} -1 & 0 & 0 \\ 0 & 1 & 0 \\ 0 & 0 & 1 \end{bmatrix}$	$\begin{bmatrix} -1 & 0 & 0 \\ 0 & 1 & 0 \\ 0 & 0 & -1 \end{bmatrix}$	$\begin{bmatrix} 1 & 0 & 0 \\ 0 & -1 & 0 \\ 0 & 0 & -1 \end{bmatrix}$	$\begin{bmatrix} 1 & 0 & 0 \\ 0 & -1 & 0 \\ 0 & 0 & 1 \end{bmatrix}$
$x^{O_{\overline{D}_i}}$	$\begin{bmatrix} -L \\ 0 \\ 0 \end{bmatrix}$	$\begin{bmatrix} L \\ 0 \\ 0 \end{bmatrix}$	$\begin{bmatrix} 0 \\ -W \\ 0 \end{bmatrix}$	$\begin{bmatrix} 0 \\ W \\ 0 \end{bmatrix}$
$x^{\overline{A}_i}$	$\begin{bmatrix} -\frac{L}{2} \\ -\frac{W}{2} \le y \le \frac{W}{2} \\ -\frac{H}{2} \le z \le \frac{H}{2} \end{bmatrix}$	$\begin{bmatrix} \frac{L}{2} \\ -\frac{W}{2} \le y \le \frac{W}{2} \\ -\frac{H}{2} \le z \le \frac{H}{2} \end{bmatrix}$	$\begin{bmatrix} -\frac{L}{2} \le x \le \frac{L}{2} \\ -\frac{W}{2} \\ -\frac{H}{2} \le z \le \frac{H}{2} \end{bmatrix}$	$\begin{bmatrix} -\frac{L}{2} \le x \le \frac{L}{2} \\ \frac{W}{2} \\ -\frac{H}{2} \le z \le \frac{H}{2} \end{bmatrix}$
x^{A_i}	$\begin{bmatrix} -\frac{L}{2} \\ y^{\overline{A}} \\ z^{\overline{A}} \end{bmatrix}$	$\begin{bmatrix} \frac{L}{2} \\ y^{\overline{A}} \\ -z^{\overline{A}} \end{bmatrix}$	$\begin{bmatrix} x^{\overline{A}} \\ -\frac{W}{2} \\ -z^{\overline{A}} \end{bmatrix}$	$\begin{bmatrix} x^{\overline{A}} \\ \frac{W}{2} \\ z^{\overline{A}} \end{bmatrix}$

Table 4.6: Admissible loading cases of normal 3D woven composites

	$\{\gamma_1 \quad \gamma_2 \quad \gamma_3 \quad \gamma_4\}$	Admissible loading
Case 1	$\{1 \quad 1 \quad 1 \quad 1\}$	$\begin{bmatrix} \langle\sigma_{11}\rangle & 0 & 0 \\ 0 & \langle\sigma_{22}\rangle & 0 \\ 0 & 0 & \langle\sigma_{33}\rangle \end{bmatrix}$
Case 2	$\{-1 \quad -1 \quad -1 \quad -1\}$	$\begin{bmatrix} 0 & \langle\sigma_{12}\rangle & 0 \\ \langle\sigma_{21}\rangle & 0 & 0 \\ 0 & 0 & 0 \end{bmatrix}$
Case 3	$\{1 \quad -1 \quad 1 \quad -1\}$	$\begin{bmatrix} 0 & 0 & 0 \\ 0 & 0 & \langle\sigma_{23}\rangle \\ 0 & \langle\sigma_{32}\rangle & 0 \end{bmatrix}$
Case 4	$\{-1 \quad 1 \quad -1 \quad 1\}$	$\begin{bmatrix} 0 & 0 & \langle\sigma_{13}\rangle \\ 0 & 0 & 0 \\ \langle\sigma_{31}\rangle & 0 & 0 \end{bmatrix}$

4.6 Meshfree implementation

4.6.1 Framework of the meshfree program

As detailed in the introduction of Chapter 2, the use of the UC modelling methodology for predicting the elastic properties of woven composites involves three aspects, namely, i) identifying a UC and modelling the internal architecture of the UC, ii) modelling the elastic behaviours of individual constituents, and iii) applying proper PBCs to the UC for subsequent calculations of the volume average quantities and thus the elastic properties. Given that all the above three aspects have been addressed, the final step is to implement the above framework by using a suitable meshfree method, i.e. the standard weak-form meshfree method in the case of predicting the elastic properties, and consequently to fulfil the aim of *addressing the problems associated with analytical approaches and the FEM-based approaches by using a meshfree-based UC modelling methodology*. For this sake, an in-house computer program that implements the high-fidelity analytical mUC models, the elasticity constitutive models of the constituents and the PBCs listed in Appendix B has been developed in combination with the standard weak-form meshfree method, and it is termed as the *standard meshfree program* for convenience.

The program was coded using the programming language FORTRAN, and it provides the user with an option of choosing one of the three shape function construction techniques to predict the elastic properties of plain, twill or 3D woven composites, on the condition of providing four types of inputs, which will be detailed later. A flow chart showing the basic framework of this program is given in Fig. 4.35. As is clearly seen from this figure, the program starts by providing it with the four types of inputs. Based on these inputs, a domain representing the mUC of a given type of woven composites is discretised with field nodes and background cells. Then, a support domain is defined for each integration point in each background cell, and the meshfree-based shape functions corresponding to the support nodes of the integration point are calculated. By using the high-fidelity mUC model, the relative location and consequently the material type of each integration point can be determined. Next, the corresponding material model can be applied to obtain the elasticity matrix of the integration point in the GCS and thus to calculate its nodal stiffness matrix, $\mathbf{K}_{IJ}$, using Eq. (3.88). Assembling all the nodal stiffness matrices using Eq. (3.92) forms the global stiffness matrix, $\mathbf{K}$. After that, the PBC for a given admissible loading

case is enforced to obtain the displacement constraint based system of equations, as given in Eq. (3.108), based on which, the displacements of all field nodes can be solved. Finally, the strain and stress of each integration point can be calculated using the relations of $\boldsymbol{\varepsilon} = \boldsymbol{Lu}$ and $\boldsymbol{\sigma} = \boldsymbol{C\varepsilon}$, and thus the volume average stress of the mUC can be obtained by using Eq. (2.64). By combining the volume average stress, $\langle\boldsymbol{\sigma}\rangle$, and the macroscopic strain applied, $\langle\boldsymbol{\varepsilon}\rangle$, the effective or homogenised elastic properties can be calculated.
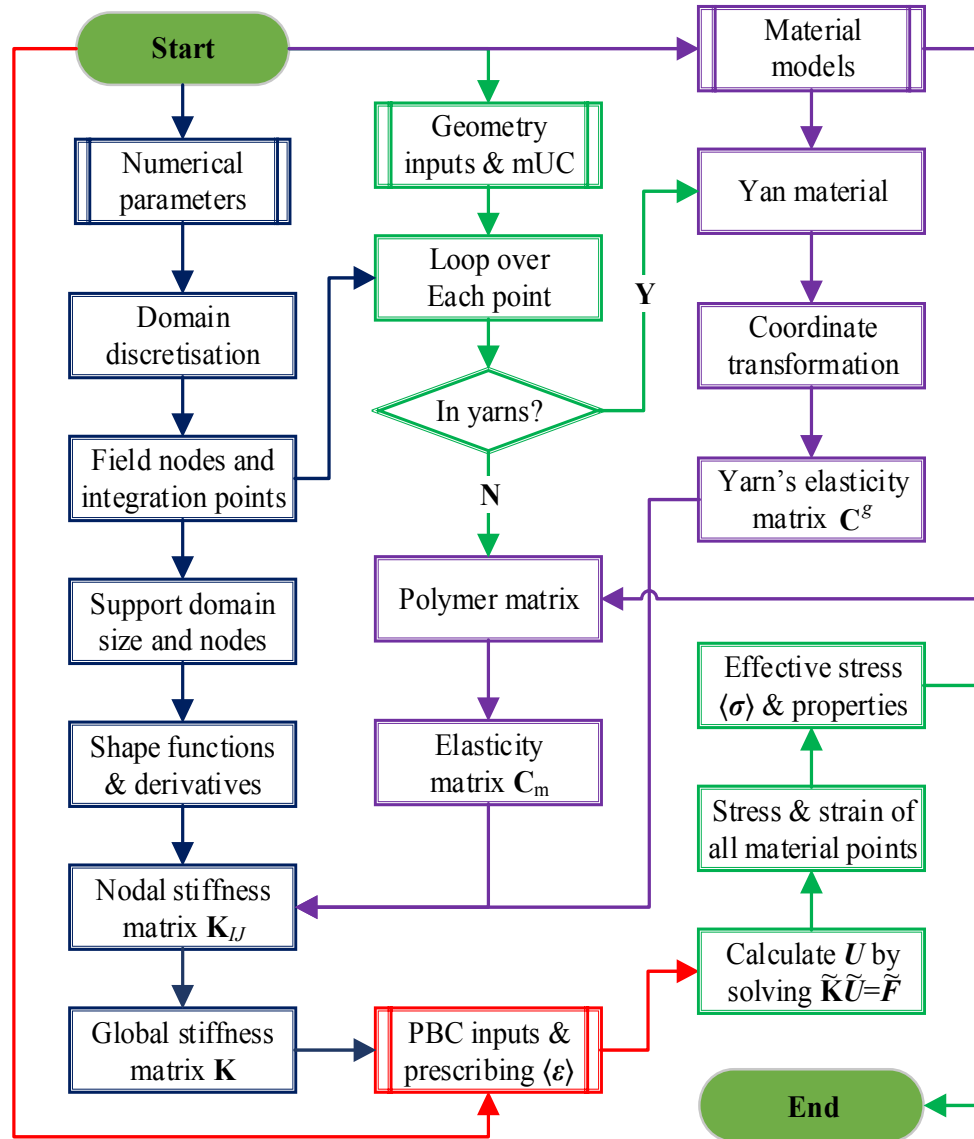
Figure 4.35: Flow chart of the standard meshfree program

It should be noted that the use of the standard weak-form meshfree method in the program has been reflected not only in discretising the mUC domain using field nodes but also in calculating the shape functions, the nodal stiffness matrices and the strains of all material

points from the displacements of field nodes. In the following four sections, the inputs of the meshfree program, the choice of numerical parameters, the strategy of UC domain discretisation and the highlights of the meshfree-based implementation will be detailed.

4.6.2 Summary of input parameters

The input parameters of this program are summarised in Table 4.7. As can be seen from the table, the inputs consist of four groups, namely, i) the geometry parameters for the mUCs of plain, twill and 3D woven composites, ii) the numerical parameters for domain discretisation, determination of support domain size and shape function calculations, iii) the material parameters for the polymer matrix and yarn material, and iv) the prescribed macroscopic strain $\langle \boldsymbol{\varepsilon} \rangle$ for a given admissible loading case.

Table 4.7: Summary of the inputs of the standard meshfree program

Type	Variable	Description
Geometry parameters	WCT	Weave type (1: plain, 2: twill, 3: 3D)
	UCT	UC type (1: normal, 2: off-axis)
	$L, W, H, H_{\mathrm{w}}, ...$	Dimensional parameters
	$\lambda_{\mathrm{w}}, \lambda_{\mathrm{fa}}, \lambda_{\mathrm{fb}}, \lambda_{\mathrm{b}}$	Dimensionless parameters
Numerical parameters	nFx, nFy, nFz	No. of nodes in each direction
	nCx, nCy, nCz	No. of cells in each direction
	$\alpha_{\mathrm{s}}, d_{\mathrm{c}x}, d_{\mathrm{c}y}, d_{\mathrm{c}z}$	Support domain parameters
	$\theta, q, a_0, a_1, a_2, a_3$	Constants for RBF and MK
Material properties	$E_{\mathrm{m}}, v_{\mathrm{m}}$	Material properties of matrix
	$E_{\mathrm{L}}, E_{\mathrm{T}}, v_{\mathrm{LT}}, v_{\mathrm{TT}}, G_{\mathrm{LT}}$	Material properties of yarn material
PBC	ALC	Admissible loading case (1, 2, …)
	$\langle \boldsymbol{\varepsilon} \rangle$	Prescribed macroscopic strain

Here, it should be noted that the use of variable WCT allows the user to choose a specific type of woven composites by assigning an integer, i.e. 1 for plain woven composites, 2 for twill woven composites and 3 for 3D woven composites. It should be further noted that apart from including the normal mUCs presented in this chapter, which are used to predict the elastic properties in the normal directions, the off-axis mUCs, which will be

presented in Chapter 5, have also been included in this meshfree program for the sake of predicting the elastic properties in off-axis directions. In terms of variable ALC, it is used to determine the type of admissible loading case. The range of this variable is dependent on the woven composites being predicted. For example, if it is to predict the properties of normal plain woven composites, this variable should have four options, i.e. 1, 2, 3 and 4, as indicated in Table 4.2.

4.6.3 Choice of numerical parameters

Clearly, the first, third and fourth groups of parameters in Table 4.7 are fixed for a given type of woven composites and a given admissible loading case. However, the inputs in the second group are numerical parameters, and they are to be determined. Here, it should be noted that there is no open parameter in the MLS technique. To determine the optimum values of these parameters, sensitivity studies can be performed to examine the influence of their values on the numerical results obtained. However, since there are more than 15 open parameters, conducting sensitivity studies for such a large number of free parameters would be a difficult task on one hand and exceed the main scope of the present research on the other hand.

Table 4.8: Constants for the RBF and MK techniques

	θ	q	a_0	a_1	a_2	a_3
RBF	0.75	0.5	0.75	1.0	1.0	1.0
	θ	a_0	a_1	a_2	a_3	
MK	1	0	$1/d_{cx}$	$1/d_{cy}$	$1/d_{cz}$	

For simplicity, the parameters of the RBF and MK techniques are fixed to be within the commonly used ranges [154], and their specific values used in this research are listed in Table 4.8, where the last three parameters of the MK technique are defined to be the reciprocals of the average nodal spacing in the X, Y and Z directions, i.e. d_{cx}, d_{cy} and d_{cz}. Based on the above simplification, sensitivity studies would need to be performed to identify the optimum values only for the remaining seven parameters (i.e. nFx, nFy, nFz, nCx, nCy, nCz and α_s), which will be addressed in detail in Section 4.7.1.

4.6.4 Strategy of domain discretisation

Theoretically, the domain representing the mUC can be discretised based on arbitrarily distributed field nodes. However, a uniform distribution of field nodes is chosen in this work since such a distribution produces symmetrical node pairs on the boundary of the domain, simplifying the procedure for enforcing PBCs. Here, it should be noted that if an arbitrary distribution of field nodes is used, further treatments such as that based on the polynomial interpolation [147] need to be imposed to ensure that the PBCs applied to the arbitrarily defined boundary nodes are consistent. In terms of the discretisation of the domain for conducting numerical integrations, a Lagrangian background grid consisting of regularly distributed cells is imposed for simplicity, and the first order Gauss-Legendre quadrature is used to calculate the integrals associated with each background cell.

4.6.5 Highlights of meshfree-based implementation

As discussed in the first Chapter, one of the highlights of this research is the development of the meshfree-based UC modelling methodology to simultaneously address the problem of a reduced accuracy in analytical approaches and the concern of highly complex and time-consuming pre-processing in the FEM-based approaches, i.e. the needs for explicitly creating constituent geometries of woven composites, discretising the geometries using high quality elements and meshes and assigning the ever-changing material orientations for the wavy yarns. Clearly, the problem of a reduced accuracy in analytical approaches, which originates from the geometry simplifications required to implement the analytical nature, has been naturally addressed by the development of high-fidelity mUCs with the internal features such as the cross-section and waviness of yarns being treated detailly. In terms of the complexity that inherently exists in the FEM-based approaches, it has been eliminated by implementing the high-fidelity mUC models using the standard weak-form meshfree method, as will be demonstrated in the following paragraphs.

The elimination of the complexity associated with the FEM-based approaches by using the standard weak-form meshfree method can be illustrated based on Fig. 4.20. As can be seen in the figure, there is no need to explicitly create the geometries for the constituents of the woven composites of homogenisation. Instead, what needed is to firstly assume a domain block with its overall dimensions being the same as those of the mUC model. Then, this domain block is discretised using a number of field nodes, as well as a number

133

of background cells. After that, numerical integrations are performed over all background cells. Here, depending on the order of the integration, a number of material or integration points are assigned for each background cell, and a support domain and thus a number of support nodes are identified for each integration point, based on which the meshfree-based shape functions corresponding to the support nodes are calculated for subsequent calculations of the nodal stiffness matrix, $\mathbf{K}_{IJ}$, and thus the global stiffness matrix $\mathbf{K}$.
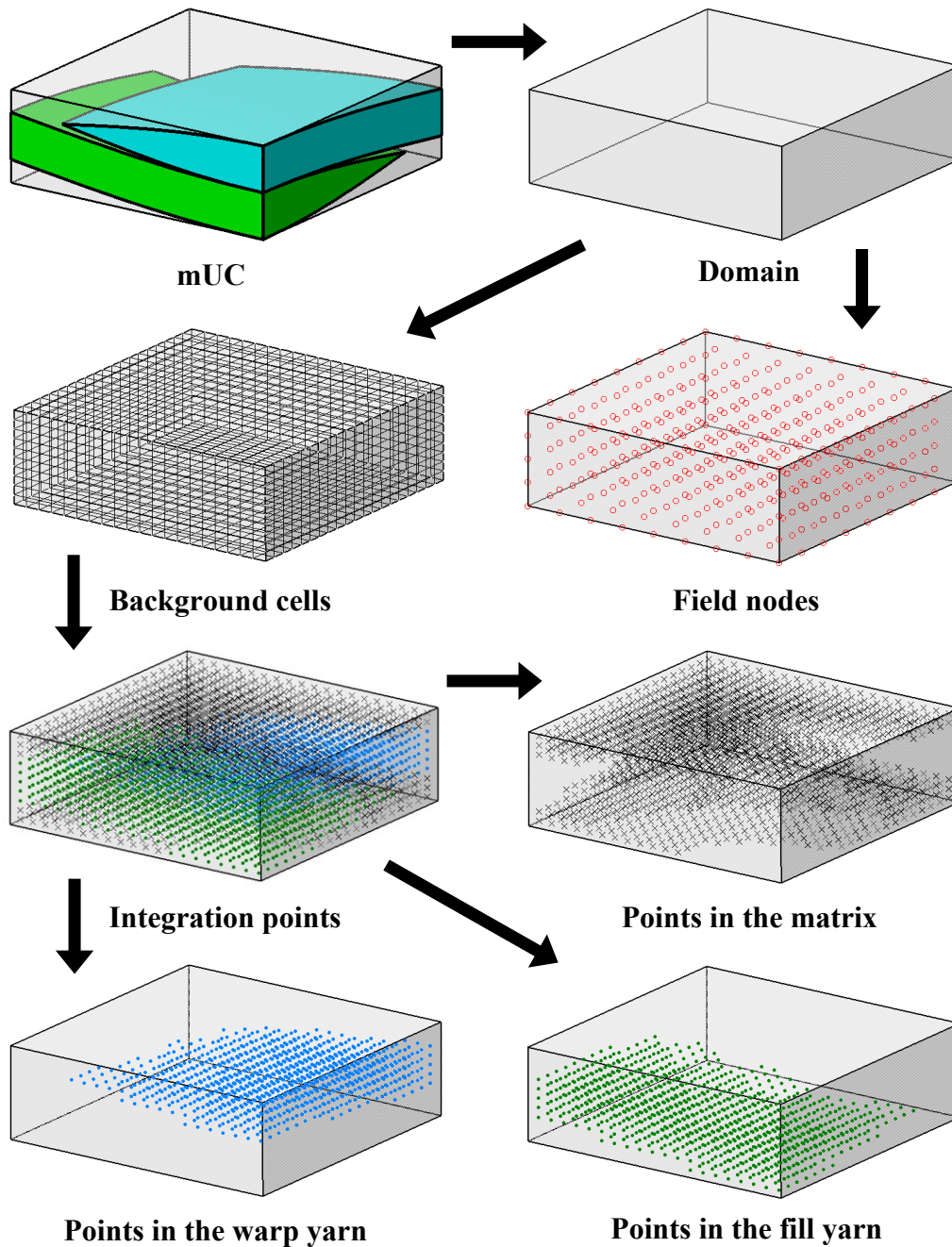
Figure 4.36: Meshfree discretisation of the domain representing the mUC

Here, it should be noted that before calculating the nodal stiffness matrix the relative location of each integration point is identified based on the analytical equations developed for describing the surfaces of the yarns in the mUC. If an integration point is not within the yarns, it belongs to the polymer matrix, and the elasticity matrix for isotropic materials, $\mathbf{C}_{\mathrm{m}}$, as defined in Eq. (2.5), is substituted into Eq. (3.88) to calculate its nodal stiffness matrix. On the contrary, if an integration point belongs to a yarn, the elasticity matrix for transversely isotropic materials in the LCS, $\mathbf{C}^{l}$, as defined in Eq. (2.13), is utilised for subsequent calculation of the nodal stiffness matrix. Here, it should be pointed out that if there exists waviness in the yarn to which the integration point belongs, its undulation angle (i.e. material orientation) needs to be calculated by using the analytical equation developed for describing the yarn's waviness. Then, based on Eq. (2.54) or the procedure described in Section 2.4.3, the elasticity matrix in the LCS can be transformed into that in the GCS, $\mathbf{C}^{g}$, which is the constitutive matrix that can be directly substituted into Eq. (3.88) to calculate the nodal stiffness matrix.

From the above description, we can see that the node-based domain discretisation makes it possible to eliminate the needs for explicitly creating constituent geometries of woven composites and discretising them with elements. Also, based on the high-fidelity mUC models, the relative location of each integration point can be identified and thus the internal architecture of woven composites can be *implicitly* implemented in combination with the standard weak-form meshfree method. Furthermore, the need for assigning the ever-change material orientation of the wavy yarns can be effectively avoided by using the analytical equations developed for describing the waviness of yarns and the coordinate transformation defined between the elasticity matrix in the LCS and that in the GCS. In sum, it is the combination of the high-fidelity mUC models with the standard weak-form meshfree method that the problems that inherently exist in analytical approaches and the FEM-based approaches are simultaneously addressed. Therefore, it is expected that the meshfree-based UC modelling methodology is an accurate and simple approach for the prediction of the elastic properties of woven composites. In the next section, a number of numerical examples will be presented and discussed to confirm the effectiveness and accuracy of the meshfree-based UC modelling approach.

4.7 Results and discussion

4.7.1 Examples on plain woven composites

The examples that will be presented in this section are mainly based on EP121-C15-53, which is the plain woven CFRP composite material that was utilised in Section 4.1.2 to observe and fit the cross-section and waviness of typical yarns in woven composites. The geometry configuration and material inputs of this material are given in Table 4.9. In this table, the values of the geometry parameters are averaged ones and were obtained by measuring the micrographs of this material. For the material properties of the epoxy resin of yarn material, they were determined from the experimental tests that will be detailed in Section 5.5.1.

In this section, eight numerical examples will be discussed, with the first six examples being based on EP121-C15-53. To be specific, the first two examples were conducted to predict the elastic properties in the normal and off-axis directions. In the subsequent three examples, numerical studies were performed to investigate the sensitivity of the predicted results to the open numerical parameters, i.e. the number of field nodes, the number of background cells and the support domain scaling coefficient. For the fifth example, it was designed to compare the results calculated by utilising the three types of shape function construction techniques, i.e. the MLS, RBF and MK techniques. In terms of the last two examples, two additional types of plain woven composites that have been investigated in the published research were considered, and the results derived by utilising the meshfree approach were compared with those found in the literature.

Table 4.9: Geometry information and material inputs of EP121-C15-53

Weave geometry	L	W	H	λ	
	1.0	1.0	0.28	0.9	
Yarn property	E_{L}	E_{T}	v_{LT}	v_{TT}	G_{LT}
	161.64	10.57	0.27	0.33	5.52
Matrix property	E_{m}	v_{m}			
	3.11	0.36			

4.7.1.1 Elastic properties in the normal directions

In the first example, which was conducted to predict the elastic properties in the normal directions, the domain representing the normal plain woven mUC was discretised with a total number of 13×13×7 field nodes, i.e. 1183 nodes, as well as a number of 60×60×30 background cells, i.e. 108000 cells. Also, the MK technique was utilised, and the support domain scaling coefficient, α_s, was set to 2.5. Here, it should be noted that the values of the above numerical parameters were determined from the sensitivity studies that will be presented later. The predicted elastic properties of this material in the normal directions are given in Table 4.10, where in the subscripts the three numbers, 1, 2 and 3, represent the warp, fill and through-the-thickens directions, respectively. The reference range of the elastic modulus of this material in the warp or fill direction, which was adapted from the datasheet on the material supplier's website [193], has also been listed in the table for comparison. As can be clearly seen from this table, the predicted elastic modulus in the warp or fill direction is in the reference range, partially validating the normal plain woven mUC and the meshfree-based modelling approach.

Table 4.10: Predicted *normal* elastic properties of EP121-C15-53 (moduli in GPa)

Property	E_1/E_2	E_3	v_{12}	v_{23}/v_{13}	G_{12}	G_{23}/G_{31}
Predicted	53.681	9.086	0.045	0.409	3.557	2.828
Gurit [193]	50 ~ 55	-	-	-	-	-

4.7.1.2 Elastic properties in the off-axis directions

In the second example, which was aimed to predict the elastic properties in the off-axis directions, the domain representing the off-axis plain woven mUC model, which will be described in Section 5.2.1, was discretised with a total number of 10×20×7 field nodes, i.e. 1400 nodes, as well as a number of 45×90×30 background cells, i.e. 121500 cells. Here, the values of these parameters were determined by simply scaling those used in discretising the normal mUC model. Specifically, if the number of nodes or cells used to discretise the domain representing the normal mUC model in the X direction is n_x and the dimensions of the normal and off-axis mUCs in this direction are denoted as L and L_0, respectively, the number of fields nodes utilised to discretise the domain representing

the off-axis mUC model is then determined as $n_x L_0 / L$. In this example, the MK technique was again used, and the support domain scaling coefficient, α_s, was also set to 2.5. Table 4.11 shows the predicted results, where in the subscripts the lowercase letters, a and b, represent the 45° and 135° directions. It is evident from this figure that the predicted elastic modulus in the 45° or 135° direction agrees well with the experimental value, which was measured from a uniaxial tension test conducted at a strain rate approximately of 10^{-5}/s. This again confirms the accuracy and effectiveness of the meshfree-based UC modelling approach in predicting the elastic properties of plain woven composites.

Here, it is should be noted that off-axis mUCs have also been developed for twill and 3D woven composites, and they will be presented in Chapter 5. However, no examples on predicting the off-axis elastic properties of twill or 3D woven composites will be given, owing to the inaccessibility of composites for conducting tests and the unavailability of experimental or numerical results in the published research, at the time of undertaking the present research.

Table 4.11: Predicted *off-axis* elastic properties of EP121-C15-53 (moduli in GPa)

Property	E_a/E_b	E_3	ν_{ab}	ν_{b3}/ν_{a3}	G_{ab}	G_{b3}/G_{3a}
Predicted	10.864	8.986	0.595	0.158	10.273	2.796
Experiment	10.379	-	-	-	-	-

4.7.1.3 Sensitivity to domain discretisation with field nodes

Although the number of open parameters in Table 4.7 has been significantly reduced by fixing the constants of the RBF and MK techniques to their commonly used values, it is still not an easy task to investigate the influence of the remaining seven parameters on the predicted results. For further simplifying the investigation, the numbers of field nodes used to discretise the mUC domain in the three directions. i.e. nFx, nFy and nFz, were controlled such that they are proportional to each other, i.e. $nFx : nFy : nFz = 2 : 2 : 1$. The same treatment was also applied to the parameters relating to the numbers of background cells in the three directions, i.e. nCx, nCy and nCz, with their relative ratios being fixed in the same way, i.e. $nCx : nCy : nCz = 2 : 2 : 1$. Based on such treatments, the sensitivity study for the open parameters can be simplified into the following three cases:

1) Sensitivity study of the total number of field nodes, $N_{\mathrm{F}} = n\mathrm{F}x \times n\mathrm{F}y \times n\mathrm{F}z$;

2) Sensitivity study of the number of background cells, $N_{\mathrm{C}} = n\mathrm{C}x \times n\mathrm{C}y \times n\mathrm{C}z$;

3) Sensitivity study of the support domain scaling coefficient α_{s}.

Table 4.12: Elastic properties predicted by using different N_{F} (moduli in GPa)

N_{F}	E_1	E_3	v_{12}	v_{23}	G_{12}	G_{23}
75	54.037	9.403	0.047	0.396	3.577	3.041
196	53.925	9.260	0.046	0.404	3.572	2.968
405	53.802	9.177	0.046	0.407	3.570	2.904
726	53.817	9.135	0.045	0.409	3.569	2.859
1183	53.739	9.078	0.045	0.410	3.561	2.828
1800	53.768	9.078	0.045	0.411	3.561	2.824
2601	53.755	9.083	0.045	0.411	3.565	2.827
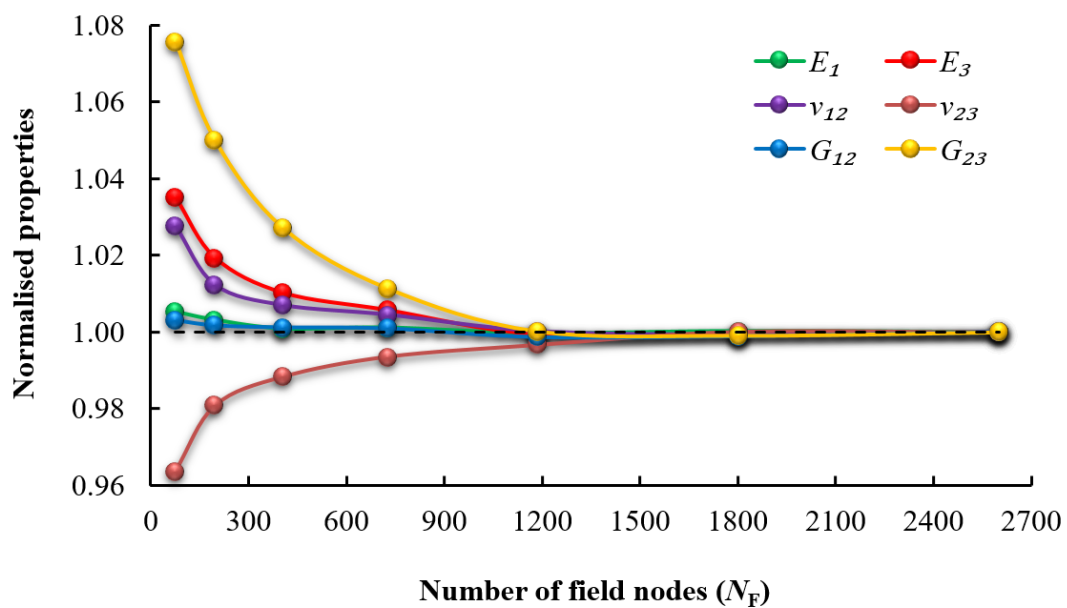
Figure 4.37: Variations of the predicted results on the number of field nodes

In the sensitivity study of the number of field nodes, the number of background cells was set to a high value (i.e. 256000) to minimise its influence on the sensitivity study as much as possible. Similarly, the support domain scaling coefficient was set to be 2.5, which is a value in the typical range of α_{s}, i.e. 2.0~3.0, as suggested in [154]. Table 4.12 lists the elastic properties predicted by varying the total number of field nodes from 75 to 2601.

To better examine the sensitivities of the predicted results with respect to the number of field nodes, all the results in Table 4.12 were normalised against those corresponding to the case of $N_F = 2601$, and the resulting curves are shown in Fig. 4.37. Clearly, it can be seen that all the curves diverge when the number of field nodes is smaller than 1183, i.e. 13×13×7, after which they converge to the same plateau, meaning that a total number of 1183 field nodes should be enough for obtaining convergent results.

4.7.1.4 Sensitivity to domain discretisation with background cells

Table 4.13: Predicted elastic properties at different N_C (moduli in GPa)

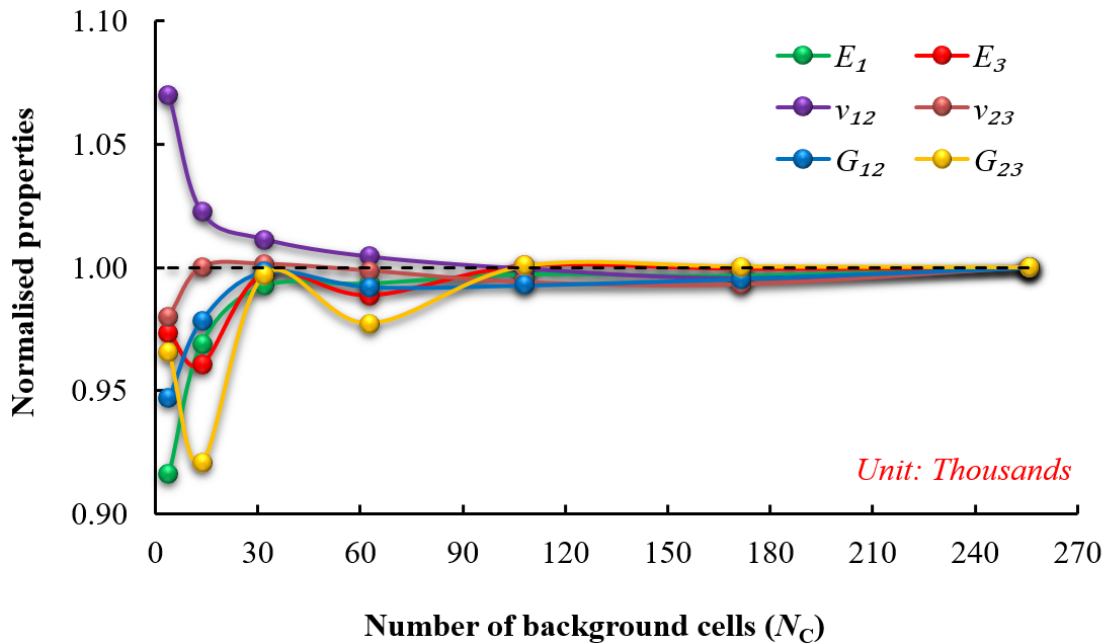| N_C	E_1	E_3	v_{12}	v_{23}	G_{12}	G_{23}
4000	49.259	8.843	0.048	0.403	3.377	2.730
13500	52.087	8.727	0.046	0.411	3.489	2.603
32000	53.353	9.065	0.046	0.412	3.560	2.819
62500	53.401	8.983	0.045	0.411	3.538	2.763
108000	53.603	9.092	0.045	0.409	3.540	2.828
171500	53.569	9.081	0.045	0.409	3.549	2.828
256000	53.755	9.083	0.045	0.411	3.565	2.827

Figure 4.38: Variations of the results on the number of background cells

140

To minimise the coupling effects caused by the other two factors in the sensitivity study of the number of background cells, the number of field nodes was set to a high value, i.e. 2601, while the support domain scaling coefficient was set to 2.5. Table 4.13 shows the results predicted by varying the total number of background cells from 4000 to 25600. To better reveal the sensitivities of the predicted results on the number of background cells, all the results in Table 4.13 were again normalised against those corresponding to the case of $N_C = 256000$, and the resulting curves are shown in Fig. 4.38. It is clearly seen in this figure that the predicted elastic properties converge only when the number of background cells exceeds a threshold of 108000, i.e. $60 \times 60 \times 30$.

4.7.1.5 Sensitivity to support domain size

In the sensitivity study of the support domain scaling coefficient, α_s, the number of field nodes and that of background cells to were fixed to their thresholds, i.e. 1183 and 108000. Table 4.14 lists the results predicted by varying the value of α_s was varied from 2 to 4. Again, all the results in this table were normalised to those corresponding to the case of $\alpha_s = 2.5$, and the resulting curves are shown in Fig. 4.39.

Table 4.14: Predicted elastic properties at different α_s (moduli in GPa)

α_s	E_1	E_3	v_{12}	v_{23}	G_{12}	G_{23}
2.00	53.876	9.136	0.045	0.409	3.570	2.834
2.25	53.876	9.115	0.045	0.410	3.569	2.832
2.50	53.681	9.086	0.045	0.409	3.557	2.828
2.75	53.819	9.110	0.045	0.410	3.569	2.838
3.00	53.269	9.013	0.045	0.405	3.534	2.840
3.25	53.573	9.049	0.046	0.409	3.564	2.834
3.50	52.677	8.725	0.045	0.405	3.469	2.659
3.75	52.468	8.669	0.045	0.404	3.447	2.630
4.00	49.900	8.033	0.037	0.364	3.053	2.401

An examination of Fig 4.39 suggests that the sensitivities of the predicted results in this case are different from those in the former cases. Specifically, the predicted results in the former two cases show monotonic convergences, with the results diverging if the value of the parameter of investigation is smaller than the threshold and becoming convergent

if the threshold is exceeded. On the contrary, the predicted results in this case converge only when the value of α_s is in a range of approximately 2.0~3.25 and diverge if the value of α_s is not in this range. Here, it should be noted that the case of $\alpha_s < 2$ is not considered since meshfree calculations often fail owing to the presence of singularity in the moment matrix in the calculation of meshfree shape functions.
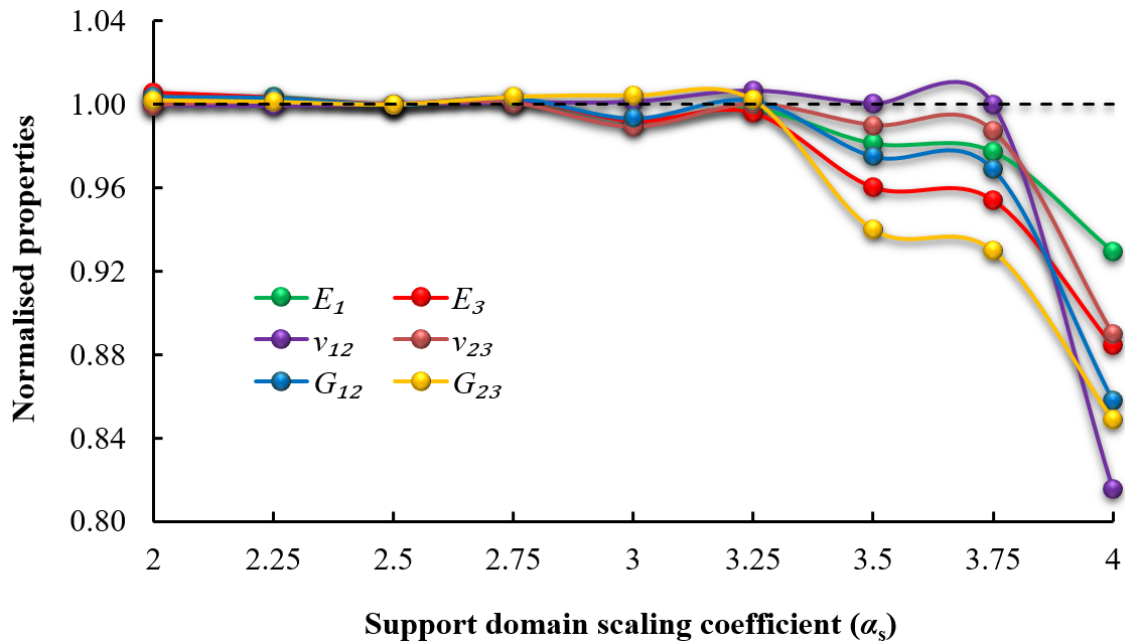
Figure 4.39: Variations of the predicted results on the scaling coefficient (α_s)

The convergent range of the support domain scaling coefficient derived here is similar to that suggested in [154], which is 2.0~3.0. This finding indicates that when performing a meshfree analysis the size of a support domain should be defined such that it is neither too small nor too large. The reason for a support domain being not too small is that if it is not big enough, there will be an insufficient number of support nodes to approximate filed variables, which may result in a reduced accuracy and in some cases computational failures, such as the presence of singularity in the moment matrix. On the other hand, if a support domain is excessively large, it may include the field nodes that do not have any influence on the point being interpolated, leading to excessive computational costs and a reduced accuracy in the results obtained, as indicated in Fig. 4.39.

In the above sensitivity analysis, the curves in Fig. 4.39 were by normalising all the results in Table 4.14 against those corresponding to the case of $\alpha_s = 2.5$. However, it should be

noted that the normalisation can be performed based on the results corresponding to any other cases since the convergences of the resulting curves do not depend on the way of conducting the normalisation, as suggested in Fig. 4.40, where the curves were obtained by normalising all the data in Table 4.14 against those corresponding to the case of $\alpha_s = 3.5$. As can be seen clearly in this figure, although the resulting curves have been altered compared to those shown in Fig. 4.39, it can be concluded that the convergent range of the support domain scaling coefficient is still 2.0~3.25.
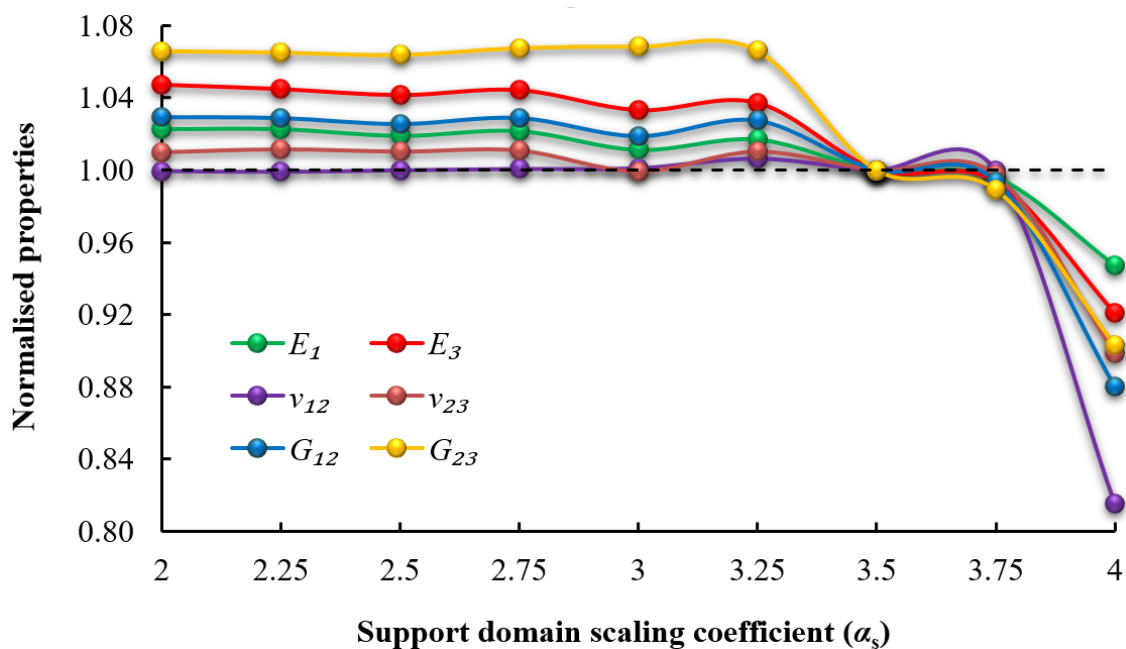
Figure 4.40: Results normalised to those corresponding to the case of $\alpha_s = 3.5$

4.7.1.6 Comparison between MLS, RBF and MK

In addition to the above sensitivity studies, further numerical calculations were performed to compare the results obtained by using the three shape function construction techniques, i.e. the MLS, RBF and MK techniques, and the predicted results are given in Table 4.15. Here in this table, the differences between the results obtained by using these techniques were also calculated. It is clearly shown in this table that the elastic properties predicted by utilising the three techniques agree reasonably well with each other, with a maximum difference of only 3.77%. Furthermore, it can be found that the RBF and MK techniques are able to produce closer predictions, compared to the MLS technique. It is believed that the presence of smaller differences by using the RBF and MK techniques is due to the

fact that both the RBF and MK techniques possess the Kronecker delta function property, whereas the MLS technique does not.

Table 4.15: Results predicted by using MLS, RBF & MK (moduli in GPa)

Property	E_1/E_2	E_3	v_{12}	v_{23}/v_{13}	G_{12}	G_{23}/G_{31}
A: MLS	53.681	9.086	0.045	0.409	3.557	2.828
B: RBF	53.097	9.119	0.046	0.410	3.574	2.935
C: MK	53.083	9.106	0.046	0.410	3.566	2.894
|(A-B)/A|	1.09%	0.36%	2.02%	0.29%	0.48%	3.77%
|(A-C)/A|	1.11%	0.22%	1.80%	0.34	0.26%	2.35%
|(B-C)/A|	0.03%	0.13%	0.22%	0.05%	0.22%	1.42%

4.7.1.7 Comparison of the meshfree method with other methods

Table 4.16: Inputs for CF-Composite-A (adapted from [131] & [194])

Weave geometry	L	W	H	λ	
	2.0	2.0	0.196	0.911	
Yarn property	E_L	E_T	v_{LT}	v_{TT}	G_{LT}
	137.3	10.79	0.26	0.46	5.394
Matrix property	E_m	v_m			
	4.511	0.38			

To further validate the meshfree-based modelling approach and the normal plain woven mUC model, two additional types of plain woven composites that have been examined in the published research were considered in the present work, and their elastic properties were calculated by using the meshfree method. The first type of material was based on the plain woven composites investigated by Tanov and Tabiei [131] and Jiang *et al.* [194] using analytical approaches. For convenience, this material is denoted as CF-Composite-A. The inputs for this material are listed in Table 4.16, and they were adapted from [131] and [194]. Here, the dimensionless parameter, λ, was calculated by using Eq. (4.17), and the yarn volume fraction used in calculating λ was 0.58. For easy comparison, the elastic properties predicted using the meshfree method, as well those found in the literature, are

listed in Table 4.17. As can be seen from this table, the meshfree-based predictions agree well with both the analytical results and the experimental data.

Table 4.17: Summary of outputs for CF-Composite-A (moduli in GPa)

Approach	E_1/E_2	E_3	v_{12}	v_{23}/v_{13}	G_{12}	G_{23}/G_{31}
Four-cell [131]	45.08	10.12	0.056	0.464	3.8	2.763
Sub-cell [194]	46.35	-	0.052	-	3.83	-
Exp. [195]	49.80	-	0.068	-	3.83	-
MLS	45.896	10.120	0.058	0.465	3.654	3.017
RBF	46.131	10.104	0.057	0.465	3.641	2.836
MK	46.038	10.104	0.057	0.466	3.642	2.843

Table 4.18: Inputs for CF-Composite-B (adapted from [95])

Weave geometry	L	W	H	λ	
	1.0	1.0	0.188	1.0	
Yarn property	E_L	E_T	v_{LT}	v_{TT}	G_{LT}
	170.0	12.84	0.33	0.27	9.06
Matrix property	E_m	v_m			
	4.35	0.36			

Table 4.19: Summary of outputs for CF-Composite-B (moduli in GPa)

Approach	E_1/E_2	E_3	v_{12}	v_{23}/v_{13}	G_{12}	G_{23}/G_{31}
FEM [95]	69.646	11.289	0.042	0.417	7.007	4.372
Exp. [196]	67.5	-	-	-	-	-
MLS	66.029	11.401	0.046	0.395	6.743	4.052
RBF	65.282	11.413	0.046	0.395	6.751	4.278
MK	65.679	11.397	0.046	0.395	6.741	4.087

The second type of material was based on the plain woven CFRP composites investigated by Bacarreza *et al.* [95] using the FEM. The inputs for this material, which is here referred to as CF-Composite-B, were adapted from [95], and they are listed in Table 4.18. Table

4.19 shows the resulted derived by utilising different types of methods, from which it can be found that the meshfree-based predictions are in good agreement with the FEM results and the experimental data.

4.7.2 An example on twill woven composites

To validate the normal twill woven mUC model, a meshfree example was performed by considering the twill woven CFRP composites investigated by Dixit *et al.* [98]. The inputs for this material, which were adapted from [98], are detailed in Table 4.20, and the meshfree-based results are presented in Table 4.21, in comparison with the FEM results [98] and the experimental values given in [96]. Clearly, the meshfree-based results show reasonable agreements with both the FEM and experimental results.

Table 4.20: Inputs for the twill woven composites (adapted from [98])

Weave geometry	L	W	H	λ	
	1.0	1.0	0.22	0.4	
Yarn property	E_L	E_T	v_{LT}	v_{TT}	G_{LT}
	220.69	13.79	0.20	0.25	8.97
Matrix property	E_m	v_m			
	3.10	0.39			

Table 4.21: Outputs for the twill woven composites (moduli in GPa)

Approach	E_1/E_2	E_3	v_{12}	v_{23}/v_{13}	G_{12}	G_{23}/G_{31}
FEM [98]	56.97	8.81	0.062	0.406	4.05	2.31
Exp. [96]	55.25	-	0.055	-	3.55	-
MLS	58.355	9.010	0.057	0.396	4.015	2.588
RBF	58.466	8.947	0.055	0.398	3.755	2.365
MK	58.598	8.930	0.056	0.401	3.749	2.415

4.7.3 An example on 3D woven composites

To validate the improved normal mUC model for 3D orthogonal woven composites in terms of predicting the elastic properties, a meshfree example was also conducted based

on the composites investigated by Li *et al.* [145] and Bogdanovich [101]. The inputs for this type of material are given in Table 4.22, where the dimensionless parameter for each type of yarn was determined as the ratio of the width of the yarn with respect to the dimension of the mUC. Furthermore, it is worth noting that the geometry parameter, H_b, is not included since it is not an independent variable, i.e. $H_b = H - 2H_w - H_{fa} - H_{fb}$. Table 4.23 shows the results predicted by using the improved mUC model in combination with the meshfree method, as well as those found in the literature. Here, it can be found that the meshfree-based results are in good agreements with the FEM and experimental results, confirming the accuracy and effectiveness of the improved mUC model and the meshfree-based UC modelling approach.

Table 4.22: Inputs for the 3D woven composites (adapted from [145] & [101])

	L	W	H	λ_w	λ_{fa}
Weave geometry	2.309	2.54	2.472	0.821	0.667
	λ_{fb}	λ_b	H_w	H_{fa}	H_{fb}
	0.937	0.179	0.637	0.292	0.614
Yarn property	E_L	E_T	v_{LT}	v_{TT}	G_{LT}
	53.12	14.46	0.266	0.268	4.24
Matrix property	E_m	v_m			
	3.17	0.35			

Table 4.23: Outputs for the 3D woven composites (moduli in GPa)

Approach	E_1	E_2	E_3	v_{12}	v_{23}	v_{13}	G_{12}	G_{23}	G_{31}
Ref. [145]	24.61	22.38	10.78	0.132	0.319	0.316	3.11	3.69	3.37
FEM [101]	27.31	25.70	9.98	0.125	0.448	0.432	3.58	3.52	3.34
Exp. [101]	24.68	20.75	-	0.11	-	-	-	-	-
MLS	24.162	21.512	10.470	0.133	0.324	0.312	3.083	3.341	3.079
RBF	24.185	21.468	10.502	0.134	0.327	0.315	3.086	3.393	3.117
MK	24.067	21.317	10.471	0.132	0.325	0.314	3.077	3.391	3.118

4.8 Summary

In this chapter, some basic concepts and assumptions in the geometry modelling of woven composites were firstly introduced. Then, the high-fidelity normal mUC models that have been developed for plain, twill and 3D woven composites were detailed. Here, analytical equations were formulated for describing the internal architecture of each type of woven composites, and the flexibility of some of these models was evaluated in comparison with the models found in the literature. Following the geometry modelling, the main concepts and the basic equations in the equivalence approach were briefed. Based on this approach, the PBCs for the normal mUC models under each admissible loading case were derived. After that, an in-house computer program which implements the mUC models using the standard weak-form meshfree method was introduced from the perspectives of its basic framework, the input parameters, the determination of the numerical parameters and the strategy for discretising the domain of homogenisation. Following the description of this program, it was argued that the combination of the high-fidelity mUCs with the meshfree method is capable of addressing the problems that exist in analytical approaches and the FEM-based approaches. Finally, a number of numerical examples conducted using the meshfree-based program to predict the normal and/or off-axis elastic properties of plain, twill and 3D orthogonal woven composites were presented. Good agreements were found between the meshfree-based predictions and those found in the literature, confirming the accuracy and effectiveness of the meshfree-based UC modelling approach and the high-fidelity mUC models. In some of these examples, the sensitivities of the predicted results to the open numerical parameters were also examined. It was found that the utilisation of higher numbers of field nodes and background cells generally produces better predictions, while the support domain scaling coefficient should be chosen in a relatively small range (i.e. 2.0 - 3.25) to maintain a reasonable degree of accuracy in the predictions. In addition, it was shown that the three types of shape function construction techniques were able to produce reasonable predictions, although the results predicted using the MLS technique were of slight differences compared to those obtained using the RBF and MK techniques. It is believed that the presence of the small discrepancies is as a consequence of the lack of the Kronecker delta function property only in the MLS technique.

# CHAPTER 5: MECHANICAL RESPONSE PREDICTION

5.1 Introduction

Apart from the prediction of the elastic properties of woven composites, which has been addressed in the previous chapter, another significant part of the present work is to extend the meshfree-based unit cell (UC) modelling approach for predicting the overall response of woven composites, and the corresponding procedure again involves three similar steps, namely, geometry modelling, constitutive modelling and overall response calculation. Clearly, for geometry modelling, the normal minimum unit cell (mUC) models presented in Chapter 4 can be directly used to predict the overall response under normal loading conditions, e.g. a load is applied in the warp direction. However, since woven composites feature different behaviours if loaded in different directions, off-axis mUC models have also been developed to evaluate the overall response under off-axis loading scenarios, which will be addressed in the second section of this chapter. For constitutive modelling, the inelastic behaviours of the constituents such as the nonlinear and strain rate-dependent behaviour of the polymer matrix and the anisotropic post-failure of the yarn material must be characterised to ensure an accurate prediction of the overall response, which will be detailed in Section 5.3. In terms of the last step, it involves implementing the mUC models and the constitutive models based on the explicit weak-form meshfree method and thus calculating the overall response for a prescribe history of periodic boundary conditions (PBCs), which will be discussed in Section 5.4. Following the above sections, a number of numerical examples for predicting the overall response of woven composites will be presented, and the predicted results will be discussed in comparison with experimental results, if applicable.

Here, it should be noted that woven composites may have different geometry dimensions in the warp and weft directions. An example of such type of woven composites is shown

in Fig. 5.1a, from where it can be seen that the length of periodicity in the warp direction is not equal to that in the weft direction, i.e. $L \neq W$. For convenience, this type of woven composites is often termed as non-balanced woven composites. From Fig. 5.1a, it is also indicated that the non-balanced nature necessitates the use of a non-orthogonal coordinate system and thus creates a non-rectangular unit cell (UC), complicating the derivation of PBCs and the enforcement of off-axis loading conditions. In view of such complexity in non-balanced woven composites, the prediction of the *off-axis* properties or response in the present research is restricted to balanced woven composites since their off-axis mUCs can still be modelled in orthogonal coordinate systems, as illustrated in Fig. 5.2a.
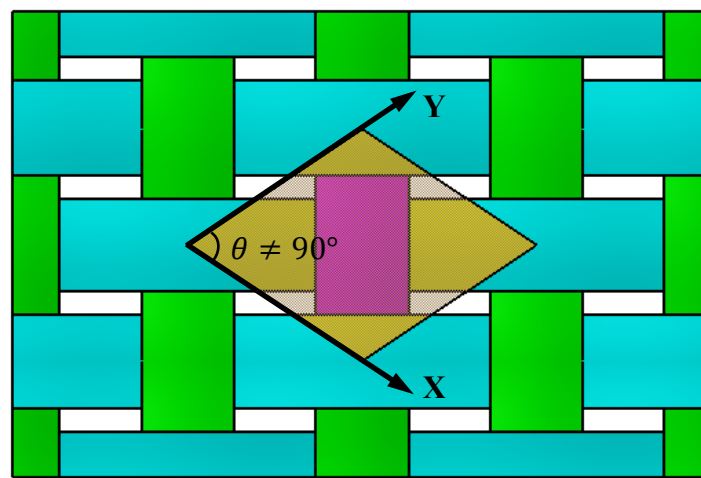
(a) Non-balanced woven composites and off-axis UC
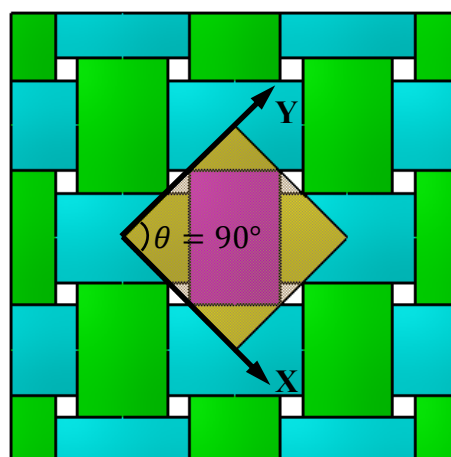

(b) Balanced woven composites and off-axis UC

Figure 5.1: Comparison of non-balanced & balanced woven composites

5.2 Off-axis mUCs and PBCs

5.2.1 Plain woven composites

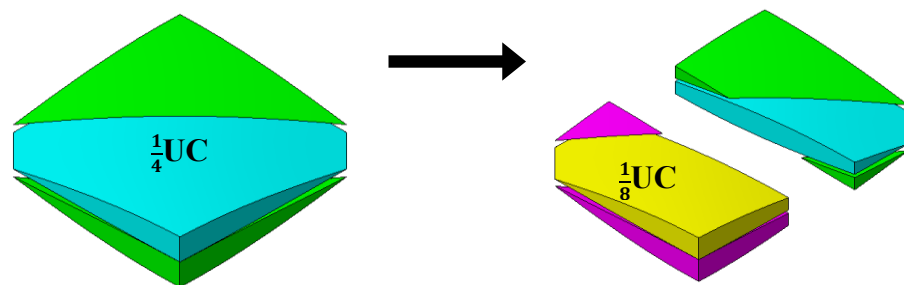#### 5.2.1.1 Off-axis mUC for plain woven composites

Similar to identifying the normal mUC for plain woven composites, the off-axis mUC can be obtained by exploiting all the symmetries in a step-by-step manner, as shown in Fig. 5.2. Here, it should be noted that the off-axis mUC is only 1/8 of the full-size UC.
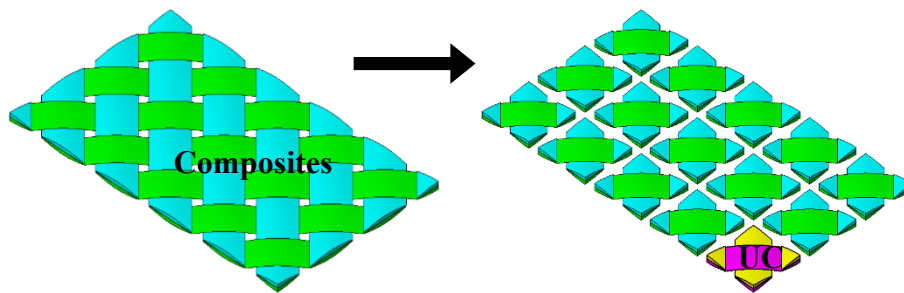
(a) Composite ply → full-size UC by using translational symmetries
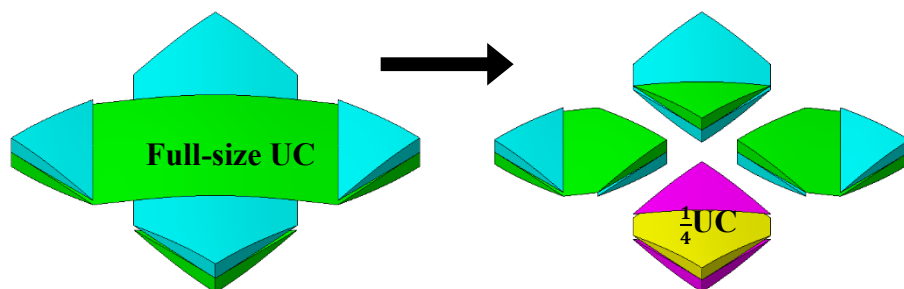
(b) Full-size UC → $\frac{1}{4}$UC by using reflectional symmetries

(c) $\frac{1}{4}$UC → $\frac{1}{8}$UC by using rotational symmetries

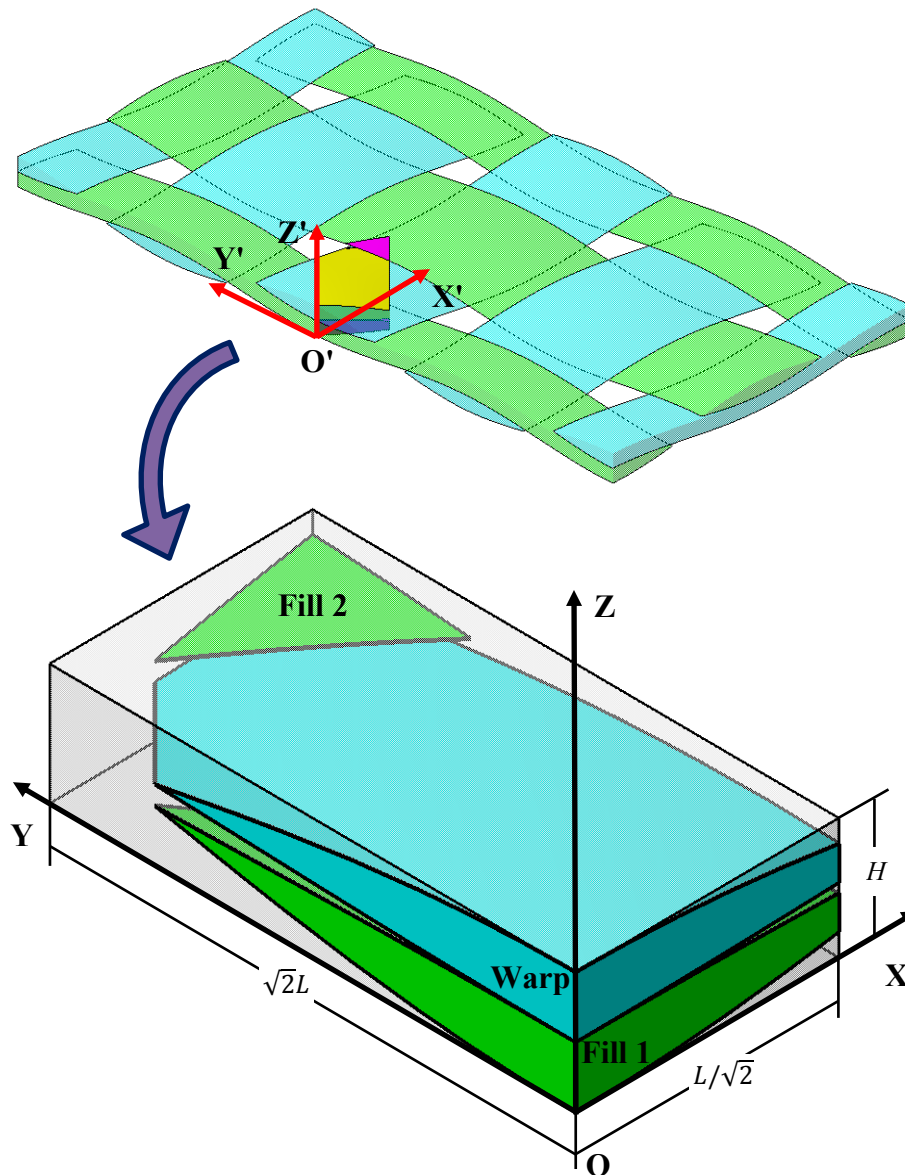**Figure 5.2: Domain reduction for off-axis plain woven composites**

Figure 5.3: The off-axis mUC model for plain woven composites

Due to the off-axis nature, it is problematic to directly describe the internal architecture of an mUC in its local coordinate system (LCS), i.e. OXYZ, as indicated in Fig. 5.3. To simplify this process, the description of an mUC can be initially addressed in the global coordinate system (GCS) of the composite material, i.e. O'X'Y'Z', based on which, the equations for describing the internal architecture of the off-axis mUC in the GCS can be rotated back to the LCS. Since the two coordinate systems can be brought together by rotating the LCS anti-clockwise with respect to its Z-axis for 45º, the transformation between the coordinate vectors of any given point, **A**, in the two coordinate systems can be expressed as follows:

$$\begin{Bmatrix} x' \\ y' \\ z' \end{Bmatrix} = \begin{bmatrix} \frac{\sqrt{2}}{2} & \frac{\sqrt{2}}{2} & 0 \\ -\frac{\sqrt{2}}{2} & \frac{\sqrt{2}}{2} & 0 \\ 0 & 0 & 1 \end{bmatrix} \begin{Bmatrix} x \\ y \\ z \end{Bmatrix} \tag{5.1}$$

where $\{x'\ y'\ z'\}^{\mathrm{T}}$ and $\{x\ y\ z\}^{\mathrm{T}}$ are the coordinate vectors of point **A** in the GCS and the LCS, respectively.

Using the transformation defined in Eq. (5.1) and combining the analytical equations that have been developed for describing the internal architecture of the normal mUC of plain woven composites, as detailed in Section 4.2, the analytical equations for describing the off-axis mUC of plain woven composites can be easily deduced, as summarised in Table C.1, Appendix C.

5.2.2.2 PBCs for off-axis plain woven composites

By comparing Fig. 5.2 and Fig. 4.2, it can be found that the symmetries used to obtain the off-axis mUC are not the same as those utilised in the case of obtaining the normal mUC. Thus, the PBCs derived for the normal mUC are not applicable to the off-axis mUC. Here, the equivalence approach is again employed to obtain the PBCs for the off-axis mUC of plain woven composites. However, it must be pointed out that the generic form of PBC equation, which has been defined in Eq. (4.87) and does not include the time dimension, are not directly applicable to the case of predicting the overall response. This is because in predicting the overall response of woven composites, a history of time-dependent PBCs needs to be prescribed to create an external dynamic loading such that a time-dependent relation between the volume average stress and strain can be subsequently derived, which consequently forms the overall response of the woven composites of homogenisation. To enable the equivalence approach for deriving PBCs for the case of predicting the overall response, Eq. (4.87) should be modified by including the time dimension, as follows:

$$\boldsymbol{u}(A,t) - \gamma \mathbf{T} \boldsymbol{u}(\bar{A},t) = -\langle \boldsymbol{\varepsilon}(t) \rangle \mathbf{T} \boldsymbol{x}^{O_{\bar{D}}} \tag{5.2}$$

However, it can be found by comparing the above equation with Eq. (4.87) that the only difference is the addition of a time variable in Eq. (5.2). This means that the PBCs for the case of predicting the overall response can be alternatively obtained by initially applying Eq. (4.87) to derive time-independent PBC equations and subsequently including the time

variables within the equations. Given that the only difference between the PBCs of the two cases is time, the time variable will be neglected for simplicity when presenting the PBCs for the case of predicting the overall response.
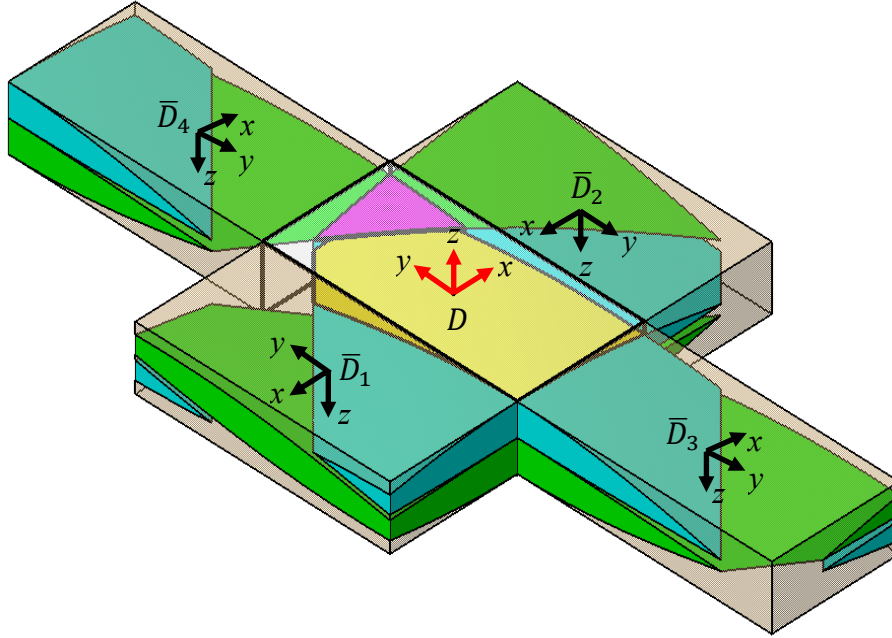

Figure 5.4: Off-axis mUC & adjacent subdomains of plain woven composites

Table 5.1: Relations between off-axis plain woven mUC & adjacent subdomains

	$\overline{D}_1$	$\overline{D}_2$	$\overline{D}_3$	$\overline{D}_4$
$\boldsymbol{T}_i$	$\begin{bmatrix} -1 & 0 & 0 \\ 0 & 1 & 0 \\ 0 & 0 & -1 \end{bmatrix}$	$\begin{bmatrix} -1 & 0 & 0 \\ 0 & -1 & 0 \\ 0 & 0 & -1 \end{bmatrix}$	$\begin{bmatrix} 1 & 0 & 0 \\ 0 & -1 & 0 \\ 0 & 0 & -1 \end{bmatrix}$	$\begin{bmatrix} 1 & 0 & 0 \\ 0 & -1 & 0 \\ 0 & 0 & -1 \end{bmatrix}$
$\boldsymbol{x}^{O\overline{D}_i}$	$\begin{bmatrix} -L_o \\ 0 \\ 0 \end{bmatrix}$	$\begin{bmatrix} L_o \\ 0 \\ 0 \end{bmatrix}$	$\begin{bmatrix} 0 \\ -W_o \\ 0 \end{bmatrix}$	$\begin{bmatrix} 0 \\ W_o \\ 0 \end{bmatrix}$
$\boldsymbol{x}^{\bar{A}_i}$	$\begin{bmatrix} -\frac{L_o}{2} \\ -\frac{W_o}{2} \le y \le \frac{W_o}{2} \\ -\frac{H}{2} \le z \le \frac{H}{2} \end{bmatrix}$	$\begin{bmatrix} \frac{L_o}{2} \\ -\frac{W_o}{2} \le y \le \frac{W_o}{2} \\ -\frac{H}{2} \le z \le \frac{H}{2} \end{bmatrix}$	$\begin{bmatrix} -\frac{L_o}{2} \le x \le \frac{L_o}{2} \\ -\frac{W_o}{2} \\ -\frac{H}{2} \le z \le \frac{H}{2} \end{bmatrix}$	$\begin{bmatrix} -\frac{L_o}{2} \le x \le \frac{L_o}{2} \\ \frac{W_o}{2} \\ -\frac{H}{2} \le z \le \frac{H}{2} \end{bmatrix}$
$\boldsymbol{x}^{A_i}$	$\begin{bmatrix} -\frac{L_o}{2} \\ y^{\bar{A}} \\ -z^{\bar{A}} \end{bmatrix}$	$\begin{bmatrix} \frac{L_o}{2} \\ -y^{\bar{A}} \\ -z^{\bar{A}} \end{bmatrix}$	$\begin{bmatrix} x^{\bar{A}} \\ -\frac{W_o}{2} \\ -z^{\bar{A}} \end{bmatrix}$	$\begin{bmatrix} x^{\bar{A}} \\ \frac{W_o}{2} \\ -z^{\bar{A}} \end{bmatrix}$

Fig. 5.4 identifies the off-axis mUC (denoted as D), as well as its adjacent and physically equivalent subdomains (denoted as $\bar{D}_1, \bar{D}_2, \bar{D}_3$ and $\bar{D}_4$). The lower and upper subdomains have been again excluded to reveal the mUC. Based on this figure, the geometry relations between the off-axis mUC and its adjacent subdomains can be determined, as detailed in Table 5.1. Here, it should be noted that the symbols, L_o and W_o, denote the overall length and width of the off-axis mUC, and they are equal to $L/\sqrt{2}$ and $\sqrt{2}L$, as indicated in Fig. 5.3. Then, by enforcing the admissibility condition, as defined in Eq. (4.81) or (4.82), all admissible loading cases can be identified and the relating load reversal factors can be obtained, as shown in Table 5.2. Finally, based on the quantities calculated above and Eq. (4.87) or (5.2), the PBC that should be applied to each pair of equivalent boundary nodes for each admissible loading case for the off-axis mUC of plain woven composites can be derived, as summarised in Tables D.1~D.4, Appendix D.

Table 5.2: Admissible loading cases of off-axis plain woven composites

|	$\{\gamma_1 \quad \gamma_2 \quad \gamma_3 \quad \gamma_4\}$	Admissible loading
Case 1	$\{1 \quad 1 \quad 1 \quad 1\}$	$\begin{bmatrix} \langle\sigma_{11}\rangle & 0 & 0 \\ 0 & \langle\sigma_{22}\rangle & 0 \\ 0 & 0 & \langle\sigma_{33}\rangle \end{bmatrix}$
Case 2	$\{-1 \quad 1 \quad -1 \quad -1\}$	$\begin{bmatrix} 0 & \langle\sigma_{12}\rangle & 0 \\ \langle\sigma_{21}\rangle & 0 & 0 \\ 0 & 0 & 0 \end{bmatrix}$
Case 3	$\{-1 \quad 1 \quad 1 \quad 1\}$	$\begin{bmatrix} 0 & 0 & 0 \\ 0 & 0 & \langle\sigma_{23}\rangle \\ 0 & \langle\sigma_{32}\rangle & 0 \end{bmatrix}$
Case 4	$\{1 \quad 1 \quad -1 \quad -1\}$	$\begin{bmatrix} 0 & 0 & \langle\sigma_{13}\rangle \\ 0 & 0 & 0 \\ \langle\sigma_{31}\rangle & 0 & 0 \end{bmatrix}$

5.2.2 Twill woven composites

5.2.2.1 Off-axis mUC for twill woven composites

For twill woven composites, its off-axis mUC can be obtained by performing the domain reduction operations detailed in Fig. 5.5. Again, the off-axis mUC is only 1/8 of the full off-axis UC as no symmetry can be further exploited. To ease the description of the yarns, the off-axis mUC model is initially addressed in the normal coordinate system of twill

woven composites and then rotated back to the LCS of the off-axis mUC, as demonstrated in Fig. 5.6. Here, it should be noted that each of the yarns in this mUC is comprised of a straight part and a wavy part, and thus should be described using two sets of equations. Using the transformation defined in Eq. (5.1) and combining the normal mUC developed for twill woven composites, as detailed in Section 4.3, each yarn in the off-axis mUC of twill woven composites can be described, as summarised in Tables C.2 – C.3, Appendix C. Here, when describing a yarn, the part that is not currently being addressed is shaded in grey. Also, the subscripts, s and w, denote the straight and wavy parts, respectively.
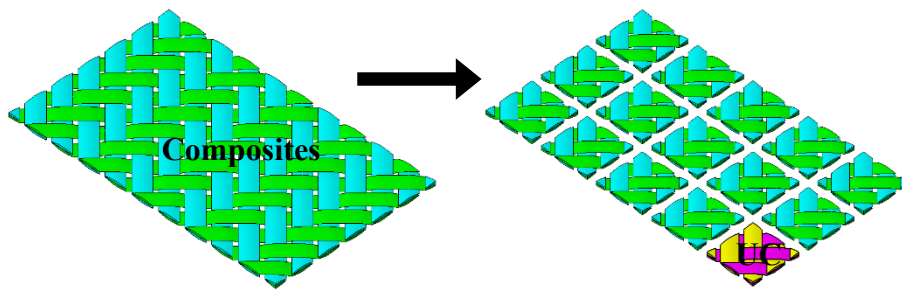
(a) Composite ply → full-size UC by using translational symmetries
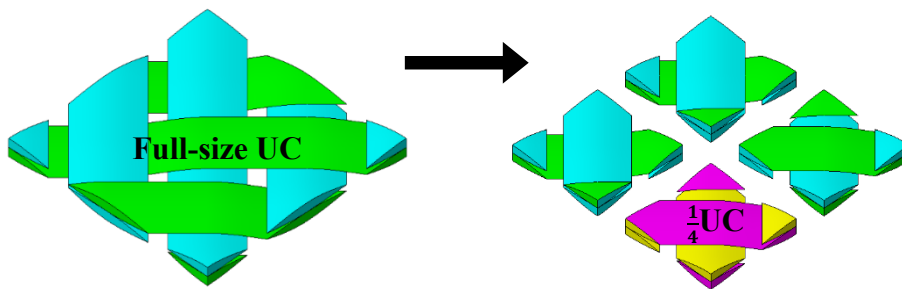
(b) Full-size UC → $\frac{1}{4}$UC by using translational & reflectional symmetries
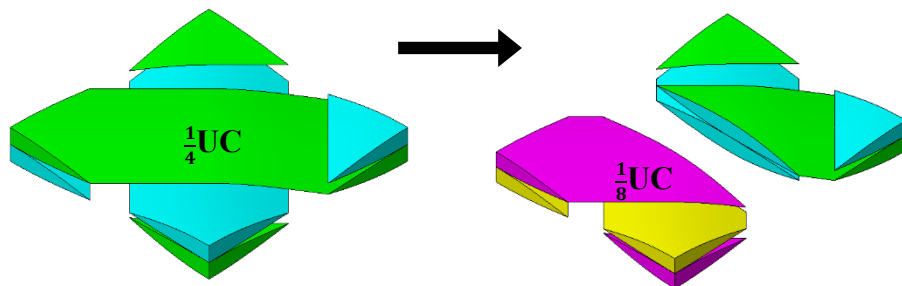
(c) $\frac{1}{4}$UC → $\frac{1}{8}$UC by using rotational symmetries only

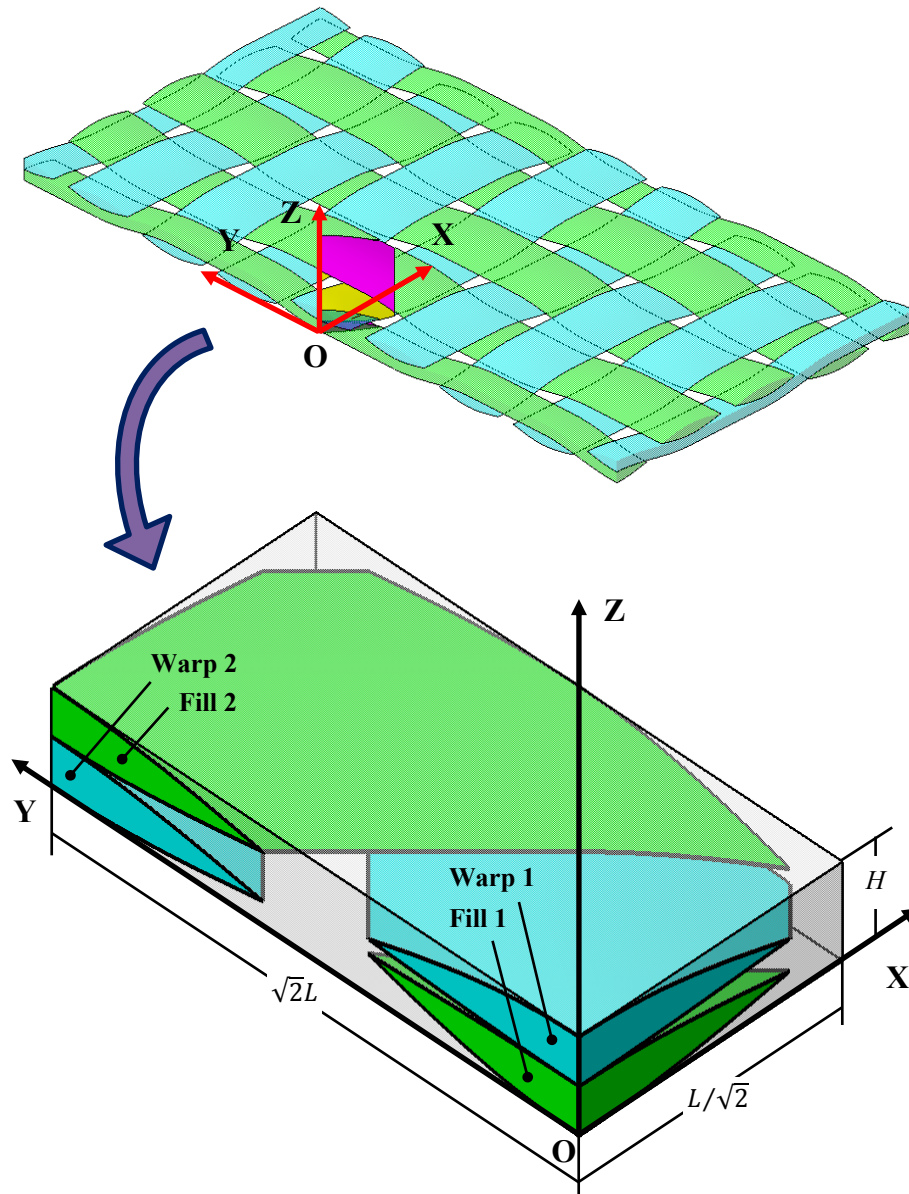**Figure 5.5: Domain reduction for off-axis twill woven composites**

Figure 5.6: The off-axis mUC model for twill woven composites

5.2.2.2 PBCs for off-axis twill woven composites

Fig. 5.7 shows the off-axis mUC and its adjacent subdomains. Based on this, the geometry relations between the off-axis mUC and the four subdomains are calculated, as listed in Table 5.3, where the symbols, L_o and W_o, denote the overall length and width of the off-axis mUC, and they are equal to $L/\sqrt{2}$ and $\sqrt{2}L$. By enforcing the admissibility condition, all admissible loading cases and the relating load reversal factors are then determined, as summarised in Table 5.4. By utilising Eq. (4.87) or (5.2) and the results listed in Tables 5.3 and 5.4, the PBC that should be applied to each pair of equivalent boundary nodes for each

admissible loading case for the off-axis mUC of twill woven composites is derived, as summarised in Tables D.5~D.8, Appendix D.
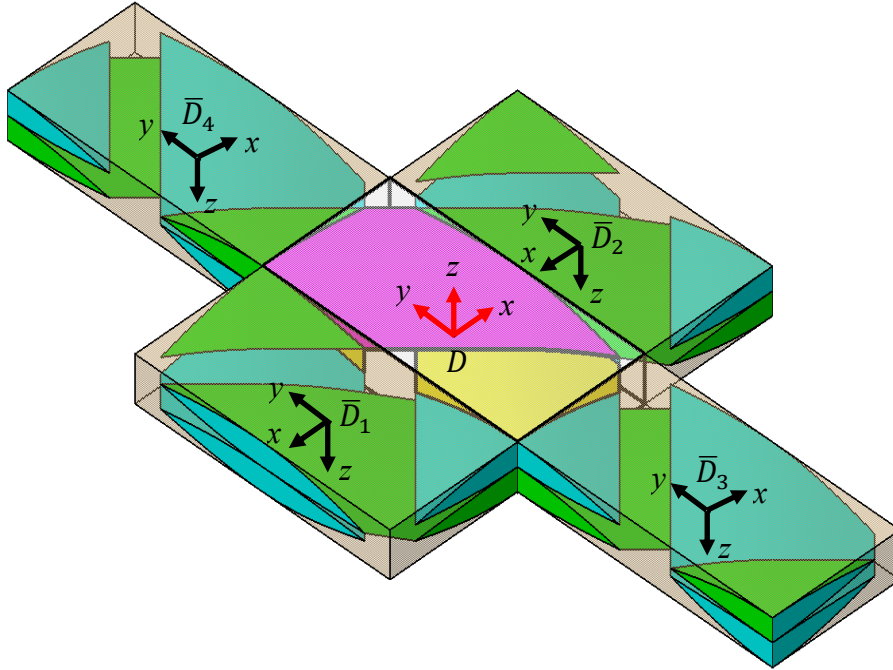

Figure 5.7: Off-axis mUC & adjacent subdomains of twill woven composites

**Table 5.3: Relations between off-axis twill woven mUC & adjacent subdomains**

	$\overline{D}_1$	$\overline{D}_2$	$\overline{D}_3$	$\overline{D}_4$
$\boldsymbol{T}_i$	$\begin{bmatrix} -1 & 0 & 0 \\ 0 & 1 & 0 \\ 0 & 0 & -1 \end{bmatrix}$	$\begin{bmatrix} -1 & 0 & 0 \\ 0 & 1 & 0 \\ 0 & 0 & -1 \end{bmatrix}$	$\begin{bmatrix} 1 & 0 & 0 \\ 0 & 1 & 0 \\ 0 & 0 & -1 \end{bmatrix}$	$\begin{bmatrix} 1 & 0 & 0 \\ 0 & 1 & 0 \\ 0 & 0 & -1 \end{bmatrix}$
$\boldsymbol{x}^{O\overline{D}_i}$	$\begin{bmatrix} -L_o \\ 0 \\ 0 \end{bmatrix}$	$\begin{bmatrix} L_o \\ 0 \\ 0 \end{bmatrix}$	$\begin{bmatrix} 0 \\ -W_o \\ 0 \end{bmatrix}$	$\begin{bmatrix} 0 \\ W_o \\ 0 \end{bmatrix}$
$\boldsymbol{x}^{\overline{A}_i}$	$\begin{bmatrix} -\frac{L_o}{2} \\ -\frac{W_o}{2} \leq y \leq \frac{W_o}{2} \\ -\frac{H}{2} \leq z \leq \frac{H}{2} \end{bmatrix}$	$\begin{bmatrix} \frac{L_o}{2} \\ -\frac{W_o}{2} \leq y \leq \frac{W_o}{2} \\ -\frac{H}{2} \leq z \leq \frac{H}{2} \end{bmatrix}$	$\begin{bmatrix} -\frac{L_o}{2} \leq x \leq \frac{L_o}{2} \\ -\frac{W_o}{2} \\ -\frac{H}{2} \leq z \leq \frac{H}{2} \end{bmatrix}$	$\begin{bmatrix} -\frac{L_o}{2} \leq x \leq \frac{L_o}{2} \\ \frac{W_o}{2} \\ -\frac{H}{2} \leq z \leq \frac{H}{2} \end{bmatrix}$
$\boldsymbol{x}^{A_i}$	$\begin{bmatrix} -\frac{L_o}{2} \\ y^{\overline{A}} \\ -z^{\overline{A}} \end{bmatrix}$	$\begin{bmatrix} \frac{L_o}{2} \\ y^{\overline{A}} \\ -z^{\overline{A}} \end{bmatrix}$	$\begin{bmatrix} x^{\overline{A}} \\ \frac{W_o}{2} \\ -z^{\overline{A}} \end{bmatrix}$	$\begin{bmatrix} x^{\overline{A}} \\ -\frac{W_o}{2} \\ -z^{\overline{A}} \end{bmatrix}$

**Table 5.4: Admissible loading cases of off-axis twill woven composites**

	$\{\gamma_1 \quad \gamma_2 \quad \gamma_3 \quad \gamma_4\}$	Admissible loading
Case 1	$\{1 \quad 1 \quad 1 \quad 1\}$	$\begin{bmatrix} \langle\sigma_{11}\rangle & 0 & 0 \\ 0 & \langle\sigma_{22}\rangle & 0 \\ 0 & 0 & \langle\sigma_{33}\rangle \end{bmatrix}$
Case 2	$\{-1 \quad -1 \quad 1 \quad 1\}$	$\begin{bmatrix} 0 & \langle\sigma_{12}\rangle & 0 \\ \langle\sigma_{21}\rangle & 0 & 0 \\ 0 & 0 & 0 \end{bmatrix}$
Case 3	$\{-1 \quad -1 \quad -1 \quad -1\}$	$\begin{bmatrix} 0 & 0 & 0 \\ 0 & 0 & \langle\sigma_{23}\rangle \\ 0 & \langle\sigma_{32}\rangle & 0 \end{bmatrix}$
Case 4	$\{1 \quad 1 \quad -1 \quad -1\}$	$\begin{bmatrix} 0 & 0 & \langle\sigma_{13}\rangle \\ 0 & 0 & 0 \\ \langle\sigma_{31}\rangle & 0 & 0 \end{bmatrix}$

5.2.3 3D woven composites

5.2.3.1 Off-axis mUC for 3D woven composites
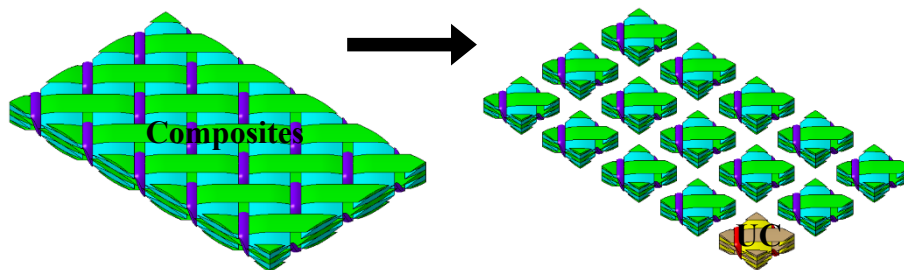
(a) Composite ply → full UC by using translational symmetries
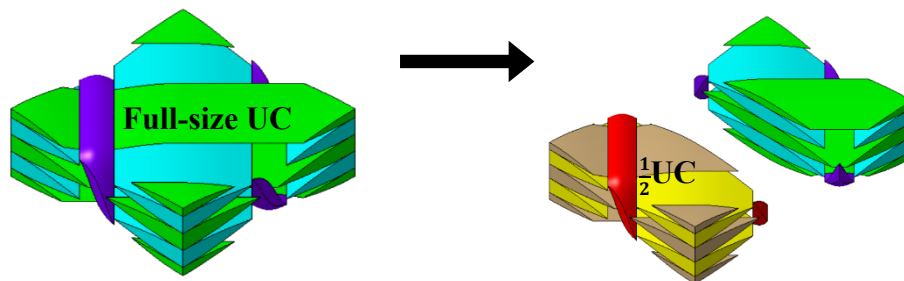
(b) Full-size UC → $\frac{1}{2}$UC by using rotational symmetries only

Figure 5.8: Domain reduction for off-axis 3D orthogonal woven composites

The procedure for identifying the off-axis mUC for 3D orthogonal woven composites is illustrated in Fig. 5.8. Here, it is clearly suggested that the full-size UC can be reduced only into a half-size UC and no symmetry can be further exploited. For facilitating the geometry description, the approach of initially addressing the off-axis mUC in the normal coordinate system and then rotating the resulting equations for describing the yarns back to the LCS of the off-axis mUC is again employed, as illustrated in Fig. 5.9, where it is shown that the overall length and width of this mUC are $\sqrt{2}L$ and $2\sqrt{2}L$, respectively. For clarity, the warp, fill and binder yarns are numbered in black, red and white colours.
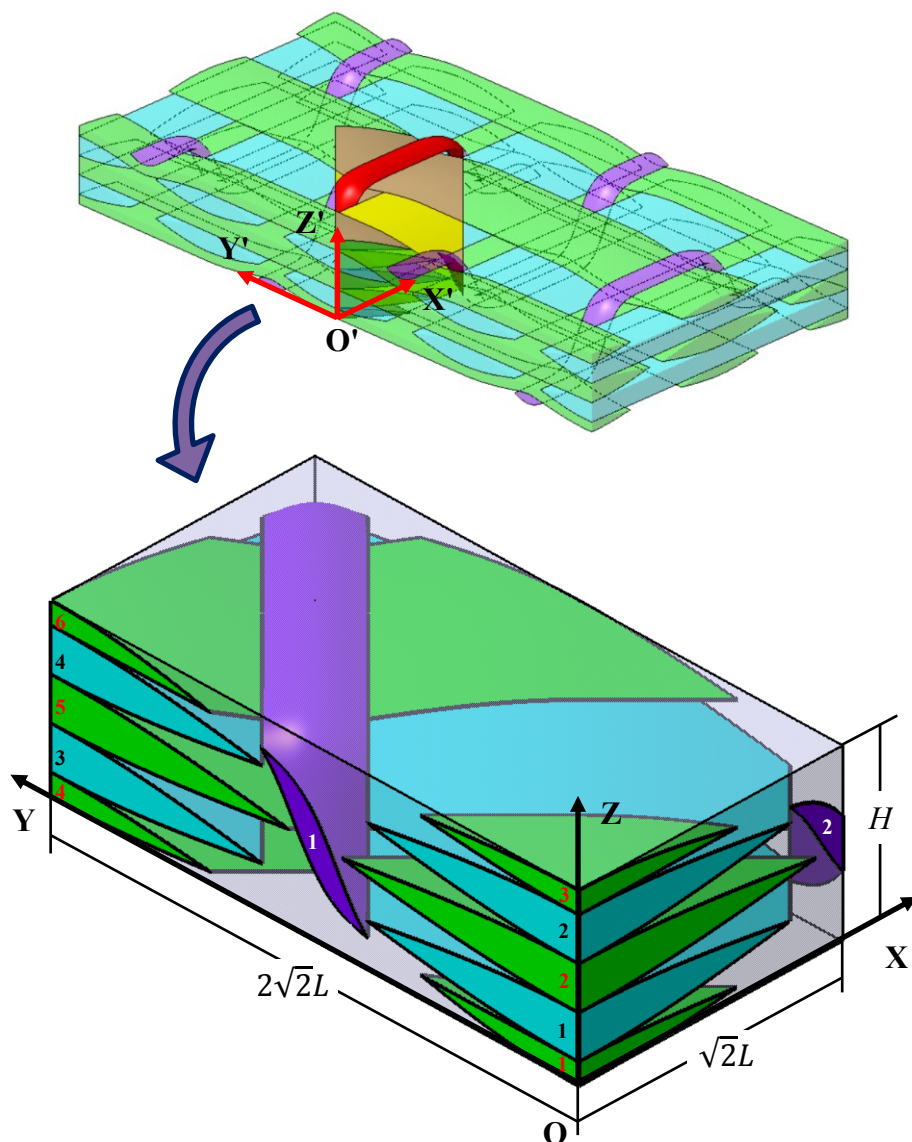

Figure 5.9: The off-axis mUC model for 3D woven composites

Compared to the normal mUC of 3D woven composites, the off-axis mUC is much more complex as it contains over ten yarns. In addition, some of the yarns are comprised of two or more parts that should be described using different sets of equations. The yarns falling into this type are fill yarns 1, 3, 4 & 6 and binder yarn 1. The equations for describing the surfaces and waviness of the yarns in the off-axis mUC are summarised in Tables C4 – C8, Appendix C.

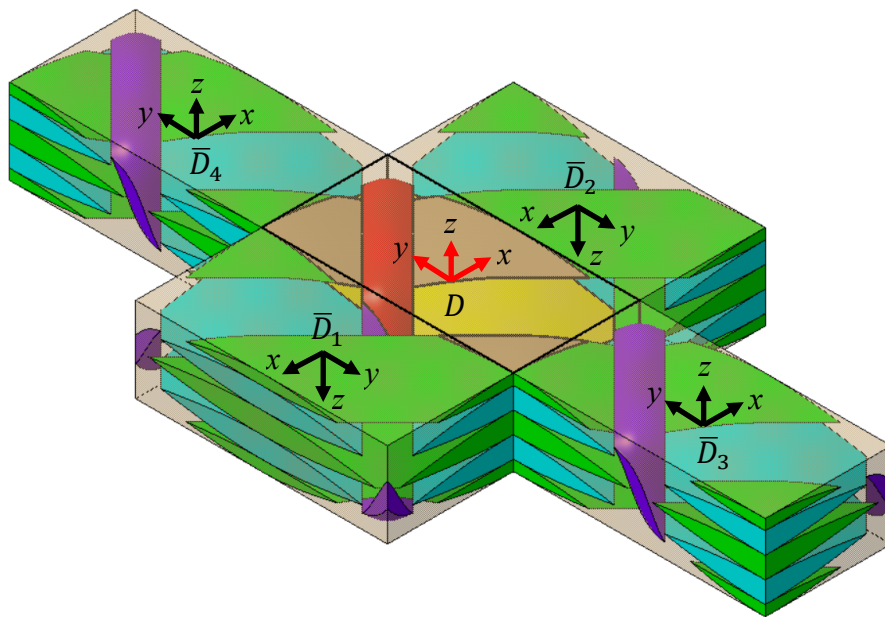*5.2.3.2 PBCs for off-axis 3D woven composites*

Figure 5.10: Off-axis mUC & adjacent subdomains of 3D woven composites

The off-axis mUC and its adjacent subdomains of 3D woven composites are illustrated in Fig. 5.10, based on which, the geometry relations between the off-axis mUC and the four subdomains are then obtained, as listed in Table 5.5. Here, the symbols, L_o and W_o, denote the overall length and width of the off-axis mUC, and they are equal to $\sqrt{2}L$ and $2\sqrt{2}L$, respectively. By enforcing the admissibility condition, all admissible loading cases and the corresponding load reversal factors can be determined. However, it is interesting to note that all loading conditions are admissible for this type of off-axis UC, as indicated in Table 5.6. Based on the data listed in Tables 5.5 and 5.6, the PBC that should be applied to each pair of equivalent nodes can be easily calculated. The PBCs for the off-axis mUC of 3D woven composites are detailed in Table D.9, Appendix D.

Table 5.5: Relations between off-axis 3D woven mUC & adjacent subdomains

	$\overline{D}_1$	$\overline{D}_2$	$\overline{D}_3$	$\overline{D}_4$
$\boldsymbol{T}_i$	$\begin{bmatrix} -1 & 0 & 0 \\ 0 & -1 & 0 \\ 0 & 0 & -1 \end{bmatrix}$	$\begin{bmatrix} -1 & 0 & 0 \\ 0 & -1 & 0 \\ 0 & 0 & -1 \end{bmatrix}$	$\begin{bmatrix} 1 & 0 & 0 \\ 0 & 1 & 0 \\ 0 & 0 & 1 \end{bmatrix}$	$\begin{bmatrix} 1 & 0 & 0 \\ 0 & 1 & 0 \\ 0 & 0 & 1 \end{bmatrix}$
$\boldsymbol{x}^{O_{\overline{D}_i}}$	$\begin{bmatrix} -L_o \\ 0 \\ 0 \end{bmatrix}$	$\begin{bmatrix} L_o \\ 0 \\ 0 \end{bmatrix}$	$\begin{bmatrix} 0 \\ -W_o \\ 0 \end{bmatrix}$	$\begin{bmatrix} 0 \\ W_o \\ 0 \end{bmatrix}$
$\boldsymbol{x}^{\overline{A}_i}$	$\begin{bmatrix} -\frac{L_o}{2} \\ -\frac{W_o}{2} \le y \le \frac{W_o}{2} \\ -\frac{H}{2} \le z \le \frac{H}{2} \end{bmatrix}$	$\begin{bmatrix} \frac{L_o}{2} \\ -\frac{W_o}{2} \le y \le \frac{W_o}{2} \\ -\frac{H}{2} \le z \le \frac{H}{2} \end{bmatrix}$	$\begin{bmatrix} -\frac{L_o}{2} \le x \le \frac{L_o}{2} \\ -\frac{W_o}{2} \\ -\frac{H}{2} \le z \le \frac{H}{2} \end{bmatrix}$	$\begin{bmatrix} -\frac{L_o}{2} \le x \le \frac{L_o}{2} \\ \frac{W_o}{2} \\ -\frac{H}{2} \le z \le \frac{H}{2} \end{bmatrix}$
$\boldsymbol{x}^{A_i}$	$\begin{bmatrix} -\frac{L_o}{2} \\ -y^{\overline{A}} \\ -z^{\overline{A}} \end{bmatrix}$	$\begin{bmatrix} \frac{L_o}{2} \\ -y^{\overline{A}} \\ -z^{\overline{A}} \end{bmatrix}$	$\begin{bmatrix} x^{\overline{A}} \\ \frac{W_o}{2} \\ z^{\overline{A}} \end{bmatrix}$	$\begin{bmatrix} x^{\overline{A}} \\ -\frac{W_o}{2} \\ z^{\overline{A}} \end{bmatrix}$

Table 5.6: Admissible loading case of off-axis 3D woven composites

	$\{\gamma_1 \quad \gamma_2 \quad \gamma_3 \quad \gamma_4\}$	Admissible loading
Case 1	$\{1 \quad 1 \quad 1 \quad 1\}$	$\begin{bmatrix} \langle\sigma_{11}\rangle & \langle\sigma_{12}\rangle & \langle\sigma_{13}\rangle \\ \langle\sigma_{21}\rangle & \langle\sigma_{22}\rangle & \langle\sigma_{23}\rangle \\ \langle\sigma_{31}\rangle & \langle\sigma_{32}\rangle & \langle\sigma_{33}\rangle \end{bmatrix}$

5.3 Material modelling

The overall response of a woven composite material is determined by not only the internal architecture but also many other factors, such as the type of fibre or polymer matrix used, the surface treatment made to the fibres and the manufacturing process for fabricating the composite material. For instance, in carbon fibre-reinforced polymer (CFRP) composites, electrochemical treatment is often employed to partially oxidise carbon fibre surface so as to promote the adhesion of fibres to the resin matrix and thus to improve the transverse behaviour of the composite material. However, instead of considering all the factors that may influence the overall response of woven composites, the present work focuses on the

most dominant ones, i.e. the material behaviours of resin matrix and yarns. In addition, as it is not practical to develop a single material model that suits various kinds of woven composites, the material modelling in the present work is addressed only for the most commonly used constituents, i.e. polymer matrix and glass/carbon fibre yarns.

Similar to unidirectional composites, woven composites feature distinct responses when loaded in different directions. In the fibre directions (e.g. the warp direction), the material behaviour is primarily driven by yarns, typically exhibiting linearly elastic response prior to failure, followed by anisotropic post failure behaviour. Depending on the type of fibre yarns used, the initial elastic response can be accompanied by a different degree of strain-rate sensitivity. For example, woven composites with glass-fibre yarns are often found to be strain-rate dependent, while those with carbon-fibre yarns are generally insensitive to strain rate. In terms of the material behaviour in bias directions, particularly in 45° to the warp or fill direction, woven composites often show strong nonlinear and rate-dependent response. It is commonly believed that such kind of behaviour is closely associated with that of polymer matrix, which consists of long chain molecules with a chain length of up to 10^5 atoms and behaves viscoelastically at small strains and becomes nonlinear when the strain applied is large enough.

Based on the above analysis, the present research assumes that the yarn material in woven composites can be treated as unidirectional composites in the local material coordinate system, and thus it will be modelled as a transversely isotropic material with linearly elastic response prior to failure and anisotropic post-failure behaviour. Since some types of yarns in woven composites may be sensitive to loading rate, the strain-rate dependence of the yarn material in the fibre directions will also be considered. Due to the presence of intra-yarn polymer matrix, the yarn material in woven composites may contribute to some degree of nonlinearity and strain-rate dependence in the transverse directions. However, it is believed that such nonlinearity and rate-dependence are insignificant compared to those of the polymer matrix outside of yarns. Therefore, in this work, the nonlinearity and rate-dependence of the yarn material in the transverse directions will not be considered independently. Instead, it will be compensated in the utilisation of a viscoplasticity model to describe the nonlinear, rate-dependent response of the polymer matrix. In the following four sections, the material modelling in the present research will be detailed from the perspectives of i) the nonlinearity and strain-rate dependence of the polymer matrix, ii) the

rate-dependence of the yarn material in the fibre directions, iii) the failure criteria for identifying the damage initiation of the yarn material and iv) the analytical formulation for describing the damage evolution of the yarn material.

5.3.1 Nonlinearity and rate-dependence of polymer matrix

Extensive studies have been conducted by many researchers to model the nonlinear, rate-dependent behaviour of the polymer matrix in composites. The commonly used methods can be categorised into physically-based approaches and phenomenological approaches. In the former type of approaches, the response of a polymer is often modelled based on the physical mechanisms that drive the deformation. For instance, the deformation of a polymer is often assumed to be as a result of the motion of molecular chains over potential barriers [197] or the unwinding of molecular kinks [198], and the degree of change in the material state due to these molecular mechanisms is assumed to be associated with the competition between the applied stress (which drives the material away from its original state) and the internal stress (which is defined to model the resistance to deformation and tends to drive the material back to its original state, and is often assumed to evolve with stress, inelastic strain and inelastic strain rate). In general, this type of approaches models the nonlinear, rate-dependent deformation of a polymer on one hand as a function of some molecular parameters, such as activation energy and volume, molecular radius, angle of molecular rotation and thermal constants, and meanwhile as a function of state variables representing the resistance to deformation. Since these approaches address the modelling of the deformation of polymers from a molecular perspective, they are also referred to as molecular approaches.

In the latter category of approaches, the nonlinearity and rate-dependence of polymers are often phenomenologically described by directly using or modifying a plasticity-based or viscoplasticity-based theory that has been developed for metals. For example, without making any modification, Zhang and Moore [199] and Valisetty and Teply [200] adopted the techniques that were originally developed for metals to predict the uniaxial tensile response of polymers. Another notable example is that the viscoplasticity theory based on overstress (VBO), which was originally formulated by Krempl and Ho [201] for metals, was modified by Bordonaro [202] to characterise the response of polymers under a variety of loading conditions such as creep, relaxation and unloading. In the modified model, the

phenomena that are encountered in the deformation of polymers but not in that of metals, e.g. nonlinear unloading, were also considered. Recently, in order to model the nonlinear, strain-rate dependent response of the matrix constituent in polymer matrix composites, Goldberg and Stouffer [42] modified the constitutive equations of a viscoplasticity-based model that was initially developed by Ramaswamy and Stouffer [203] for metals. In their work, the original equations defining the effective stress, the effective inelastic strain and the inelastic strain tensor in the classical J2 plasticity theory were reasonable modified to account for the effect of loading rate on the response of the polymer matrix. Since these approaches model the deformation of polymers by adapting a viscoplasticity-based theory, they are also referred to as viscoplasticity-based approaches.

In this research, instead of trying to develop new constitutive models, the model developed by Goldberg and Stouffer [42], which will be termed as the Goldberg-Stouffer model in this thesis, is adopted to describe the nonlinear, rate-dependent response of the polymer matrix in woven composites. The main reason for choosing this model is that it is not as complex as the models developed using molecular approaches, where a relatively large number of molecular parameters need to be obtained before they can be utilised. Another reason for using the Goldberg-Stouffer model is that it has been found to correlate well with experimental data [42] and that its effectiveness in predicting the nonlinear, rate-dependent response of polymer matrix in composite materials has been validated by many other researchers including Tabiei *et al.* [130, 135, 136] and Gerlach *et al.* [18].

5.3.1.1 The Goldberg-Stouffer model

In the Goldberg-Stouffer model, the total strain rate, $\dot{\varepsilon}_{ij}$, is considered to be a sum of the inelastic strain rate, $\dot{\varepsilon}_{ij}^{\mathrm{I}}$, and the elastic strain rate, $\dot{\varepsilon}_{ij}^{\mathrm{E}}$, which is defined by $\dot{\sigma}_{ij} = c_{ijkl}\dot{\varepsilon}_{kl}^{\mathrm{E}}$, where $\dot{\sigma}_{ij}$ is the stress rate and c_{ijkl} is the elasticity tensor. For the inelastic strain rate, it is modelled as a function of the applied stress and the internal stress, as follows:

$$\dot{\varepsilon}_{ij}^{\mathrm{I}} = D_0 \exp\left(-\frac{1}{2}\left(\frac{Z_0^2}{3J_2}\right)^{n_\mathrm{r}}\right)\frac{S_{ij}-\Omega_{ij}}{\sqrt{J_2}} \tag{5.3}$$

where D_0 is a material constant denoting the maximum inelastic strain rate; Z_0 represents the initial hardness of polymer matrix; n_r is a parameter describing the dependence of the response of polymer matrix on strain rate; S_{ij} refers to as the deviatoric stress; Ω_{ij} is a

tensorial state variable; the term, $S_{ij} - \Omega_{ij}$, which is the difference between the deviatoric stress and the tensorial state variable, is termed as the overstress, and J_2 is the second invariant of overstress. Here, the deviatoric stress and the second invariant of overstress take the following classical forms, as follows, where δ_{ij} is the Kronecker delta tensor:

$$S_{ij} = \sigma_{ij} - \frac{\sigma_{kk}}{3}\delta_{ij} \tag{5.4}$$

$$J_2 = \frac{1}{2}(S_{ij} - \Omega_{ij})(S_{ij} - \Omega_{ij}) \tag{5.5}$$

The use of the tensorial state variable in Eq. (5.3) is to model the resistance to molecular flow in polymer matrix, and thus this variable is also termed as the "internal stress", which is an analogy to the concept of "back stress" in metals. This internal stress is assumed to be equal to zero if the polymer matrix is in the original state and evolve with the inelastic strain, as follows:

$$\dot{\Omega}_{ij} = \frac{2}{3}q\Omega_{\mathrm{m}}\dot{\varepsilon}^{\mathrm{I}}_{ij} - q\Omega_{ij}\dot{\varepsilon}^{\mathrm{I}}_{\mathrm{eff}} \tag{5.6}$$

where q is a material parameter representing the "hardening" rate of polymer matrix; Ω_{m} is the value of the internal stress at "saturation", which is the point where the stress-strain curve becomes flat; and $\dot{\varepsilon}^{\mathrm{I}}_{\mathrm{eff}}$ is the effective inelastic strain rate, which defined by:

$$\dot{\varepsilon}^{\mathrm{I}}_{\mathrm{eff}} = \sqrt{\frac{2}{3}\dot{\varepsilon}^{\mathrm{I}}_{ij}\dot{\varepsilon}^{\mathrm{I}}_{ij}} \tag{5.7}$$

5.3.1.2 Determination of material constants

To employ the above viscoplasticity-based model, all material constants (i.e. $D_0, Z_0, n_{\mathrm{r}}, q$ and Ω_{m}) must be determined. For parameter D_0, it is the limiting value of the inelastic strain rate and can be assumed to be 10^4 times the maximum applied total strain rate, as suggested in [42]. For the remaining parameters, they can be determined based on the uniaxial forms of Eqs. (5.3) and (5.6), as follows [42]:

$$\dot{\varepsilon}^{\mathrm{I}} = \frac{2}{\sqrt{3}}D_0\exp\left(-\frac{1}{2}\left(\frac{Z_0}{|\sigma-\Omega|}\right)^{2n_{\mathrm{r}}}\right)\frac{\sigma-\Omega}{|\sigma-\Omega|} \tag{5.8}$$

$$\dot{\Omega} = q\Omega_{\mathrm{m}}\dot{\varepsilon}^{\mathrm{I}} - q\Omega|\dot{\varepsilon}^{\mathrm{I}}| \tag{5.9}$$

where $\dot{\varepsilon}^{\mathrm{I}}$ is the uniaxial strain rate, σ is the uniaxial stress, Ω is the uniaxial form of the internal stress, and $\dot{\Omega}$ is the uniaxial form of the internal stress rate.

To determine Z_0, n_{r} and Ω_{m}, natural logarithm operations are performed on both sides of Eq. (5.8), which results in:

$$\ln\left(\frac{\sqrt{3}\dot{\varepsilon}^{\mathrm{I}}}{2D_0}\right) = -\frac{1}{2}\left(\frac{Z_0}{|\sigma-\Omega|}\right)^{2n_{\mathrm{r}}} + \ln\left(\frac{\sigma-\Omega}{|\sigma-\Omega|}\right) \tag{5.10}$$

Here, it should be noted that the second term of the right side of this equation vanishes as it has been assumed to be under uniaxial tensile loading. Assume the test for determining these parameters has been conducted to the state of saturation. By substituting the values of the inelastic strain rate, the uniaxial stress and the internal stress at saturation, i.e. $\dot{\varepsilon}_0$, σ_{s} and Ω_{m}, back into Eq. (5.10), it yields:

$$\ln\left[-2\ln\left(\frac{\sqrt{3}\dot{\varepsilon}_0}{2D_0}\right)\right] = -2n_{\mathrm{r}}\ln(\sigma_{\mathrm{s}} - \Omega_{\mathrm{m}}) + 2n_{\mathrm{r}}\ln(Z_0) \tag{5.11}$$

The above equation can be rewritten as:

$$y = -2n_{\mathrm{r}}x + 2n_{\mathrm{r}}\ln(Z_0) \tag{5.12}$$

where

$$x = \ln(\sigma_{\mathrm{s}} - \Omega_{\mathrm{m}}) \tag{5.13}$$

$$y = \ln\left[-2\ln\left(\frac{\sqrt{3}\dot{\varepsilon}_0}{2D_0}\right)\right] \tag{5.14}$$

As Eq. (5.12) correlates x with y, a number of uniaxial tensile tests (e.g. n tests) can be conducted at several constant strain rates. Based on these tests, a set of data pairs, x_i and y_i ($i = 1, 2, \dots, n$), can be obtained to perform a least-squares regression analysis. Then, the values of n_{r} and Z_0 can be derived since the slope and the intercept of the best fit line are equal to $-2n_{\mathrm{r}}$ and $2n_{\mathrm{r}}\ln(Z_0)$. Here, it should be noted that in calculating x_i, the value of Ω_{m} can be initially estimated to be 50% ~ 75% of the highest value of the uniaxial stresses at saturation [42], and the value of Ω_{m} should be adjusted until an optimal fit to the data is reached.

In terms of q, it can be determined based on Eq. (5.9). It is often assumed that the internal stress reaches a maximum if the polymer matrix is at saturation, which means that the exponential term in Eq. (5.8) approaches zero. Moreover, it is assumed that the condition at saturation [42] is:

$$\exp(-q\varepsilon_s^I) = 0.01 \tag{5.15}$$

where ε_s^I is the inelastic strain at saturation.

Solving the above equation determines the value of q. Here, it should be noted that if the inelastic strains at saturation in the tensile tests vary with the loading rate, all the values of q should be calculated for subsequent regression analysis. Alternatively, the value of q can be determined from the average value of the inelastic strains at saturation.

5.3.1.3 Solution algorithm for the Goldberg-Stouffer model

The constitutive equations in the Goldberg-Stouffer model, i.e. Eqs. (5.3) ~ (5.7), generate either a differential equation for each component of the tensorial variables or a first-order tensorial differential equation that does not have a closed-form solution. To approximate the solutions of these equations, one of the techniques that can be utilised is the iterative, implicit trapezoidal rule integration procedure described in [42]. However, as this model will be implemented using the explicit weak-form meshfree method, the four-step Runge-Kutta method described in [135] is adopted to explicitly estimate solutions. Before using this solution technique, the rate forms of the constitutive equations should be transformed into the incremental forms, as follows, where dt is time increment:

$$d\varepsilon_{ij}^I = \left[D_0\exp\left(-\frac{1}{2}\left(\frac{Z_0^2}{3J_2}\right)^{n_r}\right)\frac{S_{ij}-\Omega_{ij}}{\sqrt{J_2}}\right]dt \tag{5.16}$$

$$d\Omega_{ij} = \frac{2}{3}q\Omega_m d\varepsilon_{ij}^I - q\Omega_{ij}d\varepsilon_{eff}^I \tag{5.17}$$

$$d\varepsilon_{eff}^I = \sqrt{\frac{2}{3}d\varepsilon_{ij}^I d\varepsilon_{ij}^I} \tag{5.18}$$

Essentially, when utilising the explicit weak-form meshfree method to predict the overall response of woven composites, the four-step Runge-Kutta technique estimates the values

of the tensorial variables at the current step from those at the previous step. At the current step, the following variables are known and can be used to as input parameters:

1) The stress $\sigma_{ij}^{(n)}$ at the previous step

2) The internal stress $\Omega_{ij}^{(n)}$ at the previous step

3) The inelastic strain $\varepsilon_{ij}^{I(n)}$ at the previous step

4) The total strain $\varepsilon_{ij}^{(n)}$ at the previous step

5) The total strain $\varepsilon_{ij}^{(n+1)}$ at the current step

6) The total strain rate $\dot{\varepsilon}_{ij}^{(n+1)}$ at the current step

Based on the above input parameters, the four-step Runge-Kutta method can be advanced in a four-step manner, as follows. In the first step, it is assumed that:

$$\sigma_{ij} = \sigma_{ij}^{(n)} \ \& \ \Omega_{ij} = \Omega_{ij}^{(n)} \tag{5.19}$$

By substituting $\dot{\varepsilon}_{ij}^{(n+1)}$, σ_{ij} and Ω_{ij} into Eqs. (5.16) ~ (5.18), the unknown variables, $d\varepsilon_{ij}^{I}$ and $d\Omega_{ij}$, can be calculated and are denoted as:

$$d\varepsilon_{ij}^{I1} = d\varepsilon_{ij}^{I} \ \& \ d\Omega_{ij}^{1} = d\Omega_{ij} \tag{5.20}$$

Then, the inelastic strain, the tensorial stress and the internal stress can be initially updated, as follows:

$$\varepsilon_{ij}^{I1} = \varepsilon_{ij}^{I(n)} + \frac{1}{2} d\varepsilon_{ij}^{I1} \tag{5.21}$$

$$\sigma_{ij}^{1} = c_{ijkl} \left(\varepsilon_{kl}^{(n+1)} - \varepsilon_{kl}^{I1} \right) \tag{5.22}$$

$$\Omega_{ij}^{1} = \Omega_{ij}^{(n)} + \frac{1}{2} d\Omega_{ij}^{1} \tag{5.23}$$

At the second step, the tensorial stress and the internal stress updated in the first step are used as the input parameters and substituted into Eqs. (5.16) ~ (5.18), and the results are denoted as:

$$d\varepsilon_{ij}^{I2} = d\varepsilon_{ij}^{I} \ \& \ d\Omega_{ij}^{2} = d\Omega_{ij} \tag{5.24}$$

Again, the inelastic strain, the tensorial stress and the internal stress can be updated in a similar way, as follows:

$$\varepsilon_{ij}^{I2} = \varepsilon_{ij}^{I(n)} + \frac{1}{2} d\varepsilon_{ij}^{I2} \tag{5.25}$$

$$\sigma_{ij}^2 = c_{ijkl}\left(\varepsilon_{kl}^{(n+1)} - \varepsilon_{kl}^{I2}\right) \tag{5.26}$$

$$\Omega_{ij}^2 = \Omega_{ij}^{(n)} + \frac{1}{2} d\Omega_{ij}^2 \tag{5.27}$$

After that, the tensorial stress and the internal stress calculated in Eqs. (5.26) and (5.27) are accepted as the input parameters for the third step to update Eqs. (5.16) ~ (5.18), which results in:

$$d\varepsilon_{ij}^{I3} = d\varepsilon_{ij}^{I} \ \& \ d\Omega_{ij}^3 = d\Omega_{ij} \tag{5.28}$$

$$\varepsilon_{ij}^{I3} = \varepsilon_{ij}^{I(n)} + d\varepsilon_{ij}^{I3} \tag{5.29}$$

$$\sigma_{ij}^3 = c_{ijkl}\left(\varepsilon_{kl}^{(n+1)} - \varepsilon_{kl}^{I3}\right) \tag{5.30}$$

$$\Omega_{ij}^3 = \Omega_{ij}^{(n)} + d\Omega_{ij}^3 \tag{5.31}$$

At the last step, the incremental variables can be updated again by substituting the results obtained in the third step into Eqs. (5.16) ~ (5.18), which gives:

$$d\varepsilon_{ij}^{I4} = d\varepsilon_{ij}^{I} \ \& \ d\Omega_{ij}^4 = d\Omega_{ij} \tag{5.32}$$

After completing the above four-step calculations, the inelastic strain, the tensorial stress and the internal stress at the current step can be approximated, as follows:

$$\varepsilon_{ij}^{I(n+1)} = \varepsilon_{ij}^{I(n)} + \frac{1}{6} d\varepsilon_{ij}^{I1} + \frac{1}{3} d\varepsilon_{ij}^{I2} + \frac{1}{3} d\varepsilon_{ij}^{I3} + \frac{1}{6} d\varepsilon_{ij}^{I4} \tag{5.33}$$

$$\sigma_{ij}^{(n+1)} = c_{ijkl}\left(\varepsilon_{kl}^{(n+1)} - \varepsilon_{kl}^{I(n+1)}\right) \tag{5.34}$$

$$\Omega_{ij}^{(n+1)} = \Omega_{ij}^{(n)} + \frac{1}{6} d\Omega_{ij}^1 + \frac{1}{3} d\Omega_{ij}^2 + \frac{1}{3} d\Omega_{ij}^3 + \frac{1}{6} d\Omega_{ij}^4 \tag{5.35}$$

5.3.2 Rate-dependence of yarn material

In the present work, the logarithm scaling approach that was initially proposed by Weeks and Sun [204] is employed to model the rate-dependent behaviour of the yarn material in the fibre/longitudinal direction. Specifically, the rate-dependence in the fibre direction is described by scaling the longitudinal Young's modulus, as follows:

$$E_{\text{L}} = \begin{cases} E_{\text{L0}} \left(1 + C_{\text{EL}} \ln \frac{|\dot{\varepsilon}|}{\dot{\varepsilon}_0}\right) & |\dot{\varepsilon}| \geq \dot{\varepsilon}_0 \\ E_{\text{L0}} & |\dot{\varepsilon}| < \dot{\varepsilon}_0 \end{cases} \tag{5.36}$$

where E_{L} denotes the rate-dependent elastic modulus, $\dot{\varepsilon}_0$ stands for the reference strain-rate and is often taken as a relatively low strain-rate, such as 10^{-5}/s, E_{L0} is the longitudinal elastic modulus measured at the reference strain-rate, $\dot{\varepsilon}$ is the average strain-rate applied to the yarn material, and C_{EL} is a scaling parameter which describes the rate-dependence of the yarn material in the fibre direction and needs to be fitted against experimental results. Here, it should be noted that the above formulation is exclusively designed for strain-rate sensitive yarn materials, such as glass-fibre yarns. In terms of strain-rate insensitive yarn materials, such as carbon-fibre yarns, no rate-dependence in the elastic modulus should be taken into account.

As the above formulation is aimed to describe the rate-dependent behaviour of the yarn constituent in woven composites, conducting experimental tests at the scale of the yarn constituent to tune the scaling parameter would be problematic. A more practical solution is to firstly fabricate unidirectional composite specimens with the same types of material constituents as those in the yarn material. Then, a number of uniaxial tensile tests should be conducted at different constant strain rates to obtain experimental data pairs, i.e. $x_i = \log \dot{\varepsilon}_i - \log \dot{\varepsilon}_0$ and $y_i = (E_{\text{L}})_i$. Here, it should be noted that if the volume fraction of the unidirectional composite specimens is different from that of the yarn material, these data pairs need to be normalised. Finally, based on the normalised data pairs, a least-squares regression analysis can be performed to obtain the best fit line, and the scaling parameter, C_{EL}, can be fitted as E_{L0} is known and the slope of the best fit line is equal to $E_{\text{L0}} C_{\text{EL}}$.

5.3.3 Damage initiation and evolution of constituents

5.3.3.1 Damage initiation of yarn material

As the yarn material in woven composites is assumed to be unidirectional composites in the local material coordinate system, its failure can be largely identified by adapting the criteria developed for unidirectional composites. In the present research, the well-known Hashin's failure criteria [205], which were developed for unidirectional composites, are generalised to identify the damage initiation of the yarn material in woven composites. Specifically, six failure modes are defined for the yarn material, and each failure mode is assumed to initiate if the failure function reaches unity. In the following paragraphs, the six failure modes and the corresponding failure functions will be detailed. For simplicity, the meaning of the quantities in the failure functions are summarised in advance. σ_{ii} and τ_{ij} denotes the normal and shear stress components; X_T and X_C represent the tensile and compressive strengths in the longitudinal or fibre direction; Y_T and Y_C refer to the tensile and compressive strengths in the in-plane transverse direction; Z_T and Z_C are the tensile and compressive strengths in the out-of-plane transverse direction; S_{LT}, S_{TT} and S_{TL} are the shear strengths of the yarn material in the corresponding action planes; and the symbol "$\langle \ \rangle$" denotes the Macaulay brackets. Since this symbol is exactly the same as the volume average operator, see in Eq. (2.64), it should be noted that the utilisation of this symbol in this section only suggests that the Macaulay bracket operation is performed, i.e.:

$$\langle \sigma \rangle = \begin{cases} \sigma & \sigma \geq 0 \\ 0 & \sigma < 0 \end{cases} \tag{5.37}$$

✧ *Mode 1: Tensile fibre failure in the fibre direction* $(\sigma_{11} \geq 0)$

In the fibre direction, the response of the yarn material in woven composites is primarily driven by the fibres, and the failure in this direction occurs typically in the form of tensile fibre fracture. The main contributing factor to this failure mode is the tensile stress in the fibre direction, whose increase promotes the failure. However, when defining the failure function, the contribution from the in-plane shear stress and the out-of-plane stress should not be neglected as they are parallel to the fibre direction. Therefore, in a similar way of defining failure in Hashin's damage model [205], tensile fibre failure in the yarn material is assumed to be as a result of the quadratic interactions between the longitudinal tensile and shear stresses, and the failure function is defined as follows:

$$f_{1fT} = \left(\frac{\langle \sigma_{11} \rangle}{X_T}\right)^2 + \frac{\tau_{12}^2}{S_{LT}^2} + \frac{\tau_{31}^2}{S_{TL}^2} = 1 \tag{5.38}$$

✧ *Mode 2: Compressive fibre failure in the fibre direction* ($\sigma_{11} < 0$)

When subjected to compression in the longitudinal direction, the dominant failure mode shown in the yarn material is compressive fibre failure (e.g. buckling and kinking of fibres). Under compression, the increase of the compressive stress in the fibre direction promotes the presence of this failure mode. However, the compressive stresses in the in-plane and out-of-plane transverse directions tend to prevent the fibres from buckling or kinking and thus discourage the presence of compressive fibre failure. Therefore, the failure function for this failure mode is defined based on the competition between the compressive stress in the fibre direction ($\sigma_{11} < 0$) and those in the transverse directions, as follows:

$$f_{1fC} = \left(\frac{-\sigma_{11} - \langle -\frac{\sigma_{22} + \sigma_{33}}{2} \rangle}{X_C} \right)^2 = 1 \qquad (5.39)$$

✧ *Mode 3: Matrix cracking under in-plane transverse tension* ($\sigma_{22} \geq 0$)

If the yarn material in woven composites is loaded in transverse directions, the potential failure modes include intra-yarn matrix cracking, matrix shear and matrix-fibre interface debonding, which is still a matrix-dominated failure mode [206]. However, in the case of in-plane transverse tension, the dominant failure mode is matrix cracking, and it is often believed that this failure mode is closely associated with the tensile loading, as well as the shear forces in the in-plane transverse direction. Therefore, the function for this failure mode is defined based on the transverse tensile and shear stresses, as follows:

$$f_{2mC} = \left(\frac{\langle \sigma_{22} \rangle}{Y_T} \right)^2 + \frac{\tau_{12}^2}{S_{LT}^2} + \frac{\tau_{23}^2}{S_{TT}^2} = 1 \qquad (5.40)$$

✧ *Mode 4: Matrix shear under in-plane transverse compression* ($\sigma_{22} < 0$)

In the case of in-plane transverse compression, the predominant failure mode of the yarn material becomes matrix shear failure, which is as a consequence of randomly distributed fibres running through the matrix. In the present research, the failure criterion formulated by Hashin [205] for identifying matrix compression failure in unidirectional composites is directly employed, as follows:

$$f_{2mS} = \left(\frac{\langle -\sigma_{22} \rangle}{2S_{TT}} \right)^2 + \left[\left(\frac{Y_C}{2S_{TT}} \right)^2 - 1 \right] \frac{\sigma_{22}}{Y_C} + \frac{\tau_{12}^2}{S_{LT}^2} = 1 \qquad (5.41)$$

✧ *Mode 5: Matrix cracking under out-of-plane transverse tension* ($\sigma_{33} \geq 0$)

For the yarn material in woven composites, the potential failure modes in the out-of-plane direction and the contributing factors to these failure modes are similar to those in the in-plane direction. Therefore, the failure function for identifying matrix cracking under out-of-plane transverse tension can be defined in a similar way, as follows:

$$f_{3mC} = \left(\frac{\langle \sigma_{33} \rangle}{Z_T}\right)^2 + \frac{\tau_{23}^2}{S_{TT}^2} + \frac{\tau_{31}^2}{S_{TL}^2} = 1 \tag{5.42}$$

✧ *Mode 6: Matrix shear under out-of-plane transverse compression* ($\sigma_{33} < 0$)

Under out-of-plane transverse compression, the failure in the yarn material is primarily in the form of matrix shear, which is similar to failure mode 4. Thus, the failure function for this failure mode is defined in a similar form to Eq. (5.41), as follows:

$$f_{3mS} = \left(\frac{\langle -\sigma_{33} \rangle}{2S_{TT}}\right)^2 + \left[\left(\frac{Z_C}{2S_{TT}}\right)^2 - 1\right]\frac{\sigma_{33}}{Z_C} + \frac{\tau_{31}^2}{S_{TL}^2} = 1 \tag{5.43}$$

5.3.3.2 Damage initiation of polymer matrix

It should be noted that the Goldberg model discussed above describes only the deformation of a polymer prior to failure, suitable functions should be defined to characterise the post-failure behaviour. Considering that polymers exhibit a low degree of stress variation after saturation, the maximum strain criterion is used to identify the point where damage in the polymer matrix initiates, as follows, where ε_{mf} stands for the failure strain, and ε_{eff} is the total effective strain:

$$f_m = \left(\frac{\varepsilon_{eff}}{\varepsilon_{mf}}\right)^2 = 1 \tag{5.44}$$

After implementing this failure criterion for homogenising the overall response of woven composites, the total effective strain ε_{eff}, and the failure function f_m will be calculated at each time step. If this failure condition is met for a material point in the polymer matrix, the elasticity matrix defined in Eq. (2.13) should be updated by reducing the values of the elastic and shear moduli uniformly based on the degree of damage, which will be addressed later in Section 5.3.3.4. When using the criterion defined in Eq. (5.44), it should be noted that the failure strain of a polymer matrix may vary with strain-rate as a result of the rate-

dependence of the polymer matrix. To take such a phenomenon into account, the following logarithm formulation can be used to scale the failure strain:

$$\varepsilon_{\mathrm{mf}} = \begin{cases} \varepsilon_{\mathrm{m0}} \left(1 \pm C_{\mathrm{m}\varepsilon}\ln\frac{|\dot{\varepsilon}|}{\dot{\varepsilon}_0}\right) & |\dot{\varepsilon}| \geq \dot{\varepsilon}_0 \\ \varepsilon_{\mathrm{m0}} & |\dot{\varepsilon}| < \dot{\varepsilon}_0 \end{cases} \tag{5.45}$$

where $\varepsilon_{\mathrm{mf}}$ refers to the rate-dependent failure strain, $\dot{\varepsilon}_0$ represents the reference strain-rate, $\varepsilon_{\mathrm{m0}}$ stands for the failure strain measured at the reference strain-rate, $\dot{\varepsilon}$ denotes the average strain rate applied to the polymer matrix, and $C_{\mathrm{m}\varepsilon}$ is a material parameter describing the rate-dependence of the failure strain against the strain-rate. Here, this material parameter should be fitted by using a procedure similar to that in Section 5.3.2. Also, it should be noted that the positive sign should be utilised if the failure strain is found to increase with strain-rate; otherwise, the negative sign should be used.

5.3.3.3 Damage evolution of yarn material

✧ Formulations based on Weibull distribution

To accurately predict the overall response of woven composites, it is critical to identify how damage will develop after damage initiation. One of the commonly used techniques is to employ a Weibull function based formulation [207] to phenomenologically describe the damage evolution as a function of the applied stress or strain, see [130, 131, 135, 136, 208]. The uniaxial form of the commonly used Weibull function based formulation for describing the damage evolution in composite materials can be written as:

$$\omega = 1 - \exp\left[-\frac{1}{\alpha \exp(1)}\left(\frac{E|\varepsilon|}{X}\right)^\alpha\right] \tag{5.46}$$

where ε refers to the strain, X denotes the strength, E is Young's modulus, α is a material parameter used to describe the rate of damage evolution, ω is the damage variable, with the value of 0 representing the undamaged or virgin state and the value of 1 denoting the state of complete failure.

However, it can be found after taking a closer examination that there are two problems in the above formulation. On one hand, if a failure criterion is applied to identify the point where damage initiates, the use of this formulation means that damage will initiate at zero

stress or strain, which is generally not desirable. On the other hand, if a failure criterion is utilised, e.g. $E|\varepsilon| = X$, the value of the damage calculated using this formulation for the point of damage initiation, where the damage is expected to be zero, is not equal to zero:

$$\omega_0 = 1 - \exp\left(-\frac{1}{\alpha\exp(1)}\right) \neq 0 \tag{5.47}$$

To eliminate the above limitations, an improved formulation is proposed in the present work for predicting the damage evolution of the yarn material in woven composites. The uniaxial form of the proposed formulation is written as follows:

$$\omega = \begin{cases} 0 & E|\varepsilon| < X \\ 1 - \exp\left\{-\frac{1}{\exp(1)}\left[\left(\frac{E|\varepsilon|}{X}\right)^{\beta} - 1\right]\right\} & E|\varepsilon| \geq X \end{cases} \tag{5.48}$$

where β is a material parameter used to describe the rate of damage evolution. Here, it is interesting to note that the proposed formulation still complies with the standard Weibull function based formulation to some extent. Specifically, the proposed formulation can be rewritten into a special case of the standard Weibull function based formulation by setting α as 1, as follows:

$$\omega = \begin{cases} 0 & E|\varepsilon| < X \\ 1 - \exp\left\{-\frac{1}{\alpha\exp(1)}\left[\left(\frac{E|\varepsilon|}{X}\right)^{\beta} - 1\right]^{\alpha}\right\} & E|\varepsilon| \geq X \end{cases} \tag{5.49}$$
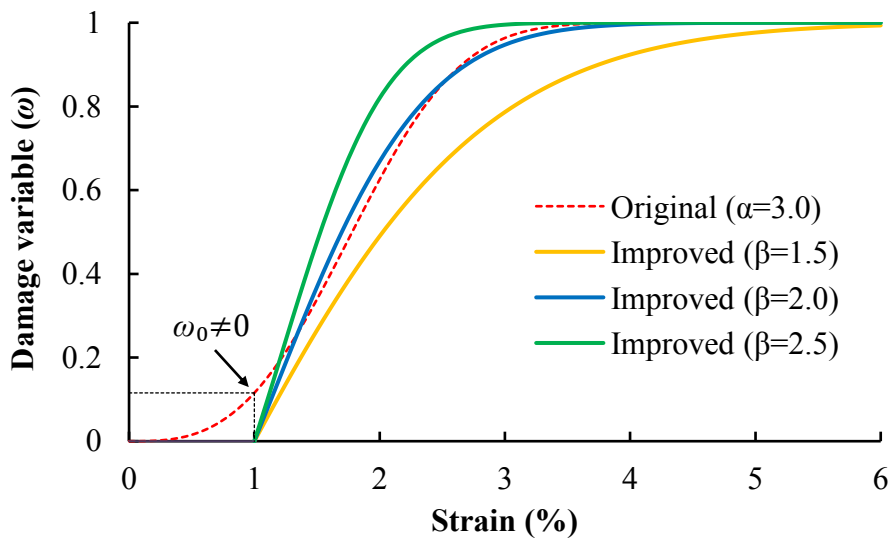
Figure 5.11: Comparison between the standard and improved formulations

Fig. 5.11 shows a comparison between the standard and the improved formulations, where the same values of E and X were utilised to produce the curves based on Eqs. (5.46) and (5.48), respectively. It is clearly demonstrated in this figure that both the problem of non-zero damage at the point of damage initiation and that of damage propagating from zero stress or strain have been effectively avoided by utilising the improved formulation. Also, this figure suggests that by changing the value of the material parameter, β, the rate of damage evolution can be easily adjusted for the yarn material of investigation.

In the present work, the improved formulation given in Eq. (5.48) is extended to model the damage evolutions associated with the six failure modes, as previously described in Section 5.3.3.1. Specifically, the functions to be used to represent the damage evolution of the six failure modes of the yarn material are defined as follows:

$$\omega_{1fT} = \begin{cases} 0 & f_{1fT} < 1 \\ 1 - \exp\{-[(f_{1fT})^{\beta_1} - 1]/\exp(1)\} & f_{1fT} \geq 1 \end{cases} \qquad (5.50)$$

$$\omega_{1fC} = \begin{cases} 0 & f_{1fC} < 1 \\ 1 - \exp\{-[(f_{1fC})^{\beta_2} - 1]/\exp(1)\} & f_{1fC} \geq 1 \end{cases} \qquad (5.51)$$

$$\omega_{2mC} = \begin{cases} 0 & f_{2mC} < 1 \\ 1 - \exp\{-[(f_{2mC})^{\beta_3} - 1]/\exp(1)\} & f_{2mC} \geq 1 \end{cases} \qquad (5.52)$$

$$\omega_{2mS} = \begin{cases} 0 & f_{2mS} < 1 \\ 1 - \exp\{-[(f_{2mS})^{\beta_4} - 1]/\exp(1)\} & f_{2mS} \geq 1 \end{cases} \qquad (5.53)$$

$$\omega_{3mC} = \begin{cases} 0 & f_{3mC} < 1 \\ 1 - \exp\{-[(f_{3mC})^{\beta_5} - 1]/\exp(1)\} & f_{3mC} \geq 1 \end{cases} \qquad (5.54)$$

$$\omega_{3mS} = \begin{cases} 0 & f_{3mS} < 1 \\ 1 - \exp\{-[(f_{3mS})^{\beta_6} - 1]/\exp(1)\} & f_{3mS} \geq 1 \end{cases} \qquad (5.55)$$

where $\beta_1 \sim \beta_6$ are the material parameters used to describe the rates of damage evolution corresponding to the six failure modes. Here, each constant can be fitted from a uniaxial test. For example, the ith parameter β_i ($i = 1, 2, \ldots, 6$) can be determined by minimising a least-squares function that is based on the differences between the stresses measured at the post-failure stage, σ_j ($j = 1, 2, \ldots, n$), and the predicted stresses, $\hat{\sigma}_j$:

$$g(\beta_i) = \sqrt{(\sigma_1 - \hat{\sigma}_1)^2 + \cdots + (\sigma_j - \hat{\sigma}_j)^2 + \cdots + (\sigma_n - \hat{\sigma}_n)^2} \tag{5.56}$$

where $\hat{\sigma}_j$ can be calculated based on the measured post-failure strain, ε_j, as follows:

$$\hat{\sigma}_j = \exp\left\{-\left[(E|\varepsilon_j|/X)^{\beta_i} - 1\right]/\exp(1)\right\} E\varepsilon_j \tag{5.57}$$

✧ *Calculation of the damaged elasticity matrix*

To account for the degradation of material stiffness resulted from the damage evolution in the yarn material, the concept of the damaged elasticity matrix, $\mathbf{C}(\omega)$, is employed to replace the original elasticity matrix. For simplicity, the damaged elasticity matrix can be defined using its inverse, i.e. $\mathbf{S}(\omega)$, which can be divided into a direct part $\mathbf{S}_d(\omega)$ and a shear part $\mathbf{S}_s(\omega)$, as follows:

$$\mathbf{C}(\omega) = \mathbf{S}^{-1}(\omega) = \begin{bmatrix} \mathbf{S}_d^{-1}(\omega) & \mathbf{0} \\ \mathbf{0} & \mathbf{S}_s^{-1}(\omega) \end{bmatrix} \tag{5.58}$$

$$\mathbf{S}_d(\omega) = \begin{bmatrix} \dfrac{1}{E_L(1-\omega_1)} & -\dfrac{v_{LT}}{E_L\sqrt{(1-\omega_1)(1-\omega_2)}} & -\dfrac{v_{TL}}{E_T\sqrt{(1-\omega_1)(1-\omega_3)}} \\ -\dfrac{v_{LT}}{E_L\sqrt{(1-\omega_1)(1-\omega_2)}} & \dfrac{1}{E_T(1-\omega_2)} & -\dfrac{v_{TT}}{E_T\sqrt{(1-\omega_2)(1-\omega_3)}} \\ -\dfrac{v_{TL}}{E_T\sqrt{(1-\omega_1)(1-\omega_3)}} & -\dfrac{v_{TT}}{E_T\sqrt{(1-\omega_2)(1-\omega_3)}} & \dfrac{1}{E_T(1-\omega_3)} \end{bmatrix} \tag{5.59}$$

$$\mathbf{S}_s(\omega) = \begin{bmatrix} \dfrac{1}{G_{LT}(1-\omega_4)} & \dfrac{1}{G_{TT}(1-\omega_5)} & \dfrac{1}{G_{TL}(1-\omega_6)} \end{bmatrix} \tag{5.60}$$

where

$$\omega_1 = (\omega_{1fT}\langle\sigma_{11}\rangle - \omega_{1fC}\langle-\sigma_{11}\rangle)/\sigma_{11} \tag{5.61}$$

$$\omega_2 = (\omega_{2mC}\langle\sigma_{22}\rangle - \omega_{2mS}\langle-\sigma_{22}\rangle)/\sigma_{22} \tag{5.62}$$

$$\omega_3 = (\omega_{3mC}\langle\sigma_{33}\rangle - \omega_{3mS}\langle-\sigma_{33}\rangle)/\sigma_{33} \tag{5.63}$$

$$\omega_4 = 1 - (1-\omega_{1fT})(1-\omega_{1fC})(1-\omega_{2mC})(1-\omega_{2mS}) \tag{5.64}$$

$$\omega_5 = 1 - (1-\omega_{2mC})(1-\omega_{2mS})(1-\omega_{3mC})(1-\omega_{3mS}) \tag{5.65}$$

$$\omega_6 = 1 - (1-\omega_{3mC})(1-\omega_{3mS})(1-\omega_{1fT})(1-\omega_{1fC}) \tag{5.66}$$

5.3.3.4 Damage evolution of polymer matrix

In terms of the damage evolution of the polymer matrix, it is assumed to follow a similar formulation to the yarn material, as follows:

$$\omega_m = \begin{cases} 0 & |f_m| \leq 1 \\ 1 - \exp\{-[(|f_m|)^{\beta_m} - 1]/\exp(1)\} & |f_m| > 1 \end{cases} \tag{5.67}$$

where β_m is a constant used to describe the rate of damage evolution. The degradation of the stiffness of the polymer matrix due to damage can be taken into account by modifying the elasticity matrix into $C_m(1 - \omega_m)$.

5.3.4 Deformation of woven fabric under shear

Under in-plane tension in the warp or fill direction, the straightening effects of yarns in plain woven composites is limited due to a low degree of waviness. However, as a result of a low stiffness of the matrix phase, plain woven composites are susceptible to in-plane shear loading, causing reorientations in the warp and fill yarns the mutually perpendicular state to a fully locked position. In this work, the approach developed by Tabiei and Ivanov [209] for describing the deformation of a flexible woven fabric is adapted. Specifically, the reorientation of woven yarns under shear is modelled by modifying the in-plane shear modulus G_{LT} into μG_{LT}, where μ is a discount factor. For plain woven composites, this factor is assumed to have a value of G_m/G_{LT} if the warp and fill yarns are in the original state and linearly increase to unity when the yarns are compacted to a fully locked position. Considering the geometrical relations of the yarns in the fully locked positions, the value of this factor at different strain values can be determined, as follows, where G_m is the shear modulus of the matrix, and $\langle \varepsilon_{11} \rangle$ is the volume average strain applied in the X direction:

$$\mu = \begin{cases} \frac{(G_{LT}-G_m)\langle\varepsilon_{11}\rangle+G_m\varepsilon_a}{G_{LT}\varepsilon_a} & \varepsilon_a \leq \langle\varepsilon_{11}\rangle < 0 \\ \frac{(G_{LT}-G_m)\langle\varepsilon_{11}\rangle+G_m\varepsilon_b}{G_{LT}\varepsilon_b} & \varepsilon_b > \langle\varepsilon_{11}\rangle \geq 0 \\ 1 & \text{Otherwise} \end{cases} \tag{5.68}$$

$$\varepsilon_a = \sqrt{2}\sin(0.5\arcsin(\lambda)) - 1 \tag{5.69}$$

$$\varepsilon_b = \sqrt{2}\cos(0.5\arcsin(\lambda)) - 1 \tag{5.70}$$

5.4 Meshfree implementation

5.4.1 Framework of the meshfree program

Similar to the case of predicting the elastic properties of woven composites, an in-house computer program implementing the high-fidelity mUC models and the material models described in Section 5.3 has been developed in combination with the explicit weak-form meshfree method for predicting the overall response of woven composites. This program, which will be termed as the *explicit meshfree program*, was coded using the programming language FORTRAN. It allows the user to predict the overall response of plain, twill or 3D woven composites, on the condition of providing four types of inputs, i.e. geometry configurations, numerical parameters, material properties and loading conditions, which will be discussed later.

Fig. 5.12 details the flow chart of this computer program. Clearly, the upper-left block of this program is similar to the left block of the standard meshfree program (see Fig. 4.35), except that the lumped mass matrix, $\mathbf{M}_L$, rather than the global stiffness matrix should be calculated. Then, based on the quantities calculated initially and the loading condition prescribed, the meshfree-based explicit time integration is performed. Here, at each time step, the acceleration, velocity and displacement of all field nodes are computed directly, and thus the strains of all integration points can be derived for the subsequent calculation of the stresses of all material points. For the points located within the yarns, the material model for identifying the damage initiation and evolution in the yarn material is utilised to calculate the stresses; otherwise, the viscoplasticity-based model is used to determine the material state of the polymer matrix and calculate the stresses, as detailed in Fig. 5.13, where it is shown that the four-step Runge-Kutta method has been utilised to obtain stable solutions of the inelastic strain, the internal stress and the total stress based on the results from the previous step. After completing the calculations for all the time steps, a history of the volume average stress can be derived, and its combination with the history of the strain prescribed yields the overall response of the woven composites of prediction. It is worth noting that the quantities in the upper-left block of Fig. 5.12 are independent of time. Therefore, this part of codes should be executed only once, before the execution of the subsequent explicit time integration. On the other hand, the codes corresponding to the remaining parts of the meshfree program should be performed for all the time steps.
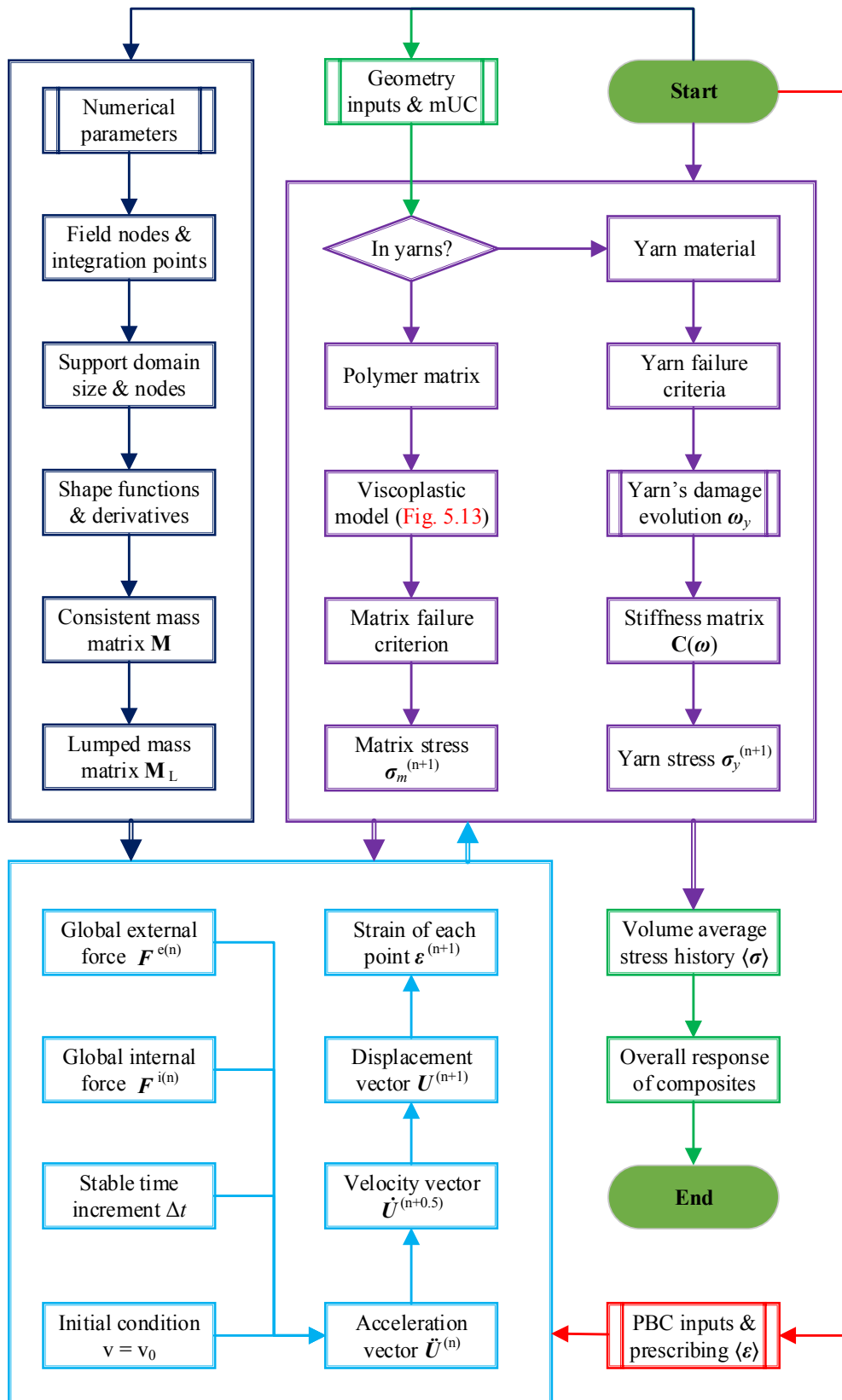
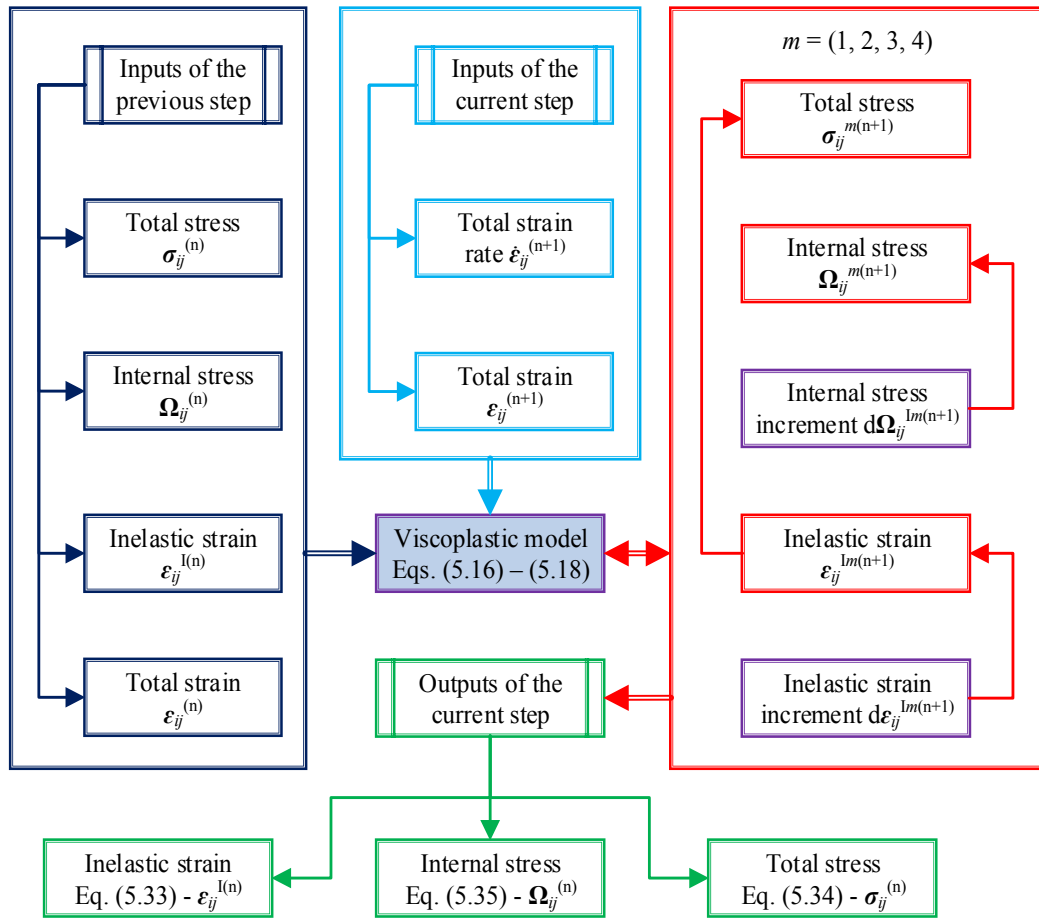**Figure 5.12: Flow chart of the explicit meshfree program**

Figure 5.13: Flow chart of the viscoplasticity-based model

5.4.2 Further details of the meshfree program

Table 5.7 lists the input parameters of the explicit meshfree program, which also consist of the geometry parameters for the mUC models of the three types of woven composites, the numerical parameters for domain discretisation, determination of support domain and shape function calculations, iii) the material parameters for the polymer matrix and yarn material, and iv) the prescribed strain. Here, it should be noted that the use of the explicit meshfree program in this work for predicting the overall response of woven composites is based on the domain discretisation strategy previously detailed in Section 4.6.4. Thus, the numerical parameters can be determined by directly performing the procedures discussed in Sections 4.6 and 4.7. However, to save computational time and costs, the conclusions that have been summarised in Section 4.7 can also be used for the determination of the open numerical parameters for the case of homogenising the overall response of woven composites.

Table 5.7: Inputs for the computer program for overall response prediction

Type	Variable	Description
Geometry parameters	WCT	Weave type (1: plain, 2: twill, 3: 3D)
	UCT	UC type (1: normal, 2: off-axis)
	$L, W, H, H_w, ...$	Dimensional parameters
	$\lambda_w, \lambda_{fa}, \lambda_{fb}, \lambda_b$	Dimensionless parameters
Numerical parameters	nFx, nFy, nFz	No. of nodes in each direction
	nCx, nCy, nCz	No. of cells in each direction
	$\alpha_s, d_{cx}, d_{cy}, d_{cz}$	Support domain parameters
	$\theta, q, a_0, a_1, a_2, a_3$	Constants for RBF and MK
Material properties	$E_m, v_m, C_{m\varepsilon}, \varepsilon_{m0}, \beta_m, \rho_m$	Material properties of polymer matrix
	$D_0, Z_0, n_r, q, \Omega_m$	Viscoplasticity model parameters
	$E_L, E_T, v_{LT}, v_{TT}, G_{LT}, C_{EL}, \rho_y$	Material properties of yarn material
	$X_T, X_C, Y_T, Y_C, Z_T, Z_C, S_{LT}, ...$	Material strengths of yarn material
	$\beta_1, \beta_2, \beta_3, \beta_4, \beta_5, \beta_6$	Parameters for the damage evolution
PBC	ALC	Admissible loading case (1, 2, 3 or 4)
	$\langle \boldsymbol{\varepsilon}(t) \rangle$	Prescribed macroscopic strain

5.5 Results and discussion

5.5.1 Examples on plain woven composites

To evaluate the accuracy and effectiveness of the UC models, the material models and the meshfree-based UC modelling methodology for predicting the overall response of woven composites, two sets of numerical examples were conducted for a plain woven composite material under in-plain normal and off-axis tensile loading conditions, as detailed in Table 5.8. The first set of numerical simulations was based on the normal mUC of plain woven composites and to predict the responses of the composites subjected to tension in the warp direction (0°) with three different strain rates, i.e. 10^{-1}/s, 10^{-3}/s and 10^{-5}/s, while the second set of simulations was based on the off-axis mUC and to predict the responses subjected to tension in the off-axis direction (45°) with the three strain rates.

Table 5.8: Details of the two sets of numerical simulations for EP121-C15-53

	Simulation	Rate (s^{-1})	Loading direction	mUC	PBC
Set A	A1	10^{-1}	Warp (0°)	Normal	See Table B.1
	A2	10^{-3}	Warp (0°)	Normal	See Table B.1
	A3	10^{-5}	Warp (0°)	Normal	See Table B.1
Set B	B1	10^{-1}	Off-axis (45°)	Off-axis	See Table D.1
	B2	10^{-3}	Off-axis (45°)	Off-axis	See Table D.1
	B3	10^{-5}	Off-axis (45°)	Off-axis	See Table D.1

5.5.1.1 Geometry information and numerical parameters

The composite material of prediction here is the one that has been previously utilised in Sections 4.1.2 and 4.7.1, and it is based on the EP121-C15-53 prepreg. Further details of this composite material can be found on the supplier website [193]. Thus, the geometry inputs for the two sets of numerical simulations are the same as those listed in Table 4.9. To determine the values of the open numerical parameters that have been employed in the two sets of simulations, sensitivity studies of all the parameters to the predicted response should be performed. However, to save computational time, the conclusions summarised from the sensitivity studies presented in Section 4.7.1 were directly utilised to determine the values of these parameters in the simulations in Set A, as shown in Table 5.9. In terms of the numerical parameters in the simulations in Set B, the numbers of field nodes and background cells were scaled based on the ratios of the overall dimensions of the off-axis mUC to those of the normal mUC. For example, if the ratio of the length of the off-axis mUC to that of the normal mUC is r_{L} and the number of field nodes in the length direction of the normal mUC is $n\text{F}x$, the number of field nodes in the length direction of the off-axis mUC will be $n\text{F}x \times r_{\text{L}}$.

Table 5.9: Numerical inputs for the two sets of numerical simulations

Set	Set A	Set B
No. of field nodes	13×13×7	10×20×7
No. of background cells	60×60×30	45×90×30
Domain scaling parameter	$\alpha_s = 2.5$	$\alpha_s = 2.5$

5.5.1.2 Determination of matrix properties and viscoplastic parameters

To determine the material properties and parameters in the viscoplasticity-based material model, a number of uniaxial tensile tests were conducted on the polymer matrix of the composites system of investigation, i.e. EP 121 matrix, according to the testing standard ASTM D638-14 [210] and the fitting procedure described in Section 5.3.1.2. The tests were comprised of six samples, with each sample further consisting of five specimens tested at the same constant strain rate to obtain averaged results.

Table 5.10: The averaged results of the six uniaxial tensile tests for EP 121

Sample	#1	#2	#3	#4	#5	#6
$\dot{\varepsilon}_0$	10^{-5}	10^{-4}	10^{-3}	10^{-2}	10^{-1}	1
σ_s	72.32	72.91	74.68	77.85	80.07	85.54
ε_s^I	4.56%	4.61%	4.47%	4.42%	4.39%	4.25%
ε_{mf}	7.13%	7.21%	7.00%	6.92%	6.86%	6.65%
x	2.373	2.427	2.572	2.789	2.917	3.176
y	3.731	3.614	3.482	3.329	3.149	2.929

The regression line shown is $y = -1.173x + 6.797$ with $R^2 = 0.989$.
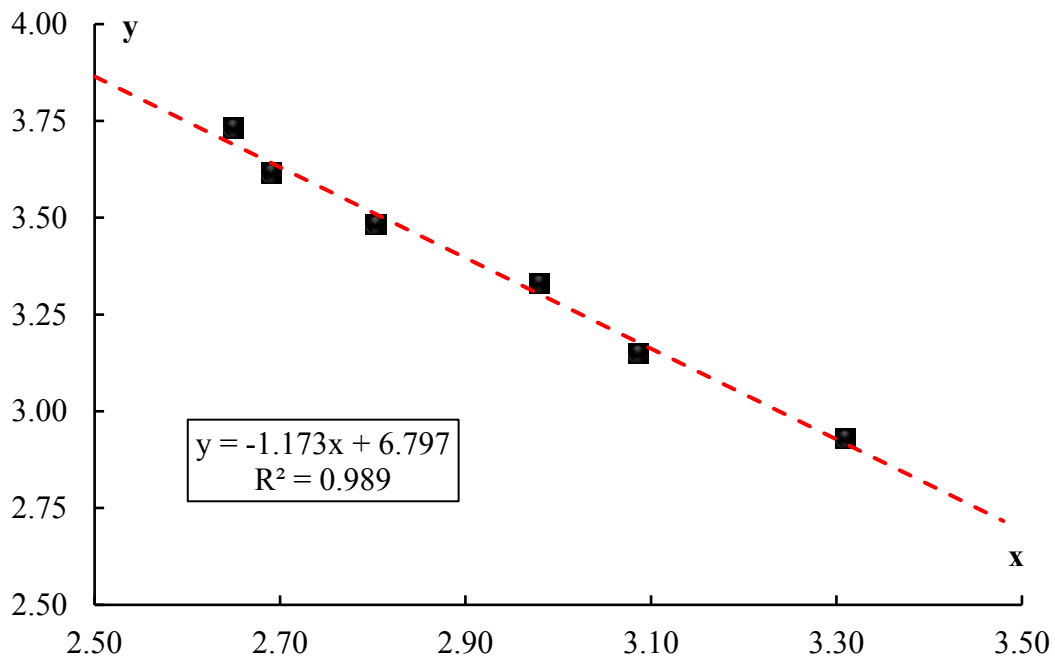
Figure 5.14: Regression analysis for determining the viscoplastic parameters

Table 5.10 shows the results of the six samples of tests, where $\dot{\varepsilon}_0$ denotes the testing strain rate, σ_s and ε_s^I stand for the stress and inelastic strain at saturation, ε_{mf} represents the stain at failure initiation. Here, it should be noted that the values of (x, y) were calculated based on Eqs. (5.13) and (5.14). Also, when calculating x and y, D_0 was chosen to be 10^4 times the maximum strain-rate, and Ω_m was estimated to be 68% of the maximum saturation stress. Based on the data in Table 5.10, a least-squares regression analysis was performed, and the equation of the best fit line is shown in Fig. 5.14. By comparing the best fit line against Eq. (5.12), the values of n_r and Z_0 were calculated, i.e. $n_r = 0.586$ and $Z_0 = 330$ MPa. In terms of parameter q, its value was calculated by solving Eq. (5.15), where the value of the inelastic strain used in this calculation was chosen to be the average of the tested values of ε_s^I.
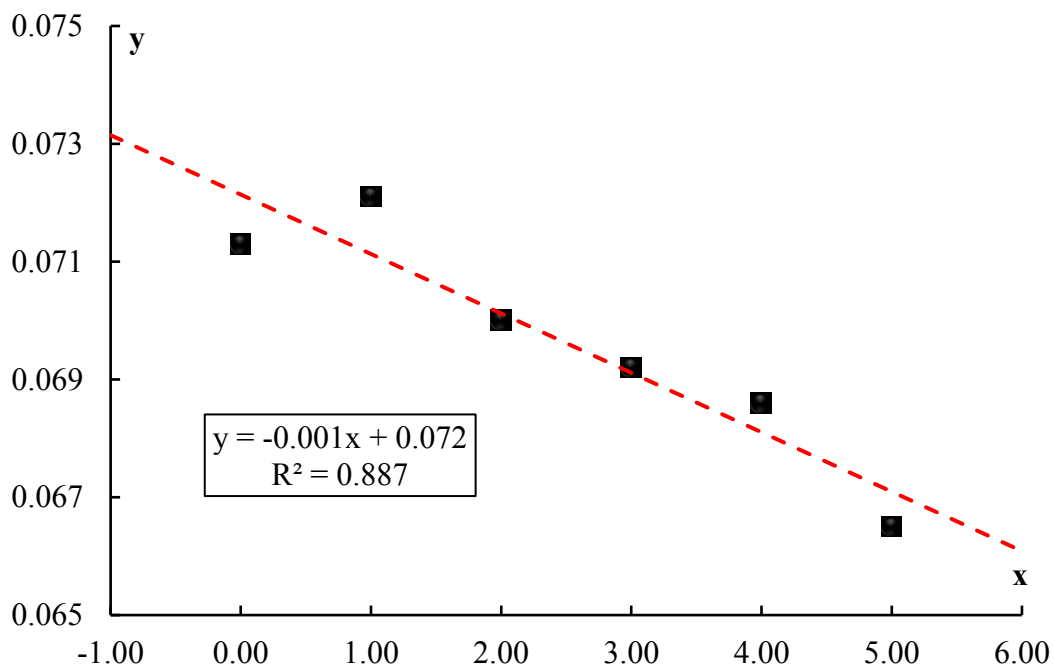
Figure 5.15: Least-squares regression analysis for determining parameter $C_{m\varepsilon}$

The results of the above uniaxial tests were employed to determine the elastic modulus, Poisson's ratio of the polymer matrix, and also the failure strain scaling coefficient, $C_{m\varepsilon}$, whose value was determined after performing the regression analysis shown in Fig. 5.15. Here, it is worth noting that the negative sign version of Eq. (5.45) was applied to conduct the regression analysis as the failure strain decreases with increasing strain-rate. Further, based on the data of these tests, the damage evolution parameter, β_m, was determined by

using the parameter fitting approach previously described in Section 5.3.3.3. The material properties and parameters of the resin matrix are summarised in Table 5.11.

Table 5.11: Material inputs of EP121-C15-53 (Modulus in GPa, Strength in MPa)

	E_{m}	v_{m}	$\varepsilon_{\mathrm{m0}}$	$C_{\mathrm{m\varepsilon}}$	β_{m}	$\rho_{\mathrm{m}}(\mathrm{g/cm^3})$
EP 121 epoxy resin	3.11	0.36	7.13%	0.014	3.8	1.264
	$D_0\ (\mathrm{s^{-1}})$	Z_0	n_{r}	q	Ω_{m}	
	10000	330	0.586	103	58	
	E_{L}	E_{T}	v_{LT}	v_{TT}	G_{LT}	$\rho_y(\mathrm{g/cm^3})$
3k HTA40 carbon-fibre yarn	161.64	10.57	0.27	0.33	5.52	1.614
	$X_{\mathrm{T}}/X_{\mathrm{C}}$	$Y_{\mathrm{T}}/Y_{\mathrm{C}}$	$Z_{\mathrm{T}}/Z_{\mathrm{C}}$	S_{LT}	S_{TT}	S_{TL}
	2687/1622	58/263	58/263	95	78	80
	β_1	β_2	β_3	β_4	β_5	β_6
	9.0	7.6	4.7	2.8	4.7	2.8

5.5.1.3 Determination of yarn properties and damage parameters

The yarn material in this plain woven composite was made from 3k HTA40 carbon fibres. Due to the unavailability of experimental facilities and the difficulty of conducting in-site tests at the yarn scale at the time of undertaking this research, all material properties of this yarn material were determined from testing unidirectional composite specimens that have the same material constituents and FVF as the yarn material. The basic properties such as the elastic moduli and strength parameters were directly obtained based on uniaxial tension, compression and shear tests. However, these tests were performed to determine only the in-plane properties. For the out-of-plane properties such as Z_{T}, they were assumed to be the same as those in the in-plane transverse direction, as given in Table 5.11.

In terms of the parameters in the damage evolution model, they were also approximated using uniaxial tests, where the specimens were loaded to complete failure, and both stress and strain data were collected to perform the least-squares procedure described in Section 5.3.3.3. Specifically, for the parameter corresponding to the damage evolution of tensile fibre failure, β_1, uniaxial tensile tests were performed on specimens in the longitudinal

direction. Based on the recorded strain data, the predicted stresses were computed using Eq. (5.57). In combination with the measured stress data, Eq. (5.56) was applied to form a least-squares function of β_1, which can be determined by minimising the function. For the parameter associated with compressive fibre failure, β_2, it was determined by conducting compression tests in the longitudinal direction. In terms of the parameters associated with matrix cracking and shear due to in-plane tensile and compressive loading, i.e. β_3 and β_4, they were evaluated after doing in-plane tension and compressive tests in the transverse direction, respectively. However, no test was performed for parameters β_5 and β_6 as the associated failure modes are similar to modes 3 and 4, and their values were assumed to be the same as β_3 and β_4. For clarity, the values of these damage evolution parameters are detailed in the last row of Table 5.11. However, it should be pointed out that the values determined using uniaxial tests on unidirectional specimens are with approximations since the failure modes in the tested unidirectional composites may not be completely identical to those in the yarn material of investigation.

5.5.1.4 Experimental tests for validating the two sets of numerical simulations
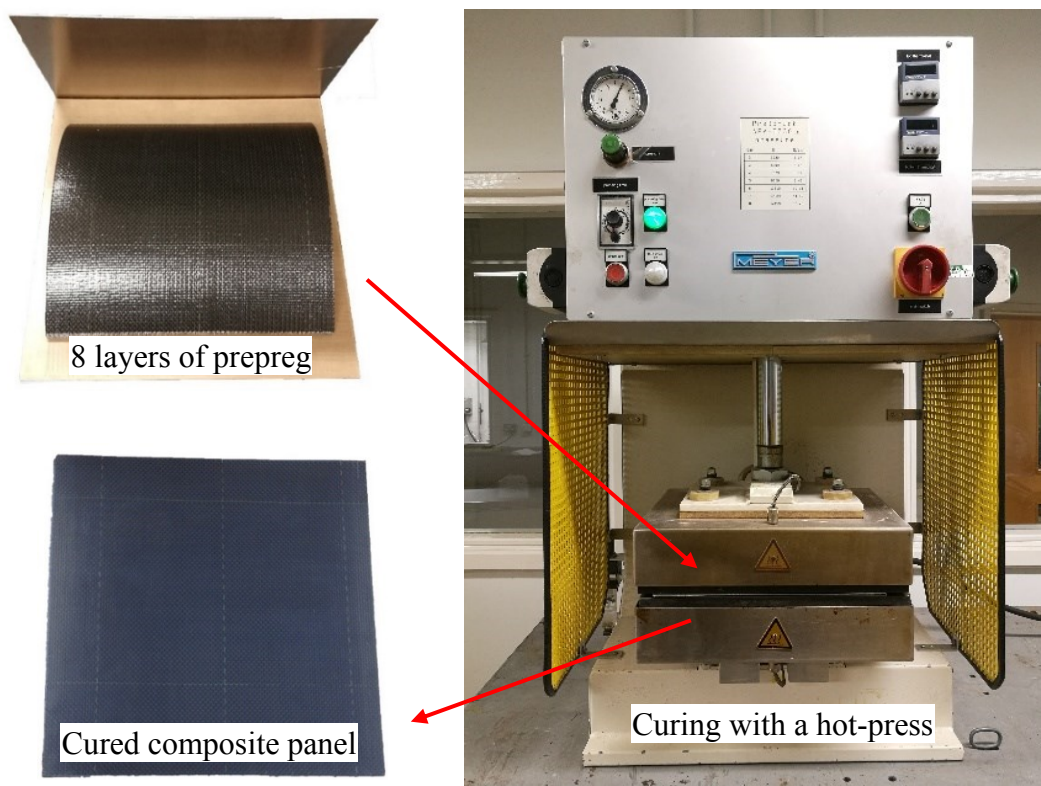
Figure 5.16: Fabrication of composite panels using a hot-press machine

To experimentally evaluate the two sets of meshfree-based simulations, composite panels based on 8 layers of EP121-C15-53 prepreg were fabricated by using a hot-press machine, as shown in Fig. 5.16. The panels were cured under the conditions of a dwell temperature of 135 °C for approximately 70 min and a pressure of 2 bars, and then cut into 0° and 45° specimens on a waterjet cutting machine, the use of which was to reduce the damage that may cause to the specimens during cutting.

Figure 5.17: Uniaxial tensile tests on a hydraulic Instron machine

According to ASTM D3039 [2] and the loading conditions in the two sets of numerical simulations, as detailed in Table 5.8, two sets of experimental tests were conducted on an Instron testing machine, as shown in Fig. 5.17. Here, the first set was comprised of three uniaxial tensile tests conducted on 0° specimens subjected to strain rates of approximately 10^{-1}/s, 10^{-3}/s and 10^{-5}/s, respectively, and the geometry configuration of these specimens are illustrated in Fig. 5.18a, where it is shown that glass fibre-reinforced plastic (GFRP) tabs were adhered to the testing specimens with a two-component epoxy resin for the sake of minimising gripping damage to the specimens. In terms of the second set of tests, they

were designed to obtain the overall responses of the plain woven composites subjected to the three strain rates of loading (10^{-1}/s, 10^{-3}/s and 10^{-5}/s) in the off-axis direction, i.e. 45° to the warp direction. The geometry configuration of the 45° specimens is shown in Fig. 5.18b. For each loading rate, three repeated tests were conducted, aiming to reduce the influence of uncertainties on the experimental results.
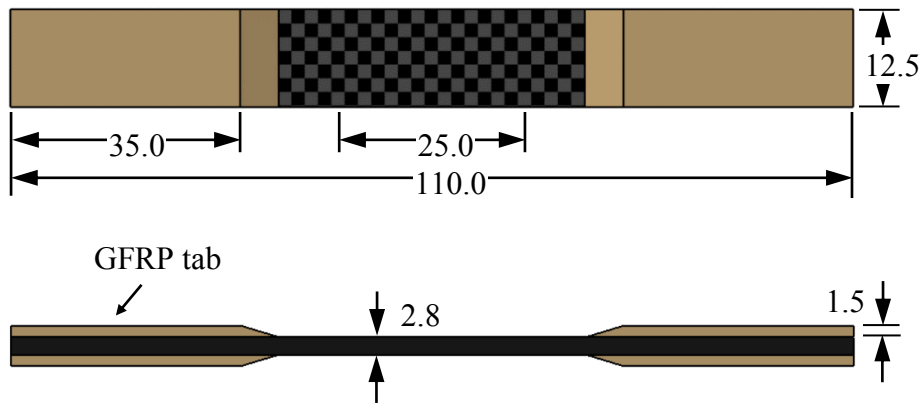
(a) Geometry configuration of 0° specimen (unit: mm)
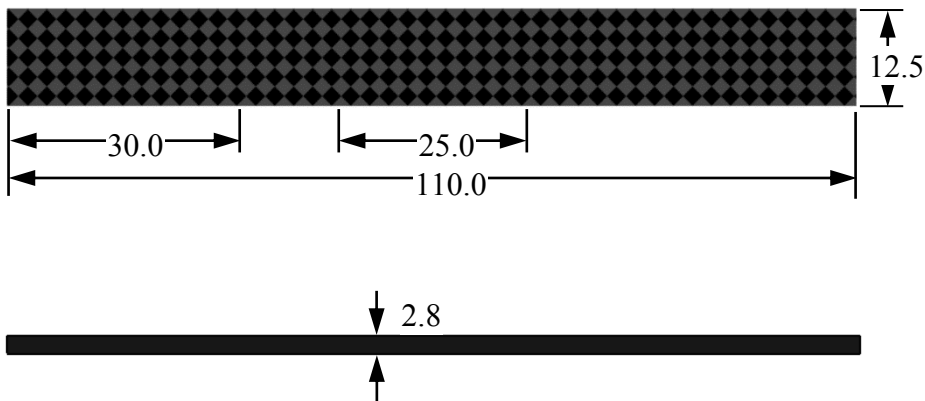
(b) Geometry configuration of 45° specimen (unit: mm)

Figure 5.18: Geometry configurations of the composite specimens

5.5.1.5 Comparison of meshfree simulations with experiment results

Fig. 5.19 compares the predicted and measured stress-strain responses of the plain woven CFRP composites subjected to the three rates of tensile loading in the warp/0° direction. In this figure, only the responses predicted based on the MLS technique are presented for clarity (a comparison among the MLS, RBF and MK techniques in terms of their accuracy

in the predictions will be discussed later). Clearly, the stress-strain curves predicted by using the meshfree-based UC modelling approach are generally in good agreement with those measured by the experimental tests, with the stress exhibiting a linear increase with the strain before reaching a maximum point. After this point, the stress drops instantly to zero, which is associated with the presence of fibre fracture, as highlighted in Fig. 5.20.
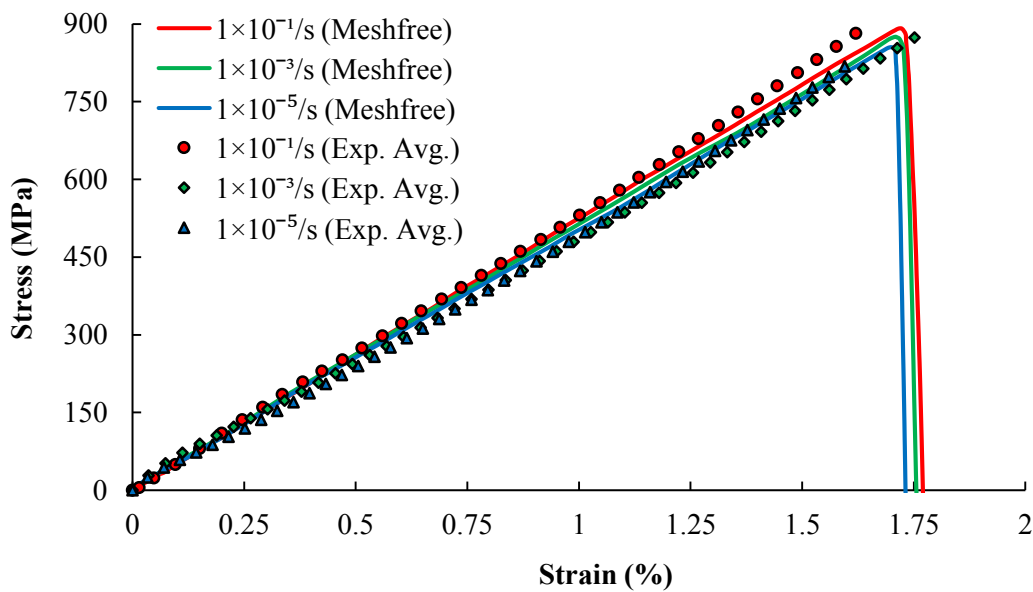
Figure 5.19: Meshfree-based predictions & experimental results for 0° tension
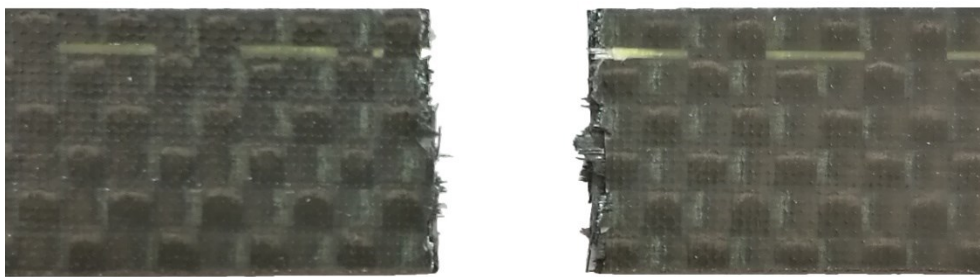
Figure 5.20: Typical failure mode of the CFRP composites after 0° tension

Also, it can be found in Fig. 5.19 that there is no significant difference in the stress-strain curves measured under the three different strain rates, suggesting that the response of the plain woven CFRP composites in the warp direction is strain-rate insensitive. In view of the fact that carbon fibres are rate-independent, the evidence of strain-rate insensitivity observed in the tests confirms that the overall response of woven composites in the fibre directions is mainly driven by the fibres. By comparing the predicted stress-strain curves,

it is also confirmed that the rate-independent behaviour of this type of woven composites in the warp direction, as observed in the tests, has been effectively captured by the use of the meshfree-based UC approach.
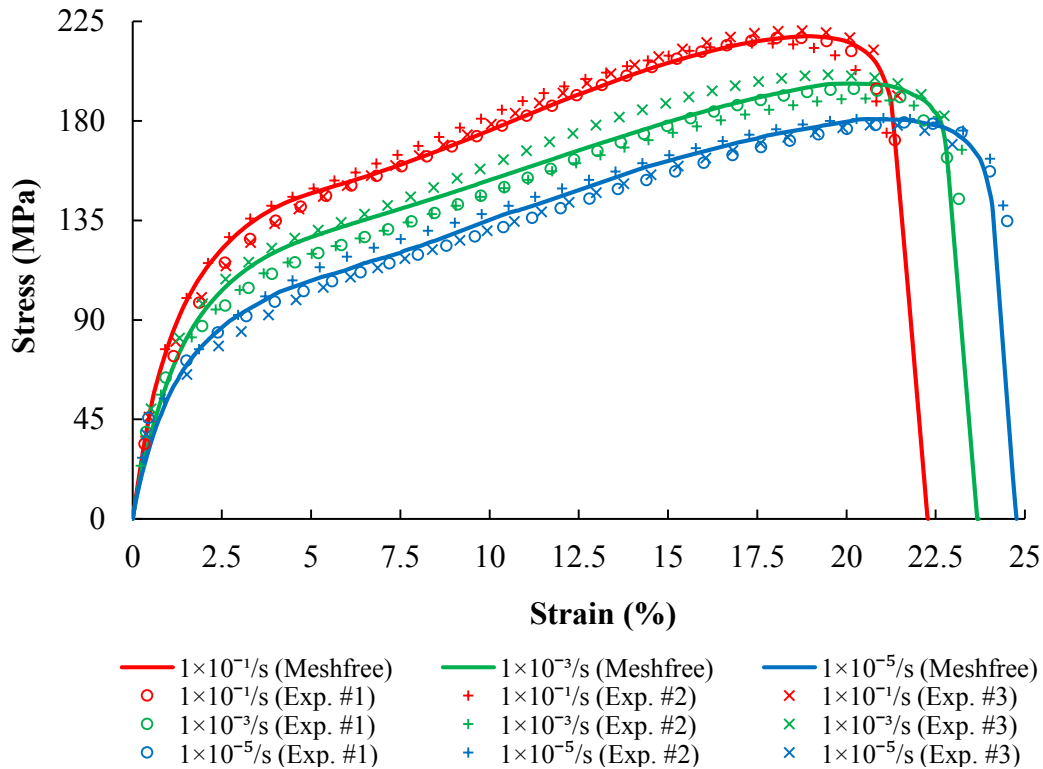
Figure 5.21: Meshfree-based predictions and experimental results for 45° tension

Fig. 5.21 shows the predicted stress-strain curves of the plain woven CFRP composites under the three rates of loading in the off-axis/45° direction, as well as the corresponding experimental results. Again, the stress-strain curves predicted using the meshfree-based UC approach agree reasonably well with the experimental results. In particular, both the strain rate-dependent behaviour and the nonlinear response in the off-axis direction of this composite material have been successfully captured. Also, it is evident that the feature of the notably increased maximum stress with increasing strain rate, as well as that of the moderately decreased failure strain with increasing strain rate, have been predicted by the use of the meshfree-based approach. Furthermore, it is interesting to note that the above rate-dependent features are similar to those observed in the tests that were conducted for determining the material properties and viscoplasticity-based parameters of the polymer matrix. Therefore, it is established that the material behaviour of woven composite in the off-axis direction is primarily associated with that of the polymer matrix.

Apart from the above findings, it should be noted that the failure strain of this type of composites, either obtained by the meshfree-based predictions or the experimental tests, is within the range of around 22% - 25%, which is much larger than both that of the polymer matrix (approximately 7%) and that of the carbon fibres (approximately 1.7%). It is believed that such a large deformation in the off-axis direction of the composites was due to the fact that the presence of matrix cracking and shear, as evidenced in a typically failed specimen shown in Fig. 5.22, reduced its constraint on the woven fabric, leading to an exceptionally large degree of deformation in the off-axis direction of the composites.

Figure 5.22: Typical failure mode of the CFRP composites after 45° tension

The evidence demonstrated above, i.e. good agreements between the predicted responses and the corresponding experimental results, clearly suggests that the meshfree-based UC modelling approach is effective in predicting the responses of plain woven composites subjected to different rates of loading in both the normal and off-axis directions. Thus, it is theoretically expected that this approach would be able to predict the overall response of any other type of woven composites in any direction, as long as a matching UC model is developed and suitable material models are applied to describe the behaviours of the material constituents. Apart from this, it should be pointed out that although the modelling approach discussed in this chapter is based on the explicit weak-form meshfree method, the nature of the meshfree-based implementation here is essentially the same as that based on the standard weak-form meshfree method, as discussed in the last chapter. Thus, one of the highlights of the research presented in this chapter is its capability of addressing the problem of a reduced accuracy in the analytical approaches and eliminating the concern of having highly complex and time-consuming pre-processing in the FEM-based approaches, making it an accurate but simple approach. Another evident highlight of the research in this chapter is that it has extended the capability of the UC modelling methodology from

traditionally the homogenisation of the elastic properties to the prediction of the overall response of woven composites at the scale of UC.

5.5.1.6 Comparison among the MLS, RBF and MK techniques

To compare the difference in the MLS, RBF and MK techniques, numerical simulations were also conducted based on the three techniques to predict the responses of the plain woven CFRP composites under a strain rate of 10^{-1}/s loaded in the normal and off-axis directions. Fig. 5.23 shows the stress-strain curves predicted for the case of 0° tension, as well as the experiment result. Clearly, all the predicted responses exhibit good agreement with the experiment result. Also, it can be seen that the RBF and MK techniques produce very close predictions, while the MLS technique gives a slightly different result, with its predicted value of the ultimate failure strain being higher than those obtained based on the other two techniques.

The overall response predicted for the case of 45° tension is shown in Fig. 5.24. Again, the RBF and MK techniques generate closer predictions than the MLS technique does. It is believed that the presence of the slightly different predictions when using the MLS technique is as a consequence of the lack of the Kronecker delta function property in the MLS technique.
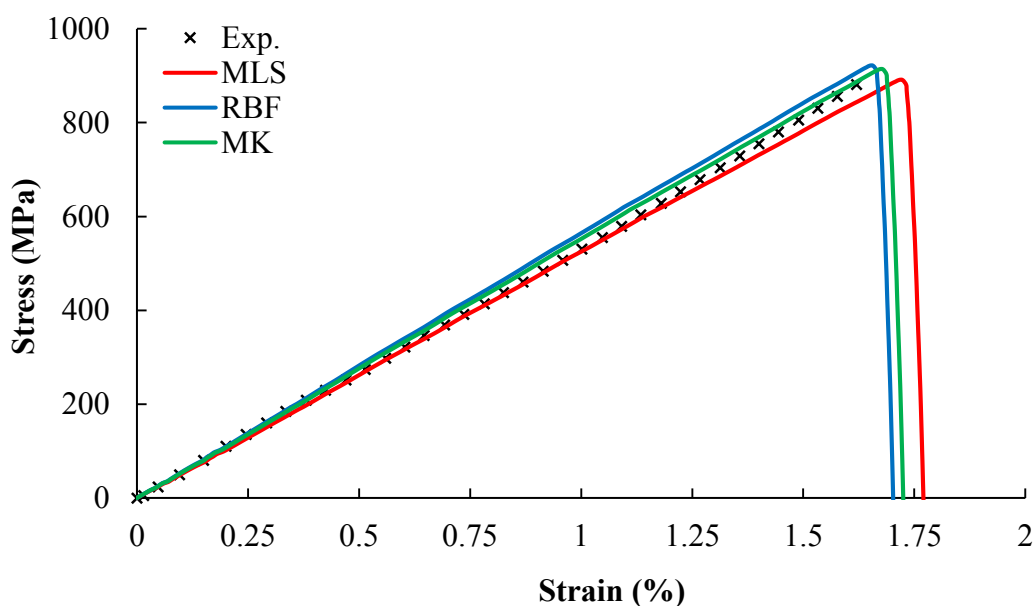
Figure 5.23: The 0° tensile response predicted based on MLS, MK and RBF
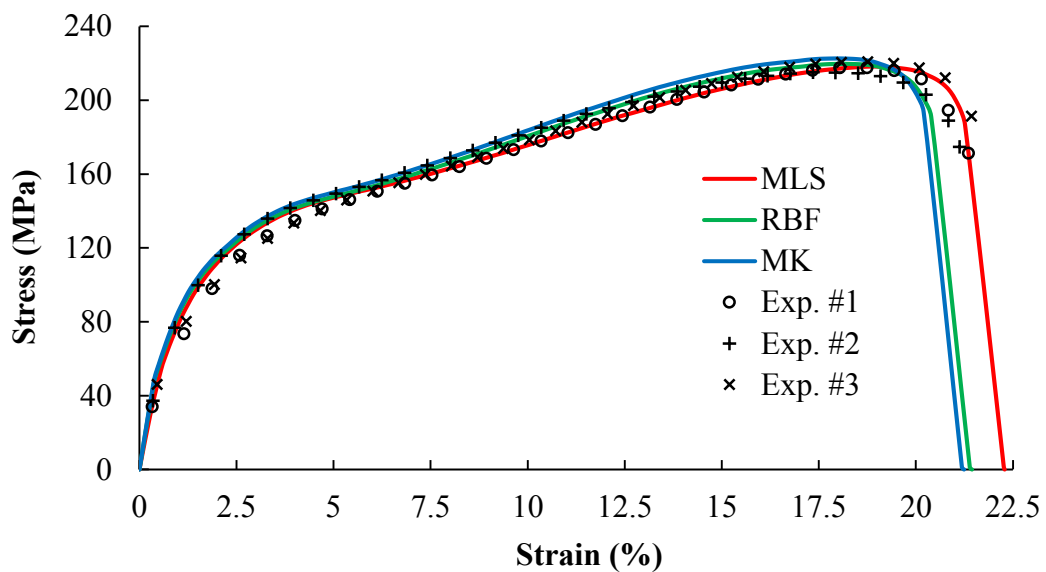
Figure 5.24: The 45° tensile response predicted based on MLS, MK and RBF

5.5.2 Application to plain, twill and 3D woven composites

Obtaining prior knowledge of the influences of fibre tow size and weaving architecture on the overall response is often essential for the successful design of woven composite materials and structures. For this reason, the meshfree-based UC approach was applied to analyse the responses of plain, twill and 3D woven composites, as follows. However, due to the unavailability of material data for twill and 3D woven composites, the numerical examples that will be presented were based on the same set of material data, as given in Table 5.11. Furthermore, to save computational time, all the numerical simulations were performed using the same type of shape function approximation technique (i.e. the MLS technique) and at a relatively high strain rate (i.e. 10^{-1}/s)

5.5.2.1 Influence of fibre tow width on the response

The first example was to investigate the influence of fibre tow width on the responses of twill woven composites subjected to 0° and 45° tensile loadings. For each loading case, three meshfree-based simulations were conducted on 2/2 twill woven composites with an overall dimension of 1mm × 1mm × 0.32mm and its fibre tow size being 0.8mm, 0.9 mm and 1.0 mm, respectively. Here, these fibre tow widths correspond to the values of the

dimensionless parameter, λ, being 0.4, 0.45 and 0.5, and the yarn volume fractions being 50.93%, 57.29% and 63.66%, respectively.
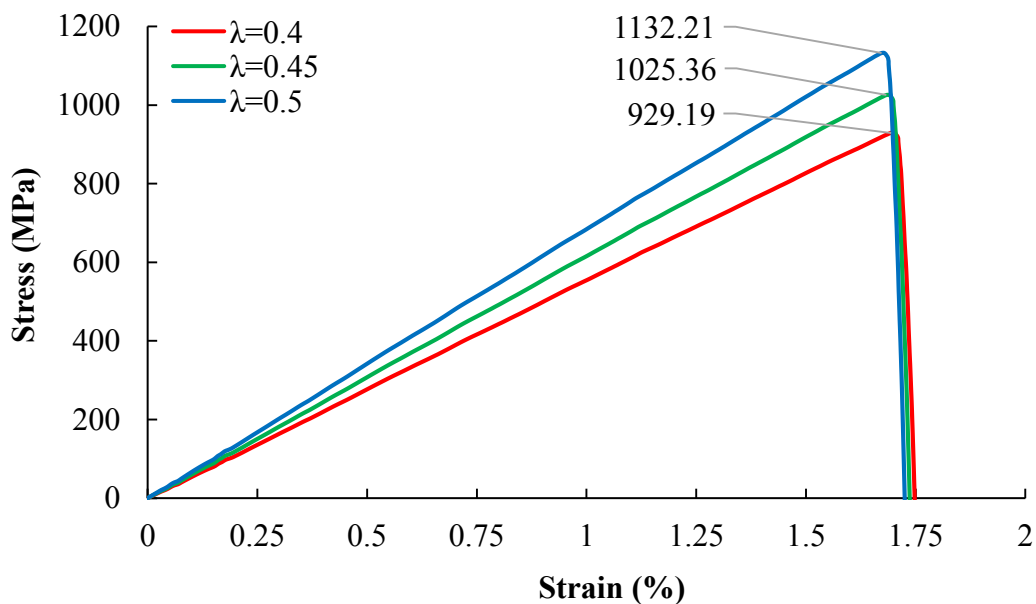
Figure 5.25: Variation of the 0° tensile response on fibre tow width (or λ)

Fig. 5.25 shows the stress-strain responses predicted for the twill woven composites under 0° tensile loading, which clearly illustrated that both the maximum stress and the elastic modulus increase with the increase of λ. To analyse the underlying mechanism that drives the presence of this phenomenon, the values of the elastic moduli, the differences in these values and the differences in the values of the dimensionless parameter are calculated, as listed in Table 5.12. From this table, it can be seen that the elastic modulus in the case of $\lambda = 0.5$ is over 20% higher than that in the case of $\lambda = 0.4$. However, it is interesting to find that the percentages of the increases in the elastic modulus are similar to those of the increases in the dimensionless parameter, which are equivalent to the same percentages of the increases in tow width. Such a finding again confirms that the behaviour of woven composites in the fibre directions is primarily driven by that of the yarn material.

Apart from the above findings, it should be noted that the predicted value of the failure strain (approximately 1.75%) is almost independent of fibre yarn's width, as indicated in Fig. 5.25. This is believed to be due to the fact that the increase in fibre yarn's width does not change the overall dimension (i.e. the size of the UC) of the composites, and thus it would not produce significant influence on the value of the failure strain.

Table 5.12: Variation of the elastic modulus on tow width the value of λ

Case	E	$\Delta E\%$	$\Delta\lambda\%$
$\lambda = 0.4$	54.85	-	-
$\lambda = 0.45$	60.81	10.86%	12.5%
$\lambda = 0.5$	67.71	23.45%	25.0%

Fig. 5.26 shows the predicted stress-strain responses of the twill woven composites under 45° tensile loading. Unlike in the case of 0° tension, the increase of fibre tow size in this case does not generate significant variation in the maximum stress and the initial elastic modulus. In general, this is attributed to the fact that the response of woven composites in the off-axis direction is mainly dominated by the polymer matrix, and consequently the influence of the change in tow width on the response in this direction is reduced. Another feature of the results given in Fig. 5.26 is that the predicted failure strain shows a slight decrease with increasing yarn width, which can be explained by the fact that the increase of the yarn width leaves less space between adjacent yarns in the woven fabric, reducing the easiness of the deformation of the composites in the off-axis direction.
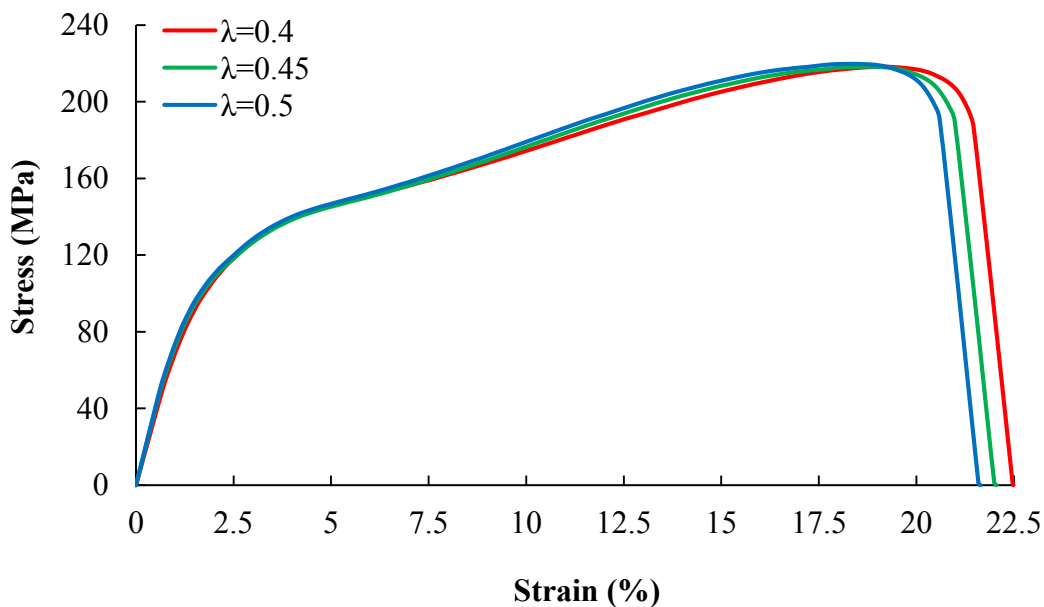
Figure 5.26: Variation of the 45° tensile response on fibre tow width (or λ)

5.5.2.2 Influence of weave architecture on the response

The second example was to numerically investigate the influence of weave architecture on the response of woven composites subjected to 0° and 45° tensile loading conditions. For this sake, meshfree-based simulations were performed for plain, twill and 3D woven composites. In these simulations, the same yarn volume fraction (i.e. 50.93%) was utilised to exclude the influence of yarn's volume fraction on the response. The geometry inputs for the three types of woven composites are detailed in Table 5.13.

Table 5.13: Geometry inputs for the three types of woven composites

	L	W	H	λ	
Plain					
	1.0	1.0	0.32	0.8	
Twill	L	W	H	λ	
	1.0	1.0	0.32	0.4	
3D	L	W	H	λ_{w}	λ_{fa}
	1.0	1.0	1.0	0.85	0.45
	λ_{fb}	λ_{b}	H_{w}	H_{fa}	H_{fb}
	0.9	0.25	0.25	0.125	0.25
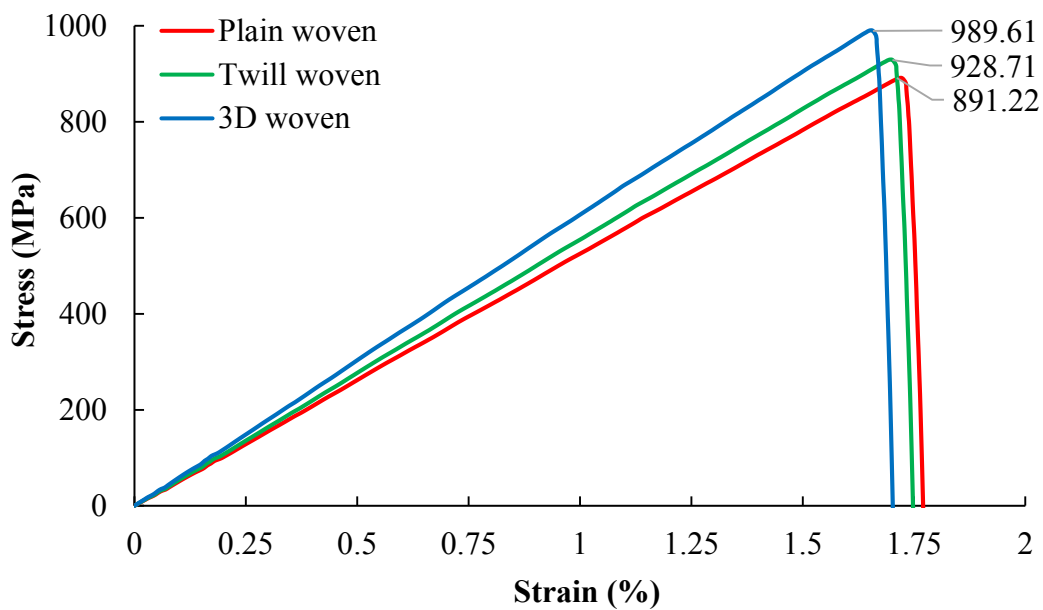
Figure 5.27: Variation of the 0° tensile response on weave structure

Fig 5.27 shows the stress-strain responses predicted for the case of 0° tension. Here, it is evident that 3D woven composites appear to be stiffer than both the other two types of woven composites, and twill woven composites are stiffer than plain woven composites. Since the three types of woven composites have the same yarn volume, the presence of different stiffness can be explained by the difference in the percentage of straight yarns in warp/0° direction. Specifically, the percentages of straight yarns are 0% in plain woven composites, 50% in twill woven composites and up to 90% in 3D woven composites, as indicated in Figs. 4.9, 4.14 and 4.21. Given that the average waviness in the warp direction is highest in plain woven composites and lowest in 3D woven composites and that the presence of waviness in woven composites has led to a reduction in the material stiffness in the fibre direction, the results presented in Fig. 5.27 can thus be justified.
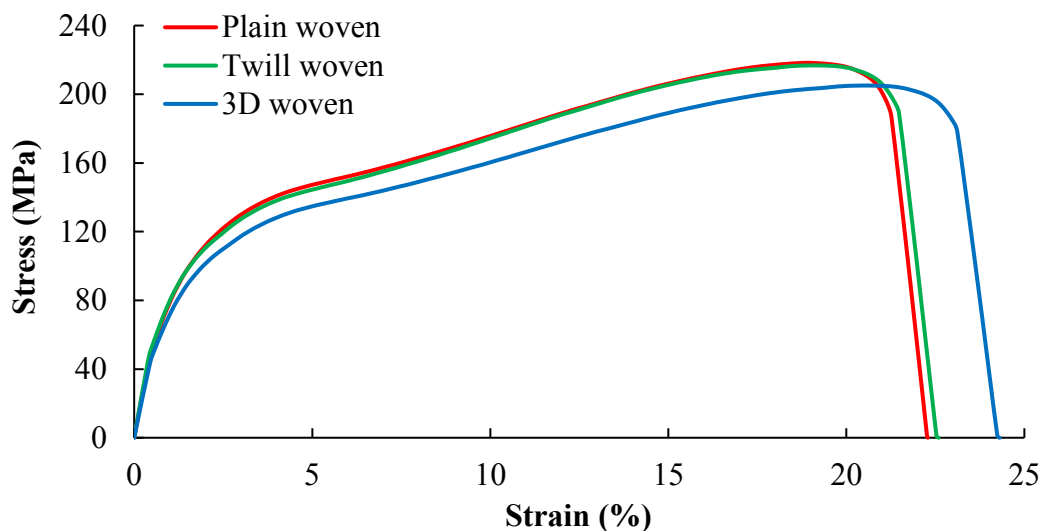
Figure 5.28: Variation of the 40° tensile response on weave structure

The overall stress-strain curves predicted for the case of 45° tension is shown in Fig. 5.28. Here, it can be clearly seen that the response of plain woven composites in this direction is almost identical to that of twill woven composites, while 3D woven composites tend to have an increased failure strain and a lower maximum stress. The presence of a decreased overall stiffness of 3D woven composites in the off-axis direction may be explained by the fact that there is no interlacing between the warp and weft yarns, which results in an easier deformation in the fabric of 3D woven composites, in comparison to that in both plain and twill woven composites.

5.6 Summary

In this chapter, the off-axis mUC models of the three types of woven composites, as well as the corresponding PBCs, were firstly detailed. Then, the material models for describing the behaviours of the two constituents in woven composites were described. Specifically, a viscoplasticity-based model was selected to characterise the nonlinear, rate-dependent behaviour of the polymer matrix. For the yarn material, Hashin's damage criteria were extended to identify the damage initiations of six failure modes and an improved Weibull function based formulation was proposed to describe the damage evolutions associated with the six failure modes. After that, an in-house computer program which implements the mUCs and the material models based on the explicit weak-form meshfree method was introduced. This computer program, which is referred to as the explicit meshfree program, was then applied to predict the responses of plain woven CFRP composites subjected to tension in the normal and off-axis directions and under different strain rates. It was shown that the meshfree-based predictions agree reasonably well with the experimental results, validating the accuracy and effectiveness of the meshfree-based UC approach in terms of predicting the overall response of woven composites. Finally, additional examples were presented to demonstrate the capability of the meshfree-based UC modelling in terms of predicting the overall response of all three types of woven composites, based on which an understanding of the influences of fibre tow width and weave structure on the overall response of woven composites was qualitatively achieved.

Based on the numerical examples given in this chapter, it was concluded that one of the highlights of the research in this chapter is that the use of the meshfree-based approach simultaneously addresses the problem of a reduced accuracy in analytical approaches and the concern of the complexity in explicitly creating the geometries of the constituents and the subsequent pre-processing in the FEM-based approaches. Also, it was highlighted that the proposed approach extends the capability of the UC modelling methodology from the homogenisation of the elastic properties to the prediction of the overall response of woven composites at the scale of UC.

CHAPTER 6: CONCLUSION AND FUTURE WORK

6.1 Main conclusions

In this research, a meshfree-based unit cell (UC) modelling approach has been proposed for predicting both the elastic properties and the overall response of woven composites in the normal and off-axis directions. In the course of developing such an approach, high-fidelity UC models have been proposed to describe the internal features or architecture of three commonly used types of woven composites, and in-house computer programs have been coded to implement and discretise the UC models by using the standard and explicit weak-form meshfree methods. Since the UC models developed are capable of describing the internal features of woven composites in high-fidelity and meanwhile the meshfree-based discretisation is able to avoid the needs for explicitly creating the geometries of the constituents and the subsequent time-consuming pre-processing, the main contribution of this research is from a methodological point of view that it has successfully addressed the problems inherently existing in traditional UC modelling approaches, i.e. the concern of a reduced accuracy in analytical approaches and the problem of high complexity in the finite element method (FEM)-based approaches. In the numerical examples presented in Chapters 4 and 5, it has been shown that the meshfree-based predictions for the elastic properties and the overall responses of woven composites agree reasonably well with the experimental data and those found in the relevant literature. Thus, the main contribution of this research can also be interpreted from a practical point of view as an extension of the capability of the UC modelling methodology in the modelling of woven composites, from only the homogenisation of the elastic properties in the normal directions to that of the elastic properties in both the normal and off-axis directions, as well as to the prediction of the responses including the nonlinear, rate-dependent behaviour of woven composites subjected to in-plane loading in both the normal and off-axis directions. According to the

evidence discussed above, it can be concluded that the two research questions posed in Section 1.2 have been reasonably answered, and thus the aim of the present research has been successfully achieved.

Given that the meshfree-based modelling approach is effective for predicting the elastic properties and the overall responses of woven composites and considering that the high-fidelity nature in modelling the geometries of woven composites lose the possibility of adapting this approach for multiscale or numerical analysis up to the structural scale, due to the limited computational power available today, one of the practical implications of the present research is that the proposed approach can be utilised as a simple but accurate approach for identifying whether a simplified UC model is accurate enough if it is used to conduct a multiscale analysis. Another practical implication is that the meshfree-based models are very effective to perform qualitative analysis for different woven composites, as shown in Section 5.5.2, which makes it useful for obtaining an initial understanding and thus facilitating the design of woven composites in the early stage.

Apart from the above conclusions, the findings and results in the development of high-fidelity UC models, the implementation of UC models using meshfree methods and the constitutive modelling for the overall response prediction of woven composites will also be concluded in detail in the following three sections.

6.1.1 Development of high-fidelity UC models

In developing high-fidelity UC models for woven composites, a UC should be defined as small as possible to reduce the number of yarns to be described using analytical equations and more importantly to reduce the domain of homogenisation and thus the computational costs. In general, the smallest or minimum unit cell (mUC) of a woven composite material can be identified by exploiting the symmetries in a step-by-step manner, from initially the composite ply, the full-size UC, the medium UC(s) to the smallest UC. In such a process, the symmetries that can be utilised are comprised of translation, rotation, reflection and/or a combination of them. As a result of conducting a homogenisation based on the mUC, the standard form of PBC cannot be applied. Instead, it should be modified in accordance with the reductions that have been performed to obtain the mUC. However, a desirable way is to employ the equivalence approach as it is capable of deriving the PBCs of a UC at any size in a generic manner.

To analytically describe the internal features of woven composites as accurate as possible, it is would be beneficial to fabricate composite specimens to observe the microstructures including the cross-sections and waviness of yarns, based on which analytical functions can be proposed to fit these features. For instance, it has been shown in Section 4.1 that trigonometric functions are generally adequate to describe the cross-sectional shapes and waviness of both the warp and fill yarns in woven composites. However, for binder yarns, hyperbolic tangent functions should be employed to allow for an adequate description of the high variation in the waviness of this type of yarns. Furthermore, it has been suggested that each yarn of woven composites can be generally assumed to have a constant cross-sectional shape throughout the whole yarn. The main advantage of this assumption is that it facilitates the description of the lower and upper surfaces of yarns.

In this research, the geometry modelling of an mUC, i.e. the development of analytical equations for describing the lower and upper surfaces and the waviness of each yarn, has been performed in a manner of initially describing the cross-section and waviness of each yarn separately and then combining the analytical equations together. This means that it would be very flexible and straightforward to accommodate this approach for developing high-fidelity analytical UCs for not only the commonly used woven composites but also textile composites with complex internal architectures, as long as the cross-sections and waviness of fibre yarns are properly described.

6.1.2 Implementation with meshfree methods

As concluded earlier in this chapter, the most significant highlight of combining meshfree methods and the UC modelling methodology is that it allows to maintain a high degree of accuracy in the predictions by the use of high-fidelity UC models and meanwhile avoid the complexity and time-consuming pre-processing in the FEM-based approaches, i.e. the needs for explicitly creating the geometries of the constituents, discretising the geometries using high-quality elements and assigning the ever-changing material orientations for the wavy yarns. However, it should be noted that the meshfree method for homogenising the elastic properties must be different from that for predicting the overall response of woven composites. Specifically, for the former case, which can be treated as a static problem of linear elasticity, the standard weak-form meshfree method should be employed. In terms of the latter case, which should be treated as a dynamic problem with initial conditions,

the explicit weak-form meshfree method must be utilised. Here, the dynamic loading in the latter case is achieved by prescribing time-dependent PBCs on the boundaries of the mUC of prediction. In addition, since the PBCs applied to the mUC of homogenisation in both cases are treated as external loading and they are presented mainly in the form of displacement constraints, they must be implemented by using the displacement constraint elimination methods described in Sections 3.6.2 and 3.6.3.

Apart from the above findings, it has been found from the numerical examples presented in this thesis that the accuracy of the meshfree-based predictions depends on the choice of the open numerical parameters, i.e. the total number of field nodes, the total number of background cells and the support domain scaling coefficient. In general, the increase in the number of field nodes or background cells tends to produce convergent predictions. However, the value of the support domain scaling coefficient must be carefully chosen in a relatively small range from approximately 2.0 to 3.25. If the value of this coefficient is smaller the lower value of this range, it can cause singularity problems in the calculation of the moment matrix. On the contrary, if its value is larger than the upper value of this range, the convergence of the predicted results may not be always guaranteed. In addition to the choice of the numerical parameters, it has been found that the use of different shape function construction techniques generally produce similar predictions as far as the open numerical parameters are properly chosen.

6.1.3 Material modelling for overall response prediction

For homogenising the elastic properties of woven composites, it is adequate to assume the polymer matrix to be an isotropic and linearly elastic material and the yarn material to have a transversely isotropic and linearly elastic behaviour. However, for predicting the overall responses of woven composites, the nonlinear and rate-dependent response of the polymer matrix and the failure behaviour of the yarn material must be considered. In general, the nonlinearity and rate-dependence of the polymer matrix can be described by using the viscoplasticity-based model detailed in Section 5.3.1. For the yarn material, the damage initiations can be identified by generalising Hashin's failure criteria from 2D to 3D and the damage evolutions can be characterised using the improved Weibull function based formulations, as discussed in Section 5.3.3.

Due to the consideration of yarn's waviness in developing UCs for homogenising the elastic properties of woven composites, it is preferable to initially address the mechanics quantities of wavy yarns in their local coordinate system (LCS) and then transform the LCS-based quantities back to the global coordinate system (GCS) of the UC. In the case of predicting the overall responses of woven composites, the same approach should also be employed to facilitate the determination of the damage state of the yarn material, i.e. the identification of the damage initiations and the calculation of the associated damage evolutions.

6.2 Future work

As concluded in the last section, the meshfree-based UC modelling approach is effective for predicting the elastic properties and overall responses of woven composites. However, as the development of such an approach involves various aspects of knowledge including geometry modelling of woven composites, meshfree methods and constitutive modelling of composites, there are inevitably some limitations that have not been well addressed in this research. Thus, in the following several paragraphs, recommendations for future work will be summarised from the perspective of eliminating these limitations.

One of the limitations of this research is that the off-axis mUC models developed are only applicable to balanced woven composites, which are a class of woven composites whose dimension in the warp direction has to be equal to that in the fill direction. Thus, the first recommendation for future work is to improve the off-axis models so that they are suitable for predicting the properties and response of non-balanced woven composites. To achieve this goal, non-orthogonal coordinate systems such as the one shown in Fig. 5.1a may be employed, and coordinate transformations between the orthogonal coordinate system (see Fig. 5.1b) and the non-orthogonal coordinate system must be defined.

Second, the meshfree methods in this research are based on weak-form formulations. This means that there is a need for using background cells to conduct numerical integrations, which makes the meshfree-based UC modelling approach computationally expensive on one hand and not truly meshfree on the other hand. In contrast to weak-form meshfree methods, strong-form meshfree methods such as the meshfree collocation methods [154, 182] do not require the use of background meshes for numerical integrations. Thus, it is

worth to replace the weak-form meshfree methods with strong-form ones and investigate the applicability of strong-form meshfree methods for the homogenisation of the elastic properties and the prediction of the overall responses of woven composites.

Another limitation of the present research is that the yarn material in woven composites is assumed to be transversely isotropic, without modelling the debonding of fibre-matrix interface. Since the transverse response of the yarn material is determined jointly by the two constituents and the bonding behaviour of fibre-matrix interface, it is beneficial to develop or employ a cohesive model to reasonably account for the bonding behaviour of fibre-matrix interface.

Finally, the material models given in Chapter 5 are valid only for predicting the overall response of woven composites under in-plane tensile loading conditions and at relatively low strain rates. Using the same models for predicting the compressive response could be problematic owing to the fact that the deformation responses and failure mechanisms of woven composites under compression are generally different from those under tension. Thus, a future direction of the present research would be improving the current material models such that they can be applied to predict the responses of woven composites under more complex loading conditions including compression. Another important direction is to test and adapt the current models for higher strain rate applications. The significance of improving the material models for higher strain rate applications would be that the need for performing time-consuming and financially prohibitive experimental trials (e.g. split Hopkinson pressure bar tests) for the sake of characterising high strain-rate responses of woven composites can be partially mitigated.

REFERENCES

[1] R. D. Rawlings and F. L. Matthews, *Composite Materials: Engineering and Science*. Woodhead Publishing, 1999.

[2] *Standard Test Method for Tensile Properties of Polymer Matrix Composite Materials*, ASTM D3039/D3039M-14, 2014.

[3] *Standard Test Method for Compressive Properties of Polymer Matrix Composite Materials with Unsupported Gage Section by Shear Loading*, ASTM D3410/D3410M-16, 2016.

[4] *Standard Test Method for Compressive Properties of Polymer Matrix Composite Materials Using a Combined Loading Compression (CLC) Test Fixture*, ASTM D6641/D6641M-14, 2014.

[5] *Standard Test Method for in-Plane Shear Properties of Polymer Matrix Composite Materials by the Rail Shear Method*, ASTM D4255/D4255M-15A, 2015.

[6] *Standard Test Method for Shear Properties of Composite Materials by the V-Notched Beam Method*, ASTM D5379/D5379M-12, 2012.

[7] *Standard Test Method for Flexural Properties of Polymer Matrix Composite Materials*, ASTM D7264/D7264M-15, 2015.

[8] B. Song, W. N. Chen, and T. Weerasooriya, "Quasi-static and dynamic compressive behaviors of a S-2 glass/SC15 composite," *Journal of Composite Materials,* vol. 37, no. 19, pp. 1723-1743, 2003.

[9] F. Fereshteh-Saniee, G. H. Majzoobi, and M. Bahrami, "An experimental study on the behavior of glass-epoxy composite at low strain rates," *Journal of Materials Processing Technology,* vol. 162-163, pp. 39-45, 2005.

[10] E. Sevkat, B. Liaw, F. Delale, and B. B. Raju, "Drop-weight impact of plain-woven hybrid glass-graphite/toughened epoxy composites," *Composites Part A,* vol. 40, no. 8, pp. 1090-1110, 2009.

[11] I. M. Daniel, B. T. Werner, and J. S. Fenner, "Strain-rate-dependent failure criteria for composites," *Composites Science and Technology,* vol. 71, no. 3, pp. 357-364, 2011.

References

[12] N. Perogamvros, T. Mitropoulos, and G. Lampeas, "Drop tower adaptation for medium strain rate tensile testing," *Experimental Mechanics,* vol. 56, no. 3, pp. 419-436, 2016.

[13] Z. Xu, F. Yang, Z. W. Guan, and W. J. Cantwell, "An experimental and numerical study on scaling effects in the low velocity impact response of CFRP laminates," *Composite Structures,* vol. 154, pp. 69-78, 2016.

[14] H. Zhao and G. Gary, "An experimental investigation of compressive failure strength of fibre-reinforced polymer-matrix composite plates under impact loading," *Composites Science and Technology,* vol. 57, no. 3, pp. 287-292, 1997.

[15] H. Eskandari and J. A. Nemes, "Dynamic testing of composite laminates with a tensile split Hopkinson bar," *Journal of Composite Materials,* vol. 34, no. 4, pp. 260-273, 2000.

[16] A. Gilat, R. K. Goldberg, and G. D. Roberts, "Experimental study of strain-rate-dependent behavior of carbon/epoxy composite," *Composites Science and Technology,* vol. 62, no. 10-11, pp. 1469-1476, 2002.

[17] A. Haque, "High strain rate responses and failure analysis in polymer matrix composites - An experimental and finite element study," *Journal of Composite Materials,* vol. 39, no. 5, pp. 423-450, 2005.

[18] R. Gerlach, C. R. Siviour, N. Petrinic, and J. Wiegand, "Experimental characterisation and constitutive modelling of RTM-6 resin under impact loading," *Polymer,* vol. 49, no. 11, pp. 2728-2737, 2008.

[19] R. Gerlach *et al.*, "The interface between matrix pockets and fibre bundles under impact loading," *Composites Science and Technology,* vol. 69, no. 11-12, pp. 2024-2026, 2009.

[20] R. Gerlach, C. R. Siviour, N. Petrinic, and J. Wiegand, "Experimental characterisation of the strain rate dependent failure and damage behaviour of 3D composites," presented at the DYMAT International Conferences, 2009.

[21] R. Gerlach, C. Kettenbeil, and N. Petrinic, "A new split Hopkinson tensile bar design," *International Journal of Impact Engineering,* vol. 50, pp. 63-67, 2012.

[22] R. Gerlach, C. R. Siviour, J. Wiegand, and N. Petrinic, "In-plane and through-thickness properties, failure modes, damage and delamination in 3D woven carbon fibre composites subjected to impact loading," *Composites Science and Technology,* vol. 72, no. 3, pp. 397-411, 2012.

[23] R. Gerlach, C. R. Siviour, J. Wiegand, and N. Petrinic, "The strain rate dependent material behavior of S-GFRP extracted from GLARE," *Mechanics of Advanced Materials and Structures,* vol. 20, no. 7, pp. 505-514, 2013.

[24] N. Wang and C. Cho, "Dynamic compressive behaviors of multi directional woven composite laminates at different strain rates," *Polymers & Polymer Composites,* vol. 22, no. 2, pp. 169-175, 2014.

[25] H. Koerber, J. Xavier, P. P. Camanho, Y. E. Essa, and F. M. de la Escalera, "High strain rate behaviour of 5-harness-satin weave fabric carbon-epoxy composite under compression and combined compression-shear loading," *International Journal of Solids and Structures,* vol. 54, pp. 172-182, 2015.

[26] J. T. Tzeng and A. S. Abrahamian, "An experimental method for compressive properties of laminated composites at high rates of loading," *Journal of Thermoplastic Composite Materials,* vol. 11, no. 2, pp. 133-143, 1998.

[27] M. P. Flanagan, M. A. Zikry, J. W. Wall, and A. El-Shiekh, "An experimental investigation of high velocity impact and penetration failure modes in textile composites," *Journal of Composite Materials,* vol. 33, no. 12, pp. 1080-1103, 1999.

[28] J. M. Boteler, A. M. Rajendran, and D. Grove, "Shock wave profiles in polymer matrix composite," 2000, vol. 505, no. 1, pp. 563-566.

[29] S. Beard and F. K. Chang, "Design of braided composites for energy absorption," *Journal of Thermoplastic Composite Materials,* vol. 15, no. 1, pp. 3-12, 2002.

[30] F. P. Yuan, L. Tsai, V. Prakash, D. P. Dandekar, and A. M. Rajendran, "Dynamic shear strength of S2 glass fiber reinforced polymer composites under shock compression," *Journal of Applied Physics,* vol. 103, no. 10, 2008.

[31] T. J. Copponnex, "Analysis and evaluation of the single-fibre fragmentation test," *Composites Science and Technology,* vol. 56, no. 8, pp. 893-909, 1996.

[32] G. Désarmot and J. P. Favre, "Advances in pull-out testing and data analysis," *Composites Science and Technology,* vol. 42, no. 1-3, pp. 151-187, 1991.

[33] P. J. Herrerafranco and L. T. Drzal, "Comparison of methods for the measurement of fiber matrix adhesion in composites," *Composites,* vol. 23, no. 1, pp. 2-27, 1992.

[34] S. Sockalingam, "Fiber-matrix interface characterization through the microbond test," *International Journal of Aeronautical and Space Sciences,* vol. 13, no. 3, pp. 282-295, 2012.

[35] I. Verpoest, M. Desaeger, J. Ivens, and M. Wevers, "Interfaces in polymer matrix composites - from micromechanical tests to macromechanical properties," *Makromolekulare Chemie-Macromolecular Symposia,* vol. 75, pp. 85-98, 1993.

[36] S. Zhandarov and E. Mader, "Characterization of fiber/matrix interface strength: Applicability of different tests, approaches and parameters," *Composites Science and Technology,* vol. 65, no. 1, pp. 149-160, 2005.

[37] X. F. Zhou, H. D. Wagner, and S. R. Nutt, "Interfacial properties of polymer composites measured by push-out and fragmentation tests," *Composites Part A,* vol. 32, no. 11, pp. 1543-1551, 2001.

[38] H. T. Hahn and S. W. Tsai, "Nonlinear elastic behavior of unidirectional composite laminae," *Journal of Composite Materials,* vol. 7, no. 1, pp. 102-118, 1973.

[39] H. T. Hahn, "Nonlinear behavior of laminated composites," *Journal of Composite Materials,* vol. 7, no. 2, pp. 257-271, 1973.

[40] J. Aboudi, "The nonlinear behavior of unidirectional and laminated composites - A micromechanical approach," *Journal of Reinforced Plastics and Composites,* vol. 9, no. 1, pp. 13-32, 1990.

[41] S. V. Thiruppukuzhi and C. T. Sun, "Models for the strain-rate-dependent behavior of polymer composites," *Composites Science and Technology,* vol. 61, no. 1, pp. 1-12, 2001.

[42] R. K. Goldberg and D. C. Stouffer, "Strain rate dependent analysis of a polymer matrix composite utilizing a micromechanics approach," *Journal of Composite Materials,* vol. 36, no. 7, pp. 773-793, 2002.

[43] M. Vogler, R. Rolfes, and P. P. Camanho, "Modeling the inelastic deformation and fracture of polymer composites - Part I: Plasticity model," *Mechanics of Materials,* vol. 59, pp. 50-64, 2013.

[44] U. Santhosh and J. Ahmad, "An approach for nonlinear modeling of polymer matrix composites," *Journal of Composite Materials,* vol. 48, no. 14, pp. 1755-1765, 2014.

[45] J. J. Ye, Y. Y. Qiu, Z. Zhai, and X. F. Chen, "Strain rate influence on nonlinear response of polymer matrix composites," *Polymer Composites,* vol. 36, no. 5, pp. 800-810, 2015.

[46] M. Kashtalyan and C. Soutis, "Modelling off-axis ply matrix cracking in continuous fibre-reinforced polymer matrix composite laminates," *Journal of Materials Science,* vol. 41, no. 20, pp. 6789-6799, 2006.

[47] F. Lachaud, C. Espinosa, L. Michel, P. Rahme, and R. Piquet, "Modelling strategies for simulating delamination and matrix cracking in composite laminates," *Applied Composite Materials,* vol. 22, no. 4, pp. 377-403, 2015.

[48] T. Sadowski and K. Osina, "Stress induced damage theory in application to modelling of matrix cracking in laminate polymer composites," *Computational Materials Science,* vol. 43, no. 1, pp. 51-58, 2008.

[49] P. A. Smith and S. L. Ogin, "Characterization and modelling of matrix cracking in a (0/90)(2s) GFRP laminate loaded in flexure," *Proceedings of the Royal Society A - Mathematical Physical and Engineering Sciences,* vol. 456, no. 2003, pp. 2755-2770, 2000.

[50] N. A. Pertsev, A. E. Romanov, and V. I. Vladimirov, "Disclination-dislocation model for the kink bands in polymers and fiber composites," *Journal of Materials Science,* vol. 16, no. 8, pp. 2084-2090, 1981.

References

[51] P. S. Steif, "A model for kinking in fiber composites II: Kink band formation," *International Journal of Solids and Structures,* vol. 26, no. 5-6, pp. 563-569, 1990.

[52] N. A. Fleck, L. Deng, and B. Budiansky, "Prediction of kink width in compressed fiber composites," *Journal of Applied Mechanics,* vol. 62, no. 2, pp. 329-337, 1995.

[53] J. Lankford, "Compressive failure of fiber-reinforced composites - Buckling, kinking, and the role of the interphase," *Journal of Materials Science,* vol. 30, no. 17, pp. 4343-4348, 1995.

[54] X. H. Liu, P. M. Moran, and C. F. Shih, "The mechanics of compressive kinking in unidirectional fiber reinforced ductile matrix composites," *Composites Part B,* vol. 27, no. 6, pp. 553-560, 1996.

[55] R. M. Christensen and S. J. DeTeresa, "The kink band mechanism for the compressive failure of fiber composite materials," *Journal of Applied Mechanics,* vol. 64, no. 1, pp. 1-6, 1997.

[56] A. R. Atilgan, "A nonlinear model for the kinking behavior of unidirectional polymer matrix composites," *Journal of Applied Mathematics and Mechanics,* vol. 78, no. 3, pp. 212-216, 1998.

[57] Y. B. Fu and Y. T. Zhang, "Continuum-mechanical modelling of kink-band formation in fibre-reinforced composites," *International Journal of Solids and Structures,* vol. 43, no. 11-12, pp. 3306-3323, 2006.

[58] S. T. Pinho, L. Iannucci, and P. Robinson, "Physically-based failure models and criteria for laminated fibre-reinforced composites with emphasis on fibre kinking - Part I: Development," *Composites Part A,* vol. 37, no. 1, pp. 63-73, 2006.

[59] S. T. Pinho, L. Iannucci, and P. Robinson, "Physically-based failure models and criteria for laminated fibre-reinforced composites with emphasis on fibre kinking - Part II: FE implementation," *Composites Part A,* vol. 37, no. 5, pp. 766-777, 2006.

[60] A. K. Ataabadi, S. Ziaei-Rad, and H. Hosseini-Toudeshky, "Compression failure and fiber-kinking modeling of laminated composites," *Steel and Composite Structures,* vol. 12, no. 1, pp. 53-72, 2012.

[61] O. Allix, N. Feld, E. Baranger, J. M. Guimard, and C. Ha-Minh, "The compressive behaviour of composites including fiber kinking: Modelling across the scales," *Meccanica,* vol. 49, no. 11, pp. 2571-2586, 2014.

[62] J. L. Wind, S. Steffensen, and H. M. Jensen, "Comparison of a composite model and an individually fiber and matrix discretized model for kink band formation," *International Journal of Non-Linear Mechanics,* vol. 67, pp. 319-325, 2014.

[63] L. Lammerant and I. Verpoest, "Modelling of the interaction between matrix cracks and delaminations during impact of composite plates," *Composites Science and Technology,* vol. 56, no. 10, pp. 1171-1178, 1996.

[64] A. Corigliano, M. Ricci, and R. Frassine, "Rate-Dependent Interface Models for the Analysis of Delamination in Polymer-Matrix Composites," in *Computational Mechanics: New Trends and Applications*, H. P. Rossmanith, Ed. Rotterdam: Balkema, 1997, pp. 139-146.

[65] S. M. Lee, "Mode II delamination failure mechanisms of polymer matrix composites," *Journal of Materials Science,* vol. 32, no. 5, pp. 1287-1295, 1997.

[66] F. Shen, K. H. Lee, and T. E. Tay, "Modeling delamination growth in laminated composites," *Composites Science and Technology,* vol. 61, no. 9, pp. 1239-1251, 2001.

[67] L. Greve and A. K. Pickett, "Delamination testing and modelling for composite crash simulation," *Composites Science and Technology,* vol. 66, no. 6, pp. 816-826, 2006.

[68] A. Riccio, M. Zarrelli, and N. Tessitore, "A numerical model for delamination growth simulation in non-crimp fabric composites," *Composites Science and Technology,* vol. 67, no. 15-16, pp. 3345-3359, 2007.

[69] I. Tawk, P. Navarro, J. F. Ferrero, J. J. Barrau, and E. Abdullah, "Composite delamination modelling using a multi-layered solid element," *Composites Science and Technology,* vol. 70, no. 2, pp. 207-214, 2010.

[70] I. Guiamatsia and G. D. Nguyen, "A generic approach to constitutive modelling of composite delamination under mixed-mode loading conditions," *Composites Science and Technology,* vol. 72, no. 2, pp. 269-277, 2012.

[71] C. Santiuste, A. Olmedo, X. Soldani, and H. Miguelez, "Delamination prediction in orthogonal machining of carbon long fiber-reinforced polymer composites," *Journal of Reinforced Plastics and Composites,* vol. 31, no. 13, pp. 875-885, 2012.

[72] P. Upadhyaya, S. Roy, M. H. Haque, and H. Lu, "A micromechanical viscoelastic cohesive layer model for predicting delamination in high temperature polymer matrix composites," *Proceedings of the American Society for Composites,* 2013.

[73] K. Friedrich, T. Goda, K. Varadi, and B. Wetzel, "Finite element simulation of the fiber-matrix debonding in polymer composites produced by a sliding indentor: Part I - Normally oriented fibers," *Journal of Composite Materials,* vol. 38, no. 18, pp. 1583-1606, 2004.

[74] T. Goda, K. Varadi, B. Wetzel, and K. Friedrich, "Finite element simulation of the fiber-matrix debonding in polymer composites produced by a sliding indentor: Part II - Parallel and anti-parallel fiber orientation," *Journal of Composite Materials,* vol. 38, no. 18, pp. 1607-1618, 2004.

[75] M. Zabihpoor and S. Adibnazari, "Simulation of fiber/matrix debonding in unidirectional composites under fatigue loading," *Journal of Reinforced Plastics and Composites,* vol. 26, no. 8, pp. 743-760, 2007.

[76] T. J. Vaughan and C. T. McCarthy, "Micromechanical modelling of the transverse damage behaviour in fibre reinforced composites," *Composites Science and Technology,* vol. 71, no. 3, pp. 388-396, 2011.

[77] W. S. Yang, Y. Pan, and A. A. Pelegri, "Multiscale modeling of matrix cracking coupled with interfacial debonding in random glass fiber composites based on volume elements," *Journal of Composite Materials,* vol. 47, no. 27, pp. 3389-3400, 2013.

[78] B. Nedjar, "Plasticity-based modelling of fibre/matrix debonding in unidirectional composites," *Composite Structures,* vol. 108, pp. 41-48, 2014.

[79] Q. H. Meng and Z. Q. Wang, "Theoretical model of fiber debonding and pull-out in unidirectional hybrid-fiber-reinforced brittle-matrix composites," *Journal of Composite Materials,* vol. 49, no. 14, pp. 1739-1751, 2015.

[80] B. Nedjar, "Directional damage gradient modeling of fiber/matrix debonding in viscoelastic UD composites," *Composite Structures,* vol. 153, pp. 895-901, 2016.

[81] T. Arabatti, N. K. Parambil, and S. Gururaja, "Micromechanical modeling of damage development in polymer composites," *Advanced Composites Letters,* vol. 25, no. 3, pp. 56-62, 2016.

[82] E. J. Barbero, G. F. Abdelal, and A. Caceres, "A micromechanics approach for damage modeling of polymer matrix composites," *Composite Structures,* vol. 67, no. 4, pp. 427-436, 2005.

[83] M. Lidgett, R. Brooks, N. Warrior, and K. A. Brown, "Virtual modelling of microscopic damage in polymer composite materials at high rates of strain," *Plastics Rubber and Composites,* vol. 40, no. 6-7, pp. 324-332, 2011.

[84] F. Wang, Y. Q. Wei, and Z. Q. Chen, "Micromechanical modeling of the effect of progressive damage on the tensile behavior in fiber-reinforced polymer composites," *Multi-Functional Materials and Structures II,* vol. 79-82, pp. 1347-1350, 2009.

[85] T. Ishikawa and T. W. Chou, "Stiffness and strength behaviour of woven fabric composites," *Journal of Materials Science,* vol. 17, pp. 3211-3220, 1982.

[86] T. Ishikawa, "Antisymmetric elastic properties of composite plates of satin weave cloth," *Fibre Science and Technology,* vol. 15, pp. 127-145, 1981.

[87] T. Ishikawa and T. W. Chou, "Elastic behavior of woven hybrid composites," *Journal of Composite Materials,* vol. 16, pp. 2-19, 1982.

[88] T. Ishikawa and T. W. Chou, "One-dimensional micromechanical analysis of woven fabric composites," *AIAA Journal,* vol. 21, no. 12, pp. 1714-1721, 1983.

[89] T. J. Whitney and T. W. Chou, "Modeling of 3-D angle-interlock textile structural composites," *Journal of Composite Materials,* vol. 23, pp. 890-911, 1989.

[90] N. K. Naik and P. S. Shembekar, "Elastic behavior of woven fabric composites: I - Lamina analysis," *Journal of Composite Materials,* vol. 26, no. 15, pp. 2196-2225, 1992.

[91] N. K. Naik and P. S. Shembekar, "Elastic behavior of woven fabric composites: III - Laminate design," *Journal of Composite Materials,* vol. 26, no. 17, pp. 2522-2541, 1992.

[92] P. S. Shembekar and N. K. Naik, "Elastic behavior of woven fabric composites: II - Laminate analysis," *Journal of Composite Materials,* vol. 26, no. 15, pp. 2226-2246, 1992.

[93] P. W. Chung and K. K. Tamma, "Woven fabric composites - Developments in engineering bounds, homogenization and application," *International Journal for Numerical Methods in Engineering,* vol. 45, no. 12, pp. 1757-1790, 1999.

[94] P. H. Wen and M. H. Aliabadi, "Mesh-free micromechanical model for woven fabric composite elastic moduli," *Journal of Multiscale Modelling,* vol. 1, no. 2, pp. 303-319, 2009.

[95] O. Bacarreza, D. Abe, M. H. Aliabadi, and N. K. Ragavan, "Micromechanical modeling of advanced composites," *Journal of Multiscale Modelling,* vol. 04, no. 02, pp. 2-20, 2012.

[96] S. P. Ng, P. C. Tse, and K. J. Lau, "Numerical and experimental determination of in-plane elastic properties of 2/2-twill weave fabric composites," *Composites Part B,* vol. 29, no. 6, pp. 735-744, 1998.

[97] J. Whitcomb and X. D. Tang, "Effective moduli of woven composites," *Journal of Composite Materials,* vol. 35, no. 23, pp. 2127-2144, 2001.

[98] A. Dixit, H. S. Mali, and R. K. Misra, "A micromechanical unit cell model of 2×2 twill woven fabric textile composite for multi scale analysis," *Journal of The Institution of Engineers (India): Series E,* vol. 95, no. 1, pp. 1-9, 2014.

[99] P. Tan, L. Long, and G. P. Steven, "Modelling approaches for orthogonal woven composites," *Journal of Reinforced Plastics and Composites,* vol. 17, no. 6, pp. 545-577, 1998.

[100] C. S. Lee, S. W. Chung, H. Shin, and S. J. Kim, "Virtual material characterization of 3D orthogonal woven composite materials by large-scale computing," *Journal of Composite Materials,* vol. 39, no. 10, pp. 851-863, 2005.

[101] A. E. Bogdanovich, "Multi-scale modeling, stress and failure analyses of 3-D woven composites," *Journal of Materials Science,* vol. 41, no. 20, pp. 6547-6590, 2006.

[102] S. V. Lomov *et al.*, "Mathematical modelling of internal geometry and deformability of woven preforms," *International Journal of Forming Processes,* vol. 6, no. 3-4, pp. 413-442, 2003.

[103] S. V. Lomov and I. Verpoest, "Compression of woven reinforcements: A mathematical model," *Journal of Reinforced Plastics and Composites,* vol. 19, no. 16, pp. 1329-1350, 2000.

[104] B. El Said, S. D. Green, and S. R. Hallett, "Kinematic modelling of 3D woven fabric deformation for structural scale features," *Composites Part A,* vol. 57, pp. 95-107, 2014.

[105] S. D. Green, M. Y. Matveev, A. C. Long, D. Ivanov, and S. R. Hallett, "Mechanical modelling of 3D woven composites considering realistic unit cell geometry," *Composite Structures,* vol. 118, pp. 284-293, 2014.

[106] Y. Mahadik and S. Hallett, "Effect of fabric compaction and yarn waviness on 3D woven composite compressive properties," *Composites Part A,* vol. 42, no. 11, pp. 1592-1600, 2011.

[107] S. D. Green, A. C. Long, B. EI Said, and S. R. Hallett, "Numerical modelling of 3D woven preform deformations," *Composite Structures,* vol. 108, pp. 747-756, 2013.

[108] D. Durville, "Numerical simulation of entangled materials mechanical properties," *Journal of Materials Science* vol. 40, no. 22, pp. 5941-5948, 2005.

[109] D. Durville, "Simulation of the mechanical behaviour of woven fabrics at the scale of fibers," *International Journal of Material Forming,* vol. 3, pp. 1241-1251, 2010.

[110] S. V. Lomov, A. V. Gusakov, G. Huysmans, A. Prodromou, and I. Verpoest, "Textile geometry preprocessor for meso-mechanical models of woven composites," *Composites Science and Technology,* vol. 60, no. 11, pp. 2083-2095, 2000.

[111] S. V. Lomov and I. Verpoest, "Integrated model of textile composite reinforcements," *Advances in Composite Materials and Structures VII,* vol. 9, pp. 367-376, 2000.

[112] University of Nottingham - Textile Composites Research. (11/2016). *TexGen - An open source software for modelling the geometry of textile structures*. Available: http://texgen.sourceforge.net/index.php/Main_Page

[113] M. Sherburn, F. Robitaille, A. Long, and C. Rudd, "Geometric pre-processor for the calculation of physical properties of textiles," presented at the 2nd International Industrial Simulation Conference 2004, Malaga, 2004.

[114] M. Sherburn, "Geometric and Mechanical Modelling of Textiles," PhD, University of Nottingham, 2007.

[115] D. Abe, "Micromechanical Modelling of Woven Composites for the Evaluation of Elastic Moduli," MSc, Imperial College London, 2011.

References

[116] LSTC. (11/2016). *LS-DYNA keywords user's manual (Version 971)*. Available: http://lstc.com/pdf/ls-dyna_971_manual_k.pdf

[117] University of Delaware - Center for Composite Materials. (11/2016). *MAT162 Software*. Available: http://www.ccm.udel.edu/software/mat162/

[118] A. Matzenmiller, J. Lubliner, and R. L. Taylor, "A constitutive model for anisotropic damage in fiber-composites," *Mechanics of Materials,* vol. 20, no. 125-152, 1995.

[119] B. A. Gama and J. W. Gillespie, "Finite element modeling of impact, damage evolution and penetration of thick-section composites," *International Journal of Impact Engineering,* vol. 38, no. 4, pp. 181-197, 2011.

[120] B. Z. Haque and J. W. Gillespie, "Progressive composite damage modeling in LS-DYNA using MAT162: Part A - Properties and parameters," presented at the Proceedings of the American Society for Composites: Thirtieth Technical Conference, East Lansing, 2015.

[121] B. Z. Haque and J. W. Gillespie, "Progressive composite damage modeling in LS-DYNA using MAT162: Part B - Model validating experiments," presented at the Proceedings of the American Society for Composites: Thirtieth Technical Conference, East Lansing, 2015.

[122] S. T. Jenq, H. S. Jing, and C. Chung, "Predicting the ballistic limit for plain woven glass epoxy composite laminate," *International Journal of Impact Engineering,* vol. 15, no. 4, pp. 451-464, 1994.

[123] L. E. Schwer and R. G. Whirley, "Impact of a 3D woven textile composite thin panel: Damage and failure modeling," *Mechanics of Composite Materials and Structures,* vol. 6, no. 1, pp. 9-30, 1999.

[124] L. Iannucci, "Progressive failure modelling of woven carbon composite under impact," *International Journal of Impact Engineering,* vol. 32, no. 6, pp. 1013-1043, 2006.

[125] L. Iannucci and M. L. Willows, "An energy based damage mechanics approach to modelling impact onto woven composite materials - Part I: Numerical models," *Composites Part A,* vol. 37, no. 11, pp. 2041-2056, 2006.

[126] L. Iannucci and M. L. Willows, "An energy based damage mechanics approach to modelling impact onto woven composite materials - Part II: Experimental and numerical results," *Composites Part A,* vol. 38, no. 2, pp. 540-554, 2007.

[127] N. K. Naik, P. Shrirao, and B. C. K. Reddy, "Ballistic impact behaviour of woven fabric composites: Parametric studies," *Materials Science and Engineering A - Structural Materials Properties Microstructure and Processing,* vol. 412, no. 1-2, pp. 104-116, 2005.

References

[128] N. K. Naik, P. Shrirao, and B. C. K. Reddy, "Ballistic impact behaviour of woven fabric composites: Formulation," *International Journal of Impact Engineering,* vol. 32, no. 9, pp. 1521-1552, 2006.

[129] W. K. Binienda and R. K. Goldberg, "Dynamic testing and characterization of woven/braided polymer composites: A review," *Applied Mechanics Reviews,* vol. 64, no. 5, 2011.

[130] S. B. Aminjikarai and A. Tabiei, "A strain-rate dependent 3-D micromechanical model for finite element simulations of plain weave composite structures," *Composite Structures,* vol. 81, no. 3, pp. 407-418, 2007.

[131] R. Tanov and A. Tabiei, "Computationally efficient micromechanical models for woven fabric composite elastic moduli," *Journal of Applied Mechanics - Transactions of the ASME,* vol. 68, no. 4, pp. 553-560, 2001.

[132] O. Bacarreza, M. H. Aliabadi, and A. Apicella, "Multi-scale failure analysis of plain-woven composites," *The Journal of Strain Analysis for Engineering Design,* vol. 47, no. 6, pp. 379-388, 2012.

[133] L. Raimondo and M. H. Aliabadi, "Multiscale progressive failure analysis of plain-woven composite materials," *Journal of Multiscale Modelling,* vol. 1, no. 2, pp. 263–301, 2009.

[134] A. Tabiei and I. Ivanov, "Materially and geometrically non-linear woven composite micro-mechanical model with failure for finite element simulations," *International Journal of Non-Linear Mechanics,* vol. 39, no. 2, pp. 175-188, 2004.

[135] A. Tabiei and I. Ivanov, "Micro-mechanical model with strain-rate dependency and damage for impact simulation of woven fabric composites," *Mechanics of Advanced Materials and Structures,* vol. 14, no. 5, pp. 365-377, 2007.

[136] A. Tabiei, W. T. Yia, and R. Goldberg, "Non-linear strain rate dependent micro-mechanical composite material model for finite element impact and crashworthiness simulation," *International Journal of Non-Linear Mechanics,* vol. 40, no. 7, pp. 957-970, 2005.

[137] B. Z. Sun, Y. K. Liu, and B. H. Gu, "A unit cell approach of finite element calculation of ballistic impact damage of 3-D orthogonal woven composite," *Composites Part B,* vol. 40, no. 6, pp. 552-560, 2009.

[138] J. Z. Mao, X. S. Sun, M. Ridha, V. B. C. Tan, and T. E. Tay, "A modeling approach across length scales for progressive failure analysis of woven composites," *Applied Composite Materials,* vol. 20, no. 3, pp. 213-231, 2012.

[139] M. Pankow, A. M. Waas, C. F. Yen, and S. Ghiorse, "Modeling the response, strength and degradation of 3D woven composites subjected to high rate loading," *Composite Structures,* vol. 94, no. 5, pp. 1590-1604, 2012.

References

[140] P. Römelt and P. R. Cunningham, "A multi-scale finite element approach for modelling damage progression in woven composite structures," *Composite Structures,* vol. 94, no. 3, pp. 977-986, 2012.

[141] O. Cousigné, D. Moncayo, D. Coutellier, P. Camanho, and H. Naceur, "Numerical modeling of nonlinearity, plasticity and damage in CFRP-woven composites for crash simulations," *Composite Structures,* vol. 115, pp. 75-88, 2014.

[142] E. Obert, F. Daghia, P. Ladevèze, and L. Ballere, "Micro and meso modeling of woven composites: Transverse cracking kinetics and homogenization," *Composite Structures,* vol. 117, pp. 212-221, 2014.

[143] B. A. Bednarcyk, B. Stier, J. W. Simon, S. Reese, and E. J. Pineda, "Meso- and micro-scale modeling of damage in plain weave composites," *Composite Structures,* vol. 121, pp. 258-270, 2015.

[144] C. C. Jr, H. B. Dexter, and I. S. Raju, "A review of the NASA textile composites research," NASA Langley Research Center, Hampton, Virginia 2004, Available: https://ntrs.nasa.gov/archive/nasa/casi.ntrs.nasa.gov/20040105589.pdf.

[145] L. Y. Li, P. H. Wen, and M. H. Aliabadi, "Meshfree modeling and homogenization of 3D orthogonal woven composites," *Composites Science and Technology,* vol. 71, no. 15, pp. 1777-1788, 2011.

[146] R. Hill, "A self-consistent mechanics of composite materials," *Journal of the Mechanics and Physics of Solids,* vol. 13, no. 4, pp. 213-222, 1965.

[147] V. D. Nguyena, E. Bécheta, C. Geuzaineb, and L. Noelsa, "Imposing periodic boundary condition on arbitrary meshes by polynomial interpolation," *Computational Materials Science,* pp. 1-28, 2011.

[148] S. Hazanov, "Hill condition and overall properties of composites," *Archive of Applied Mechanics,* vol. 68, pp. 385-394, 1998.

[149] M. Amieur, S. Hazanov, and C. Huet, "Numerical and Experimental Assessment of the Size and Boundary Conditions Effects for the Overall Properties of Granular Composite Bodies Smaller Than the Representative Volume," in *IUTAM Symposium on Anisotropy, Inhomogeneity and Nonlinearity in Solid Mechanics*, vol. 39, D. F. Parker and A. H. England, Eds. Dordrecht: Springer, 1995, pp. 149-154.

[150] S. Hazanov and C. Huet, "Order relationships for boundary conditions effect in heterogeneous bodies smaller than the representative volume," *Journal of the Mechanics and Physics of Solids,* vol. 42, no. 12, pp. 1995-2011, 1994.

[151] F. Larsson, K. Runesson, S. Saroukhani, and R. Vafadari, "Computational homogenization based on a weak format of micro-periodicity for RVE-problems," *Computer Methods in Applied Mechanics and Engineering* vol. 200, no. 1-4, pp. 11-26, 2011.

[152] T. Kanit, S. Forest, I. Galliet, V. Mounoury, and D. Jeulin, "Determination of the size of the representative volume element for random composites: Statistical and numerical approach," *International Journal of Solids and Structures,* vol. 40, no. 13-14, pp. 3647–3679, 2003.

[153] K. Terada, M. Hori, T. Kyoya, and N. Kikuchi, "Simulation of the multi-scale convergence in computational homogenization approaches," *International Journal of Solids and Structures,* vol. 37, no. 16, pp. 2285–2311, 2000.

[154] G. R. Liu and Y. T. Gu, *An Introduction to Meshfree Methods and Their Programming*. Dordrecht: Springer, 2005.

[155] P. Lancaster and K. Salkauskas, "Surfaces generated by moving least squares methods," *Mathematics of Computation,* vol. 37, no. 155, pp. 141-158, 1981.

[156] B. Nayroles, G. Touzot, and P. Villon, "Generalizing the finite element method: Diffuse approximation and diffuse elements," *Computational Mechanics,* vol. 10, no. 5, pp. 307-318, 1992.

[157] T. Belytschko, Y. Y. Lu, and L. Gu, "Element-free Galerkin methods," *International Journal for Numerical Methods in Engineering,* vol. 37, no. 2, pp. 229-256, 1994.

[158] G. R. Liu, *Meshfree Methods: Moving Beyond the Finite Element Method*, 2nd ed. Boca Raton: CRC Press, 2012.

[159] R. L. Hardy, "Theory and applications of the multiquadric-biharmonic method (20 years of discovery 1968–1988)," *Computers & Mathematics with Applications,* vol. 19, no. 8-9, pp. 163-208, 1990.

[160] L. Gu, "Moving kriging interpolation and element-free Galerkin method," *International Journal for Numerical Methods in Engineering,* vol. 56, no. 1, pp. 1-11, 2003.

[161] D. G. Krige, "A statistical approach to some basic mine valuation problems on the Witwatersrand," *Journal of the Chemical, Metallurgical and Mining Society of South Africa,* vol. 52, no. 6, pp. 119-139, 1951.

[162] G. Matheron, "Principles of geostatistics," *Economic Geology,* vol. 58, pp. 1246-1266, 1963.

[163] J. Sacks, S. Schiller, and W. J. Welch, "Design for computer experiments," *Technometrics,* vol. 31, no. 1, pp. 41-47, 1989.

[164] C. Snell, D. G. Vesey, and P. Mullord, "The application of a general finite difference method to some boundary value problems," *Computers & Structures,* vol. 13, no. 4, pp. 547-552, 1981.

[165] V. Girault, "Theory of a GDM on irregular networks," *SIAM Journal on Numerical Analysis,* vol. 11, pp. 260-282, 1974.

References

[166] V. Pavlin and N. Perrone, "Finite difference energy techniques for arbitrary meshes applied to linear plate problems," *International Journal for Numerical Methods in Engineering,* vol. 14, no. 5, pp. 647-664, 1979.

[167] T. Liszka and J. Orkisz, "The finite difference method at arbitrary irregular grids and its application in applied mechanics," *Computers & Structures,* vol. 11, no. 1-2, pp. 83-95, 1983.

[168] E. J. Kansa, "Multiquadrics - A scattered data approximation scheme with applications to computational fluid-dynamics - I: Surface approximations and partial derivative estimates," *Computers & Mathematics with Applications,* vol. 19, no. 8-9, pp. 127-145, 1990.

[169] X. Liu, G.R. Liu, K. Tai, and K.Y. Lam, "Radial point interpolation collocation method (RPICM) for partial differential equations," *Computers & Mathematics with Applications,* vol. 50, no. 8-9, pp. 1425-1442, 2005.

[170] X. Zhang, K. Z. Song, M. W. Lu, and X. Liu, "Meshless methods based on collocation with radial basis functions," *Computational Mechanics,* vol. 26, no. 4, pp. 333-343, 2000.

[171] Z. Wu, "Hermite-Birkhoff interpolation of scattered data by radial basis functions," *Approximation Theory and its Applications,* vol. 8, no. 2, pp. 1-10, 1992.

[172] E. Oñate, S. Idelsohn, O. Z. Zienkiewicz, and R. L. Taylor, "A finite point method in computational mechanics - Applications to convective transport and fluid flow," *International Journal for Numerical Methods in Engineering,* vol. 39, no. 22, pp. 3839–3866, 1996.

[173] E. Oñate, "Derivation of stabilized equations for numerical solution of advective-diffusive transport and fluid flow problems," *Computer Methods in Applied Mechanics and Engineering,* vol. 151, no. 1-2, pp. 233-265, 1998.

[174] E. Oñate, F. Perazzo, and J. Miquel, "A finite point method for elasticity problem," *Computers & Structures,* vol. 79, no. 22-25, pp. 2151-2163, 2001.

[175] G. R. Liu and Y. T. Gu, "A point interpolation method for two-dimensional solids," *International Journal for Numerical Methods in Engineering,* vol. 50, no. 4, pp. 937-951, 2001.

[176] J. G. Wang and G. R. Liu, "A point interpolation meshless method based on radial basis functions," *International Journal for Numerical Methods in Engineering,* vol. 54, no. 11, pp. 1623-1648, 2002.

[177] W. K. Liu, S. Jun, and Y. F. Zhang, "Reproducing kernel particle methods," *International Journal for Numerical Methods in Engineering,* vol. 20, pp. 1081-1106, 1995.

References

[178] S. N. Atluri and T. L. Zhu, "A new meshless local Petrov-Galerkin (MLPG) approach in computational mechanics," *Computational Mechanics,* vol. 22, no. 2, pp. 117-127, 1998.

[179] S. N. Atluri and T. L. Zhu, "A new meshless local Petrov-Galerkin (MLPG) approach to nonlinear problems in computer modeling and simulation," *Computer Modeling and Simulation in Engineering,* vol. 3, no. 3, pp. 187-196, 1998.

[180] S. N. Atluri and T. L. Zhu, "The meshless local Petrov-Galerkin (MLPG) approach for solving problems in elsto-statics," *Computational Mechanics,* vol. 25, no. 2-3, pp. 169-179, 2000.

[181] G. R. Liu and Y. T. Gu, "A local radial point interpolation method (LR-PIM) for free vibration analyses of 2-D solids," *Journal of Sound and Vibration,* vol. 246, no. 1, pp. 29-46, 2001.

[182] G. R. Liu, L. Yan, J. G. Wang, and Y. T. Gu, "Point interpolation method based on local residual formulation using radial basis functions," *Structural Engineering and Mechanics,* vol. 14, no. 6, pp. 713-732, 2002.

[183] G. R. Liu and Y. T. Gu, "A truly meshless method based on the strong-weak form," in *Advances in Meshfree and X-FEM Methods*, Singapore, 2002, pp. 259-261.

[184] G. R. Liu and Y. T. Gu, "A meshfree method: Meshfree weak-strong (MWS) form method for 2D solids," *Computational Mechanics,* vol. 33, no. 1, pp. 2-14, 2003.

[185] L. B. Lucy, "A numerical approach to the testing of the fission hypothesis," *Astronomical Journal,* vol. 82, pp. 1013-1024, 1977.

[186] R. A. Gingold and J. J. Monaghan, "Smoothed particle hydrodynamics - Theory and application to non-spherical stars," *Monthly Notices of the Royal Astronomical Society,* vol. 181, pp. 375-389, 1977.

[187] B. N. Cox and G. Flanagan, *Handbook of Analytical Methods for Textile Composites*. NASA CR 45770, 1997.

[188] S. Li, C. Zhou, H. Yu, and L. Li, "Formulation of a unit cell of a reduced size for plain weave textile composites," *Computational Materials Science,* vol. 50, no. 5, pp. 1770-1780, 2011.

[189] X. D. Tang and J. D. Whitcomb, "General techniques for exploiting periodicity and symmetries in micromechanics analysis of textile composites," *Journal of Composite Materials,* vol. 37, no. 13, pp. 1167-1189, 2003.

[190] J. D. Whitcomb, C. D. Chapman, and X. D. Tang, "Derivation of boundary conditions for micromechanics analyses of plain and satin weave composites," *Journal of Composite Materials,* vol. 34, no. 9, pp. 724-747, 2000.

[191] N. V. De Carvalho, S. T. Pinho, and P. Robinson, "Reducing the domain in the mechanical analysis of periodic structures, with application to woven

composites," *Composites Science and Technology,* vol. 71, no. 7, pp. 969-979, 2011.

[192] N. V. De Carvalho, S. T. Pinho, and P. Robinson, "A mathematical framework for reducing the domain in the mechanical analysis of periodic structures," pp. 1-18

[193] Gurit. Datasheet/EP121 - Epoxy prepreg co-curable with phenolics (v3) [Online]. Available: https://www.gurit.com/-/media/Gurit/Datasheets/ep-121.pdf

[194] Y. W. Jiang, A. Tabiei, and G. J. Simitses, "A novel micromechanics-based approach to the derivation of constitutive equations for local/global analysis of a plain-weave fabric composite," *Composites Science and Technology,* vol. 60, no. 9, pp. 1825–1833, 2000.

[195] T. Ishikawa, M. Matsushima, Y. Hayashi, and T. W. Chou, "Experimental confirmation of the theory of elastic moduli of fabric composites," *Journal of Composite Materials,* vol. 19, no. 5, pp. 443-458, 1985.

[196] US Department of Defense, Composite Materials Handbook - Polymer Matrix Composites - Material Properties, 2002. [Online]. Available.

[197] I. M. Ward and J. Sweeney, *Mechanical Properties of Solid Polymers*. West Sussex: JohnWiley & Sons, Ltd, 2013.

[198] M. C. Boyce, D. M. Parks, and A. S. Argon, "Large inelastic deformation of glassy polymers: Part I - Rate dependent constitutive model," *Mechanics of Materials,* vol. 7, pp. 15-33, 1988.

[199] C. Zhang and I. D. Moor, "Nonlinear mechanical response of high density polyethylene: Part II - Uniaxial constitutive model," *Mechanics of Materials,* vol. 37, pp. 414-420, 1997.

[200] R. R. Valisetty and J. L. Teply, "Overall instantaneous viscoplastic properties of composites," *Journal of Composite Materials,* vol. 26, pp. 1708-1724, 1992.

[201] E. Krempl and K. Ho, "An Overstress Model for Solid Polymer Deformation Behavior Applied to Nylon 66," Time Dependent and Nonlinear Effects in Polymers and Composites, R. Schapery and C. Sun, Eds.: ASTM International, 2000. [Online]. Available.

[202] C. M. Bordonaro, "Rate Dependent Mechanical Behavior of High Strength Plastics: Experiment and Modeling," PhD, Rensselaer Polytechnic Institute, 1995.

[203] D. C. Stouffer and L. T. Dame, *Inelastic Deformation of Metals: Models, Mechanical Properties, and Metallurgy*. New York: John Wiley and Sons, 1996.

[204] C. A. Weeks and C. T. Sun, "Modelling non-linear rate-dependent behaviour in fibre-reinforced composites," *Composites Science and Technology,* vol. 58, pp. 603-611, 1998.

[205] Z. Hashin, "Failure criteria for unidirectional fiber composites," *Journal of Applied Mechanics,* vol. 47, pp. 329-334, 1980.

[206] A. C. Prickett, "Intralaminar Cracking of Fibre Reinforced Composites: A Fracture Mechanics and ToF-SIMS Study," PhD, University of Surrey, 2001.

[207] W. Weibull, *A Statistical Theory of the Strength of Materials*. Stockholm: Generalstabens Litografiska Anstalts Förlag, 1939.

[208] P. H. Wen and M. H. Aliabadi, "Damage mechanics analysis of plain woven fabric composite micromechanical model for mesh-free simulations," *Journal of Composite Materials,* vol. 46, pp. 2239-2253, 2012.

[209] A. Tabiei and I. Ivanov, "Computational micro-mechanical model of flexible woven fabric for finite element impact simulation," *International Journal for Numerical Methods in Engineering,* vol. 53, pp. 1259-1276, 2002.

[210] *Standard Test Method for Tensile Properties of Plastics*, ASTM D638-14, 2014.

APPENDIX A

A.1 I/O data for the MLS example

Table A.1: I/O data for the MLS calculations at the central point

Field nodes			Linear polynomial			Quadratic polynomial		
No.	x	y	$\phi_I(x)$	$\partial\phi_I/\partial x$	$\partial\phi_I/\partial y$	$\phi_I(x)$	$\partial\phi_I/\partial x$	$\partial\phi_I/\partial y$
1	-0.50	-0.50	0.009	-0.050	-0.050	0.012	-0.063	-0.063
2	-0.50	-0.25	0.020	-0.111	-0.092	0.023	-0.119	-0.097
3	-0.50	0.00	0.037	-0.199	0.000	0.040	-0.201	0.000
4	-0.50	0.25	0.020	-0.111	0.092	0.023	-0.119	0.097
5	-0.50	0.50	0.009	-0.050	0.050	0.012	-0.063	0.063
6	-0.25	-0.50	0.020	-0.092	-0.111	0.023	-0.097	-0.119
7	-0.25	-0.25	0.045	-0.204	-0.204	0.045	-0.184	-0.184
8	-0.25	0.00	0.082	-0.368	0.000	0.075	-0.310	0.000
9	-0.25	0.25	0.045	-0.204	0.204	0.045	-0.184	0.184
10	-0.25	0.50	0.020	-0.092	0.111	0.023	-0.097	0.119
11	0.00	-0.50	0.037	0.000	-0.199	0.040	0.000	-0.201
12	0.00	-0.25	0.082	0.000	-0.368	0.075	0.000	-0.310
13	0.00	0.00	0.147	0.000	0.000	0.127	0.000	0.000
14	0.00	0.25	0.082	0.000	0.368	0.075	0.000	0.310
15	0.00	0.50	0.037	0.000	0.199	0.040	0.000	0.201
16	0.25	-0.50	0.020	0.092	-0.111	0.023	0.097	-0.119
17	0.25	-0.25	0.045	0.204	-0.204	0.045	0.184	-0.184
18	0.25	0.00	0.082	0.368	0.000	0.075	0.310	0.000
19	0.25	0.25	0.045	0.204	0.204	0.045	0.184	0.184
20	0.25	0.50	0.020	0.092	0.111	0.023	0.097	0.119
21	0.50	-0.50	0.009	0.050	-0.050	0.012	0.063	-0.063
22	0.50	-0.25	0.020	0.111	-0.092	0.023	0.119	-0.097
23	0.50	0.00	0.037	0.199	0.000	0.040	0.201	0.000
24	0.50	0.25	0.020	0.111	0.092	0.023	0.119	0.097
25	0.50	0.50	0.009	0.050	0.050	0.012	0.063	0.063
			$\Sigma\phi_I = 1$			$\Sigma\phi_I = 1$		

A.2 I/O data for the RBF example

Table A.2: I/O data for the RBF calculations at the central point

Field nodes			MQF method			GQF method		
No.	x	y	$\phi_I(x)$	$\partial\phi_I/\partial x$	$\partial\phi_I/\partial y$	$\phi_I(x)$	$\partial\phi_I/\partial x$	$\partial\phi_I/\partial y$
1	-0.50	-0.50	0.000	-0.052	-0.052	0.000	0.000	0.000
2	-0.50	-0.25	0.000	-0.062	0.055	0.000	0.000	0.000
3	-0.50	0.00	0.000	0.798	0.000	0.000	0.374	0.000
4	-0.50	0.25	0.000	-0.062	-0.055	0.000	0.000	0.000
5	-0.50	0.50	0.000	-0.052	0.052	0.000	0.000	0.000
6	-0.25	-0.50	0.000	0.055	-0.062	0.000	0.000	0.000
7	-0.25	-0.25	0.000	0.051	0.051	0.000	0.000	0.000
8	-0.25	0.00	0.000	-3.320	0.000	0.000	-2.750	0.000
9	-0.25	0.25	0.000	0.051	-0.051	0.000	0.000	0.000
10	-0.25	0.50	0.000	0.055	0.062	0.000	0.000	0.000
11	0.00	-0.50	0.000	0.000	0.798	0.000	0.000	0.374
12	0.00	-0.25	0.000	0.000	-3.320	0.000	0.000	-2.750
13	0.00	0.00	1.000	0.000	0.000	1.000	0.000	0.000
14	0.00	0.25	0.000	0.000	3.320	0.000	0.000	2.750
15	0.00	0.50	0.000	0.000	-0.798	0.000	0.000	-0.374
16	0.25	-0.50	0.000	-0.055	-0.062	0.000	0.000	0.000
17	0.25	-0.25	0.000	-0.051	0.051	0.000	0.000	0.000
18	0.25	0.00	0.000	3.320	0.000	0.000	2.750	0.000
19	0.25	0.25	0.000	-0.051	-0.051	0.000	0.000	0.000
20	0.25	0.50	0.000	-0.055	0.062	0.000	0.000	0.000
21	0.50	-0.50	0.000	0.052	-0.052	0.000	0.000	0.000
22	0.50	-0.25	0.000	0.062	0.055	0.000	0.000	0.000
23	0.50	0.00	0.000	-0.798	0.000	0.000	-0.374	0.000
24	0.50	0.25	0.000	0.062	-0.055	0.000	0.000	0.000
25	0.50	0.50	0.000	0.052	0.052	0.000	0.000	0.000
			$\Sigma\phi_I = 1$			$\Sigma\phi_I = 1$		

A.3 I/O data for the MK example

Table A.3: I/O data for the MK calculations at the central point
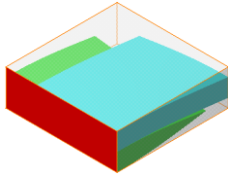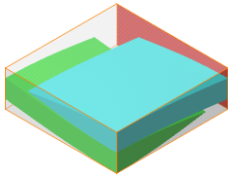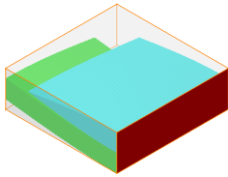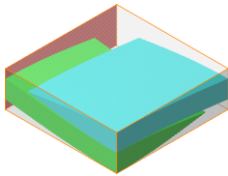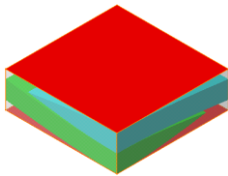
Field nodes			Linear polynomial			Quadratic polynomial		
No.	x	y	$\phi_I(x)$	$\partial\phi_I/\partial x$	$\partial\phi_I/\partial y$	$\phi_I(x)$	$\partial\phi_I/\partial x$	$\partial\phi_I/\partial y$
1	-0.50	-0.50	0.000	-0.103	-0.103	0.000	-0.103	-0.103
2	-0.50	-0.25	0.000	0.158	0.085	0.000	0.158	0.085
3	-0.50	0.00	0.000	0.401	0.000	0.000	0.401	0.000
4	-0.50	0.25	0.000	0.158	-0.085	0.000	0.158	-0.085
5	-0.50	0.50	0.000	-0.103	0.103	0.000	-0.103	0.103
6	-0.25	-0.50	0.000	0.085	0.158	0.000	0.085	0.158
7	-0.25	-0.25	0.000	-0.130	-0.130	0.000	-0.130	-0.130
8	-0.25	0.00	0.000	-2.930	0.000	0.000	-2.930	0.000
9	-0.25	0.25	0.000	-0.130	0.130	0.000	-0.130	0.130
10	-0.25	0.50	0.000	0.085	-0.158	0.000	0.085	-0.158
11	0.00	-0.50	0.000	0.000	0.401	0.000	0.000	0.401
12	0.00	-0.25	0.000	0.000	-2.930	0.000	0.000	-2.930
13	0.00	0.00	1.000	0.000	0.000	1.000	0.000	0.000
14	0.00	0.25	0.000	0.000	2.930	0.000	0.000	2.930
15	0.00	0.50	0.000	0.000	-0.401	0.000	0.000	-0.401
16	0.25	-0.50	0.000	-0.085	0.158	0.000	-0.085	0.158
17	0.25	-0.25	0.000	0.130	-0.130	0.000	0.130	-0.130
18	0.25	0.00	0.000	2.930	0.000	0.000	2.930	0.000
19	0.25	0.25	0.000	0.130	0.130	0.000	0.130	0.130
20	0.25	0.50	0.000	-0.085	-0.158	0.000	-0.085	-0.158
21	0.50	-0.50	0.000	0.103	-0.103	0.000	0.103	-0.103
22	0.50	-0.25	0.000	-0.158	0.085	0.000	-0.158	0.085
23	0.50	0.00	0.000	-0.401	0.000	0.000	-0.401	0.000
24	0.50	0.25	0.000	-0.158	-0.085	0.000	-0.158	-0.085
25	0.50	0.50	0.000	0.103	0.103	0.000	0.103	0.103
			$\Sigma\phi_I = 1$			$\Sigma\phi_I = 1$		

APPENDIX B

B.1 PBCs for normal plain woven mUC
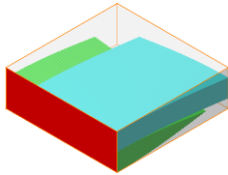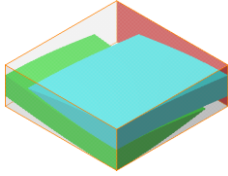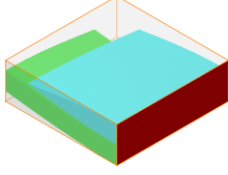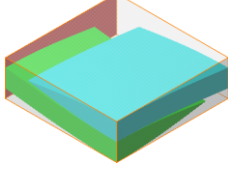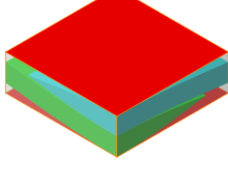
B.1.1 Normal loading case $\langle\sigma_{11}\rangle$, $\langle\sigma_{22}\rangle$ and $\langle\sigma_{33}\rangle$

Table B.1: PBCs for normal plain woven composites under normal loading

		$\boldsymbol{u}(A) - \gamma\mathbf{T}\boldsymbol{u}(\bar{A})$	=	$-\langle\boldsymbol{\varepsilon}\rangle\mathbf{T}\boldsymbol{x}^{O_{\bar{D}}}$
S_1		$\begin{bmatrix} u_1\left(-\frac{L}{2},y,z\right) \\ \cancel{u_2\left(-\frac{L}{2},y,z\right)} \\ \cancel{u_3\left(-\frac{L}{2},y,z\right)} \end{bmatrix} - \begin{bmatrix} -u_1\left(-\frac{L}{2},y,z\right) \\ \cancel{u_2\left(-\frac{L}{2},y,z\right)} \\ \cancel{u_3\left(-\frac{L}{2},y,z\right)} \end{bmatrix}$	=	$\begin{bmatrix} -L\langle\varepsilon_{11}\rangle \\ \cancel{0} \\ \cancel{0} \end{bmatrix}$
S_2		$\begin{bmatrix} u_1\left(\frac{L}{2},y,-z\right) \\ u_2\left(\frac{L}{2},y,-z\right) \\ u_3\left(\frac{L}{2},y,-z\right) \end{bmatrix} - \begin{bmatrix} -u_1\left(\frac{L}{2},y,z\right) \\ u_2\left(\frac{L}{2},y,z\right) \\ -u_3\left(\frac{L}{2},y,z\right) \end{bmatrix}$	=	$\begin{bmatrix} L\langle\varepsilon_{11}\rangle \\ 0 \\ 0 \end{bmatrix}$
S_3		$\begin{bmatrix} \cancel{u_1\left(x,-\frac{W}{2},z\right)} \\ u_2\left(x,-\frac{W}{2},z\right) \\ \cancel{u_3\left(x,-\frac{W}{2},z\right)} \end{bmatrix} - \begin{bmatrix} \cancel{u_1\left(x,-\frac{W}{2},z\right)} \\ -u_2\left(x,-\frac{W}{2},z\right) \\ \cancel{u_3\left(x,-\frac{W}{2},z\right)} \end{bmatrix}$	=	$\begin{bmatrix} \cancel{0} \\ -W\langle\varepsilon_{22}\rangle \\ \cancel{0} \end{bmatrix}$
S_4		$\begin{bmatrix} u_1\left(x,\frac{W}{2},-z\right) \\ u_2\left(x,\frac{W}{2},-z\right) \\ u_3\left(x,\frac{W}{2},-z\right) \end{bmatrix} - \begin{bmatrix} u_1\left(x,\frac{W}{2},z\right) \\ -u_2\left(x,\frac{W}{2},z\right) \\ -u_3\left(x,\frac{W}{2},z\right) \end{bmatrix}$	=	$\begin{bmatrix} 0 \\ W\langle\varepsilon_{22}\rangle \\ 0 \end{bmatrix}$
$S_5 \,\&\, S_6$		$\begin{bmatrix} u_1\left(x,y,\frac{H}{2}\right) \\ u_2\left(x,y,\frac{H}{2}\right) \\ u_3\left(x,y,\frac{H}{2}\right) \end{bmatrix} - \begin{bmatrix} u_1\left(x,y,-\frac{H}{2}\right) \\ u_2\left(x,y,-\frac{H}{2}\right) \\ u_3\left(x,y,-\frac{H}{2}\right) \end{bmatrix}$	=	$\begin{bmatrix} 0 \\ 0 \\ H\langle\varepsilon_{33}\rangle \end{bmatrix}$

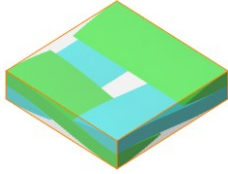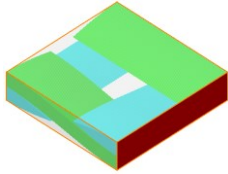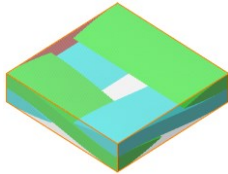*B.1.2 Shear loading case $\langle \sigma_{12} \rangle$*

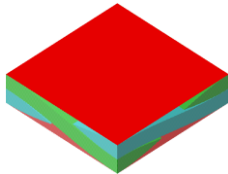**Table B.2: PBCs for normal plain woven composites under shear loading $\langle \sigma_{12} \rangle$**

		$\boldsymbol{u}(A) - \gamma \mathbf{T}\boldsymbol{u}(\bar{A})$	$=$	$-\langle \boldsymbol{\varepsilon} \rangle \mathbf{T} \boldsymbol{x}^{O_{\bar{D}}}$
S_1		$\begin{bmatrix} \cancel{u_1\left(-\frac{L}{2}, y, z\right)} \\ u_2\left(-\frac{L}{2}, y, z\right) \\ u_3\left(-\frac{L}{2}, y, z\right) \end{bmatrix} - \begin{bmatrix} \cancel{u_1\left(-\frac{L}{2}, y, z\right)} \\ -u_2\left(-\frac{L}{2}, y, z\right) \\ -u_3\left(-\frac{L}{2}, y, z\right) \end{bmatrix}$	$=$	$\begin{bmatrix} \cancel{0} \\ -L\langle \varepsilon_{12} \rangle \\ 0 \end{bmatrix}$
S_2		$\begin{bmatrix} u_1\left(\frac{L}{2}, y, -z\right) \\ u_2\left(\frac{L}{2}, y, -z\right) \\ u_3\left(\frac{L}{2}, y, -z\right) \end{bmatrix} - \begin{bmatrix} u_1\left(\frac{L}{2}, y, z\right) \\ -u_2\left(\frac{L}{2}, y, z\right) \\ u_3\left(\frac{L}{2}, y, z\right) \end{bmatrix}$	$=$	$\begin{bmatrix} 0 \\ L\langle \varepsilon_{12} \rangle \\ 0 \end{bmatrix}$
S_3		$\begin{bmatrix} u_1\left(x, -\frac{W}{2}, z\right) \\ \cancel{u_2\left(x, -\frac{W}{2}, z\right)} \\ u_3\left(x, -\frac{W}{2}, z\right) \end{bmatrix} - \begin{bmatrix} -u_1\left(x, -\frac{W}{2}, z\right) \\ \cancel{u_2\left(x, -\frac{W}{2}, z\right)} \\ -u_3\left(x, -\frac{W}{2}, z\right) \end{bmatrix}$	$=$	$\begin{bmatrix} -W\langle \varepsilon_{12} \rangle \\ \cancel{0} \\ 0 \end{bmatrix}$
S_4		$\begin{bmatrix} u_1\left(x, \frac{W}{2}, -z\right) \\ u_2\left(x, \frac{W}{2}, -z\right) \\ u_3\left(x, \frac{W}{2}, -z\right) \end{bmatrix} - \begin{bmatrix} -u_1\left(x, \frac{W}{2}, z\right) \\ u_2\left(x, \frac{W}{2}, z\right) \\ u_3\left(x, \frac{W}{2}, z\right) \end{bmatrix}$	$=$	$\begin{bmatrix} W\langle \varepsilon_{12} \rangle \\ 0 \\ 0 \end{bmatrix}$
S_5 & S_6		$\begin{bmatrix} u_1\left(x, y, \frac{H}{2}\right) \\ u_2\left(x, y, \frac{H}{2}\right) \\ u_3\left(x, y, \frac{H}{2}\right) \end{bmatrix} - \begin{bmatrix} u_1\left(x, y, -\frac{H}{2}\right) \\ u_2\left(x, y, -\frac{H}{2}\right) \\ u_3\left(x, y, -\frac{H}{2}\right) \end{bmatrix}$	$=$	$\begin{bmatrix} 0 \\ 0 \\ 0 \end{bmatrix}$

B.1.3 Shear loading case $\langle \sigma_{23} \rangle$

Table B.3: PBCs for normal plain woven composites under shear loading $\langle \sigma_{23} \rangle$

		$\boldsymbol{u}(A) - \gamma \mathbf{T} \boldsymbol{u}(\bar{A})$	$=$	$-\langle \boldsymbol{\varepsilon} \rangle \mathbf{T} \boldsymbol{x}^{O_{\bar{D}}}$
S_1		$\begin{bmatrix} u_1\left(-\frac{L}{2}, y, z\right) \\ \cancel{u_2\left(-\frac{L}{2}, y, z\right)} \\ \cancel{u_3\left(-\frac{L}{2}, y, z\right)} \end{bmatrix} - \begin{bmatrix} -u_1\left(-\frac{L}{2}, y, z\right) \\ \cancel{u_2\left(-\frac{L}{2}, y, z\right)} \\ \cancel{u_3\left(-\frac{L}{2}, y, z\right)} \end{bmatrix}$	$=$	$\begin{bmatrix} 0 \\ \cancel{0} \\ \cancel{0} \end{bmatrix}$
S_2		$\begin{bmatrix} u_1\left(\frac{L}{2}, y, -z\right) \\ u_2\left(\frac{L}{2}, y, -z\right) \\ u_3\left(\frac{L}{2}, y, -z\right) \end{bmatrix} - \begin{bmatrix} u_1\left(\frac{L}{2}, y, z\right) \\ -u_2\left(\frac{L}{2}, y, z\right) \\ u_3\left(\frac{L}{2}, y, z\right) \end{bmatrix}$	$=$	$\begin{bmatrix} 0 \\ 0 \\ 0 \end{bmatrix}$
S_3		$\begin{bmatrix} u_1\left(x, -\frac{W}{2}, z\right) \\ \cancel{u_2\left(x, -\frac{W}{2}, z\right)} \\ u_3\left(x, -\frac{W}{2}, z\right) \end{bmatrix} - \begin{bmatrix} -u_1\left(x, -\frac{W}{2}, z\right) \\ \cancel{u_2\left(x, -\frac{W}{2}, z\right)} \\ -u_3\left(x, -\frac{W}{2}, z\right) \end{bmatrix}$	$=$	$\begin{bmatrix} 0 \\ \cancel{0} \\ -W\langle \varepsilon_{23} \rangle \end{bmatrix}$
S_4		$\begin{bmatrix} u_1\left(x, \frac{W}{2}, -z\right) \\ u_2\left(x, \frac{W}{2}, -z\right) \\ u_3\left(x, \frac{W}{2}, -z\right) \end{bmatrix} - \begin{bmatrix} u_1\left(x, \frac{W}{2}, z\right) \\ -u_2\left(x, \frac{W}{2}, z\right) \\ -u_3\left(x, \frac{W}{2}, z\right) \end{bmatrix}$	$=$	$\begin{bmatrix} 0 \\ 0 \\ W\langle \varepsilon_{23} \rangle \end{bmatrix}$
S_5 & S_6		$\begin{bmatrix} u_1\left(x, y, \frac{H}{2}\right) \\ u_2\left(x, y, \frac{H}{2}\right) \\ u_3\left(x, y, \frac{H}{2}\right) \end{bmatrix} - \begin{bmatrix} u_1\left(x, y, -\frac{H}{2}\right) \\ u_2\left(x, y, -\frac{H}{2}\right) \\ u_3\left(x, y, -\frac{H}{2}\right) \end{bmatrix}$	$=$	$\begin{bmatrix} 0 \\ H\langle \varepsilon_{23} \rangle \\ 0 \end{bmatrix}$

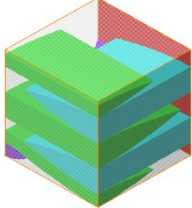*B.1.4 Shear loading case* $\langle \sigma_{13} \rangle$
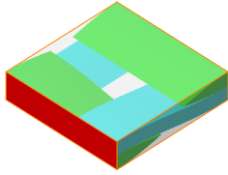
Table B.4: PBCs for normal plain woven composites under shear loading $\langle \sigma_{13} \rangle$

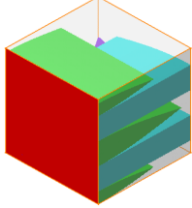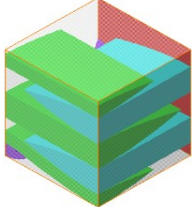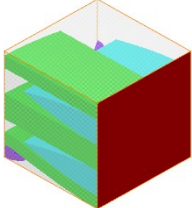|		$\boldsymbol{u}(A) - \gamma \mathbf{T}\boldsymbol{u}(\bar{A})$	=	$-\langle \boldsymbol{\varepsilon} \rangle \mathbf{T} \boldsymbol{x}^{O_{\bar{D}}}$
S_1		$\begin{bmatrix} \cancel{u_1\left(-\frac{L}{2}, y, z\right)} \\ u_2\left(-\frac{L}{2}, y, z\right) \\ u_3\left(-\frac{L}{2}, y, z\right) \end{bmatrix} - \begin{bmatrix} \cancel{u_1\left(-\frac{L}{2}, y, z\right)} \\ -u_2\left(-\frac{L}{2}, y, z\right) \\ -u_3\left(-\frac{L}{2}, y, z\right) \end{bmatrix}$	=	$\begin{bmatrix} \cancel{0} \\ 0 \\ -L\langle \varepsilon_{13} \rangle \end{bmatrix}$
S_2		$\begin{bmatrix} u_1\left(\frac{L}{2}, y, -z\right) \\ u_2\left(\frac{L}{2}, y, -z\right) \\ u_3\left(\frac{L}{2}, y, -z\right) \end{bmatrix} - \begin{bmatrix} -u_1\left(\frac{L}{2}, y, z\right) \\ u_2\left(\frac{L}{2}, y, z\right) \\ -u_3\left(\frac{L}{2}, y, z\right) \end{bmatrix}$	=	$\begin{bmatrix} 0 \\ 0 \\ L\langle \varepsilon_{13} \rangle \end{bmatrix}$
S_3		$\begin{bmatrix} \cancel{u_1\left(x, \frac{W}{2}, z\right)} \\ u_2\left(x, -\frac{W}{2}, z\right) \\ \cancel{u_3\left(x, \frac{W}{2}, z\right)} \end{bmatrix} - \begin{bmatrix} \cancel{u_1\left(x, -\frac{W}{2}, z\right)} \\ -u_2\left(x, -\frac{W}{2}, z\right) \\ \cancel{u_3\left(x, \frac{W}{2}, z\right)} \end{bmatrix}$	=	$\begin{bmatrix} \cancel{0} \\ 0 \\ \cancel{0} \end{bmatrix}$
S_4		$\begin{bmatrix} u_1\left(x, \frac{W}{2}, -z\right) \\ u_2\left(x, \frac{W}{2}, -z\right) \\ u_3\left(x, \frac{W}{2}, -z\right) \end{bmatrix} - \begin{bmatrix} -u_1\left(x, \frac{W}{2}, z\right) \\ u_2\left(x, \frac{W}{2}, z\right) \\ u_3\left(x, \frac{W}{2}, z\right) \end{bmatrix}$	=	$\begin{bmatrix} 0 \\ 0 \\ 0 \end{bmatrix}$
S_5 & S_6		$\begin{bmatrix} u_1\left(x, y, \frac{H}{2}\right) \\ u_2\left(x, y, \frac{H}{2}\right) \\ u_3\left(x, y, \frac{H}{2}\right) \end{bmatrix} - \begin{bmatrix} u_1\left(x, y, -\frac{H}{2}\right) \\ u_2\left(x, y, -\frac{H}{2}\right) \\ u_3\left(x, y, -\frac{H}{2}\right) \end{bmatrix}$	=	$\begin{bmatrix} H\langle \varepsilon_{13} \rangle \\ 0 \\ 0 \end{bmatrix}$

B.2 PBCs for normal twill woven mUC
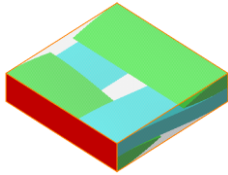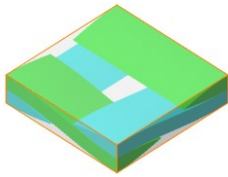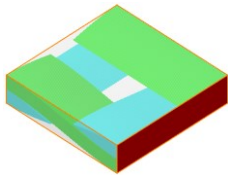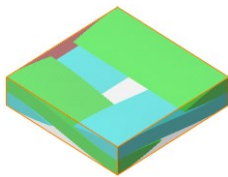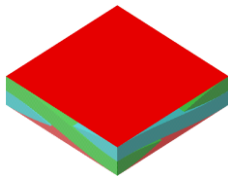
B.2.1 Normal/shear loading case $\langle\sigma_{11}\rangle$, $\langle\sigma_{22}\rangle$, $\langle\sigma_{33}\rangle$ and $\langle\sigma_{12}\rangle$

Table B.5: PBCs for normal twill woven composites under normal/shear loading

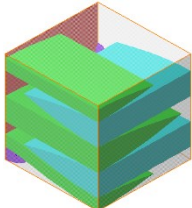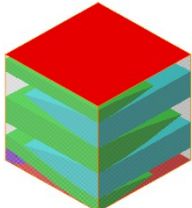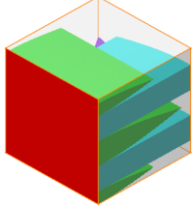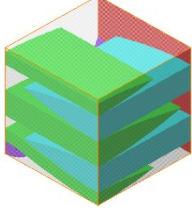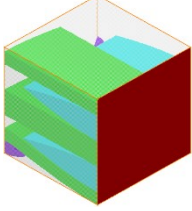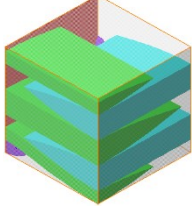|		$\boldsymbol{u}(A) - \gamma\mathbf{T}\boldsymbol{u}(\bar{A})$	$=$	$-\langle\boldsymbol{\varepsilon}\rangle\mathbf{T}\boldsymbol{x}^{O_{\bar{D}}}$
S_1		$\begin{bmatrix} u_1\left(-\frac{L}{2},-y,-z\right) \\ u_2\left(-\frac{L}{2},-y,-z\right) \\ u_3\left(-\frac{L}{2},-y,-z\right) \end{bmatrix} - \begin{bmatrix} -u_1\left(-\frac{L}{2},y,z\right) \\ -u_2\left(-\frac{L}{2},y,z\right) \\ -u_3\left(-\frac{L}{2},y,z\right) \end{bmatrix}$	$=$	$\begin{bmatrix} -L\langle\varepsilon_{11}\rangle \\ -L\langle\varepsilon_{12}\rangle \\ 0 \end{bmatrix}$
S_2		$\begin{bmatrix} u_1\left(\frac{L}{2},-y,z\right) \\ u_2\left(\frac{L}{2},-y,z\right) \\ u_3\left(\frac{L}{2},-y,z\right) \end{bmatrix} - \begin{bmatrix} -u_1\left(\frac{L}{2},y,z\right) \\ -u_2\left(\frac{L}{2},y,z\right) \\ u_3\left(\frac{L}{2},y,z\right) \end{bmatrix}$	$=$	$\begin{bmatrix} L\langle\varepsilon_{11}\rangle \\ L\langle\varepsilon_{12}\rangle \\ 0 \end{bmatrix}$
S_3		$\begin{bmatrix} u_1\left(-x,-\frac{W}{2},-z\right) \\ u_2\left(-x,-\frac{W}{2},-z\right) \\ u_3\left(-x,-\frac{W}{2},-z\right) \end{bmatrix} - \begin{bmatrix} -u_1\left(x,-\frac{W}{2},z\right) \\ -u_2\left(x,-\frac{W}{2},z\right) \\ -u_3\left(x,-\frac{W}{2},z\right) \end{bmatrix}$	$=$	$\begin{bmatrix} -W\langle\varepsilon_{12}\rangle \\ -W\langle\varepsilon_{22}\rangle \\ 0 \end{bmatrix}$
S_4		$\begin{bmatrix} u_1\left(-x,\frac{W}{2},z\right) \\ u_2\left(-x,\frac{W}{2},z\right) \\ u_3\left(-x,\frac{W}{2},z\right) \end{bmatrix} - \begin{bmatrix} -u_1\left(x,\frac{W}{2},z\right) \\ -u_2\left(x,\frac{W}{2},z\right) \\ u_3\left(x,\frac{W}{2},z\right) \end{bmatrix}$	$=$	$\begin{bmatrix} W\langle\varepsilon_{12}\rangle \\ W\langle\varepsilon_{22}\rangle \\ 0 \end{bmatrix}$
S_5 & S_6		$\begin{bmatrix} u_1\left(x,y,\frac{H}{2}\right) \\ u_2\left(x,y,\frac{H}{2}\right) \\ u_3\left(x,y,\frac{H}{2}\right) \end{bmatrix} - \begin{bmatrix} u_1\left(x,y,-\frac{H}{2}\right) \\ u_2\left(x,y,-\frac{H}{2}\right) \\ u_3\left(x,y,-\frac{H}{2}\right) \end{bmatrix}$	$=$	$\begin{bmatrix} 0 \\ 0 \\ H\langle\varepsilon_{33}\rangle \end{bmatrix}$

B.2.2 Shear loading case $\langle\sigma_{23}\rangle$ and $\langle\sigma_{13}\rangle$
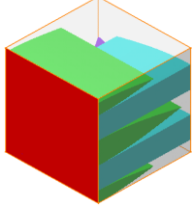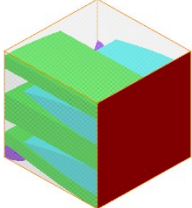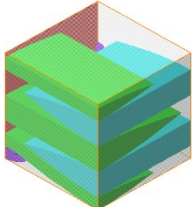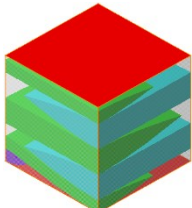
Table B.6: PBCs for normal twill woven composites under shear loading

		$\boldsymbol{u}(A) - \gamma\mathbf{T}\boldsymbol{u}(\bar{A})$	$=$	$-\langle\boldsymbol{\varepsilon}\rangle\mathbf{T}\boldsymbol{x}^{0_{\bar{D}}}$
S_1		$\begin{bmatrix} u_1\left(-\frac{L}{2},-y,-z\right) \\ u_2\left(-\frac{L}{2},-y,-z\right) \\ u_3\left(-\frac{L}{2},-y,-z\right) \end{bmatrix} - \begin{bmatrix} -u_1\left(-\frac{L}{2},y,z\right) \\ -u_2\left(-\frac{L}{2},y,z\right) \\ -u_3\left(-\frac{L}{2},y,z\right) \end{bmatrix}$	$=$	$\begin{bmatrix} 0 \\ 0 \\ -L\langle\varepsilon_{13}\rangle \end{bmatrix}$
S_2		$\begin{bmatrix} u_1\left(\frac{L}{2},-y,z\right) \\ u_2\left(\frac{L}{2},-y,z\right) \\ u_3\left(\frac{L}{2},-y,z\right) \end{bmatrix} - \begin{bmatrix} u_1\left(\frac{L}{2},y,z\right) \\ u_2\left(\frac{L}{2},y,z\right) \\ -u_3\left(\frac{L}{2},y,z\right) \end{bmatrix}$	$=$	$\begin{bmatrix} 0 \\ 0 \\ L\langle\varepsilon_{13}\rangle \end{bmatrix}$
S_3		$\begin{bmatrix} u_1\left(-x,-\frac{W}{2},-z\right) \\ u_2\left(-x,-\frac{W}{2},-z\right) \\ u_3\left(-x,-\frac{W}{2},-z\right) \end{bmatrix} - \begin{bmatrix} -u_1\left(x,-\frac{W}{2},z\right) \\ -u_2\left(x,-\frac{W}{2},z\right) \\ -u_3\left(x,-\frac{W}{2},z\right) \end{bmatrix}$	$=$	$\begin{bmatrix} 0 \\ 0 \\ -W\langle\varepsilon_{23}\rangle \end{bmatrix}$
S_4		$\begin{bmatrix} u_1\left(-x,\frac{W}{2},z\right) \\ u_2\left(-x,\frac{W}{2},z\right) \\ u_3\left(-x,\frac{W}{2},z\right) \end{bmatrix} - \begin{bmatrix} u_1\left(x,\frac{W}{2},z\right) \\ u_2\left(x,\frac{W}{2},z\right) \\ -u_3\left(x,\frac{W}{2},z\right) \end{bmatrix}$	$=$	$\begin{bmatrix} 0 \\ 0 \\ W\langle\varepsilon_{23}\rangle \end{bmatrix}$
S_5 & S_6		$\begin{bmatrix} u_1\left(x,y,\frac{H}{2}\right) \\ u_2\left(x,y,\frac{H}{2}\right) \\ u_3\left(x,y,\frac{H}{2}\right) \end{bmatrix} - \begin{bmatrix} u_1\left(x,y,-\frac{H}{2}\right) \\ u_2\left(x,y,-\frac{H}{2}\right) \\ u_3\left(x,y,-\frac{H}{2}\right) \end{bmatrix}$	$=$	$\begin{bmatrix} H\langle\varepsilon_{13}\rangle \\ H\langle\varepsilon_{23}\rangle \\ 0 \end{bmatrix}$

B.3 PBCs for normal 3D woven mUC

B.3.1 Normal loading case $\langle\sigma_{11}\rangle$, $\langle\sigma_{22}\rangle$ and $\langle\sigma_{33}\rangle$

Table B.7: PBCs for normal 3D woven composites under normal loading

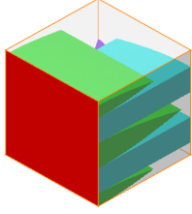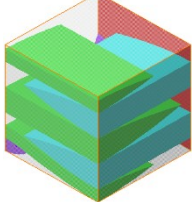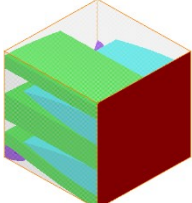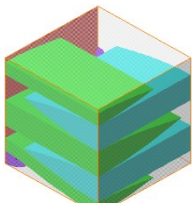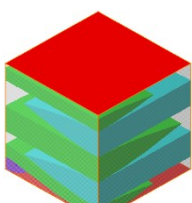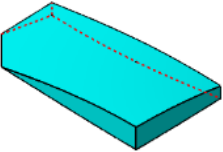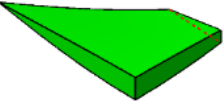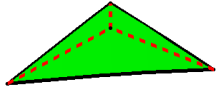|		$\boldsymbol{u}(A) - \gamma\mathbf{T}\boldsymbol{u}(\bar{A})$	$=$	$-\langle\boldsymbol{\varepsilon}\rangle\mathbf{T}\boldsymbol{x}^{O_{\bar{D}}}$
S_1		$\begin{bmatrix} u_1\left(-\frac{L}{2},y,z\right) \\ \cancel{u_2\left(-\frac{L}{2},y,z\right)} \\ \cancel{u_3\left(-\frac{L}{2},y,z\right)} \end{bmatrix} - \begin{bmatrix} -u_1\left(-\frac{L}{2},y,z\right) \\ \cancel{u_2\left(-\frac{L}{2},y,z\right)} \\ \cancel{u_3\left(-\frac{L}{2},y,z\right)} \end{bmatrix}$	$=$	$\begin{bmatrix} -L\langle\varepsilon_{11}\rangle \\ \cancel{0} \\ \cancel{0} \end{bmatrix}$
S_2		$\begin{bmatrix} u_1\left(\frac{L}{2},y,-z\right) \\ u_2\left(\frac{L}{2},y,-z\right) \\ u_3\left(\frac{L}{2},y,-z\right) \end{bmatrix} - \begin{bmatrix} -u_1\left(\frac{L}{2},y,z\right) \\ u_2\left(\frac{L}{2},y,z\right) \\ -u_3\left(\frac{L}{2},y,z\right) \end{bmatrix}$	$=$	$\begin{bmatrix} L\langle\varepsilon_{11}\rangle \\ 0 \\ 0 \end{bmatrix}$
S_3		$\begin{bmatrix} u_1\left(x,-\frac{W}{2},-z\right) \\ u_2\left(x,-\frac{W}{2},-z\right) \\ u_3\left(x,-\frac{W}{2},-z\right) \end{bmatrix} - \begin{bmatrix} u_1\left(x,-\frac{W}{2},z\right) \\ -u_2\left(x,-\frac{W}{2},z\right) \\ -u_3\left(x,-\frac{W}{2},z\right) \end{bmatrix}$	$=$	$\begin{bmatrix} 0 \\ -W\langle\varepsilon_{22}\rangle \\ 0 \end{bmatrix}$
S_4		$\begin{bmatrix} \cancel{u_1\left(x,\frac{W}{2},z\right)} \\ u_2\left(x,\frac{W}{2},z\right) \\ \cancel{u_3\left(x,\frac{W}{2},z\right)} \end{bmatrix} - \begin{bmatrix} \cancel{u_1\left(x,\frac{W}{2},z\right)} \\ -u_2\left(x,\frac{W}{2},z\right) \\ \cancel{u_3\left(x,\frac{W}{2},z\right)} \end{bmatrix}$	$=$	$\begin{bmatrix} \cancel{0} \\ W\langle\varepsilon_{22}\rangle \\ \cancel{0} \end{bmatrix}$
$S_5\ \&\ S_6$		$\begin{bmatrix} u_1\left(x,y,\frac{H}{2}\right) \\ u_2\left(x,y,\frac{H}{2}\right) \\ u_3\left(x,y,\frac{H}{2}\right) \end{bmatrix} - \begin{bmatrix} u_1\left(x,y,-\frac{H}{2}\right) \\ u_2\left(x,y,-\frac{H}{2}\right) \\ u_3\left(x,y,-\frac{H}{2}\right) \end{bmatrix}$	$=$	$\begin{bmatrix} 0 \\ 0 \\ H\langle\varepsilon_{33}\rangle \end{bmatrix}$

B.3.2 Shear loading case $\langle \sigma_{12} \rangle$

Table B.8: PBCs for normal 3D woven composites under shear loading $\langle \sigma_{12} \rangle$

		$\boldsymbol{u}(A) - \gamma \mathbf{T} \boldsymbol{u}(\bar{A})$	$=$	$-\langle \boldsymbol{\varepsilon} \rangle \mathbf{T} \boldsymbol{x}^{O\bar{D}}$
S_1		$\begin{bmatrix} u_1\left(-\frac{L}{2}, y, z\right) \\ u_2\left(-\frac{L}{2}, y, z\right) \\ u_3\left(-\frac{L}{2}, y, z\right) \end{bmatrix} - \begin{bmatrix} u_1\left(-\frac{L}{2}, y, z\right) \\ -u_2\left(-\frac{L}{2}, y, z\right) \\ -u_3\left(-\frac{L}{2}, y, z\right) \end{bmatrix}$	$=$	$\begin{bmatrix} 0 \\ -L\langle \varepsilon_{12} \rangle \\ 0 \end{bmatrix}$
S_2		$\begin{bmatrix} u_1\left(\frac{L}{2}, y, -z\right) \\ u_2\left(\frac{L}{2}, y, -z\right) \\ u_3\left(\frac{L}{2}, y, -z\right) \end{bmatrix} - \begin{bmatrix} u_1\left(\frac{L}{2}, y, z\right) \\ -u_2\left(\frac{L}{2}, y, z\right) \\ u_3\left(\frac{L}{2}, y, z\right) \end{bmatrix}$	$=$	$\begin{bmatrix} 0 \\ L\langle \varepsilon_{12} \rangle \\ 0 \end{bmatrix}$
S_3		$\begin{bmatrix} u_1\left(x, -\frac{W}{2}, -z\right) \\ u_2\left(x, -\frac{W}{2}, -z\right) \\ u_3\left(x, -\frac{W}{2}, -z\right) \end{bmatrix} - \begin{bmatrix} -u_1\left(x, -\frac{W}{2}, z\right) \\ u_2\left(x, -\frac{W}{2}, z\right) \\ u_3\left(x, -\frac{W}{2}, z\right) \end{bmatrix}$	$=$	$\begin{bmatrix} -W\langle \varepsilon_{12} \rangle \\ 0 \\ 0 \end{bmatrix}$
S_4		$\begin{bmatrix} u_1\left(x, \frac{W}{2}, z\right) \\ u_2\left(x, \frac{W}{2}, z\right) \\ u_3\left(x, \frac{W}{2}, z\right) \end{bmatrix} - \begin{bmatrix} -u_1\left(x, \frac{W}{2}, z\right) \\ u_2\left(x, \frac{W}{2}, z\right) \\ -u_3\left(x, \frac{W}{2}, z\right) \end{bmatrix}$	$=$	$\begin{bmatrix} W\langle \varepsilon_{12} \rangle \\ 0 \\ 0 \end{bmatrix}$
$S_5 \,\&\, S_6$		$\begin{bmatrix} u_1\left(x, y, \frac{H}{2}\right) \\ u_2\left(x, y, \frac{H}{2}\right) \\ u_3\left(x, y, \frac{H}{2}\right) \end{bmatrix} - \begin{bmatrix} u_1\left(x, y, -\frac{H}{2}\right) \\ u_2\left(x, y, -\frac{H}{2}\right) \\ u_3\left(x, y, -\frac{H}{2}\right) \end{bmatrix}$	$=$	$\begin{bmatrix} 0 \\ 0 \\ 0 \end{bmatrix}$

B.3.3 Shear loading case $\langle \sigma_{23} \rangle$

Table B.9: PBCs for normal 3D woven composites under shear loading $\langle \boldsymbol{\sigma_{23}} \rangle$

		$\boldsymbol{u}(A) - \gamma \mathbf{T}\boldsymbol{u}(\bar{A})$	$=$	$-\langle \boldsymbol{\varepsilon} \rangle \mathbf{T} \boldsymbol{x}^{O\bar{D}}$
S_1		$\begin{bmatrix} u_1\left(-\frac{L}{2}, y, z\right) \\ u_2\left(-\frac{L}{2}, y, z\right) \\ u_3\left(-\frac{L}{2}, y, z\right) \end{bmatrix} - \begin{bmatrix} -u_1\left(-\frac{L}{2}, y, z\right) \\ u_2\left(-\frac{L}{2}, y, z\right) \\ u_3\left(-\frac{L}{2}, y, z\right) \end{bmatrix}$	$=$	$\begin{bmatrix} 0 \\ 0 \\ 0 \end{bmatrix}$
S_2		$\begin{bmatrix} u_1\left(\frac{L}{2}, y, -z\right) \\ u_2\left(\frac{L}{2}, y, -z\right) \\ u_3\left(\frac{L}{2}, y, -z\right) \end{bmatrix} - \begin{bmatrix} u_1\left(\frac{L}{2}, y, z\right) \\ -u_2\left(\frac{L}{2}, y, z\right) \\ u_3\left(\frac{L}{2}, y, z\right) \end{bmatrix}$	$=$	$\begin{bmatrix} 0 \\ 0 \\ 0 \end{bmatrix}$
S_3		$\begin{bmatrix} u_1\left(x, -\frac{W}{2}, -z\right) \\ u_2\left(x, -\frac{W}{2}, -z\right) \\ u_3\left(x, -\frac{W}{2}, -z\right) \end{bmatrix} - \begin{bmatrix} u_1\left(x, -\frac{W}{2}, z\right) \\ -u_2\left(x, -\frac{W}{2}, z\right) \\ -u_3\left(x, -\frac{W}{2}, z\right) \end{bmatrix}$	$=$	$\begin{bmatrix} 0 \\ 0 \\ -W\langle \varepsilon_{23} \rangle \end{bmatrix}$
S_4		$\begin{bmatrix} u_1\left(x, \frac{W}{2}, z\right) \\ u_2\left(x, \frac{W}{2}, z\right) \\ u_3\left(x, \frac{W}{2}, z\right) \end{bmatrix} - \begin{bmatrix} -u_1\left(x, \frac{W}{2}, z\right) \\ u_2\left(x, \frac{W}{2}, z\right) \\ -u_3\left(x, \frac{W}{2}, z\right) \end{bmatrix}$	$=$	$\begin{bmatrix} 0 \\ 0 \\ W\langle \varepsilon_{23} \rangle \end{bmatrix}$
$S_5 \& S_6$		$\begin{bmatrix} u_1\left(x, y, \frac{H}{2}\right) \\ u_2\left(x, y, \frac{H}{2}\right) \\ u_3\left(x, y, \frac{H}{2}\right) \end{bmatrix} - \begin{bmatrix} u_1\left(x, y, -\frac{H}{2}\right) \\ u_2\left(x, y, -\frac{H}{2}\right) \\ u_3\left(x, y, -\frac{H}{2}\right) \end{bmatrix}$	$=$	$\begin{bmatrix} 0 \\ H\langle \varepsilon_{23} \rangle \\ 0 \end{bmatrix}$

B.3.4 Shear loading case $\langle\sigma_{13}\rangle$

Table B.10: PBCs for normal 3D woven composites under shear loading $\langle\sigma_{13}\rangle$

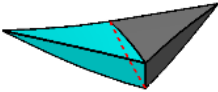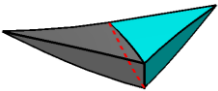|		$\boldsymbol{u}(A) - \gamma\mathbf{T}\boldsymbol{u}(\bar{A})$	$=$	$-\langle\boldsymbol{\varepsilon}\rangle\mathbf{T}\boldsymbol{x}^{O\bar{D}}$
S_1		$\begin{bmatrix} u_1\left(-\frac{L}{2},y,z\right) \\ u_2\left(-\frac{L}{2},y,z\right) \\ u_3\left(-\frac{L}{2},y,z\right) \end{bmatrix} - \begin{bmatrix} u_1\left(-\frac{L}{2},y,z\right) \\ -u_2\left(-\frac{L}{2},y,z\right) \\ -u_3\left(-\frac{L}{2},y,z\right) \end{bmatrix}$	$=$	$\begin{bmatrix} 0 \\ 0 \\ -L\langle\varepsilon_{13}\rangle \end{bmatrix}$
S_2		$\begin{bmatrix} u_1\left(\frac{L}{2},y,-z\right) \\ u_2\left(\frac{L}{2},y,-z\right) \\ u_3\left(\frac{L}{2},y,-z\right) \end{bmatrix} - \begin{bmatrix} -u_1\left(\frac{L}{2},y,z\right) \\ u_2\left(\frac{L}{2},y,z\right) \\ -u_3\left(\frac{L}{2},y,z\right) \end{bmatrix}$	$=$	$\begin{bmatrix} 0 \\ 0 \\ L\langle\varepsilon_{13}\rangle \end{bmatrix}$
S_3		$\begin{bmatrix} u_1\left(x,-\frac{W}{2},-z\right) \\ u_2\left(x,-\frac{W}{2},-z\right) \\ u_3\left(x,-\frac{W}{2},-z\right) \end{bmatrix} - \begin{bmatrix} -u_1\left(x,-\frac{W}{2},z\right) \\ u_2\left(x,-\frac{W}{2},z\right) \\ u_3\left(x,-\frac{W}{2},z\right) \end{bmatrix}$	$=$	$\begin{bmatrix} 0 \\ 0 \\ 0 \end{bmatrix}$
S_4		$\begin{bmatrix} u_1\left(x,\frac{W}{2},z\right) \\ u_2\left(x,\frac{W}{2},z\right) \\ u_3\left(x,\frac{W}{2},z\right) \end{bmatrix} - \begin{bmatrix} u_1\left(x,\frac{W}{2},z\right) \\ -u_2\left(x,\frac{W}{2},z\right) \\ u_3\left(x,\frac{W}{2},z\right) \end{bmatrix}$	$=$	$\begin{bmatrix} 0 \\ 0 \\ 0 \end{bmatrix}$
S_5 & S_6		$\begin{bmatrix} u_1\left(x,y,\frac{H}{2}\right) \\ u_2\left(x,y,\frac{H}{2}\right) \\ u_3\left(x,y,\frac{H}{2}\right) \end{bmatrix} - \begin{bmatrix} u_1\left(x,y,-\frac{H}{2}\right) \\ u_2\left(x,y,-\frac{H}{2}\right) \\ u_3\left(x,y,-\frac{H}{2}\right) \end{bmatrix}$	$=$	$\begin{bmatrix} H\langle\varepsilon_{13}\rangle \\ 0 \\ 0 \end{bmatrix}$

APPENDIX C

C.1 Off-axis mUC for plain woven composites
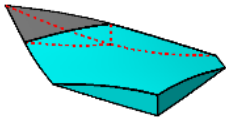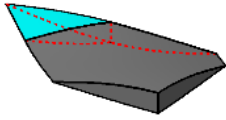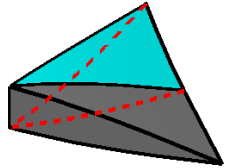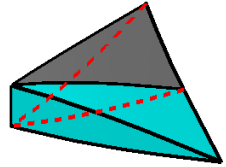
Table C.1: Analytical equations for the off-axis plain woven mUC

Yarn type	In Off-axis CS (XYZ)	In normal CS (XY'Z')
Warp yarn	$\{\lvert x - y\rvert \le \sqrt{2}\lambda W\}$ $$z_{\text{wp}}^{\text{l}} = \frac{H}{4}\left(2 + \cos A_1 - \cos\frac{B_1}{\lambda}\right)$$ $$z_{\text{wp}}^{\text{u}} = \frac{H}{4}\left(2 + \cos A_1 + \cos\frac{B_1}{\lambda}\right)$$ $$\theta_{\text{wp}} = \tan^{-1}\left(-\frac{\pi H}{8L}\sin A_1\right)$$	$\{\lvert y'\rvert \le \lambda W\}$ $$z_{\text{wp}}^{\text{l}} = \frac{H}{4}\left(2 + \cos\frac{\pi x'}{2L} - \cos\frac{\pi y'}{2\lambda W}\right)$$ $$z_{\text{wp}}^{\text{u}} = \frac{H}{4}\left(2 + \cos\frac{\pi x'}{2L} + \cos\frac{\pi y'}{2\lambda W}\right)$$ $$\theta_{\text{wp}} = \tan^{-1}\left(-\frac{\pi H}{8L}\sin\frac{\pi x'}{2L}\right)$$
Fill 1	$\{0 \le (x + y) \le \sqrt{2}\lambda L\}$ $$z_{\text{f1}}^{\text{l}} = \frac{H}{4}\left(2 - \cos\frac{A_1}{\lambda} - \cos B_1\right)$$ $$z_{\text{f1}}^{\text{u}} = \frac{H}{4}\left(2 + \cos\frac{A_1}{\lambda} - \cos B_1\right)$$ $$\theta_{\text{f1}} = \tan^{-1}\left(-\frac{\pi H}{8W}\sin B_1\right)$$	$\{0 \le x' \le \lambda L\}$ $$z_{\text{f1}}^{\text{l}} = \frac{H}{4}\left(2 - \cos\frac{\pi x'}{2\lambda L} - \cos\frac{\pi y'}{2W}\right)$$ $$z_{\text{f1}}^{\text{u}} = \frac{H}{4}\left(2 + \cos\frac{\pi x'}{2\lambda L} - \cos\frac{\pi y'}{2W}\right)$$ $$\theta_{\text{f1}} = \tan^{-1}\left(\frac{\pi H}{8W}\sin\frac{\pi y'}{2W}\right)$$
Fill 2	$\{(x + y) \ge \sqrt{2}(2 - \lambda)L\}$ $$z_{\text{f2}}^{\text{l}} = \frac{H}{4}\left(2 - \cos\frac{A_1 - \pi}{\lambda} + \cos B_1\right)$$ $$z_{\text{f2}}^{\text{u}} = \frac{H}{4}\left(2 + \cos\frac{A_1 - \pi}{\lambda} + \cos B_1\right)$$ $$\theta_{\text{f2}} = \tan^{-1}\left(\frac{\pi H}{8W}\sin B_1\right)$$	$\{x' \ge (2 - \lambda)L\}$ $$z_{\text{f2}}^{\text{l}} = \frac{H}{4}\left(2 - \cos\left(\frac{\pi x'}{2\lambda L} - \frac{\pi}{\lambda}\right) + \cos\frac{\pi y'}{2W}\right)$$ $$z_{\text{f2}}^{\text{u}} = \frac{H}{4}\left(2 + \cos\left(\frac{\pi x'}{2\lambda L} - \frac{\pi}{\lambda}\right) + \cos\frac{\pi y'}{2W}\right)$$ $$\theta_{\text{f2}} = \tan^{-1}\left(-\frac{\pi H}{8W}\sin\frac{\pi y'}{2W}\right)$$

✧ $A_1 = \dfrac{\sqrt{2}\pi(x+y)}{4L}$, $B_1 = \dfrac{\sqrt{2}\pi(x-y)}{4W}$
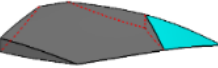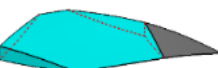
C.2 Off-axis mUC for twill woven composites

Table C.2: Analytical equations for warp yarns in the Off-axis twill woven mUC

Yarn type	In Off-axis CS (XYZ)	In normal CS (XY'Z')
Warp 1 (wavy)	$\{(x + y) \leq \sqrt{2}L\}$ & $\{\|x - y\| \leq \sqrt{2}\lambda W\}$ $z^{l}_{w1,w} = \frac{H}{4}\left(2 + \cos A_2 - \cos\frac{B_1}{\lambda}\right)$ $z^{u}_{w1,w} = \frac{H}{4}\left(2 + \cos A_2 + \cos\frac{B_1}{\lambda}\right)$ $\theta_{w1,w} = \tan^{-1}\left(-\frac{\pi H}{4L}\sin A_2\right)$	$\{x' \leq L\}$ & $\{\|y'\| \leq \lambda W\}$ $z^{l}_{w1,w} = \frac{H}{4}\left(2 + \cos\frac{\pi x'}{L} - \cos\frac{\pi y'}{2\lambda W}\right)$ $z^{u}_{w1,w} = \frac{H}{4}\left(2 + \cos\frac{\pi x'}{L} + \cos\frac{\pi y'}{2\lambda W}\right)$ $\theta_{w1,w} = \tan^{-1}\left(-\frac{\pi H}{4L}\sin\frac{\pi x'}{L}\right)$
Warp 1 (straight)	$\{(x + y) \geq \sqrt{2}L\}$ & $\{\|x - y\| \leq \sqrt{2}\lambda W\}$ $z^{l}_{w1,s} = \frac{H}{4} - \frac{H}{4}\cos\frac{B_1}{\lambda}$ $z^{u}_{w1,s} = \frac{H}{4} + \frac{H}{4}\cos\frac{B_1}{\lambda}$	$\{x' \geq L\}$ & $\{\|y'\| \leq \lambda W\}$ $z^{l}_{w1,s} = \frac{H}{4} - \frac{H}{4}\cos\frac{\pi y'}{2\lambda W}$ $z^{u}_{w1,s} = \frac{H}{4} + \frac{H}{4}\cos\frac{\pi y'}{2\lambda W}$
Warp 2 (wavy)	$\{(x + y) \geq \sqrt{2}L\}$ & $\{(x - y) \leq \sqrt{2}(\lambda - 1)W\}$ $z^{l}_{w2,w} = \frac{H}{4}\left(2 + \cos A_2 - \cos\frac{2B_1 + \pi}{2\lambda}\right)$ $z^{u}_{w2,w} = \frac{H}{4}\left(2 + \cos A_2 + \cos\frac{2B_1 + \pi}{2\lambda}\right)$ $\theta_{w2,w} = \tan^{-1}\left(-\frac{\pi H}{4L}\sin A_2\right)$	$\{x' \geq L\}$ & $\{y' \geq (1 - \lambda)W\}$ $z^{l}_{w2,w} = \frac{H}{4}\left(2 + \cos\frac{\pi x'}{L} - \cos\frac{\pi(y' - W)}{2\lambda W}\right)$ $z^{u}_{w2,w} = \frac{H}{4}\left(2 + \cos\frac{\pi x'}{L} + \cos\frac{\pi(y' - W)}{2\lambda W}\right)$ $\theta_{w2,w} = \tan^{-1}\left(-\frac{\pi H}{4L}\sin\frac{\pi x'}{L}\right)$
Warp 2 (straight)	$\{(x + y) \leq \sqrt{2}L\}$ & $\{(x - y) \leq \sqrt{2}(\lambda - 1)W\}$ $z^{l}_{w2,s} = \frac{H}{4} - \frac{H}{4}\cos\frac{2B_1 + \pi}{2\lambda}$ $z^{u}_{w2,s} = \frac{H}{4} + \frac{H}{4}\cos\frac{2B_1 + \pi}{2\lambda}$	$\{x' \leq L\}$ & $\{y' \geq (1 - \lambda)W\}$ $z^{l}_{w2,s} = \frac{H}{4} - \frac{H}{4}\cos\frac{\pi(y' - W)}{2\lambda W}$ $z^{u}_{w2,s} = \frac{H}{4} + \frac{H}{4}\cos\frac{\pi(y' - W)}{2\lambda W}$

✧ $A_2 = \frac{\sqrt{2}\pi(x+y)}{2L}, B_1 = \frac{\sqrt{2}\pi(x-y)}{4W}$
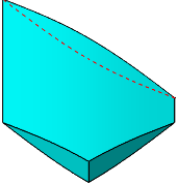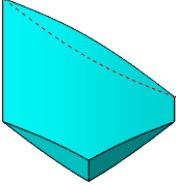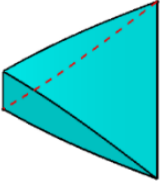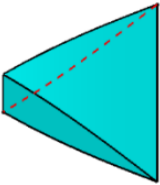
Table C.3: Analytical equations for fill yarns in the Off-axis twill woven mUC

Yarn type	In Off-axis CS (XYZ)	In normal CS (XY'Z')
Fill 1 (wavy)	$\{(x+y) \leq \sqrt{2}\lambda L\}$ & $\{(x-y) \leq 0\}$ $$z_{\mathrm{f1,w}}^{\mathrm{l}} = \frac{H}{4}\left(2 - \cos\frac{A_1}{\lambda} - \cos B_2\right)$$ $$z_{\mathrm{f1,w}}^{\mathrm{u}} = \frac{H}{4}\left(2 + \cos\frac{A_1}{\lambda} - \cos B_2\right)$$ $$\theta_{\mathrm{f1,w}} = \tan^{-1}\left(-\frac{\pi H}{4W}\sin B_2\right)$$	$\{x' \leq \lambda L\}$ & $\{y' \geq 0\}$ $$z_{\mathrm{f1,w}}^{\mathrm{l}} = \frac{H}{4}\left(2 - \cos\frac{\pi x'}{2\lambda L} - \cos\frac{\pi y'}{W}\right)$$ $$z_{\mathrm{f1,w}}^{\mathrm{u}} = \frac{H}{4}\left(2 + \cos\frac{\pi x'}{2\lambda L} - \cos\frac{\pi y'}{W}\right)$$ $$\theta_{\mathrm{f1,w}} = \tan^{-1}\left(\frac{\pi H}{4W}\sin\frac{\pi y'}{W}\right)$$
Fill 1 (straight)	$\{(x+y) \leq \sqrt{2}\lambda L\}$ & $\{(x-y) \geq 0\}$ $$z_{\mathrm{f1,s}}^{\mathrm{l}} = \frac{H}{4} - \frac{H}{4}\cos\frac{A_1}{\lambda}$$ $$z_{\mathrm{f1,s}}^{\mathrm{u}} = \frac{H}{4} + \frac{H}{4}\cos\frac{A_1}{\lambda}$$	$\{x' \leq \lambda L\}$ & $\{y' \leq 0\}$ $$z_{\mathrm{f1,s}}^{\mathrm{l}} = \frac{H}{4} - \frac{H}{4}\cos\frac{\pi x'}{2\lambda L}$$ $$z_{\mathrm{f1,s}}^{\mathrm{u}} = \frac{H}{4} + \frac{H}{4}\cos\frac{\pi x'}{2\lambda L}$$
Fill 2 (wavy)	$\{(x+y) \geq \sqrt{2}(1-\lambda)L\}$ & $\{(x-y) \geq 0\}$ $$z_{\mathrm{f2,w}}^{\mathrm{l}} = \frac{H}{4}\left(2 - \cos\frac{2A_1-\pi}{2\lambda} + \cos B_2\right)$$ $$z_{\mathrm{f2,w}}^{\mathrm{u}} = \frac{H}{4}\left(2 + \cos\frac{2A_1-\pi}{2\lambda} + \cos B_2\right)$$ $$\theta_{\mathrm{f2,w}} = \tan^{-1}\left(\frac{\pi H}{4W}\sin B_2\right)$$	$\{x' \geq (1-\lambda)L\}$ & $\{y' \leq 0\}$ $$z_{\mathrm{f2,w}}^{\mathrm{l}} = \frac{H}{4}\left(2 - \cos\frac{\pi(x'-L)}{2\lambda L} + \cos\frac{\pi y'}{W}\right)$$ $$z_{\mathrm{f2,w}}^{\mathrm{u}} = \frac{H}{4}\left(2 + \cos\frac{\pi(x'-L)}{2\lambda L} + \cos\frac{\pi y'}{W}\right)$$ $$\theta_{\mathrm{f2,w}} = \tan^{-1}\left(-\frac{\pi H}{4W}\sin\frac{\pi y'}{W}\right)$$
Fill 2 (straight)	$\{(x+y) \geq \sqrt{2}(1-\lambda)L\}$ & $\{(x-y) \leq 0\}$ $$z_{\mathrm{f2,s}}^{\mathrm{l}} = \frac{3H}{4} - \frac{H}{4}\cos\frac{2A_1-\pi}{2\lambda}$$ $$z_{\mathrm{f2,s}}^{\mathrm{u}} = \frac{3H}{4} + \frac{H}{4}\cos\frac{2A_1-\pi}{2\lambda}$$	$\{x' \geq (1-\lambda)L\}$ & $\{y' \geq 0\}$ $$z_{\mathrm{f2,s}}^{\mathrm{l}} = \frac{3H}{4} - \frac{H}{4}\cos\frac{\pi(x'-L)}{2\lambda L}$$ $$z_{\mathrm{f2,s}}^{\mathrm{u}} = \frac{3H}{4} + \frac{H}{4}\cos\frac{\pi(x'-L)}{2\lambda L}$$

✧ $A_1 = \frac{\sqrt{2}\pi(x+y)}{4L}, B_2 = \frac{\sqrt{2}\pi(x-y)}{2W}$

C.3 Off-axis mUC for 3D woven composites

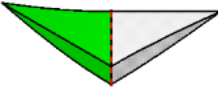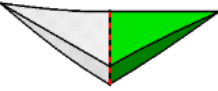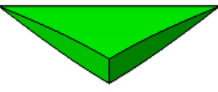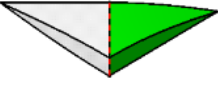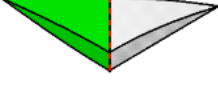**Table C.4: Analytical equations for warp yarns in the Off-axis 3D woven mUC**

Yarn type	In Off-axis CS (XYZ)	In normal CS (XY'Z')
Warp 1	$\{\lvert x - y\rvert \le \sqrt{2}\lambda_{\mathrm{w}}W\}$ $z_{\mathrm{w}1}^{\mathrm{l}} = H_1 - \dfrac{H_{\mathrm{w}}}{2}\cos\dfrac{B_1}{\lambda_{\mathrm{w}}}$ $z_{\mathrm{w}1}^{\mathrm{u}} = H_1 + \dfrac{H_{\mathrm{w}}}{2}\cos\dfrac{B_1}{\lambda_{\mathrm{w}}}$	$\{\lvert y'\rvert \le \lambda_{\mathrm{w}}W\}$ $z_{\mathrm{w}1}^{\mathrm{l}} = H_1 - \dfrac{H_{\mathrm{w}}}{2}\cos\dfrac{\pi y'}{2\lambda_{\mathrm{w}}W}$ $z_{\mathrm{w}1}^{\mathrm{u}} = H_1 + \dfrac{H_{\mathrm{w}}}{2}\cos\dfrac{\pi y'}{2\lambda_{\mathrm{w}}W}$
Warp 2	$\{\lvert x - y\rvert \le \sqrt{2}\lambda_{\mathrm{w}}W\}$ $z_{\mathrm{w}2}^{\mathrm{l}} = H_2 - \dfrac{H_{\mathrm{w}}}{2}\cos\dfrac{B_1}{\lambda_{\mathrm{w}}}$ $z_{\mathrm{w}2}^{\mathrm{u}} = H_2 + \dfrac{H_{\mathrm{w}}}{2}\cos\dfrac{B_1}{\lambda_{\mathrm{w}}}$	$\{\lvert y'\rvert \le \lambda_{\mathrm{w}}W\}$ $z_{\mathrm{w}2}^{\mathrm{l}} = H_2 - \dfrac{H_{\mathrm{w}}}{2}\cos\dfrac{\pi y'}{2\lambda_{\mathrm{w}}W}$ $z_{\mathrm{w}2}^{\mathrm{u}} = H_2 + \dfrac{H_{\mathrm{w}}}{2}\cos\dfrac{\pi y'}{2\lambda_{\mathrm{w}}W}$
Warp 3	$\{(x - y) \le \sqrt{2}(\lambda_{\mathrm{w}} - 2)W\}$ $z_{\mathrm{w}3}^{\mathrm{l}} = H_1 - \dfrac{H_{\mathrm{w}}}{2}\cos\dfrac{B_1 + \pi}{\lambda_{\mathrm{w}}}$ $z_{\mathrm{w}3}^{\mathrm{u}} = H_1 + \dfrac{H_{\mathrm{w}}}{2}\cos\dfrac{B_1 + \pi}{\lambda_{\mathrm{w}}}$	$\{y' \ge (2 - \lambda_{\mathrm{w}})W\}$ $z_{\mathrm{w}3}^{\mathrm{l}} = H_1 - \dfrac{H_{\mathrm{w}}}{2}\cos\left(\dfrac{\pi y'}{2\lambda_{\mathrm{w}}W} - \dfrac{\pi}{\lambda_{\mathrm{w}}}\right)$ $z_{\mathrm{w}3}^{\mathrm{u}} = H_1 + \dfrac{H_{\mathrm{w}}}{2}\cos\left(\dfrac{\pi y'}{2\lambda_{\mathrm{w}}W} - \dfrac{\pi}{\lambda_{\mathrm{w}}}\right)$
Warp 4	$\{(x - y) \le \sqrt{2}(\lambda_{\mathrm{w}} - 2)W\}$ $z_{\mathrm{w}4}^{\mathrm{l}} = H_2 - \dfrac{H_{\mathrm{w}}}{2}\cos\dfrac{B_1 + \pi}{\lambda_{\mathrm{w}}}$ $z_{\mathrm{w}4}^{\mathrm{u}} = H_2 + \dfrac{H_{\mathrm{w}}}{2}\cos\dfrac{B_1 + \pi}{\lambda_{\mathrm{w}}}$	$\{y' \ge (2 - \lambda_{\mathrm{w}})W\}$ $z_{\mathrm{w}4}^{\mathrm{l}} = H_2 - \dfrac{H_{\mathrm{w}}}{2}\cos\left(\dfrac{\pi y'}{2\lambda_{\mathrm{w}}W} - \dfrac{\pi}{\lambda_{\mathrm{w}}}\right)$ $z_{\mathrm{w}4}^{\mathrm{u}} = H_2 + \dfrac{H_{\mathrm{w}}}{2}\cos\left(\dfrac{\pi y'}{2\lambda_{\mathrm{w}}W} - \dfrac{\pi}{\lambda_{\mathrm{w}}}\right)$

✧ $B_1 = \dfrac{\sqrt{2}\pi(x-y)}{4W}$;

✧ $H_1 = H_{\mathrm{fa}} + \dfrac{H_{\mathrm{w}}}{2}$, $H_2 = H_{\mathrm{fa}} + H_{\mathrm{fb}} + \dfrac{3H_{\mathrm{w}}}{2}$
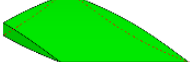
Table C.5: Analytical equations for fills 1, 2 & 3 in the Off-axis 3D woven mUC

Yarn type	In Off-axis CS (XYZ)	In normal CS (XY'Z')
Fill 1 (wavy)	$\{(x+y) \leq \sqrt{2}\lambda_{\mathrm{fa}}L\} \,\&\, \{(x-y) \leq 0\}$ $z^{\mathrm{l}}_{\mathrm{f1,w}} = H_3 - \dfrac{H_{\mathrm{fa}}}{2}\cos\dfrac{A_1}{\lambda_{\mathrm{fa}}} - \lambda H_{\mathrm{b}}\cos\dfrac{B_1}{\lambda}$ $z^{\mathrm{u}}_{\mathrm{f1,w}} = H_3 + \dfrac{H_{\mathrm{fa}}}{2}\cos\dfrac{A_1}{\lambda_{\mathrm{fa}}} - \lambda H_{\mathrm{b}}\cos\dfrac{B_1}{\lambda}$ $\theta_{\mathrm{f1,w}} = \tan^{-1}\!\left(-\dfrac{\pi H_{\mathrm{b}}}{2W}\sin\dfrac{B_1}{\lambda}\right)$	$\{x' \leq \lambda_{\mathrm{fa}}L\} \,\&\, \{y' \geq 0\}$ $z^{\mathrm{l}}_{\mathrm{f1,w}} = H_3 - \dfrac{H_{\mathrm{fa}}}{2}\cos\dfrac{\pi x'}{2\lambda_{\mathrm{fa}}L} - \lambda H_{\mathrm{b}}\cos\dfrac{\pi y'}{2\lambda W}$ $z^{\mathrm{u}}_{\mathrm{f1,w}} = H_3 + \dfrac{H_{\mathrm{fa}}}{2}\cos\dfrac{\pi x'}{2\lambda_{\mathrm{fa}}L} - \lambda H_{\mathrm{b}}\cos\dfrac{\pi y'}{2\lambda W}$ $\theta_{\mathrm{f1,w}} = \tan^{-1}\!\left(\dfrac{\pi H_{\mathrm{b}}}{2W}\sin\dfrac{\pi y'}{2\lambda W}\right)$
Fill 1 (straight)	$\{(x+y) \leq \sqrt{2}\lambda_{\mathrm{fa}}L\} \,\&\, \{(x-y) \geq 0\}$ $z^{\mathrm{l}}_{\mathrm{f1,s}} = \dfrac{H_{\mathrm{fa}}}{2} - \dfrac{H_{\mathrm{fa}}}{2}\cos\dfrac{A_1}{\lambda_{\mathrm{fa}}}$ $z^{\mathrm{u}}_{\mathrm{f1,s}} = \dfrac{H_{\mathrm{fa}}}{2} + \dfrac{H_{\mathrm{fa}}}{2}\cos\dfrac{A_1}{\lambda_{\mathrm{fa}}}$	$\{x' \leq \lambda_{\mathrm{fa}}L\} \,\&\, \{y' \leq 0\}$ $z^{\mathrm{l}}_{\mathrm{f1,s}} = \dfrac{H_{\mathrm{fa}}}{2} - \dfrac{H_{\mathrm{fa}}}{2}\cos\dfrac{\pi x'}{2\lambda_{\mathrm{fa}}L}$ $z^{\mathrm{u}}_{\mathrm{f1,s}} = \dfrac{H_{\mathrm{fa}}}{2} + \dfrac{H_{\mathrm{fa}}}{2}\cos\dfrac{\pi x'}{2\lambda_{\mathrm{fa}}L}$
Fill 2	$\{(x+y) \leq \sqrt{2}\lambda_{\mathrm{fb}}L\}$ $z^{\mathrm{l}}_{\mathrm{f2}} = H_4 - \dfrac{H_{\mathrm{fb}}}{2}\cos\dfrac{A_1}{\lambda_{\mathrm{fb}}}$ $z^{\mathrm{u}}_{\mathrm{f2}} = H_4 + \dfrac{H_{\mathrm{fb}}}{2}\cos\dfrac{A_1}{\lambda_{\mathrm{fb}}}$	$\{x' \leq \lambda_{\mathrm{fb}}L\}$ $z^{\mathrm{l}}_{\mathrm{f2}} = H_4 - \dfrac{H_{\mathrm{fb}}}{2}\cos\dfrac{\pi x'}{2\lambda_{\mathrm{fb}}L}$ $z^{\mathrm{u}}_{\mathrm{f2}} = H_4 + \dfrac{H_{\mathrm{fb}}}{2}\cos\dfrac{\pi x'}{2\lambda_{\mathrm{fb}}L}$
Fill 3 (wavy)	$\{(x+y) \leq \sqrt{2}\lambda_{\mathrm{fa}}L\} \,\&\, \{(x-y) \geq 0\}$ $z^{\mathrm{l}}_{\mathrm{f3,w}} = H_5 - \dfrac{H_{\mathrm{fa}}}{2}\cos\dfrac{A_1}{\lambda_{\mathrm{fa}}} + \lambda H_{\mathrm{b}}\cos\dfrac{B_1}{\lambda}$ $z^{\mathrm{u}}_{\mathrm{f3,w}} = H_5 + \dfrac{H_{\mathrm{fa}}}{2}\cos\dfrac{A_1}{\lambda_{\mathrm{fa}}} + \lambda H_{\mathrm{b}}\cos\dfrac{B_1}{\lambda}$ $\theta_{\mathrm{f3,w}} = \tan^{-1}\!\left(\dfrac{\pi H_{\mathrm{b}}}{2W}\sin\dfrac{B_1}{\lambda}\right)$	$\{x' \leq \lambda_{\mathrm{fa}}L\} \,\&\, \{y' \leq 0\}$ $z^{\mathrm{l}}_{\mathrm{f3,w}} = H_5 - \dfrac{H_{\mathrm{fa}}}{2}\cos\dfrac{\pi x'}{2\lambda_{\mathrm{fa}}L} + \lambda H_{\mathrm{b}}\cos\dfrac{\pi y'}{2\lambda W}$ $z^{\mathrm{u}}_{\mathrm{f3,w}} = H_5 + \dfrac{H_{\mathrm{fa}}}{2}\cos\dfrac{\pi x'}{2\lambda_{\mathrm{fa}}L} + \lambda H_{\mathrm{b}}\cos\dfrac{\pi y'}{2\lambda W}$ $\theta_{\mathrm{f3,w}} = \tan^{-1}\!\left(-\dfrac{\pi H_{\mathrm{b}}}{2W}\sin\dfrac{\pi y'}{2\lambda W}\right)$
Fill 3 (straight)	$\{(x+y) \leq \sqrt{2}\lambda_{\mathrm{fa}}L\} \,\&\, \{(x-y) \leq 0\}$ $z^{\mathrm{l}}_{\mathrm{f3,s}} = H - \dfrac{H_{\mathrm{fa}}}{2} - \dfrac{H_{\mathrm{fa}}}{2}\cos\dfrac{A_1}{\lambda_{\mathrm{fa}}}$ $z^{\mathrm{u}}_{\mathrm{f3,s}} = H - \dfrac{H_{\mathrm{fa}}}{2} + \dfrac{H_{\mathrm{fa}}}{2}\cos\dfrac{A_1}{\lambda_{\mathrm{fa}}}$	$\{x' \leq \lambda_{\mathrm{fa}}L\} \,\&\, \{y' \geq 0\}$ $z^{\mathrm{l}}_{\mathrm{f3,s}} = H - \dfrac{H_{\mathrm{fa}}}{2} - \dfrac{H_{\mathrm{fa}}}{2}\cos\dfrac{\pi x'}{2\lambda_{\mathrm{fa}}L}$ $z^{\mathrm{u}}_{\mathrm{f3,s}} = H - \dfrac{H_{\mathrm{fa}}}{2} + \dfrac{H_{\mathrm{fa}}}{2}\cos\dfrac{\pi x'}{2\lambda_{\mathrm{fa}}L}$

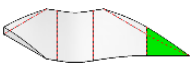✧ $A_1 = \dfrac{\sqrt{2}\pi(x+y)}{4L}$, $B_1 = \dfrac{\sqrt{2}\pi(x-y)}{4W}$;
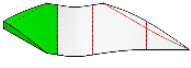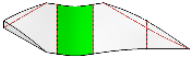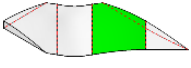
✧ $H_3 = \dfrac{H_{\mathrm{fa}}}{2} + \lambda H_{\mathrm{b}}$, $H_4 = H_{\mathrm{fa}} + H_{\mathrm{w}} + \dfrac{H_{\mathrm{fb}}}{2}$, $H_5 = H - \dfrac{H_{\mathrm{fa}}}{2} - \lambda H_{\mathrm{b}}$

Table C.6: Analytical equations for fills 4 & 5 in the Off-axis 3D woven mUC

Yarn type	In Off-axis CS (XYZ)	In normal CS (XY'Z')
Fill 4 (wavy)	$\{(x+y) \geq \sqrt{2}(2-\lambda_{\mathrm{fa}})L\}$ & $\{(x-y) \geq 0\}$ $z_{\mathrm{f4,w}}^{\mathrm{l}} = H_3 - \dfrac{H_{\mathrm{fa}}}{2}\cos\dfrac{A_1-\pi}{\lambda_{\mathrm{fa}}} - \lambda H_{\mathrm{b}}\cos\dfrac{B_1}{\lambda}$ $z_{\mathrm{f4,w}}^{\mathrm{u}} = H_3 + \dfrac{H_{\mathrm{fa}}}{2}\cos\dfrac{A_1-\pi}{\lambda_{\mathrm{fa}}} - \lambda H_{\mathrm{b}}\cos\dfrac{B_1}{\lambda}$ $\theta_{\mathrm{f4,w}} = \tan^{-1}\left(-\dfrac{\pi H_{\mathrm{b}}}{2W}\sin\dfrac{B_1}{\lambda}\right)$	$\{x' \geq (2-\lambda_{\mathrm{fa}})L\}$ & $\{y' \leq 0\}$ $z_{\mathrm{f4,w}}^{\mathrm{l}} = H_3 - \dfrac{H_{\mathrm{fa}}}{2}\cos\dfrac{\pi(x'-2L)}{2\lambda_{\mathrm{fa}}L} - \lambda H_{\mathrm{b}}\cos\dfrac{\pi y'}{2\lambda W}$ $z_{\mathrm{f4,w}}^{\mathrm{u}} = H_3 + \dfrac{H_{\mathrm{fa}}}{2}\cos\dfrac{\pi(x'-2L)}{2\lambda_{\mathrm{fa}}L} - \lambda H_{\mathrm{b}}\cos\dfrac{\pi y'}{2\lambda W}$ $= \tan^{-1}\left(\dfrac{\pi H_{\mathrm{b}}}{2W}\sin\dfrac{\pi y'}{2\lambda W}\right)$
Fill 4 (straight)	$\{(x+y) \geq \sqrt{2}(2-\lambda_{\mathrm{fa}})L\}$ & $\{(x-y) \leq 0\}$ $z_{\mathrm{f4,s}}^{\mathrm{l}} = \dfrac{H_{\mathrm{fa}}}{2} - \dfrac{H_{\mathrm{fa}}}{2}\cos\dfrac{A_1-\pi}{\lambda_{\mathrm{fa}}}$ $z_{\mathrm{f4,s}}^{\mathrm{u}} = \dfrac{H_{\mathrm{fa}}}{2} + \dfrac{H_{\mathrm{fa}}}{2}\cos\dfrac{A_1-\pi}{\lambda_{\mathrm{fa}}}$	$\{x' \geq (2-\lambda_{\mathrm{fa}})L\}$ & $\{y' \geq 0\}$ $z_{\mathrm{f4,s}}^{\mathrm{l}} = \dfrac{H_{\mathrm{fa}}}{2} - \dfrac{H_{\mathrm{fa}}}{2}\cos\dfrac{\pi(x'-2L)}{2\lambda_{\mathrm{fa}}L}$ $z_{\mathrm{f4,s}}^{\mathrm{u}} = \dfrac{H_{\mathrm{fa}}}{2} + \dfrac{H_{\mathrm{fa}}}{2}\cos\dfrac{\pi(x'-2L)}{2\lambda_{\mathrm{fa}}L}$
Fill 5	$\{(x+y) \geq \sqrt{2}(2-\lambda_{\mathrm{fb}})L\}$ $z_{\mathrm{f5}}^{\mathrm{l}} = H_4 - \dfrac{H_{\mathrm{fb}}}{2}\cos\dfrac{A_1-\pi}{\lambda_{\mathrm{fb}}}$ $z_{\mathrm{f5}}^{\mathrm{u}} = H_4 + \dfrac{H_{\mathrm{fb}}}{2}\cos\dfrac{A_1-\pi}{\lambda_{\mathrm{fb}}}$	$\{x' \geq (2-\lambda_{\mathrm{fb}})L\}$ $z_{\mathrm{f5}}^{\mathrm{l}} = H_4 - \dfrac{H_{\mathrm{fb}}}{2}\cos\dfrac{\pi(x'-2L)}{2\lambda_{\mathrm{fb}}L}$ $z_{\mathrm{f5}}^{\mathrm{u}} = H_4 + \dfrac{H_{\mathrm{fb}}}{2}\cos\dfrac{\pi(x'-2L)}{2\lambda_{\mathrm{fb}}L}$

✧ $A_1 = \dfrac{\sqrt{2}\pi(x+y)}{4L}$, $B_1 = \dfrac{\sqrt{2}\pi(x-y)}{4W}$;

✧ $H_3 = \dfrac{H_{\mathrm{fa}}}{2} + \lambda H_{\mathrm{b}}$, $H_4 = H_{\mathrm{fa}} + H_{\mathrm{w}} + \dfrac{H_{\mathrm{fb}}}{2}$

Table C.7: Analytical equations for fill 6 in the Off-axis 3D woven mUC
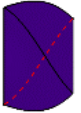
Yarn type	In Off-axis CS (XYZ)	In normal CS (XY'Z')
Fill 6 (part A)	$\{\|x + y - 2\sqrt{2}L\| \leq \sqrt{2}\lambda_{\text{fa}}L\}$ & $\{(x - y) \leq \sqrt{2}(\lambda - 2)W\}$ $z_{\text{f6,A}}^{\text{l}} = H_5 - \dfrac{H_{\text{fa}}}{2}\cos A_{\lambda1} + \lambda H_{\text{b}}\cos B_{\lambda1}$ $z_{\text{f6,A}}^{\text{u}} = H_5 + \dfrac{H_{\text{fa}}}{2}\cos A_{\lambda1} + \lambda H_{\text{b}}\cos B_{\lambda1}$ $\theta_{\text{f6,A}} = \tan^{-1}\left(\dfrac{\pi H_{\text{b}}}{2W}\sin B_{\lambda1}\right)$	$\{\|x' - 2L\| \leq \lambda_{\text{fa}}L\}$ & $\{y' \geq (2 - \lambda)W\}$ $z_{\text{f6,A}}^{\text{l}} = H_5 - \dfrac{H_{\text{fa}}}{2}\cos\dfrac{\pi(x' - 2L)}{2\lambda_{\text{fa}}L} + \lambda H_{\text{b}}\cos\dfrac{\pi(y' - 2W)}{2\lambda W}$ $z_{\text{f6,A}}^{\text{u}} = H_5 + \dfrac{H_{\text{fa}}}{2}\cos\dfrac{\pi(x' - 2L)}{2\lambda_{\text{fa}}L} + \lambda H_{\text{b}}\cos\dfrac{\pi(y' - 2W)}{2\lambda W}$ $\theta_{\text{f6,A}} = \tan^{-1}\left(-\dfrac{\pi H_{\text{b}}}{2W}\sin\dfrac{\pi(y' - 2W)}{2\lambda W}\right)$
Fill 6 (part B)	$\{\|x + y - 2\sqrt{2}L\| \leq \sqrt{2}\lambda_{\text{fa}}L\}$ & $\{\|x - y + \sqrt{2}W\| \leq \sqrt{2}(1 - \lambda)W\}$ $z_{\text{f6,B}}^{\text{l}} = H_5 - \dfrac{H_{\text{fa}}}{2}\cos A_{\lambda1} - H_\lambda\cos B_{\lambda2}$ $z_{\text{f6,B}}^{\text{u}} = H_5 + \dfrac{H_{\text{fa}}}{2}\cos A_{\lambda1} - H_\lambda\cos B_{\lambda2}$ $\theta_{\text{f6,B}} = \tan^{-1}\left(-\dfrac{\pi H_{\text{b}}}{2W}\sin B_{\lambda2}\right)$	$\{\|x' - 2L\| \leq \lambda_{\text{fa}}L\}$ & $\{\|y' - W\| \leq (1 - \lambda)W\}$ $z_{\text{f6,B}}^{\text{l}} = H_5 - \dfrac{H_{\text{fa}}}{2}\cos\dfrac{\pi(x' - 2L)}{2\lambda_{\text{fa}}L} - H_\lambda\cos\dfrac{\pi(y' - W)}{2(1 - \lambda)W}$ $z_{\text{f6,B}}^{\text{u}} = H_5 + \dfrac{H_{\text{fa}}}{2}\cos\dfrac{\pi(x' - 2L)}{2\lambda_{\text{fa}}L} - H_\lambda\cos\dfrac{\pi(y' - W)}{2(1 - \lambda)W}$ $\theta_{\text{f6,B}} = \tan^{-1}\left(\dfrac{\pi H_{\text{b}}}{2W}\sin\dfrac{\pi(y' - W)}{2(1 - \lambda)W}\right)$
Fill 6 (part C)	$\{\|x + y - 2\sqrt{2}L\| \leq \sqrt{2}\lambda_{\text{fa}}L\}$ & $\{-\sqrt{2}\lambda W \leq (x - y) \leq 0\}$ $z_{\text{f6,C}}^{\text{l}} = H_5 - \dfrac{H_{\text{fa}}}{2}\cos A_{\lambda1} + \lambda H_{\text{b}}\cos\dfrac{B_1}{\lambda}$ $z_{\text{f6,C}}^{\text{u}} = H_5 + \dfrac{H_{\text{fa}}}{2}\cos A_{\lambda1} + \lambda H_{\text{b}}\cos\dfrac{B_1}{\lambda}$ $\theta_{\text{f6,C}} = \tan^{-1}\left(\dfrac{\pi H_{\text{b}}}{2W}\sin\dfrac{B_1}{\lambda}\right)$	$\{\|x' - 2L\| \leq \lambda_{\text{fa}}L\}$ & $\{0 \leq y' \leq \lambda W\}$ $z_{\text{f6,C}}^{\text{l}} = H_5 - \dfrac{H_{\text{fa}}}{2}\cos\dfrac{\pi(x' - 2L)}{2\lambda_{\text{fa}}L} + \lambda H_{\text{b}}\cos\dfrac{\pi y'}{2\lambda W}$ $z_{\text{f6,C}}^{\text{u}} = H_5 + \dfrac{H_{\text{fa}}}{2}\cos\dfrac{\pi(x' - 2L)}{2\lambda_{\text{fa}}L} + \lambda H_{\text{b}}\cos\dfrac{\pi y'}{2\lambda W}$ $\theta_{\text{f6,C}} = \tan^{-1}\left(-\dfrac{\pi H_{\text{b}}}{2W}\sin\dfrac{\pi y'}{2\lambda W}\right)$
Fill 6 (part D)	$\{\|x + y - 2\sqrt{2}L\| \leq \sqrt{2}\lambda_{\text{fa}}L\}$ & $\{(x - y) \geq 0\}$ $z_{\text{f6,D}}^{\text{l}} = H - \dfrac{H_{\text{fa}}}{2} - \dfrac{H_{\text{fa}}}{2}\cos A_{\lambda1}$ $z_{\text{f6,D}}^{\text{u}} = H - \dfrac{H_{\text{fa}}}{2} + \dfrac{H_{\text{fa}}}{2}\cos A_{\lambda1}$	$\{\|x' - 2L\| \leq \lambda_{\text{fa}}L\}$ & $\{y' \leq 0\}$ $z_{\text{f6,D}}^{\text{l}} = H - \dfrac{H_{\text{fa}}}{2} - \dfrac{H_{\text{fa}}}{2}\cos\dfrac{\pi(x' - 2L)}{2\lambda_{\text{fa}}L}$ $z_{\text{f6,D}}^{\text{u}} = H - \dfrac{H_{\text{fa}}}{2} + \dfrac{H_{\text{fa}}}{2}\cos\dfrac{\pi(x' - 2L)}{2\lambda_{\text{fa}}L}$

✧ $A_1 = \dfrac{\sqrt{2}\pi(x+y)}{4L}$, $B_1 = \dfrac{\sqrt{2}\pi(x-y)}{4W}$;

✧ $A_{\lambda1} = \dfrac{A_1 - \pi}{\lambda_{\text{fa}}}$, $B_{\lambda1} = \dfrac{B_1 + \pi}{\lambda}$, $B_{\lambda2} = \dfrac{2B_1 + \pi}{2(1 - \lambda)}$;

✧ $H_5 = H - \dfrac{H_{\text{fa}}}{2} - \lambda H_{\text{b}}$, $H_\lambda = (1 - \lambda)H_{\text{b}}$

Table C.8: Analytical equations for binder yarns in the Off-axis 3D woven mUC

Yarn type		Surfaces & waviness in off-axis & normal coordinate systems ✧
Binder 1 (part A)	In Off-axis CS	$\{(x+y) \leq 2\sqrt{2}L\} \,\&\, \{\|x-y+\sqrt{2}W\| \leq \sqrt{2}\lambda_b W\}$ $z_{b1,A}^l = \dfrac{H}{2} + \dfrac{H_b}{2} - \dfrac{H_b}{2}\cos\dfrac{2B_1+\pi}{2\lambda_b} + m_0\tanh[s_0((x+y)/\sqrt{2}-L)] - \left\|\dfrac{H_b}{2\sin\theta_0}\right\|$ $z_{b1,A}^u = \dfrac{H}{2} - \dfrac{H_b}{2} + \dfrac{H_b}{2}\cos\dfrac{2B_1+\pi}{2\lambda_b} + m_0\tanh[s_0((x+y)/\sqrt{2}-L)] + \left\|\dfrac{H_b}{2\sin\theta_0}\right\|$ $\theta_{b1,A} = \tan^{-1}\left\{m_0 s_0\{1-\tanh^2[s_0((x+y)/\sqrt{2}-L)]\}\right\}$
	In normal CS	$\{x' \leq 2L\} \,\&\, \{\|y'-W\| \leq \lambda_b W\}$ $z_{b1,A}^l = \dfrac{H}{2} + \dfrac{H_b}{2} - \dfrac{H_b}{2}\cos\dfrac{\pi(y'-W)}{2\lambda_b W} + m_0\tanh[s_0(x'-L)] - \left\|\dfrac{H_b}{2\sin\theta_0}\right\|$ $z_{b1,A}^u = \dfrac{H}{2} - \dfrac{H_b}{2} + \dfrac{H_b}{2}\cos\dfrac{\pi(y'-W)}{2\lambda_b W} + m_0\tanh[s_0(x'-L)] + \left\|\dfrac{H_b}{2\sin\theta_0}\right\|$ $\theta_{b1,A} = \tan^{-1}\{m_0 s_0\{1-\tanh^2[s_0(x'-L)]\}\}$
Binder 1 (part B)	In Off-axis CS	$\{(x+y) \geq 2\sqrt{2}L\} \,\&\, \{\|x-y+\sqrt{2}W\| \leq \sqrt{2}\lambda_b W\}$ $z_{b1,B}^l = \dfrac{H}{2} + \dfrac{H_b}{2} - \dfrac{H_b}{2}\cos\dfrac{2B_1+\pi}{2\lambda_b} - m_0\tanh[s_0((x+y)/\sqrt{2}-3L)] - \left\|\dfrac{H_b}{2\sin\theta_1}\right\|$ $z_{b1,B}^u = \dfrac{H}{2} - \dfrac{H_b}{2} + \dfrac{H_b}{2}\cos\dfrac{2B_1+\pi}{2\lambda_b} - m_0\tanh[s_0((x+y)/\sqrt{2}-3L)] + \left\|\dfrac{H_b}{2\sin\theta_1}\right\|$ $\theta_{b1,B} = -\tan^{-1}\left\{m_0 s_0\{1-\tanh^2[s_0((x+y)/\sqrt{2}-3L)]\}\right\}$
	In normal CS	$\{x' \geq 2L\} \,\&\, \{\|y'-W\| \leq \lambda_b W\}$ $z_{b1,B}^l = \dfrac{H}{2} + \dfrac{H_b}{2} - \dfrac{H_b}{2}\cos\dfrac{\pi(y'-W)}{2\lambda_b W} - m_0\tanh[s_0(x'-3L)] - \left\|\dfrac{H_b}{2\sin\theta_1}\right\|$ $z_{b1,B}^u = \dfrac{H}{2} - \dfrac{H_b}{2} + \dfrac{H_b}{2}\cos\dfrac{\pi(y'-W)}{2\lambda_b W} - m_0\tanh[s_0(x'-3L)] + \left\|\dfrac{H_b}{2\sin\theta_1}\right\|$ $\theta_{b1,B} = -\tan^{-1}\{m_0 s_0\{1-\tanh^2[s_0(x'-3L)]\}\}$
Binder 2	In Off-axis CS	$\{\|x-y-\sqrt{2}W\| \leq \sqrt{2}\lambda_b W\}$ $z_{b2}^l = \dfrac{H}{2} + \dfrac{H_b}{2} - \dfrac{H_b}{2}\cos\dfrac{2B_1-\pi}{2\lambda_b} - m_0\tanh[s_0((x+y)/\sqrt{2}-L)] - \left\|\dfrac{H_b}{2\sin\theta_0}\right\|$ $z_{b2}^u = \dfrac{H}{2} - \dfrac{H_b}{2} + \dfrac{H_b}{2}\cos\dfrac{2B_1-\pi}{2\lambda_b} - m_0\tanh[s_0((x+y)/\sqrt{2}-L)] + \left\|\dfrac{H_b}{2\sin\theta_0}\right\|$ $\theta_{b2} = -\tan^{-1}\left\{m_0 s_0\{1-\tanh^2[s_0((x+y)/\sqrt{2}-L)]\}\right\}$
	In normal CS	$\{\|y'+W\| \leq \lambda_b W\}$ $z_{b2}^l = \dfrac{H}{2} + \dfrac{H_b}{2} - \dfrac{H_b}{2}\cos\dfrac{\pi(y'+W)}{2\lambda_b W} - m_0\tanh[s_0(x'-L)] - \left\|\dfrac{H_b}{2\sin\theta_0}\right\|$ $z_{b2}^u = \dfrac{H}{2} - \dfrac{H_b}{2} + \dfrac{H_b}{2}\cos\dfrac{\pi(y'+W)}{2\lambda_b W} - m_0\tanh[s_0(x'-L)] + \left\|\dfrac{H_b}{2\sin\theta_0}\right\|$ $\theta_{b2} = -\tan^{-1}\{m_0 s_0\{1-\tanh^2[s_0(x'-L)]\}\}$
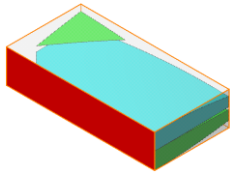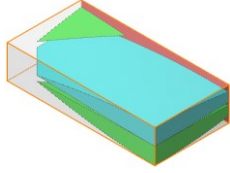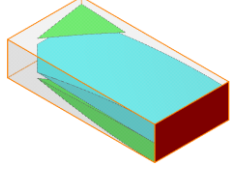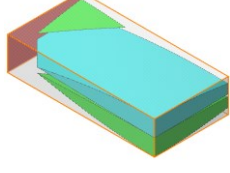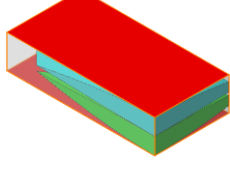
✧ $B_1 = \dfrac{\sqrt{2}\pi(x-y)}{4W}$, $\theta_0 = -\tan^{-1}\left\{\dfrac{1}{m_0 s_0\{1-\tanh^2[s_0(x'-L)]\}}\right\}$, $\theta_1 = -\tan^{-1}\left\{\dfrac{1}{m_0 s_0\{1-\tanh^2[s_0(x'-3L)]\}}\right\}$
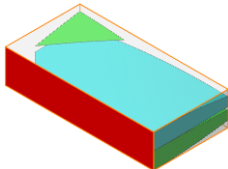
APPENDIX D

D.1 PBCs for off-axis plain woven mUC

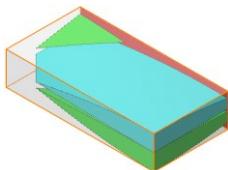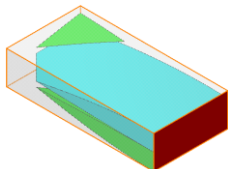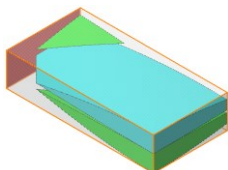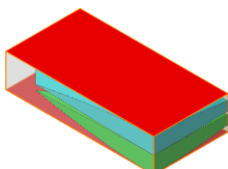*D.1.1 Normal loading case $\langle\sigma_{11}\rangle$, $\langle\sigma_{22}\rangle$ and $\langle\sigma_{33}\rangle$*

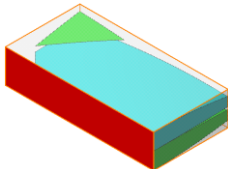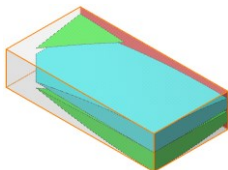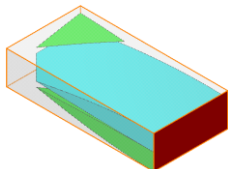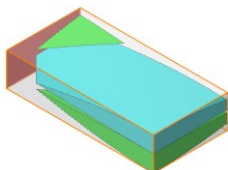**Table D.1: PBCs for off-axis plain woven composites under normal loading**

		$\boldsymbol{u}(A) - \gamma\mathbf{T}\boldsymbol{u}(\bar{A})$	$= -\langle\boldsymbol{\varepsilon}\rangle\boldsymbol{T}\boldsymbol{x}^{O_{\bar{D}}}$
S_1		$\begin{bmatrix} u_1\left(-\frac{L_o}{2},y,-z\right) \\ u_2\left(-\frac{L_o}{2},y,-z\right) \\ u_3\left(-\frac{L_o}{2},y,-z\right) \end{bmatrix} - \begin{bmatrix} -u_1\left(-\frac{L_o}{2},y,z\right) \\ u_2\left(-\frac{L_o}{2},y,z\right) \\ -u_3\left(-\frac{L_o}{2},y,z\right) \end{bmatrix}$	$= \begin{bmatrix} -L_o\langle\varepsilon_{11}\rangle \\ 0 \\ 0 \end{bmatrix}$
S_2		$\begin{bmatrix} u_1\left(\frac{L_o}{2},-y,-z\right) \\ u_2\left(\frac{L_o}{2},-y,-z\right) \\ u_3\left(\frac{L_o}{2},-y,-z\right) \end{bmatrix} - \begin{bmatrix} -u_1\left(\frac{L_o}{2},y,z\right) \\ -u_2\left(\frac{L_o}{2},y,z\right) \\ -u_3\left(\frac{L_o}{2},y,z\right) \end{bmatrix}$	$= \begin{bmatrix} L_o\langle\varepsilon_{11}\rangle \\ 0 \\ 0 \end{bmatrix}$
S_3		$\begin{bmatrix} u_1\left(x,-\frac{W_o}{2},-z\right) \\ u_2\left(x,-\frac{W_o}{2},-z\right) \\ u_3\left(x,-\frac{W_o}{2},-z\right) \end{bmatrix} - \begin{bmatrix} u_1\left(x,-\frac{W_o}{2},z\right) \\ -u_2\left(x,-\frac{W_o}{2},z\right) \\ -u_3\left(x,-\frac{W_o}{2},z\right) \end{bmatrix}$	$= \begin{bmatrix} 0 \\ -W_o\langle\varepsilon_{22}\rangle \\ 0 \end{bmatrix}$
S_4		$\begin{bmatrix} u_1\left(x,\frac{W_o}{2},-z\right) \\ u_2\left(x,\frac{W_o}{2},-z\right) \\ u_3\left(x,\frac{W_o}{2},-z\right) \end{bmatrix} - \begin{bmatrix} u_1\left(x,\frac{W_o}{2},z\right) \\ -u_2\left(x,\frac{W_o}{2},z\right) \\ -u_3\left(x,\frac{W_o}{2},z\right) \end{bmatrix}$	$= \begin{bmatrix} 0 \\ W_o\langle\varepsilon_{22}\rangle \\ 0 \end{bmatrix}$
S_5 & S_6		$\begin{bmatrix} u_1\left(x,y,\frac{H}{2}\right) \\ u_2\left(x,y,\frac{H}{2}\right) \\ u_3\left(x,y,\frac{H}{2}\right) \end{bmatrix} - \begin{bmatrix} u_1\left(x,y,-\frac{H}{2}\right) \\ u_2\left(x,y,-\frac{H}{2}\right) \\ u_3\left(x,y,-\frac{H}{2}\right) \end{bmatrix}$	$= \begin{bmatrix} 0 \\ 0 \\ H\langle\varepsilon_{33}\rangle \end{bmatrix}$

D.1.2 Shear loading case $\langle \sigma_{12} \rangle$

Table D.2: PBCs for off-axis plain woven composites under shear loading $\langle \sigma_{12} \rangle$
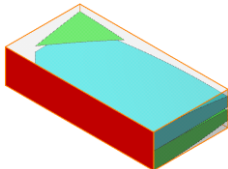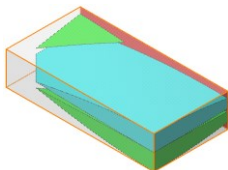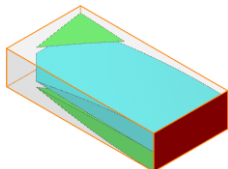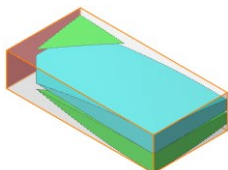
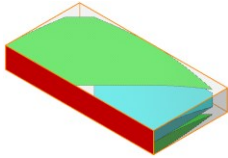|		$\boldsymbol{u}(A) - \gamma \mathbf{T} \boldsymbol{u}(\bar{A})$	$=$	$-\langle \boldsymbol{\varepsilon} \rangle \mathbf{T} \boldsymbol{x}^{O_{\bar{D}}}$
S_1		$\begin{bmatrix} u_1\left(-\frac{L_o}{2}, y, -z\right) \\ u_2\left(-\frac{L_o}{2}, y, -z\right) \\ u_3\left(-\frac{L_o}{2}, y, -z\right) \end{bmatrix} - \begin{bmatrix} u_1\left(-\frac{L_o}{2}, y, z\right) \\ -u_2\left(-\frac{L_o}{2}, y, z\right) \\ u_3\left(-\frac{L_o}{2}, y, z\right) \end{bmatrix}$	$=$	$\begin{bmatrix} 0 \\ -L_o\langle\varepsilon_{12}\rangle \\ 0 \end{bmatrix}$
S_2		$\begin{bmatrix} u_1\left(\frac{L_o}{2}, -y, -z\right) \\ u_2\left(\frac{L_o}{2}, -y, -z\right) \\ u_3\left(\frac{L_o}{2}, -y, -z\right) \end{bmatrix} - \begin{bmatrix} -u_1\left(\frac{L_o}{2}, y, z\right) \\ -u_2\left(\frac{L_o}{2}, y, z\right) \\ -u_3\left(\frac{L_o}{2}, y, z\right) \end{bmatrix}$	$=$	$\begin{bmatrix} 0 \\ L_o\langle\varepsilon_{12}\rangle \\ 0 \end{bmatrix}$
S_3		$\begin{bmatrix} u_1\left(x, -\frac{W_o}{2}, -z\right) \\ u_2\left(x, -\frac{W_o}{2}, -z\right) \\ u_3\left(x, -\frac{W_o}{2}, -z\right) \end{bmatrix} - \begin{bmatrix} -u_1\left(x, -\frac{W_o}{2}, z\right) \\ u_2\left(x, -\frac{W_o}{2}, z\right) \\ u_3\left(x, -\frac{W_o}{2}, z\right) \end{bmatrix}$	$=$	$\begin{bmatrix} -W_o\langle\varepsilon_{12}\rangle \\ 0 \\ 0 \end{bmatrix}$
S_4		$\begin{bmatrix} u_1\left(x, \frac{W_o}{2}, -z\right) \\ u_2\left(x, \frac{W_o}{2}, -z\right) \\ u_3\left(x, \frac{W_o}{2}, -z\right) \end{bmatrix} - \begin{bmatrix} -u_1\left(x, \frac{W_o}{2}, z\right) \\ u_2\left(x, \frac{W_o}{2}, z\right) \\ u_3\left(x, \frac{W_o}{2}, z\right) \end{bmatrix}$	$=$	$\begin{bmatrix} W_o\langle\varepsilon_{12}\rangle \\ 0 \\ 0 \end{bmatrix}$
S_5 & S_6		$\begin{bmatrix} u_1\left(x, y, \frac{H}{2}\right) \\ u_2\left(x, y, \frac{H}{2}\right) \\ u_3\left(x, y, \frac{H}{2}\right) \end{bmatrix} - \begin{bmatrix} u_1\left(x, y, -\frac{H}{2}\right) \\ u_2\left(x, y, -\frac{H}{2}\right) \\ u_3\left(x, y, -\frac{H}{2}\right) \end{bmatrix}$	$=$	$\begin{bmatrix} 0 \\ 0 \\ 0 \end{bmatrix}$

D.1.3 Shear loading case $\langle\sigma_{23}\rangle$

Table D.3: PBCs for off-axis plain woven composites under shear loading $\langle\sigma_{23}\rangle$

		$\boldsymbol{u}(A) - \gamma\mathbf{T}\boldsymbol{u}(\bar{A})$	$=$	$-\langle\boldsymbol{\varepsilon}\rangle\mathbf{T}\boldsymbol{x}^{O_{\bar{D}}}$
S_1		$\begin{bmatrix} u_1\left(-\frac{L_o}{2},y,-z\right) \\ u_2\left(-\frac{L_o}{2},y,-z\right) \\ u_3\left(-\frac{L_o}{2},y,-z\right) \end{bmatrix} - \begin{bmatrix} u_1\left(-\frac{L_o}{2},y,z\right) \\ -u_2\left(-\frac{L_o}{2},y,z\right) \\ u_3\left(-\frac{L_o}{2},y,z\right) \end{bmatrix}$	$=$	$\begin{bmatrix} 0 \\ 0 \\ 0 \end{bmatrix}$
S_2		$\begin{bmatrix} u_1\left(\frac{L_o}{2},-y,-z\right) \\ u_2\left(\frac{L_o}{2},-y,-z\right) \\ u_3\left(\frac{L_o}{2},-y,-z\right) \end{bmatrix} - \begin{bmatrix} -u_1\left(\frac{L_o}{2},y,z\right) \\ -u_2\left(\frac{L_o}{2},y,z\right) \\ -u_3\left(\frac{L_o}{2},y,z\right) \end{bmatrix}$	$=$	$\begin{bmatrix} 0 \\ 0 \\ 0 \end{bmatrix}$
S_3		$\begin{bmatrix} u_1\left(x,-\frac{W_o}{2},-z\right) \\ u_2\left(x,-\frac{W_o}{2},-z\right) \\ u_3\left(x,-\frac{W_o}{2},-z\right) \end{bmatrix} - \begin{bmatrix} u_1\left(x,-\frac{W_o}{2},z\right) \\ -u_2\left(x,-\frac{W_o}{2},z\right) \\ -u_3\left(x,-\frac{W_o}{2},z\right) \end{bmatrix}$	$=$	$\begin{bmatrix} 0 \\ 0 \\ -W_o\langle\varepsilon_{23}\rangle \end{bmatrix}$
S_4		$\begin{bmatrix} u_1\left(x,\frac{W_o}{2},-z\right) \\ u_2\left(x,\frac{W_o}{2},-z\right) \\ u_3\left(x,\frac{W_o}{2},-z\right) \end{bmatrix} - \begin{bmatrix} u_1\left(x,\frac{W_o}{2},z\right) \\ -u_2\left(x,\frac{W_o}{2},z\right) \\ -u_3\left(x,\frac{W_o}{2},z\right) \end{bmatrix}$	$=$	$\begin{bmatrix} 0 \\ 0 \\ W_o\langle\varepsilon_{23}\rangle \end{bmatrix}$
S_5 & S_6		$\begin{bmatrix} u_1\left(x,y,\frac{H}{2}\right) \\ u_2\left(x,y,\frac{H}{2}\right) \\ u_3\left(x,y,\frac{H}{2}\right) \end{bmatrix} - \begin{bmatrix} u_1\left(x,y,-\frac{H}{2}\right) \\ u_2\left(x,y,-\frac{H}{2}\right) \\ u_3\left(x,y,-\frac{H}{2}\right) \end{bmatrix}$	$=$	$\begin{bmatrix} 0 \\ H\langle\varepsilon_{23}\rangle \\ 0 \end{bmatrix}$

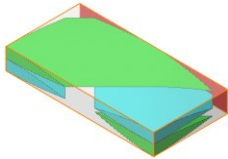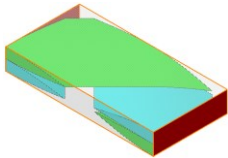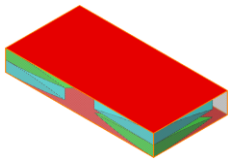*D.1.4 Shear loading case $\langle\sigma_{13}\rangle$*

Table D.4: PBCs for off-axis plain woven composites under shear loading $\langle\sigma_{13}\rangle$

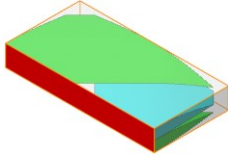|		$u(A) - \gamma \mathbf{T} u(\bar{A})$	=	$-\langle\varepsilon\rangle \mathbf{T} x^{O_{\bar{D}}}$
S_1		$\begin{bmatrix} u_1\left(-\frac{L_o}{2}, y, -z\right) \\ u_2\left(-\frac{L_o}{2}, y, -z\right) \\ u_3\left(-\frac{L_o}{2}, y, -z\right) \end{bmatrix} - \begin{bmatrix} -u_1\left(-\frac{L_o}{2}, y, z\right) \\ u_2\left(-\frac{L_o}{2}, y, z\right) \\ -u_3\left(-\frac{L_o}{2}, y, z\right) \end{bmatrix}$	=	$\begin{bmatrix} 0 \\ 0 \\ -L_o\langle\varepsilon_{13}\rangle \end{bmatrix}$
S_2		$\begin{bmatrix} u_1\left(\frac{L_o}{2}, -y, -z\right) \\ u_2\left(\frac{L_o}{2}, -y, -z\right) \\ u_3\left(\frac{L_o}{2}, -y, -z\right) \end{bmatrix} - \begin{bmatrix} -u_1\left(\frac{L_o}{2}, y, z\right) \\ -u_2\left(\frac{L_o}{2}, y, z\right) \\ -u_3\left(\frac{L_o}{2}, y, z\right) \end{bmatrix}$	=	$\begin{bmatrix} 0 \\ 0 \\ L_o\langle\varepsilon_{13}\rangle \end{bmatrix}$
S_3		$\begin{bmatrix} u_1\left(x, -\frac{W_o}{2}, -z\right) \\ u_2\left(x, -\frac{W_o}{2}, -z\right) \\ u_3\left(x, -\frac{W_o}{2}, -z\right) \end{bmatrix} - \begin{bmatrix} -u_1\left(x, -\frac{W_o}{2}, z\right) \\ u_2\left(x, -\frac{W_o}{2}, z\right) \\ u_3\left(x, -\frac{W_o}{2}, z\right) \end{bmatrix}$	=	$\begin{bmatrix} 0 \\ 0 \\ 0 \end{bmatrix}$
S_4		$\begin{bmatrix} u_1\left(x, \frac{W_o}{2}, -z\right) \\ u_2\left(x, \frac{W_o}{2}, -z\right) \\ u_3\left(x, \frac{W_o}{2}, -z\right) \end{bmatrix} - \begin{bmatrix} -u_1\left(x, \frac{W_o}{2}, z\right) \\ u_2\left(x, \frac{W_o}{2}, z\right) \\ u_3\left(x, \frac{W_o}{2}, z\right) \end{bmatrix}$	=	$\begin{bmatrix} 0 \\ 0 \\ 0 \end{bmatrix}$
S_5 & S_6		$\begin{bmatrix} u_1\left(x, y, \frac{H}{2}\right) \\ u_2\left(x, y, \frac{H}{2}\right) \\ u_3\left(x, y, \frac{H}{2}\right) \end{bmatrix} - \begin{bmatrix} u_1\left(x, y, -\frac{H}{2}\right) \\ u_2\left(x, y, -\frac{H}{2}\right) \\ u_3\left(x, y, -\frac{H}{2}\right) \end{bmatrix}$	=	$\begin{bmatrix} H\langle\varepsilon_{13}\rangle \\ 0 \\ 0 \end{bmatrix}$

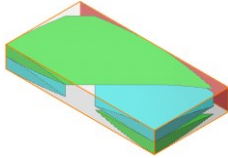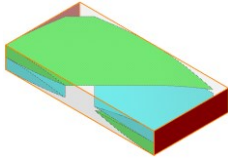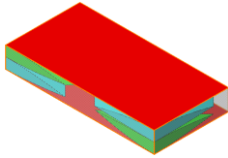## D.2 PBCs for off-axis twill woven mUC

D.2.1 Normal loading case $\langle \sigma_{11} \rangle$, $\langle \sigma_{22} \rangle$ and $\langle \sigma_{33} \rangle$

Table D.5: PBCs for off-axis twill woven composites under normal loading

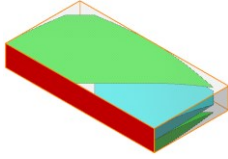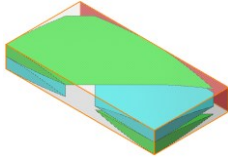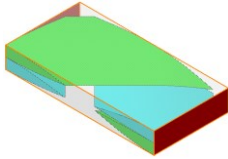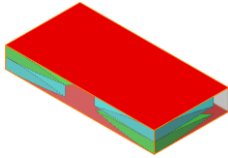|		$\boldsymbol{u}(A) - \gamma \mathbf{T}\boldsymbol{u}(\bar{A})$	$= -\langle \boldsymbol{\varepsilon} \rangle \mathbf{T} \boldsymbol{x}^{O_{\bar{D}}}$
S_1		$\begin{bmatrix} u_1\left(-\frac{L_o}{2}, y, -z\right) \\ u_2\left(-\frac{L_o}{2}, y, -z\right) \\ u_3\left(-\frac{L_o}{2}, y, -z\right) \end{bmatrix} - \begin{bmatrix} -u_1\left(-\frac{L_o}{2}, y, z\right) \\ u_2\left(-\frac{L_o}{2}, y, z\right) \\ -u_3\left(-\frac{L_o}{2}, y, z\right) \end{bmatrix}$	$= \begin{bmatrix} -L_o\langle \varepsilon_{11} \rangle \\ 0 \\ 0 \end{bmatrix}$
S_2		$\begin{bmatrix} u_1\left(\frac{L_o}{2}, y, -z\right) \\ u_2\left(\frac{L_o}{2}, y, -z\right) \\ u_3\left(\frac{L_o}{2}, y, -z\right) \end{bmatrix} - \begin{bmatrix} -u_1\left(\frac{L_o}{2}, y, z\right) \\ u_2\left(\frac{L_o}{2}, y, z\right) \\ -u_3\left(\frac{L_o}{2}, y, z\right) \end{bmatrix}$	$= \begin{bmatrix} L_o\langle \varepsilon_{11} \rangle \\ 0 \\ 0 \end{bmatrix}$
S_3 & S_4		$\begin{bmatrix} u_1\left(x, \frac{W_o}{2}, -z\right) \\ u_2\left(x, \frac{W_o}{2}, -z\right) \\ u_3\left(x, \frac{W_o}{2}, -z\right) \end{bmatrix} - \begin{bmatrix} u_1\left(x, -\frac{W_o}{2}, z\right) \\ u_2\left(x, -\frac{W_o}{2}, z\right) \\ -u_3\left(x, -\frac{W_o}{2}, z\right) \end{bmatrix}$	$= \begin{bmatrix} 0 \\ W_o\langle \varepsilon_{22} \rangle \\ 0 \end{bmatrix}$
S_5 & S_6		$\begin{bmatrix} u_1\left(x, y, \frac{H}{2}\right) \\ u_2\left(x, y, \frac{H}{2}\right) \\ u_3\left(x, y, \frac{H}{2}\right) \end{bmatrix} - \begin{bmatrix} u_1\left(x, y, -\frac{H}{2}\right) \\ u_2\left(x, y, -\frac{H}{2}\right) \\ u_3\left(x, y, -\frac{H}{2}\right) \end{bmatrix}$	$= \begin{bmatrix} 0 \\ 0 \\ H\langle \varepsilon_{33} \rangle \end{bmatrix}$

D.2.2 Shear loading case $\langle \sigma_{12} \rangle$

Table D.6: PBCs for off-axis twill woven composites under shear loading $\langle \sigma_{12} \rangle$

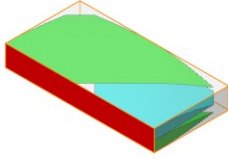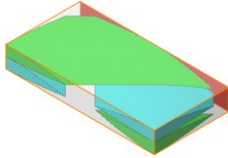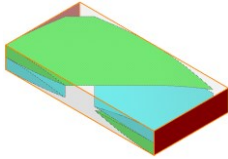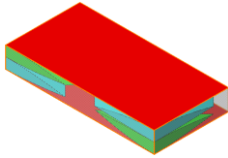|		$\boldsymbol{u}(A) - \gamma \mathbf{T}\boldsymbol{u}(\bar{A})$	$=$	$-\langle \boldsymbol{\varepsilon} \rangle \mathbf{T} x^{0_{\bar{D}}}$
S_1		$\begin{bmatrix} u_1\left(-\frac{L_o}{2}, y, -z\right) \\ u_2\left(-\frac{L_o}{2}, y, -z\right) \\ u_3\left(-\frac{L_o}{2}, y, -z\right) \end{bmatrix} - \begin{bmatrix} u_1\left(-\frac{L_o}{2}, y, z\right) \\ -u_2\left(-\frac{L_o}{2}, y, z\right) \\ u_3\left(-\frac{L_o}{2}, y, z\right) \end{bmatrix}$	$=$	$\begin{bmatrix} 0 \\ -L_o\langle\varepsilon_{12}\rangle \\ 0 \end{bmatrix}$
S_2		$\begin{bmatrix} u_1\left(\frac{L_o}{2}, y, -z\right) \\ u_2\left(\frac{L_o}{2}, y, -z\right) \\ u_3\left(\frac{L_o}{2}, y, -z\right) \end{bmatrix} - \begin{bmatrix} u_1\left(\frac{L_o}{2}, y, z\right) \\ -u_2\left(\frac{L_o}{2}, y, z\right) \\ u_3\left(\frac{L_o}{2}, y, z\right) \end{bmatrix}$	$=$	$\begin{bmatrix} 0 \\ L_o\langle\varepsilon_{12}\rangle \\ 0 \end{bmatrix}$
$S_3 \,\&\, S_4$		$\begin{bmatrix} u_1\left(x, \frac{W_o}{2}, -z\right) \\ u_2\left(x, \frac{W_o}{2}, -z\right) \\ u_3\left(x, \frac{W_o}{2}, -z\right) \end{bmatrix} - \begin{bmatrix} u_1\left(x, -\frac{W_o}{2}, z\right) \\ u_2\left(x, -\frac{W_o}{2}, z\right) \\ -u_3\left(x, -\frac{W_o}{2}, z\right) \end{bmatrix}$	$=$	$\begin{bmatrix} W_o\langle\varepsilon_{12}\rangle \\ 0 \\ 0 \end{bmatrix}$
$S_5 \,\&\, S_6$		$\begin{bmatrix} u_1\left(x, y, \frac{H}{2}\right) \\ u_2\left(x, y, \frac{H}{2}\right) \\ u_3\left(x, y, \frac{H}{2}\right) \end{bmatrix} - \begin{bmatrix} u_1\left(x, y, -\frac{H}{2}\right) \\ u_2\left(x, y, -\frac{H}{2}\right) \\ u_3\left(x, y, -\frac{H}{2}\right) \end{bmatrix}$	$=$	$\begin{bmatrix} 0 \\ 0 \\ 0 \end{bmatrix}$

D.2.3 Shear loading case $\langle \sigma_{23} \rangle$

Table D.7: PBCs for off-axis twill woven composites under shear loading $\langle \boldsymbol{\sigma_{23}} \rangle$

		$\boldsymbol{u}(A) - \gamma \mathbf{T}\boldsymbol{u}(\bar{A})$		$= $	$-\langle \boldsymbol{\varepsilon} \rangle \mathbf{T}\boldsymbol{x}^{O_{\bar{D}}}$
S_1		$\begin{bmatrix} u_1\left(-\frac{L_o}{2}, y, -z\right) \\ u_2\left(-\frac{L_o}{2}, y, -z\right) \\ u_3\left(-\frac{L_o}{2}, y, -z\right) \end{bmatrix} - \begin{bmatrix} u_1\left(-\frac{L_o}{2}, y, z\right) \\ -u_2\left(-\frac{L_o}{2}, y, z\right) \\ u_3\left(-\frac{L_o}{2}, y, z\right) \end{bmatrix}$		$=$	$\begin{bmatrix} 0 \\ 0 \\ 0 \end{bmatrix}$
S_2		$\begin{bmatrix} u_1\left(\frac{L_o}{2}, y, -z\right) \\ u_2\left(\frac{L_o}{2}, y, -z\right) \\ u_3\left(\frac{L_o}{2}, y, -z\right) \end{bmatrix} - \begin{bmatrix} u_1\left(\frac{L_o}{2}, y, z\right) \\ -u_2\left(\frac{L_o}{2}, y, z\right) \\ u_3\left(\frac{L_o}{2}, y, z\right) \end{bmatrix}$		$=$	$\begin{bmatrix} 0 \\ 0 \\ 0 \end{bmatrix}$
S_3 & S_4		$\begin{bmatrix} u_1\left(x, \frac{W_o}{2}, -z\right) \\ u_2\left(x, \frac{W_o}{2}, -z\right) \\ u_3\left(x, \frac{W_o}{2}, -z\right) \end{bmatrix} - \begin{bmatrix} -u_1\left(x, -\frac{W_o}{2}, z\right) \\ -u_2\left(x, -\frac{W_o}{2}, z\right) \\ u_3\left(x, -\frac{W_o}{2}, z\right) \end{bmatrix}$		$=$	$\begin{bmatrix} 0 \\ 0 \\ W_o\langle \varepsilon_{23} \rangle \end{bmatrix}$
S_5 & S_6		$\begin{bmatrix} u_1\left(x, y, \frac{H}{2}\right) \\ u_2\left(x, y, \frac{H}{2}\right) \\ u_3\left(x, y, \frac{H}{2}\right) \end{bmatrix} - \begin{bmatrix} u_1\left(x, y, -\frac{H}{2}\right) \\ u_2\left(x, y, -\frac{H}{2}\right) \\ u_3\left(x, y, -\frac{H}{2}\right) \end{bmatrix}$		$=$	$\begin{bmatrix} 0 \\ H\langle \varepsilon_{23} \rangle \\ 0 \end{bmatrix}$

D.2.4 Shear loading case $\langle \sigma_{13} \rangle$

Table D.8: PBCs for off-axis twill woven composites under shear loading $\langle \sigma_{13} \rangle$

		$\boldsymbol{u}(A) - \gamma \mathbf{T} \boldsymbol{u}(\bar{A})$	$=$	$-\langle \boldsymbol{\varepsilon} \rangle \mathbf{T} \boldsymbol{x}^{O_{\bar{D}}}$
S_1		$\begin{bmatrix} u_1\left(-\frac{L_o}{2}, y, -z\right) \\ u_2\left(-\frac{L_o}{2}, y, -z\right) \\ u_3\left(-\frac{L_o}{2}, y, -z\right) \end{bmatrix} - \begin{bmatrix} -u_1\left(-\frac{L_o}{2}, y, z\right) \\ u_2\left(-\frac{L_o}{2}, y, z\right) \\ -u_3\left(-\frac{L_o}{2}, y, z\right) \end{bmatrix}$	$=$	$\begin{bmatrix} 0 \\ 0 \\ -L_o\langle \varepsilon_{13} \rangle \end{bmatrix}$
S_2		$\begin{bmatrix} u_1\left(\frac{L_o}{2}, y, -z\right) \\ u_2\left(\frac{L_o}{2}, y, -z\right) \\ u_3\left(\frac{L_o}{2}, y, -z\right) \end{bmatrix} - \begin{bmatrix} -u_1\left(\frac{L_o}{2}, y, z\right) \\ u_2\left(\frac{L_o}{2}, y, z\right) \\ -u_3\left(\frac{L_o}{2}, y, z\right) \end{bmatrix}$	$=$	$\begin{bmatrix} 0 \\ 0 \\ L_o\langle \varepsilon_{13} \rangle \end{bmatrix}$
$S_3 \,\&\, S_4$		$\begin{bmatrix} u_1\left(x, \frac{W_o}{2}, -z\right) \\ u_2\left(x, \frac{W_o}{2}, -z\right) \\ u_3\left(x, \frac{W_o}{2}, -z\right) \end{bmatrix} - \begin{bmatrix} -u_1\left(x, -\frac{W_o}{2}, z\right) \\ -u_2\left(x, -\frac{W_o}{2}, z\right) \\ u_3\left(x, -\frac{W_o}{2}, z\right) \end{bmatrix}$	$=$	$\begin{bmatrix} 0 \\ 0 \\ 0 \end{bmatrix}$
$S_5 \,\&\, S_6$		$\begin{bmatrix} u_1\left(x, y, \frac{H}{2}\right) \\ u_2\left(x, y, \frac{H}{2}\right) \\ u_3\left(x, y, \frac{H}{2}\right) \end{bmatrix} - \begin{bmatrix} u_1\left(x, y, -\frac{H}{2}\right) \\ u_2\left(x, y, -\frac{H}{2}\right) \\ u_3\left(x, y, -\frac{H}{2}\right) \end{bmatrix}$	$=$	$\begin{bmatrix} H\langle \varepsilon_{13} \rangle \\ 0 \\ 0 \end{bmatrix}$

D.3 PBCs for off-axis 3D woven mUC

Table D.9: PBCs for off-axis 3D woven composites under normal/shear loading

		$u(A) - \gamma Tu(\bar{A})$		=	$-\langle \varepsilon \rangle Tx^{O_{\bar{D}}}$
S_1		$\begin{bmatrix} u_1\left(-\frac{L_o}{2}, -y, -z\right) \\ u_2\left(-\frac{L_o}{2}, -y, -z\right) \\ u_3\left(-\frac{L_o}{2}, -y, -z\right) \end{bmatrix}$	$\begin{bmatrix} -u_1\left(-\frac{L_o}{2}, y, z\right) \\ -u_2\left(-\frac{L_o}{2}, y, z\right) \\ -u_3\left(-\frac{L_o}{2}, y, z\right) \end{bmatrix}$	=	$\begin{bmatrix} -L_o\langle\varepsilon_{11}\rangle \\ -L_o\langle\varepsilon_{12}\rangle \\ -L_o\langle\varepsilon_{13}\rangle \end{bmatrix}$
S_2		$\begin{bmatrix} u_1\left(\frac{L_o}{2}, -y, -z\right) \\ u_2\left(\frac{L_o}{2}, -y, -z\right) \\ u_3\left(\frac{L_o}{2}, -y, -z\right) \end{bmatrix}$	$\begin{bmatrix} -u_1\left(\frac{L_o}{2}, y, z\right) \\ -u_2\left(\frac{L_o}{2}, y, z\right) \\ -u_3\left(\frac{L_o}{2}, y, z\right) \end{bmatrix}$	=	$\begin{bmatrix} L_o\langle\varepsilon_{11}\rangle \\ L_o\langle\varepsilon_{12}\rangle \\ L_o\langle\varepsilon_{13}\rangle \end{bmatrix}$
$S_3 \& S_4$		$\begin{bmatrix} u_1\left(x, \frac{W_o}{2}, z\right) \\ u_2\left(x, \frac{W_o}{2}, z\right) \\ u_3\left(x, \frac{W_o}{2}, z\right) \end{bmatrix}$	$\begin{bmatrix} u_1\left(x, -\frac{W_o}{2}, z\right) \\ u_2\left(x, -\frac{W_o}{2}, z\right) \\ u_3\left(x, -\frac{W_o}{2}, z\right) \end{bmatrix}$	=	$\begin{bmatrix} W_o\langle\varepsilon_{12}\rangle \\ W_o\langle\varepsilon_{22}\rangle \\ W_o\langle\varepsilon_{23}\rangle \end{bmatrix}$
$S_5 \& S_6$		$\begin{bmatrix} u_1\left(x, y, \frac{H}{2}\right) \\ u_2\left(x, y, \frac{H}{2}\right) \\ u_3\left(x, y, \frac{H}{2}\right) \end{bmatrix}$	$\begin{bmatrix} u_1\left(x, y, -\frac{H}{2}\right) \\ u_2\left(x, y, -\frac{H}{2}\right) \\ u_3\left(x, y, -\frac{H}{2}\right) \end{bmatrix}$	=	$\begin{bmatrix} H\langle\varepsilon_{13}\rangle \\ H\langle\varepsilon_{23}\rangle \\ H\langle\varepsilon_{33}\rangle \end{bmatrix}$